

# **X-RAY STRUCTURAL STUDIES OF ELECTROACTIVE FILMS**

Thesis submitted for the degree of  
Doctor of Philosophy  
at the University of Leicester

by  
Magdalena Anna Skopek MSc (Gdańsk)  
Department of Chemistry  
University of Leicester

November 2009

## X-ray Structural Studies of Electroactive Films

Magdalena A. Skopek

This thesis describes X-ray studies (XANES, EXAFS and XAS) of the structures of electroactive film modified electrodes and their response to potential. To provide insight into the composition, structure and dynamics of the studied systems EXAFS was combined with other techniques: XPS, electrochemical methods and infrared spectroscopy. The electroactive materials studied were Prussian Blue (PB) and its cobalt and nickel derivatives, iridium oxide and polypyrrole/[P(Mo<sub>3</sub>O<sub>10</sub>)<sub>4</sub>]<sup>3-</sup> composite films. Selected electroactive materials were diverse, since the study was undertaken with the aim of providing the foundations for future experiments in the area of the *dynamic in situ* EXAFS research.

For cobalt hexacyanoferrate films, cobalt was identified as the active redox site, based on clear evidence of changing bond lengths with potential. This suggests it will be an interesting candidate for future dynamic EXAFS study. The behaviour of PB films was found to be complicated to interpret because both redox sites are Fe-based and there exist additional interstitial iron species. In contrast to cobalt hexacyanoferrate, no significant changes could be observed in the Ni XAS data for the nickel derivative with Fe active redox sites. Polypyrrole/[P(Mo<sub>3</sub>O<sub>10</sub>)<sub>4</sub>]<sup>3-</sup> composite films showed changes in oxidation state of multiple Mo sites in XPS experiments. Nevertheless, they are not a promising material for a dynamic EXAFS because of the interpretational problems, similar to PB films. Iridium oxide films are another promising candidate. They were successfully characterized in *in situ* EXAFS configuration and changing bond lengths were observed as the potential (and thus Ir oxidation state) was changed.

Additionally the thesis includes nanogravimetric observation of ion exchange characteristics of polypyrrole film p-doping in an ionic liquid. It is shown that polypyrrole film redox switching in the deep eutectic ionic liquid (Ethaline) involves a very different pattern of ion transfers to aqueous media. Ionic liquid in the reduced film provides a reservoir of choline cations whose transfer (in the opposite direction to anion doping) partly satisfies electroneutrality.

Overall, the sites of redox activity were identified in a range of multi-site redox systems and structural changes were related to the injected charge. This static study is the first step in identifying systems suitable for X-ray synchrotron-based dynamic studies of electroactive film structure.

## ACKNOWLEDGEMENTS

It is a pleasure to thank the many people who made this thesis possible. First and foremost I offer my sincerest gratitude to my supervisors Rob Hillman and Steve Gurman for making this study possible, for knowledge and encouragement, patience and good humour throughout this PhD.

I am very grateful to Andrew Glidle, Karl Ryder, Mohamoud Mohamoud, Igor Efimov, Giro Frisch, Samantha Daisley, Joao Tedim, Anna Lisowska-Oleksiak, Andrzej Nowak and Monika Wilamowska for discussion, advice and the time they spend helping me out whenever I was stuck.

Beyond Physics and Chemistry many thanks to all my friends, especially Eleonora Bruzzi and Emilio Tuosto, Veronika Barinkova, Gino Varriale, Katy McKenzie, Gail Iles, Ugur Ural, Gauthier Torricelli, Nick Bezhanishvili, Michał Fornalczyk and Basia Śliwińska, Francesca Faedi and Riky, Qizhi Dong *vel* Lily, Aleksandra Kruss, Ann Beresford and Alex Goddard for the support, laugh and excellent time spent together.

I thank Mrs. Krystyna Wysocka for emotional support and sightseeing trips to the rainy and windy English countryside.

Thanks also to the guys in the Chemistry Workshop for meeting many tight deadlines and to all Staff in Chemistry Department. Also I would like to thank to Daresbury Laboratory scientists: Steven Fiddy, Bob Bilborrow, Graham Beamson and Danny Law.

I reserve my deepest gratitude for my family: Mum, Dad, Grandparents, Basia and Maja.

Special thanks to Filip, David and Alice for everything.

# LIST OF CONTENTS

<b>Abstract</b>	<b>2</b>
<b>Acknowledgements</b>	<b>3</b>
<b>I. Introduction. Aims and Scope</b>	<b>8</b>
1.1 X-ray Techniques	10
1.1.1 X-ray Photoelectron Spectroscopy	10
1.1.2 X-ray Absorption Spectroscopy	12
1.1.3 X-ray Absorption Near Edge Structure	16
1.1.4 Extended X-ray Absorption Fine Structure	18
1.1.5 Experimental Configurations for X-ray Absorption Spectroscopy	21
<i>i) Transmission Mode</i>	22
<i>ii) Fluorescence Mode</i>	23
1.1.6 Electrochemical Cells in EXAFS Spectroelectrochemistry	25
1.2 Electrochemical Techniques	26
1.2.1 Cyclic Voltammetry	28
<i>i) Nernstian (Reversible) Systems</i>	30
<i>ii) Totally Irreversible Systems</i>	31
1.2.2 Surface Adsorbed Species	32
1.2.3 Residual Currents	33
1.2.4 Mass Transport at Planar Electrodes	34
1.2.5 Fick's Laws of Diffusion	34
1.3 The Crystal Impedance Technique	35
1.3.1 The Quartz Crystal Microbalance	35
1.4 Infrared Spectroscopy	39
1.5 Chemically Modified Electrodes	40
1.5.1 Polymer Modified Electrodes	42

1.6	Ionic Liquids	44
1.7	References	47
<b>II.</b>	<b>General Experimental and Data Analysis Procedures</b>	<b>53</b>
2.1	Experimental	53
2.1.1	Electrochemical and EQCM Experimental Set-up	53
2.1.2	EXAFS Data Acquisition	55
2.1.3	Electrochemical Cells for EXAFS Spectroelectrochemistry	57
2.1.4	XPS Data Acquisition	59
2.2	Data Analysis	60
2.2.1	XAS Spectra Calibration, Background Subtraction and Normalisation	60
2.2.2	Determination of Structural Parameters from EXAFS	61
2.2.3	Atomic Concentrations from Transition Edge Steps	63
2.2.4	Spectroelectrochemical Data Analysis	64
2.3	References	66
<b>III.</b>	<b>Metal Hexacyanoferrate Electroactive Film Modified Electrodes</b>	<b>67</b>
3.1	Introduction	67
3.2	Characterization of PB and Related Metal Hexacyanoferrates	68
3.3	Iron Hexacyanoferrate $\text{Fe}[\text{Fe}(\text{CN})_6]$	71
3.4	Complications in the Preparation of Metal Hexacyanoferrates	72
3.5	Summary	72
3.6	Objectives	73
3.7	Experimental	75
3.7.1	X-ray Absorption Fine Structure	75
	<i>i) Preparation of Prussian Blue Modified Electrode</i>	75
	<i>ii) Preparation of CoHCF and NiHCF Modified Electrodes</i>	75
	<i>iii) XAS Data Collection: PB, CoHCF, NiHCF</i>	76
3.7.2	X-ray Photoelectron Spectroscopy	77
	<i>i) Preparation of Prussian Blue Modified Electrode</i>	77
	<i>ii) Preparation of CoHCF and NiHCF Modified Electrodes</i>	77

iii) XPS Data Collection and Spectra Processing: PB, CoHCF and NiHCF	77
3.7.3 Infrared Spectroscopy	78
3.8 Data Analysis	78
3.8.1 Prussian Blue Modified Electrode	78
3.8.2 CoHCF and NiHCF Modified Electrodes	79
3.9 Results	80
3.9.1 Iron Hexacyanoferrate Modified Electrode	80
3.9.2 Cobalt Hexacyanoferrate and Nickel Hexacyanoferrate Modified Electrodes	85
i) Extended X-ray Absorption Fine Structure	88
ii) X-ray Photoelectron Spectroscopy	94
iii) Infrared Spectroscopy	101
3.10 Discussion	103
3.10.1 Prussian Blue Modified Electrode	104
3.10.2 Cobalt and Nickel Hexacyanoferrate Samples	105
3.10.3 X-ray Photoelectron Spectroscopy and Infrared Spectroscopy	111
3.11 Conclusions	114
3.12 References	116
<b>IV. Anodically Deposited Iridium Oxide Electroactive Films</b>	<b>120</b>
4.1 Introduction	120
4.2 Objectives	122
4.3 Experimental and Sample Preparation	123
4.4 Data Analysis	125
4.5 Results	127
4.5.1 X-ray Photoelectron Spectroscopy	129
4.5.2 Extended X-ray Absorption Fine Structure	133
4.6 Discussion	142
4.7 Conclusions	146
4.8 References	148

<b>V. Phosphomolybdate Keggin Anion (PMo<sub>12</sub>O<sub>40</sub>)<sup>3-</sup> / Polypyrrole Hybrid Modified Electrode</b>	<b>150</b>
5.1 Introduction	150
5.2 Objectives	155
5.3 Experimental	156
5.3.1 Experimental Measurements	156
5.3.2 X-ray Photoelectron Spectroscopy	157
5.3.3 Extended X-ray Absorption Fine Structure	157
5.4 Data Analysis	158
5.5 Results and Discussion	159
5.5.1 Cyclic Voltammetry	159
5.5.2 X-ray Photoelectron Spectroscopy	162
5.5.3 X-ray Absorption Fine Structure Measurements	167
5.6 Conclusions	174
5.7 References	176
<b>VI. Nanogravimetric Observation of Ion Exchange Characteristics for Polypyrrole Film p-Doping in the Deep Eutectic Ionic Liquid Ethaline</b>	<b>179</b>
6.1 Introduction	179
6.2 Objectives	180
6.3 Experimental	181
6.4 Results	183
6.5 Discussion and Conclusions	189
6.6 References	192
<b>Conclusions</b>	<b>194</b>
<b>Publications</b>	<b>197</b>

# CHAPTER I

## INTRODUCTION

### **Aims and Scope**

The aim of the work described in this thesis was to understand performance and structural changes in electroactive film modified electrodes. A high degree of control at the molecular level is crucial in realization of the intentions of interfacial design of a modified electrode surface. As a consequence how the interface is designed is of paramount importance in determining the functioning of the final device. Most published work focuses on a single aspect - structure or dynamics – of an electrode modified with an electroactive film. Frequently, a material is extensively explored using several techniques, but the study is undertaken by different laboratories. Therefore, as even minor differences in preparation and handling can be crucial, such a body of work does not always provide a complete or consistent set of information. Here, an attempt was made to combine several techniques in such a manner as to provide insight into the composition, structure and dynamics of the target systems. The important feature is that great care was taken to prepare and handle all the samples identically. The primary experimental methods employed were:

- a) X-ray techniques: X-ray photoelectron spectroscopy (XPS), X-ray absorption near edge structure (XANES), extended X-ray absorption fine structure (EXAFS);
- b) Electrochemical techniques: cyclic voltammetry (CV), electrochemical quartz crystal microbalance (EQCM);
- c) Other spectroscopic techniques: infrared spectroscopy (IR).

It should be emphasized that, in the field of electrochemistry, EXAFS is a relatively under-explored technique. To be suitable for study with EXAFS samples and/or electrochemical cells must fulfil fairly restrictive requirements. Metals, metal complexes or metal-containing composites (for example metal species in polymer films) are frequently suitable for EXAFS study because of the ease of the detection of higher atomic number species by X-ray methods. The extended X-ray absorption fine structure technique can provide metal-ligand bond lengths, bond length changes introduced by diverse external stimuli, atomic identities and the level of (dis)order in the sample.

In the study presented in this thesis, potential control was used to introduce structural changes in electroactive films containing different types of metal redox centre. EXAFS, in combination with the techniques listed above, was used to explore the structure and changes in the structure of electrochemically deposited films of Prussian Blue and its cobalt and nickel derivatives, iridium oxide films and molybdenum Keggin-type heteropolyanions incorporated into a polymer matrix.

The thesis is structured as follows. The fundamentals of the techniques are described in Chapter I. The general experimental procedures and data analysis procedures are contained in Chapter II. In Chapters III, IV and V experimental results are presented for electrochemically-deposited Prussian Blue films and its cobalt and nickel derivatives, iridium oxide films and molybdenum Keggin type heteropolyanions incorporated into polymer matrix, respectively. In Chapter VI nanogravimetric observation of ion exchange characteristics for polypyrrole film p-doping in the ionic liquid, Ethaline, is described. The results are discussed and conclusions are drawn at the end of each chapter. The thesis ends with some generic remarks on the progress achieved and on future prospects for EXAFS studies of electroactive films.

## 1.1 X-ray Techniques

### 1.1.1 X-ray Photoelectron Spectroscopy

X-ray photoelectron spectroscopy (XPS), or electron spectroscopy for chemical analysis (ESCA) has its origins in the investigations of the photo-electric effect discovered by Hertz in 1887.<sup>1</sup> The term ESCA was introduced by K. Siegbahn, a pioneer in the use of XPS, because it provides not only information about atomic composition of a sample but also information about the structure and oxidation state of the compounds of interest.<sup>2</sup>

In XPS a beam of X-rays hits the sample's surface and interacts with core level electrons (1s, 2p, 2s orbitals etc.). For the exciting radiation of energy  $E=hn$ , equal or exceeding the binding energy  $E_B$  of an electron in a core initial state, absorption results in its ejection with kinetic energy  $E_K$ . This phenomenon, known as the photoelectric effect, leaves the atom in an excited state with a core hole. The kinetic energy of the emitted electron  $E_K$  is measured in an electron spectrometer. The binding energy of the electrons in the solid  $E_B$  can then be calculated according to:

$$E_B = hn - E_K - f \quad (1.1)$$

where  $f$  is the work function, whose precise value depends on both sample and spectrometer. Equation 1.1 assumes that the photoemission process is elastic. Therefore each characteristic X-ray (e.g. Mg  $K\alpha_{1,2}$ ) will give rise to a series of photoelectron peaks reflecting the discrete binding energies of the electrons present in a sample.

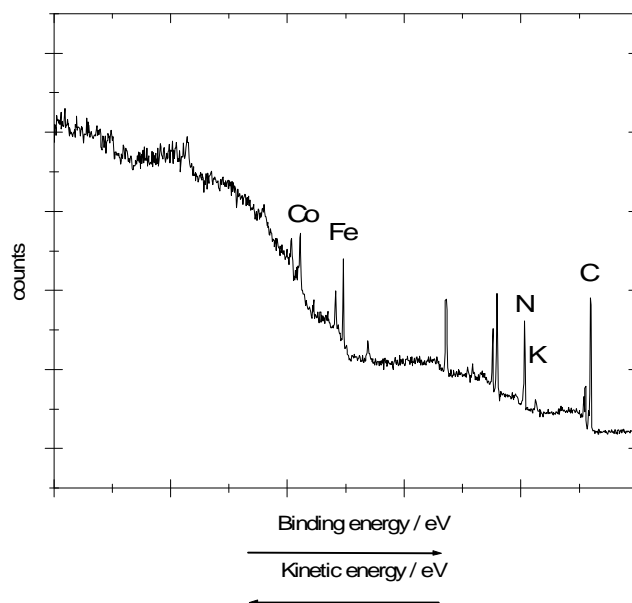


**Figure 1.1.** Wide scan X-ray photoelectron spectrum of cobalt hexacyanoferrate (CoHCF) electrodeposited film with Co, Fe, N, K, C photoelectron lines. Arrows show decreasing binding and kinetic energies.

Figure 1.1 shows a wide scan spectrum of a CoHCF film obtained at Daresbury Laboratory. A series of peaks is observed on a background. The background increases to high binding energy (low kinetic energy). It also shows characteristic rapid step-like increases on the low kinetic energy side of each peak due to energy loss of the photoelectron within the solid. It is a case of an inelastic photoemission process which occurs if the photoelectron suffers an energy change (usually loss) between photoemission and detection. Background shapes are dependant on the analysed materials and significant variation occurs in practice, and most often background shapes other than simple linear interpolation are necessary.<sup>3</sup>

Not all peaks in XPS spectra are due to simple photoelectric transitions. Secondary peaks may appear in a spectrum due to Auger transitions, plasmon structures, shake-up and shake-off energy loss processes. Peaks resulting from the excitation of the electrons which are not from the s subshell will appear in doublets. Electrons ejected from the core level can leave excited ion in one of two (XPS observable) states, characterized by

the  $j = l \pm \frac{1}{2}$  quantum number, which define the multiplicity of the state, namely  $2j+1$ . Hence, the relative intensities of the peaks in doublets are:  $(2(l-1/2)+1):(2(l+1/2)+1)$ , and for p electrons the spin-orbit splitting is: 1:2, for d electrons 2:3, and for f electrons 3:4. The energy separation of the doublet pairs depends on angular momentum and principal quantum numbers of the core level electrons. Doublets can be (widely) separated or can overlap.

XPS is a surface sensitive technique. X-rays are penetrating (microns range), but ejected photoelectrons are incapable of passing through more than a few atomic layers of a solid. Although XPS is generally regarded as non-destructive technique it is not always true. Exposure of the material to the ultra-high vacuum of the spectrometer or exposure to incident X-rays can result in damage of the sample.<sup>1</sup>

### 1.1.2 X-ray Absorption Spectroscopy

There are many X-ray techniques based on the scattering of radiation which are used for determination of the structure of the wide range of materials.<sup>4-6</sup> Commonly used example is X-ray diffraction.<sup>4, 6, 7</sup> A significantly restricting disadvantage of these methods is the fact that they require samples with a high degree of structural order, and are of no use in studying structures of disordered or amorphous materials such as electrochemically deposited films. On the contrary, X-ray absorption spectroscopy (XAS) involves the measurement of the absorption or fluorescence of a specific element within an investigated sample or molecule, giving the possibility to analyze crystalline, amorphous, liquid, or even gaseous state samples. The two regions of the X-ray spectrum of specific interest in XAS are shown in Figure 1.2. The first region, which appears near the absorption edge and includes the edge itself and pre-edge features, is most often referred to as X-ray absorption near-edge structure (XANES). The XANES region displays the structure originating from the absorption of X-ray radiation of energies just exceeding the binding energy of a core state. It results in promotion of core electrons to unoccupied atomic or molecular orbitals. XANES and the position of the edge can yield the information about the oxidation state of the absorbing element and identity of the surrounding atoms. The second region, extended X-ray absorption fine

structure (EXAFS), starts from the absorption edge and extends to approximately 1000 eV above it.

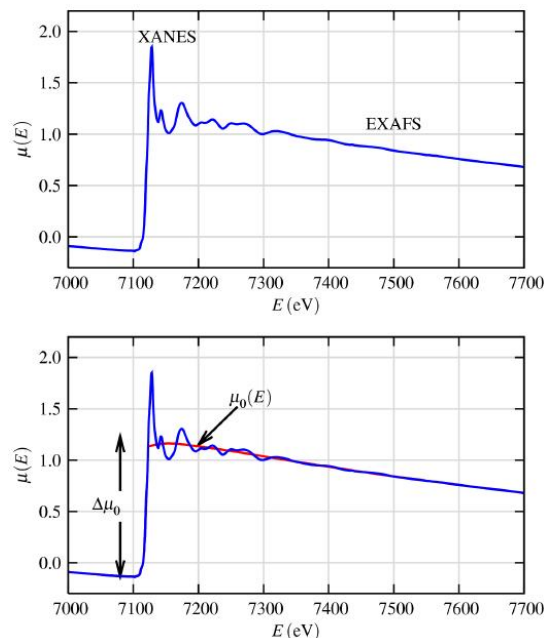


**Figure 1.2.** XAS  $\mu(E)$  for FeO. Top picture shows XAFS spectrum with identified regions of X-ray absorption near-edge structure (XANES) and extended X-ray absorption fine structure (EXAFS). On the bottom,  $\mu(E)$  is shown with smooth background function  $\mu_0(E)$  and the edge step  $\Delta\mu_0(E_0)$ .<sup>8</sup>

From EXAFS part of spectrum information such as number, identities and distances of the neighbouring atoms can be derived based on the magnitude of oscillations, energy dependence of the amplitude and frequencies of the oscillations, respectively.

Absorbance is described in terms of a linear absorption coefficient  $\mu$  ( $\text{cm}^{-1}$ ), or the mass absorption coefficient  $\mu' = \mu/\rho$  ( $\text{cm}^2\text{g}^{-1}$ ), the latter one being independent of the physical state of the sample. When an incident beam of X-rays of intensity  $I_0$  passes through a sample of uniform thickness  $x$ , they interact resulting in a transmitted reduced intensity  $I_t$  as shown in Figure 1.3. According to the Beer-Lambert law:

$$I_t(w) = I_0(w)e^{-m(w)x} \quad (1.1)$$

or:

$$\text{Absorbance} = \ln\left(\frac{I_0}{I_t}\right) = \mu x = \mu' \rho x \quad (1.2)$$

And the absorption coefficient is given by:

$$m = \frac{N\sigma}{x} = \rho \sigma \frac{N_A}{A} \quad (1.3)$$

where  $I_t$  is the transmitted intensity,  $\mu$  ( $\text{cm}^{-1}$ ) is the linear absorption coefficient,  $\mu' = \mu/\rho$  ( $\text{cm}^2\text{g}^{-1}$ ) is the mass absorption coefficient independent of the physical state of the sample,  $N_A$  ( $\text{mol}^{-1}$ ) is the Avogadro constant,  $A$  is the atomic mass,  $\rho$  is the density of the sample,  $\sigma$  ( $\text{cm}^2\text{mol}^{-1}$ ) is the absorption cross-section,  $\omega$  ( $\text{s}^{-1}$ ) is the angular frequency of the X-rays, and  $N$  is the number of atoms per  $\text{cm}^2$ .

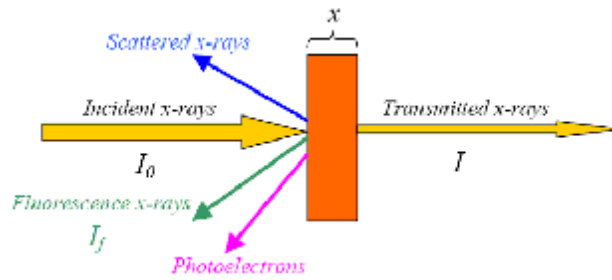


**Figure 1.3.** Interaction of X-rays with matter.<sup>9</sup>

There is a number of coexisting attenuation processes influencing the intensity of transmitted beam  $I_t$ . The absorption coefficient is the sum of these contributions as shown in Equation 1.4, and the predominant effect is strongly dependent on the energy (Figure 1.4).<sup>10</sup> Within the X-ray energy range of 1–30 keV (therefore of the main influence on XANES and EXAFS) photoelectric absorption  $\mu_{ph}$  is the major component to the absorption coefficient  $\mu$ :<sup>10</sup>

$$m = m_{ph} + m_{cs} + m_{is} + m_{pa} \quad (1.4)$$

Other contributions to Equation 1.4 involve coherent (elastic, Rayleigh) scattering  $\mu_{cs}$ , incoherent (inelastic, Compton) scattering  $\mu_{is}$ , and pair production (electron + hole, ion

or positron)  $\mu_{pa}$ . All these contributions calculated for cobalt are shown in the plot in Figure 1.4.

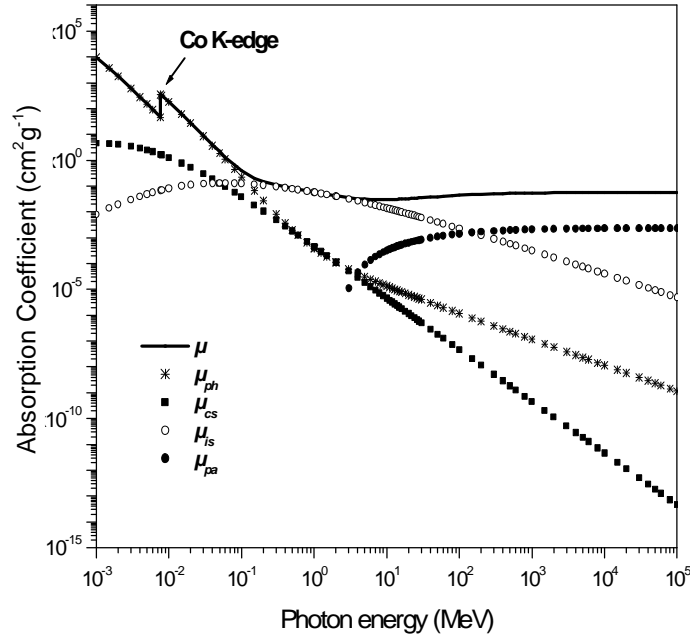


**Figure 1.4.** Total mass absorption coefficient with contributions: coherent (elastic, Rayleigh) scattering  $\mu_{cs}$ , incoherent (inelastic, Compton) scattering  $\mu_{is}$ , and pair production (electron + hole, ion or positron)  $\mu_{pa}$  calculated for cobalt as a function of photon energy.<sup>10</sup>

As the energy of the incident X-rays gradually increases, the absorption coefficient  $\mu$  slowly decreases in a manner depending on the sample density  $\rho$  and elements present in the sample. For the X-ray of energy equal to or just exceeding that of the binding energy of a core-level electron there is an abrupt rise in absorption coefficient. This discontinuity corresponds to the ejection of the core state electron to the continuum, and is called the absorption edge. In this process the electron is excited from a core level at  $E_I$  to the first fully unoccupied final state at  $E_F$  allowed by electric-dipole selection rules. It therefore follows that  $\mu$  is linked to the energy-dependent transition probability  $P$  for photoelectric absorption. In the dipole approximation<sup>11, 12</sup> the probability of X-ray absorption is given by:

$$P = \frac{2p^2 e^2}{\omega c^2 m} |\langle f | \mathbf{e} \cdot \mathbf{r} | i \rangle|^2 \mathbf{r}(E_F) \quad (1.5)$$

and:

$$m = \frac{4pe^2 w}{c} |\langle f | \mathbf{e} \cdot \mathbf{r} | i \rangle|^2 \mathbf{r}(E_F) \quad (1.6)$$

Here,  $|i\rangle$  is the initial state wavefunction for a bound electron before photoionisation,  $\langle f|$  is the final unoccupied state wavefunction for the ejected photoelectron, and  $\mathbf{r}(E_F)$  is the density of final allowed states of the photoelectron at the final state energy  $E_F$ , and  $2\pi\omega$  is the frequency of X-ray. Term  $|\mathbf{e} \cdot \mathbf{r}|$  is the electric-dipole matrix element, which contains the electric field polarisation vector  $\boldsymbol{\varepsilon}$  for the X-ray in the incident beam, and  $\mathbf{r}$ , the position vector for the location of the electron in the wavefunction;  $m$  is the rest mass of an electron and  $e$  is its charge;  $c$  is the velocity of the light, and  $w$  is the angular frequency of the X-rays.  $P$  is proportional to  $\mu$ , therefore the edge transition, known as photoionisation, is characterised by a large and abrupt increase in  $\mu$ , to give rise to the absorption edges as illustrated in Figure 1.2 and Figure 1.4.<sup>11-13</sup>

### 1.1.3 X-ray Absorption Near Edge Structure

The X-ray absorption near edge structure (XANES) includes the absorption edge together with the features appearing in the range from 10 eV below to 50 eV above it (Figure 1.2). XANES is a much larger signal than EXAFS and therefore can be done at lower concentrations, but the interpretation of XANES is more complicated as there is not a simple analytic description of XANES.<sup>8</sup> Low probability small amplitude transition peaks in the pre-edge region are the effect of the promotion of the bound, ground state electrons to the outer, partly occupied hybridised states, if such are present. Changes of shapes, positions and intensities of these features are a source of information about the existence and occupancy of discrete hybridised states just below the conduction band.

The most important feature of XANES is the absorption edge. An important application of XANES is to use the shift of the edge position to determine the valence state. Figure

1.5 shows the comparison of the XANES spectra for different iron compounds. The position of the edge depends on the binding energy  $E_B$  of the core electron. The binding energy of the electron is dependent on the structure of the material, and subsequently a shift in edge position is an indication of a valency change of the absorbing element.

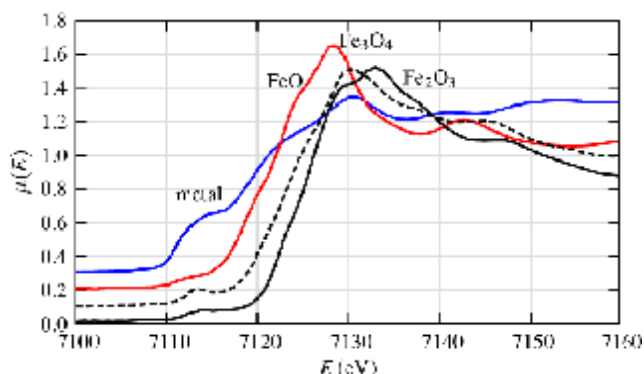


**Figure 1.5.** Comparison of Fe K-edge XANES of Fe metal and several Fe oxides. A clear relationship is visible between edge position and formal valence state. Shapes, positions and intensities of pre-edge peaks can be often correlated to oxidation state.<sup>8</sup>

Another source of information about conduction band structure and symmetry is the white line intensity. The white line is a continuation of the edge rise and is caused by the excitation of core electrons beyond the original edge transition to allowed levels in successively higher shells, if a high density of these states exists in the conduction band.<sup>13</sup> The white line may cause ambiguities in the identification of the precise edge position, which is often defined as half way up the normalised main edge height (excluding the white line). For a small white line (e.g. in metals) the edge position can be measured at the top of the white line or a half way up the full edge jump. This method is used when the relative position of the edge is more important than its absolute value (e.g. for the same samples changing redox states), providing that the size of the white line does not change with changing valency.

Precise and accurate modelling of all spectral features of XANES is still difficult, but for a lot of samples XANES analysis can be successfully based on linear combinations of spectra of known model compounds. Furthermore, although *ab initio* quantitative analyses of XANES are very rare, it is a tool providing qualitative information about the

density of unoccupied states, which are related to valence band structure and symmetry, and this is a source of quantitative information about the redox state of absorbing elements.<sup>8</sup>

#### 1.1.4 Extended X-ray Absorption Fine Structure

Fine structure above X-ray absorption edges had been reported for the first time in 1920 by Fricke<sup>14</sup> and Hertz<sup>15, 16</sup> who worked with the K-edges of magnesium, iron and chromium and with L-edges of caesium to neodymium. The term EXAFS was made up by Lytle<sup>17</sup>, and until 1970 the progress was slow as there was no theory explaining the observed spectra and because the experiments were difficult to perform before the availability of synchrotron radiation. Revival of interest in EXAFS returned with the publication of Sayers et al<sup>18</sup> where they suggested a model for understanding of observed fine structure. Another factor accelerating the development of EXAFS was availability of synchrotron radiation, which enabled the acquisition of spectra with excellent signal-to-noise ratio characteristics in minutes while in conventional X-ray tube data acquisition time varied from a few days to a few weeks and yielded very poor signal-to-noise ratios.<sup>12</sup>

The Extended X-ray Absorption Fine Structure model described here is based on the plane wave approximation.<sup>19-23</sup> Although simplistic, it illustrates the nature of the EXAFS phenomena in intelligible way. At low wave vector  $k$  values the plane wave approximation breaks down, hence the more advanced and complex spherical or curved wave theory<sup>22, 24</sup> is used for EXAFS computational simulations.<sup>19</sup>

EXAFS refers to oscillations in the slowly declining absorption coefficient. It spans from ca. 50 eV to several hundred eV beyond the absorption edge. These oscillations in absorption coefficient are explained by treating the ejected photoelectron as a spherical wave of wave vector  $k$  originating from an absorbing atom. For the photoelectron leaving the absorbing atom, a small fraction of its outgoing photoelectron wave is backscattered by surrounding atoms, giving rise to constructive and destructive interference between both waves. Figure 1.6 shows maxima and minima corresponding to interfering photoelectron waves.

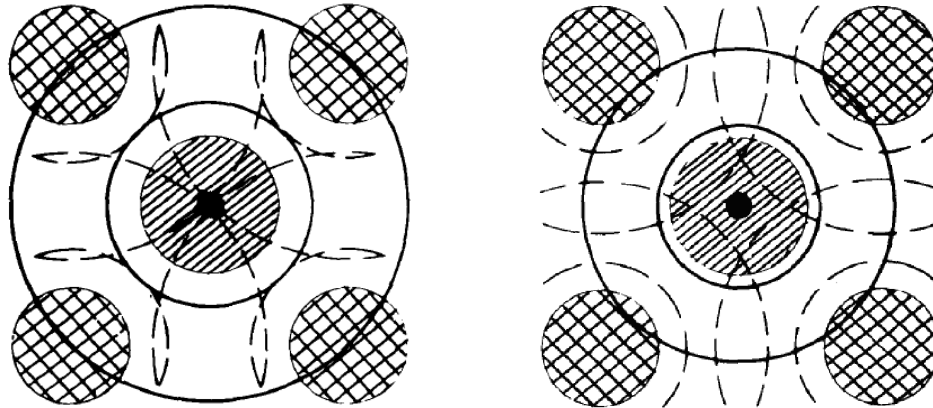


**Figure 1.6.** Schematic representation of EXAFS. The excited electronic state is centred at the central atom. The full circles represent the crests of the outgoing part of the photoelectric wave. The surrounding atoms backscatter the outgoing part as shown by the dashed lines. Constructive interference is represented on the left hand side picture and destructive interference on the right hand side picture.<sup>12</sup>

For lower energies, the wavelength  $\lambda$  of the photoelectron is large compared to the distance between the absorbing atom and the backscattering atoms. The mean free path of the photoelectron is long enough to experience multiple scattering (if the atoms are in collinear or triangular configuration) by the first and higher coordination shells giving rise to the post-edge XANES region. In the region of EXAFS photoelectrons have high kinetic energy and single scattering by the nearest neighbouring atoms dominates. If the absorbing element is a isolated free atom, there is no backscattering from the neighbouring atoms, and no oscillations are present as the absorption coefficient decays smoothly with energy. This smooth decrease for the isolated atom case is denoted as  $\mu_o$  and defines the background absorption level in XAS spectra. According to the plane wave approximation, for reasonably high energy ( $>50\text{eV}$ ), and therefore higher photoelectron  $k$  values, and moderate thermal or static disorder, EXAFS fine structure function  $\chi(E)$  is defined as:

$$c(E) = \frac{m(E) - m_0(E)}{m_0(E)} \quad (1.7)$$

where  $\mu(E)$  is the measured absorption coefficient and  $\mu_0(E)$  is a smoothly varying background function representing the absorption of a free atom. In order to relate  $\chi(E)$  to structural parameters it is necessary to convert the energy  $E$  into the photoelectron wave vector  $k$ . For the photoelectron with kinetic energy  $E_K$ :

$$E_K = \frac{p^2}{2m} = \frac{\hbar^2 k^2}{2m} \quad (1.8)$$

where  $p$  and  $m$  are, respectively, momentum and mass of an electron,  $\hbar = h/2\pi$  and  $k = 2\pi/\lambda$  is the wave vector, we can relate the electron wave vector  $k$  to the incident photon energy  $h\nu$  and binding energy  $E_0$  of a particular electronic shell of the atom as:

$$k = \sqrt{\frac{2m}{\hbar^2}(h\nu - E_0)} \quad (1.9)$$

This transformation of  $\chi(E)$  in  $E$  space gives rise to the EXAFS function  $\chi(k)$  in  $k$  space. The excitation of one electron may be treated semi-classically, with the photon being represented by an electromagnetic field, and the electron being treated quantum mechanically. Providing only back scattering at the angle  $\pi$  and single scattering events are considered, and distances are distributed harmonically, then in the plane wave approximation the EXAFS function for  $i$  shells of identical scattering atoms will be given by:<sup>23</sup>

$$c(k) = \sum_{i=1}^i A_i(k) \underbrace{\sin[2kR_i + 2d_i + j_i(k)]}_{\text{phase function}} \quad (1.10)$$

where  $A_i(k)$  is the amplitude function:

$$A_i(k) = \frac{\overbrace{S_0^2 e^{-\frac{2R_i}{I}}}_{\text{damping}} \underbrace{N_i \cdot |f_i(k)|}_{\text{backscattering}} \overbrace{e^{-2s_i^2 k^2}}_{\text{disorder}}}{kR_i^2} \quad (1.11)$$

In the above EXAFS equation  $R_i$  is the distance from the central atom to a scattering atom  $i$  and  $N_i$  is the number of scattering atoms of type  $i$ . The factor  $f_i(k)$  is the

scattering amplitude of atom  $i$ ,  $d_i$  is the phase shift undergone by the photoelectron at the central atom, and  $\varphi$  is the phase shift that the photoelectron undergoes when it bounces off the scattering atom, and returns to the central atom (hence  $2d_i$ ).  $A_i(k)$  is an amplitude reduction factor due to processes caused by multiple excitations at the central atom. (When the core electron is ejected it leaves a hole. The valence electrons rearrange because of this. These multielectron processes contribute to the edge jump, but not to EXAFS). The term  $\exp(-2\sigma_j^2 k^2)$  is another damping factor which accounts for amplitude loss due to disorder in the system. It contains the Debye-Waller factor  $\sigma_j^2$  which is the root mean square fluctuation about  $R_i$  (therefore the factor of 2). It accounts for the smearing out the EXAFS coming from a static disorder (high in the amorphous materials) and thermal vibration of the atoms. It is assumed that the fluctuation is harmonic and hence Gaussian pair distribution function, with the maximum at the mean interatomic distance  $R_j$ , a half width  $2\sigma_j$  and a standard deviation  $\sigma_j$ .

Although described in the simplistic way, the above EXAFS model shows that structural parameters such as interatomic distances, coordination numbers and (dis)order along with elemental identities of atoms present in the sample are contained in the EXAFS function. All these information can be extracted using the theoretical modelling of the EXAFS data. For the purpose of the computational EXAFS data fitting more complex rapid curved wave theory<sup>22, 24</sup> is used instead of the plane wave approximation presented here.

### 1.1.5 Experimental Configurations for X-ray Absorption Spectroscopy

Depending on the sample characteristics X-ray absorption spectra can be acquired using several different instrumental configurations sharing many common features. XAS can be measured either in transmission or decay (fluorescence, Auger emission) mode geometries. For a standard experiment, where discrete energy measurements are made, the following elements are needed:

- A method of monochromating the input beam;
- A method of measuring the intensity of the X-ray beam before and after hitting the sample;

- A data acquisition system;
- Optional elements (focusing optics, detector systems).

The choice of configuration depends on factors such as acquiring the best signal-to-noise ratio (this is associated with the concentration of absorbing atoms in the experimental material) or region of interest (e.g. interface). Two configurations described below, transmission and fluorescence mode, were used for the data acquisition presented in this thesis.

*i) Transmission Mode*

Transmission mode, illustrated in Figure 1.7, is the simplest and most straightforward method to measure EXAFS data.

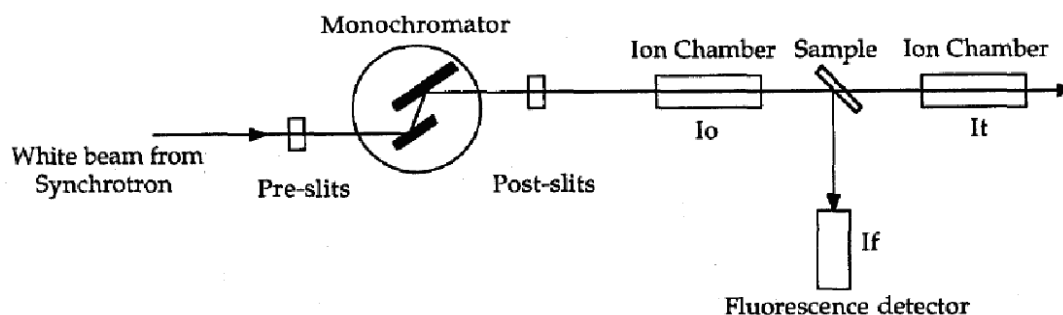


**Figure 1.7.** Schematic experimental set-up for an EXAFS experiment for a transmission measurement (signal =  $\ln(I_0/I_t)$ ), and for fluorescence measurement (signal =  $I_f/I_0$ ).<sup>25</sup>

A monochromatic and collimated beam transmitted through the sample is detected by noble gas filled ion chambers. These ion chambers consist of two parallel plates, one at high potential, in an inert gas atmosphere. Current is collected off the other plate and fed to an amplifier before measurement to record the beam intensity. The gas mixture is adjusted to absorb about 20% of the beam in the first chamber and 80% in the second. Internal simultaneous calibration of the edge energy can be achieved by placing a calibrant (a foil of pure absorber atoms of known thickness) in the beam path after the second ionisation chamber. The beam transmitted through the calibrant is then detected in a third ionisation chamber (not shown in the scheme). In this way the absorption

spectrum of the sample and of the calibrant are acquired simultaneously, and any errors in the energy scale can be corrected.

The angle of the monochromator crystals is changed to scan through the required energy range according to the modified Bragg equation:

$$n\lambda = 2d \sin \theta \left( 1 - \left[ \frac{\delta}{\sin^2 \theta} \right] \right) \quad (1.12)$$

where  $\delta$  is the decrement of refractive index resulting from refraction within the crystal. The energy can be scanned by changing the monochromator angle gradually (standard transmission XAS) or continuously (quick XAS). The sample has to be of the proper thickness, uniform and free of pinholes. X-ray absorption cross-sections are available from the databases. The thickness of the sample is estimated on this basis, depending on the elements accounting for the sample. In the ideal situation, the amount of the material in the sample should yield 60 to 80% transmittance below the absorption edge and 15 to 30 % transmittance at the top of the edge rise.<sup>26</sup>

## ii) *Fluorescence Mode*

There are two main secondary mechanisms for the decay of the excited atomic state following the X-ray absorption event: fluorescence and Auger emission. In fluorescence a higher energy electron fills the deeper core hole resulting in an X-ray of well defined energy. The second, non-radiative competing process for de-excitation is the Auger effect, in which an electron from a higher electron level fills the core hole and other electron is emitted into the continuum. With the atomic number  $Z$  or energy decrease the probability of Auger transitions rises. Fluorescence is emitted isotropically and hence the need for wide solid angle to collect as much of the signal as possible. The scattering of the incident beam is not emitted isotropically because X-rays from the synchrotron are polarised in the plane of the synchrotron ring. This greatly suppresses elastic scattering at 90° of the incident beam in the horizontal plane. Therefore solid-state detectors are placed at a right angle to the incident beam, and the sample is usually positioned at 45 ° with respect to the incident beam. Fluorescent radiation is measured

in the arrangement shown in Figure 1.7., and both,  $I_f$  and  $I_t$  can be collected simultaneously.

Another important factor is energy discrimination. This can suppress to great extent background intensity, and increase signal-to-noise level. Energy discrimination can be accomplished electronically after detection, or physically, by filtering out unwanted signal before it gets to the detector.

Fluorescence is proportional to the absorption probability, and for XAFS measured in fluorescence mode:

$$\text{Fluorescence} = \frac{I_f}{I_0} \cong m(E) \quad (1.13)$$

Equation 1.13 is over simplistic, because the probability of fluorescence is proportional to the absorption probability, but the fluorescence intensity measured in the experiment has to travel back through the sample before reaching the detector. Due to attenuation of X-rays, the fluorescence intensity (and consequently XAFS oscillations signal) can be damped because of self-absorption. This can be a serious problem in a case of concentrated samples, when XAFS can be even completely wiped out.

The low energy fluorescent photons are the most prone to the re-absorption by the sample itself, substrate and the cell. This disruption is recompensated by the consequent near-surface sensitivity of the signal. As fluorescent detection is much more sensitive, it can be used for surface studies (materials of a few nanometers of the surface layer) or diluted samples, such as impurities or additives, porous or electrochemically deposited films. Auger electrons can be also used for the XAFS measurement. The short escape depth for electrons makes this type of measurement very surface sensitive, and the method is called SEXAFS (surface EXAFS).

### 1.1.6 Electrochemical Cells in EXAFS Spectroelectrochemistry

Performance of the spectroelectrochemical cell is a critical factor influencing the quality of the acquired data. Parameters such as cell orientation with respect to optical source and detector, type of electrode, cell geometry or amount of electrolyte are designed to meet several, often conflicting electrochemical, spectroscopic and practical demands. In *situ* spectroelectrochemical cells have been used successfully for many years for XAS data acquisition.<sup>26-28</sup> Some more complicated designs allow data acquisition simultaneously in both transmission and fluorescence modes.<sup>29</sup> All components of the cell must have a minimum contribution to scattering and to the background level of absorption. Conventional three-electrode geometry with reference, counter and working electrodes is generally used, with the last one placed in the optical path. A common feature of such cells is the requirement for small solution volumes to minimize background interference from the solvent or electrolyte. When designing an in situ cell for EXAFS studies one has to keep in mind following points:

- The complete electrochemical conversion of the sample must be attained;
- Diffusional distances and cell resistance should be minimised, so the conversion is obtained in reasonable lengths of time;
- Enough material is necessary to obtain a good signal-to-noise ratio;
- Cell windows and other cell components in the X-ray beam path have to be transparent to X-rays.<sup>26</sup>

A common problem is water, which is widely used in electrochemical experiments, but in the same time is a large attenuator. To eliminate this difficulty thin layer cells are often used. For XAS experiments presented in this thesis a purpose-build cell was successfully used. Details of the cell are described in detail in the experimental chapter.

## 1.2 Electrochemical Techniques

In all experimental electrochemical techniques some electrical perturbation is applied to the working electrode (WE), and its response is recorded. Various techniques provide different, but complementary information about the studied system, such as kinetic parameters (e.g. rate constants and diffusion coefficients) or mechanistic information. Electrochemical techniques are widely used for the synthesis of electroactive films, with the possibility of monitoring the growth and degradation mechanisms during deposition and their response and behaviour in a range of contrasting environments.

A standard electrochemical cell used for electrochemical experiments (Figure 1.8) consists of the circuit of three electrodes immersed in a conducting supporting electrolyte solution.

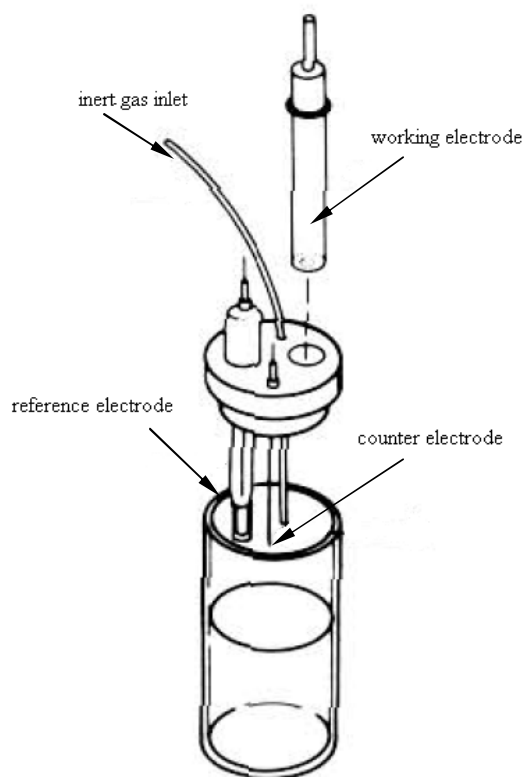


**Figure 1.8.** Scheme of a standard electrochemical cell.<sup>30</sup>

These three electrodes are: working electrode, a reference electrode (RE) and counter electrode or auxiliary electrode (CE). The processes under study occur at the WE, where the material of interest is attached in the case of modified electrodes. The WE is controlled via the potentiostat with respect to the RE. At the open circuit potential the current oscillates close to zero, because the equilibrium is reached as the electrons are exchanged at the electrode/electrolyte interfaces. No current passes through the RE electrode. It remains at equilibrium, and voltage is expressed with reference to it. To achieve this, the counter electrode is used to supply the WE with the current and avoid perturbation of the RE. In this thesis three types of reference electrodes were used: saturated mercury/mercurous chloride (saturated calomel electrode, SCE) or silver/silver chloride saturated KCl electrode (Ag/AgCl sat'd KCl) (aqueous systems), and silver wire pseudo-reference electrode (ionic liquid systems). To prevent the contamination of the bulk electrolyte, the RE contents are separated from the rest of the cell by a porous frit. In some cases the counter electrode is also separated by a frit or semi-permeable membrane to restrain the products of its reaction (if there any) from interfering with the process of interest. Constant temperature of the cell during electrochemical experiment can be maintained through the use of the water jacket and thermostat. A gas inlet is introduced if the ambient atmosphere of argon or nitrogen is required.

The supporting electrolyte is an electrically conductive medium containing free ions, and enabling the flow of current between the electrodes. It was introduced to electrochemistry for the first time in 1924 by the Czech chemist Heyrovsky.<sup>31</sup> Supporting electrolyte generally consists of ions dissolved in a liquid solvent, but solid and molten salt electrolytes are also possible. The last one will be described in detail in the chapter about ionic liquids. The mobile species in the solution, apart from their conductive role, preserve the neutrality of the working electrode.

Modified electrodes consisting of films of cobalt and nickel hexacyanoferrate, iridium oxide, molybdenum Keggin ions incorporated into a conducting polymer matrix (polypyrrole) and conducting polymer (polypyrrole) in ionic liquids are the subject of this thesis.

### 1.2.1 Cyclic Voltammetry

Cyclic voltammetry (CV) falls into the class of potentiodynamic experimental methods and is an extension of linear sweep voltammetry (LSV). CV consists of cycling the potential  $E$  of the working electrode (immersed in an unstirred solution), and measuring the resulting current  $i$ . The potential excitation signal is swept linearly at scan rate

$v = \left| \frac{dE}{dt} \right|$  ( $\text{V s}^{-1}$ ) so that the potential at any time is:

$$E(t) = E_i - vt \quad (1.14)$$

The potential of the electrode is swept between two values called switching potentials. In Figure 1.9a the excitation signal is first scanned negatively from  $+AV$  to  $-BV$  versus RE. At  $-BV$  the scan direction is reversed, and a positive scan is performed back to the original potential of  $+AV$ . The scan rate is reflected by a slope, and a second scan is indicated by the dashed line.

A plot obtained by measuring the current at the working electrode during the potential scan is called a cyclic voltammogram. The current can be considered the response signal to the potential excitation signal. A typical cyclic voltammogram for a system characterized by a reaction:



the response signal corresponding to the potential excitation signal is shown in Figure 1.9b. The initial potential  $+A$  V is applied – point ( $a$ ) at the right hand side figure. It is then scanned negatively and, when a sufficiently negative value to reduce the oxidized ( $Ox$ ) species is reached, faradaic current starts to flow ( $b$ ). The current increases exponentially ( $b \rightarrow d$ ), until the concentration of  $Ox$  at the electrode surface is depleted, causing the current to peak ( $d$ ),  $E_{pc}$ . Then the mass transfer from the bulk to the electrode surface is slower than the rate of consumption and the voltammetric response is governed by diffusion ( $d \rightarrow g$ ).

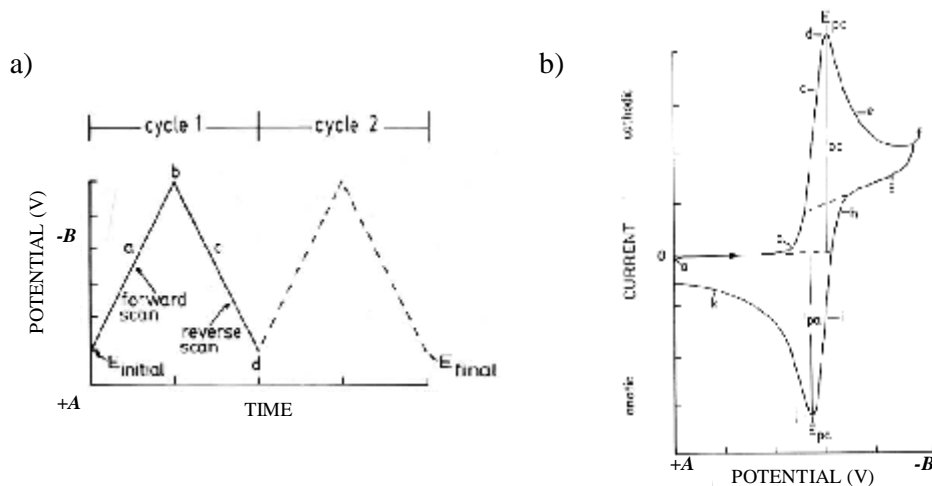


**Figure 1.9.** An example of typical signal in cyclic voltammetry experiment: the case of a species diffusing in solution. A triangular potential waveform with switching potentials at  $+A$  V and  $-B$  V (left). Response signal corresponding to the excitation signal on the left (right).<sup>30</sup>

The scan direction is switched to positive at  $-B$  V for the reverse scan. The potential is still sufficiently negative to reduce  $Ox$ , so cathodic current continues even though the potential is now scanning in the positive direction. When the electrode becomes a sufficiently strong oxidant, reduced species ( $Red$ ), which have been accumulating adjacent to the electrode, can now be oxidized. This causes anodic current ( $i \rightarrow k$ ). The first cycle is completed when the potential reaches  $+A$  V.

There are several factors which may affect the electrode reaction rate and the current, such as:

- Mass transfer of the species between the bulk and electrode surface;
- Rate of electron transfer at the electrode surface;
- Chemical reactions following or preceding the electron transfer;
- Other surface phenomena such as electrodeposition or adsorption/desorption processes.<sup>30, 32</sup>

Potential provides the driving force for the electrochemical reactions to occur:

$$\Delta G = -nFE \tag{1.16}$$

The activation parameters show an Arrhenius-like dependence on potential. Their relative timescales, thermodynamic or kinetic features can control the shape of  $i-E$  polarisation curve. On this basis different types of electrochemical responses can be characterized.

*i) Nernstian (Reversible) Systems*

If a redox system remains in equilibrium throughout the potential scan the electrochemical reaction is said to be reversible. The electrode potential and surface concentrations of *Ox* and *Red*, regardless of the current flow, are linked by an equation of the Nernst form:

$$E = E^{\circ'} + \frac{RT}{nF} \ln \frac{C_{Ox}}{C_{Red}} \quad (1.17)$$

where  $E^{\circ'}$  is the formal reduction potential. The interfacial redox kinetics are so fast that activation effects cannot be seen, and no kinetic parameters are present in the above equation. The potential and the surface concentrations are always kept in equilibrium with each other by the fast charge transfer processes, and the thermodynamic Equation 1.17 always holds.<sup>33</sup>

For a reversible wave,  $E_p$  is independent of scan rate, and peak current  $i_p$  (as well as the current at any other point of the wave) is proportional to  $v^{1/2}$ . At 25°C, for electrode area  $A$  (cm<sup>2</sup>), diffusion coefficient  $D_o$  (cm<sup>2</sup> s<sup>-1</sup>), concentration  $C_o^*$  (mol cm<sup>-3</sup>), and  $v$  (V s<sup>-1</sup>),  $i_p$  (A) is:

$$i_p = (2.69 \times 10^5) n^{3/2} A D_o^{1/2} v^{1/2} C_o^* \quad (1.18)$$

Furthermore, a convenient diagnostic for a Nernstian wave is the relation:

$$\Delta E_p = E_{pa} - E_{pc} \cong \frac{0.059}{n} \quad (1.19)$$

$$\left| \frac{i_{pa}}{i_{pc}} \right| = 1 \quad (1.20)$$

ii) *Totally Irreversible Systems*

For a totally irreversible reaction ( $Ox + ne^- \rightarrow Red$ ) the Nernst equation no longer applies. Peak current  $i_p$  (Equation 1.21) is still proportional to  $C_o^*$  and  $v^{1/2}$ , but  $E_p$  is a function of the scan rate  $v$ .

$$i_p = (2.99 \times 10^5) n (a n_a)^{1/2} A C_o^* D_o^{1/2} v^{1/2} \quad (1.21)$$

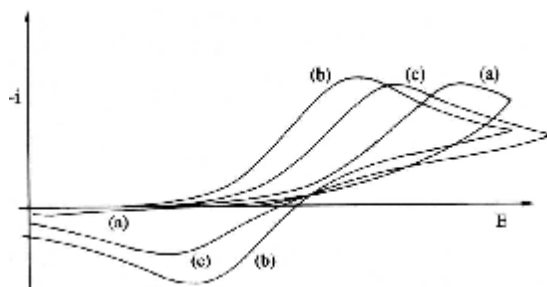


**Figure 1.10.** Cyclic voltammogram for (a) an irreversible, (b) a reversible, and (c) a quasi-reversible electron transfer reaction.<sup>34</sup>

Another type of the behaviour of electrochemical systems has been described for the first time by Matsuda and Ayabe.<sup>35</sup> They used the term quasi-reversible for reactions that show electron transfer kinetic limitations where the reverse reaction is considered.<sup>36</sup> These systems switch between reversible for slow scan rates, and irreversible behaviour for high scan rates. Figure 1.10 shows the examples of all three types of behaviour described above.

## 1.2.2 Surface Adsorbed Species

If species are uniformly adsorbed on to an electrode surface, and it is capable of undergoing a reversible one-electron transfer, it will give a cyclic voltammogram as shown in Figure 1.11.

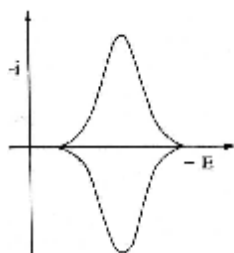


**Figure 1.11.** Cyclic voltammogram of the surface-adsorbed species.<sup>34</sup>

The symmetry of the voltammetric peaks occurs since the electrode reaction is now controlled only by electron transfer kinetics, and not by a coupled problem of diffusion and electron transfer. The differences in potentials of cathodic and anodic peaks are negligible. The areas of the two peaks are equal and provide direct measure (Equation 1.22) of the amount of charge  $Q$  required to perform the electrochemical reaction and therefore, the quantity of material adsorbed on the surface.<sup>34</sup>

$$Q = \int i dt = nFA\Gamma = nFN \quad (1.22)$$

where  $i$  is the current,  $n$  is the number of electrons transferred for each electroactive site,  $t$  is time,  $A$  is the electrode area,  $N$  (mol) is the amount of electroactive species present,  $\Gamma$  (mol cm<sup>-2</sup>) is the coverage of the electrode by this electroactive material, and  $F$  is Faraday's constant.

The values of  $i_p$ ,  $E_p$  and the peak width depend on the type of adsorption and on the relative strength of adsorption of reduced and oxidized species. For a system described by the Langmuir isotherm both peaks are equal and the peak current is given by:<sup>32</sup>

$$i_p = \frac{n^2 F^2 A \Gamma}{4RT} u \quad (1.23)$$

where  $\Gamma$  is the surface coverage:

$$\Gamma = \frac{Q}{nFA} \quad (1.24)$$

Deviation from the ideal behaviour will occur if the surface adsorbed species is not stable in either its charged or uncharged forms, or is desorbed during the potential cycling.

### 1.2.3 Residual Currents

Apart from the Faradaic current  $I_f$  associated with the system under the study one intends to measure there are also residual currents: Faradaic residual current and nonfaradaic charging (capacitive) current  $I_c$ . Both are intrinsic to the system and can limit the sensitivity of the measurement. Faradaic residual current is due to oxidation and reduction of traces of impurities (e.g. heavy metal ions or oxygen from the solvent or supporting electrolyte). Even in highly purified solutions, the non-Faradaic component can make the residual current large. The total current measured is given by:

$$I = I_f + I_c = I_f + C_d \frac{dE}{dt} = I_f + uC_d \quad (1.25)$$

where  $C_d$  is capacitance associated with the double layer charging, and  $v$  is the scan rate. It is easily seen that the contribution of double layer charging increases with increasing scan rate.

### 1.2.4 Mass Transport at Planar Electrodes

The supply of reactant and the removal of product from the electrode surface are essential to a continuing chemical change. In general, it is possible to have contributions from three forms of mass transport:

- **Diffusion** - movement of a species under the influence of a gradient of chemical potential (i.e., a concentration gradient);
- **Convection** - stirring or hydrodynamic transport. Fluid flow occurs because of natural convection (caused by density gradients) or forced convection;
- **Migration** - movement of charged species under the influence of an electric field (a gradient of electric potential).<sup>36</sup>

Mass transfer to an electrode is governed by the Nernst-Planck equation. For one-dimension along x-axis it is given as:

$$J_i(x,t) = -D_i \frac{\partial C_i(x,t)}{\partial x} - \frac{z_i F}{RT} D_i C_i(x,t) \frac{\partial f(x,t)}{\partial x} + C_i(x,t) u(x,t) \quad (1.26)$$

where  $J_i(x,t)$  is the flux of species  $i$  ( $\text{mol s}^{-1} \text{cm}^{-2}$ ) at distance  $x$  from the surface,  $D_i$  is the diffusion coefficient ( $\text{cm}^2 \text{s}^{-1}$ ),  $\partial C_i(x,t)/\partial x$  is the concentration gradient at distance  $x$ ,  $\partial f(x,t)/\partial x$  is the potential gradient,  $z_i$  and  $C_i(x,t)$  are the charge and concentration of species  $i$ , respectively, and  $v(x,t)$  is the velocity ( $\text{cm s}^{-1}$ ) with which a volume element in solution moves along the axis. The three terms on the right side of the Equation 1.26 represent the contributions of diffusion, migration and convection to the flux.<sup>36</sup>

### 1.2.5 Fick's Laws of Diffusion

For an experiment carried out with unstirred solution containing a large excess of base electrolyte diffusion is the predominant mode of mass transport, and processes of migration and convection may be neglected. In such conditions the system is described by Fick's laws of diffusion, which are differential equations describing the flux of a substance and its concentration as functions of time and position. Fick's first law states that the flux is proportional to the concentration gradient:

$$-J_i(x,t) = D_i \frac{\partial C_i(x,t)}{\partial x} \quad (1.27)$$

$J_i(x,t)$  represents the number of moles of  $i$  that pass a given location per second per  $\text{cm}^2$  of area normal to the axis of diffusion.

Fick's second law (Equation 1.28) describes the change in concentration  $i$  with time. For the one-dimensional case (e.g. large planar electrode with diffusion perpendicular to electrode surface):

$$\frac{\partial C_i(x,t)}{\partial t} = D_i \left( \frac{\partial^2 C_i(x,t)}{\partial x^2} \right) \quad (1.28)$$

## 1.3 The Crystal Impedance Technique

Piezoelectric properties and the low cost of quartz have made it an important component of many devices such as various types of gravimetric sensors, time-keeping instruments or material properties probes. The piezoelectricity is the ability to generate an electric potential in response to applied mechanical stress. This is derived from the Greek word *piezein*, meaning to press, squeeze. The piezoelectric effect is reversible, and materials exhibiting the direct piezoelectric effect (i.e. production of electricity as a reaction to stress) also exhibit the reverse piezoelectric effect (i.e. production of stress/strain when an electric field is applied). Many common materials, natural and man-made, exhibit piezoelectricity: cane sugar, topaz, bone, silk, polyvinylidene fluoride, some ceramics or quartz. In this section use of a quartz crystal as an electrochemical microbalance along with the basic principles of the technique will be described.

### 1.3.1 The Quartz Crystal Microbalance

Quartz possesses different types of piezoelectric modes of vibration. Specific modes can be enhanced depending on the crystallographic orientation in which the quartz is cut. The most common, resistant to changes in temperature, and particularly sensitive to mass changes is the thickness-shear mode (TSM). Such crystals are obtained by cutting

the quartz crystal in wafers at  $35^{\circ}15'$  with the respect to the z crystallographic axis and are called *AT-cut* crystals (Figure 1.12).<sup>32</sup>

The quartz crystal microbalance (QCM) is an acoustic wave device consisting of a thin disc of quartz with an electrode coated on each side of it (Figure 1.13). Owing to the piezoelectric properties and crystalline orientation of the quartz, the application of the voltage between these electrodes results in a shear deformation of the crystal (Figure 1.14).

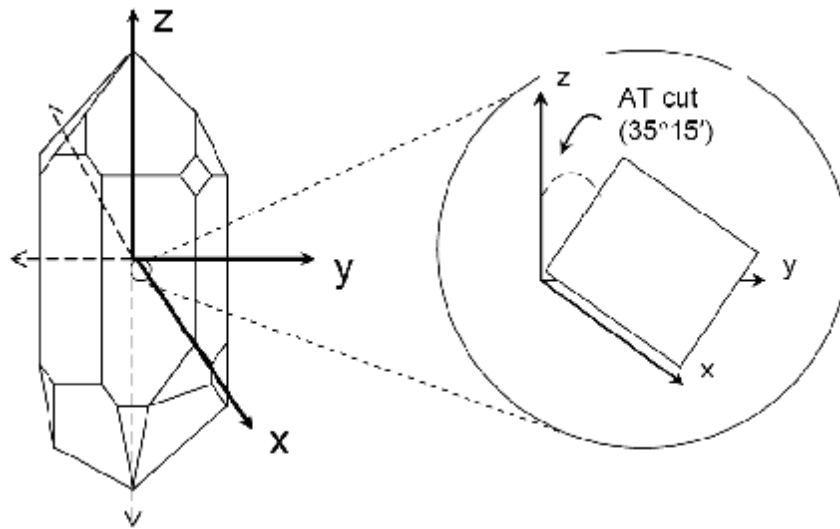


**Figure 1.12.** *AT-cut*  $\alpha$ -quartz crystal.<sup>37</sup>

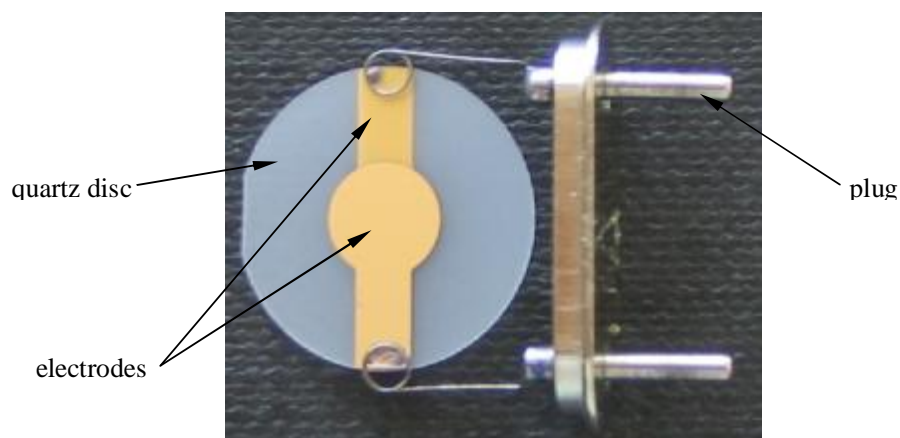


**Figure 1.13.** Thickness-shear mode resonator. Gold electrodes are attached to the both sides of the quartz crystal.

The crystal can be electrically excited to a number of resonant modes (harmonics), each corresponding to a unique standing shear wave across the crystal. If the resonator oscillating surface(s) are in contact with the medium they will interact and, as a result, mechanical properties of the contacting medium are reflected in the electrical properties of the resonator.<sup>38</sup>

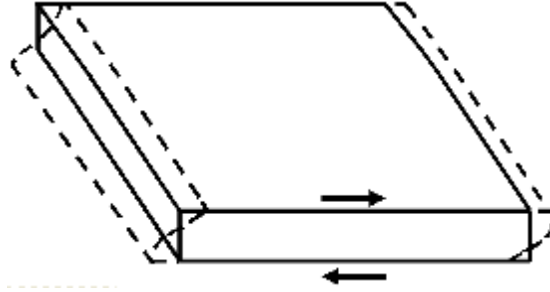


**Figure 1.14.** Schematic illustration of the fundamental thickness-shear deformation mode of an AT-cut quartz crystal.<sup>39</sup>

Monitoring the frequency response of a quartz crystal oscillator is a well established technique for the characterization of thin films. The first quantitative description was given by Sauerbrey in 1959.<sup>40</sup> The QCM technique is based on the principle that the resonant frequency change  $\Delta f$  of a quartz crystal oscillator in response to a change in the film areal density  $\Delta M$  ( $\text{g cm}^{-2}$ ) is given by:

$$\Delta f = f_{\Delta M} - f_o = - \left( \frac{-2f_o^2}{r_q \rho_q} \right) \Delta M \quad (1.29)$$

where  $\rho_q$  is the density of the crystal ( $2.65 \text{ g cm}^{-3}$ ),  $v_q$  is the wave velocity within it, and  $f_o$  is the initial frequency. For the above parameters and for a 10 MHz quartz crystal Equation 1.29 becomes:

$$\Delta m = -1.1 \cdot \Delta f \quad (1.30)$$

where  $\Delta m$  is the mass change in nanograms and  $\Delta f$  is the frequency change in Hz. The Sauerbrey model describes only thin and rigid films. In such cases, the film moves synchronously with the crystal, and is called an ideal mass layer, which is treated as a

rigidly coupled extension of the quartz. There is no amplitude loss or phase shift in the shear wave penetrating through the film. In the case of higher mass loads damping and deformation of the shear wave occurs. The relation between  $\Delta f$  and  $\Delta M$  fails to be linear hence the Sauerbrey equation can no longer be applied and more complex interpretation of the quartz response is required. The behaviour of the shear wave and its decay length  $\delta$  depends on the density  $\rho_L$  and viscosity  $\eta_L$  of the layer. The total frequency response has to be analysed with respect to appropriate contributing effect. Viscoelastic behaviour becomes apparent when the change of the frequency exceeds 2% of the value of the initial fundamental resonant frequency.<sup>37</sup> In the case of the 10 MHz quartz crystal it will be an equivalent of ca. 200 kHz frequency change ( $1 \text{ mg cm}^{-2}$  mass load).

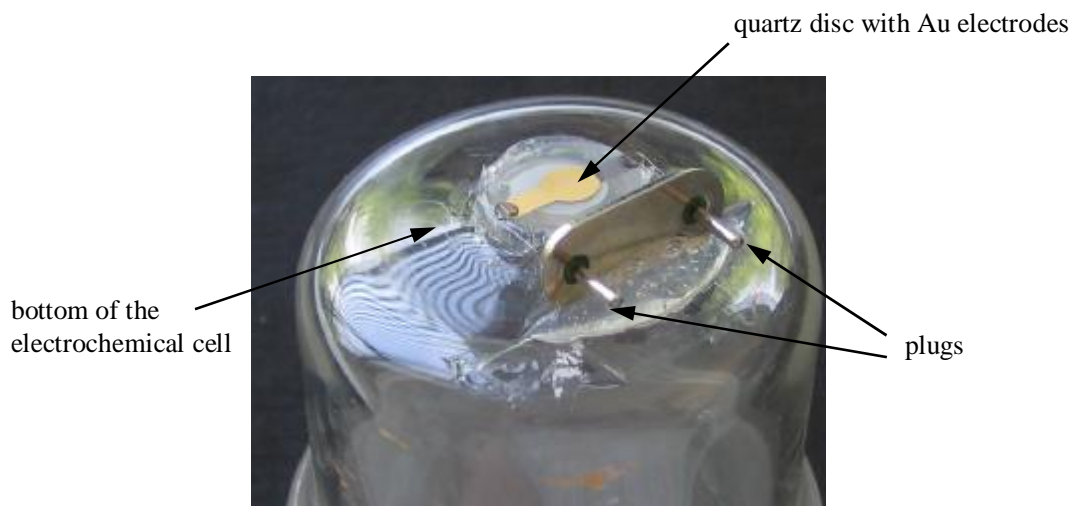


**Figure 1.15.** Electrochemical quartz crystal microbalance attached to the bottom of the electrochemical cell.

The electrochemical quartz crystal microbalance (EQCM) is a further development of the QCM technique. In the EQCM the exciting electrode of the QCM is under potential control in an electrochemical cell. It allows the study of electrochemically driven processes, for example electrodeposition or exchange of ions and solvent in the system, during electrochemical manipulation.<sup>38</sup> In a typical experimental configuration the QCM is attached to the bottom of the electrochemical cell as shown in Figure 1.15.

## 1.4 Infrared Spectroscopy

Infrared spectroscopy (IR) is one of the most common spectroscopic methods used in chemistry. It relies on absorption measurement at different IR frequencies by a material situated in the path of the IR beam. Infrared spectroscopy is used for identification of unknown substances (chemical functional groups) or characterization of their chemical structure, as different functional groups absorb characteristic frequencies of radiation. The IR region spans from the wavenumbers  $\bar{\nu}$  range of ca. 13,000 to 10  $\text{cm}^{-1}$  (or wavelengths  $\lambda$  from 0.78 to 1000  $\mu\text{m}$ ).<sup>41</sup> Wavenumbers, commonly used in IR analysis, are converted to the wavelengths by the following equation:

$$\bar{\nu}(\text{cm}^{-1}) = \frac{1}{l(\text{mm})} \cdot 10^4 \quad (1.31)$$

The plot of infrared spectra is usually presented in a form of spectrum with absorption intensity or percent transmittance as a function of wavenumber (wavelength). The infrared region is conventionally divided into three sections: near-, mid- and far-infrared. The near IR (13,000 – 4,000  $\text{cm}^{-1}$ ) has low energy and may be used for rotational spectroscopy. The mid IR (4,000 – 200  $\text{cm}^{-1}$ ) is used to study vibrational and rotational spectroscopy, and far IR (200 – 10  $\text{cm}^{-1}$ ) can excite overtone or harmonic vibrations. Most modern instruments are based on Fourier transform spectrometers (Fourier transform infrared spectroscopy, FTIR), where, instead of analysing each frequency sequentially, all frequencies are examined simultaneously.

A non-linear molecule with N atoms has  $3N-6$  distinct vibration modes. Simple molecules composed of two atoms have one bond, which may only stretch ( $3N-5$  modes). In more complex molecules with many bonds, vibrations such as symmetrical and antisymmetrical stretching, scissoring, rocking, wagging or twisting can appear in the same time. A simple example is formaldehyde, with its six modes of vibration shown in Figure 1.16. Such combination of the fundamental vibrations and/or rotations of different kinds of functional groups, together with interactions with other atoms in their proximity yields a unique and usually complex IR spectrum. Nevertheless, because of the complexity of the interactions, IR spectrum of the specific functional group may vary over a wide range of frequencies revealing even more structural information. Not

all vibrations of the molecule result in an absorption band in the infrared region. To possess infrared activity, the vibration must result in a change of dipole moment (therefore no IR absorption is observed in molecules such as  $H_2$ ,  $N_2$ , or  $O_2$ ), but it is not necessary for a compound to have a permanent dipole moment (e.g. in linear and centrosymmetric carbon dioxide molecule in the case of asymmetric stretch a dipole moment is periodically produced and  $CO_2$  reveals infrared activity).

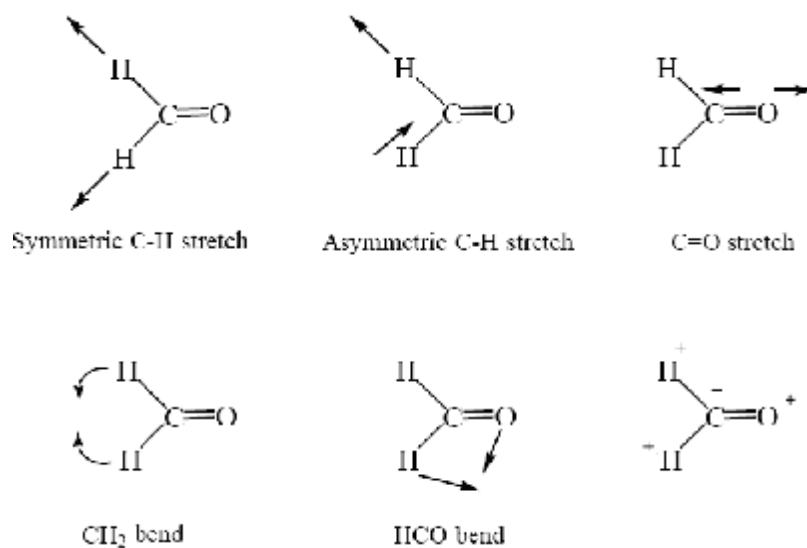


**Figure 1.16.** Six modes of vibration of formaldehyde (methanal). Out-of-plane bend + and – signify directions of motions (not atomic charges).

Although there are a variety of methods of sample preparation, the infrared spectrum of a thin film (such an electrodeposited sample) may be obtained without any further preparation by placing a sample in a holder with a slot cut for the data acquisition.

## 1.5 Chemically Modified Electrodes

According to the definition chemically modified electrode (CME) is “an electrode made of conducting or semiconducting material that is coated with a selected monomolecular, multimolecular, ionic, or polymeric film (adlayer) of a chemical modifier and that by means of Faradaic (charge-transfer) reactions or interfacial potential differences (no net

charge transfer) exhibits chemical, electrochemical, and/or optical properties of the film".<sup>42-44</sup> This still rapidly expanding area of research encompasses a relatively modern approach of electrochemical investigations since the first report on CMEs appeared in 1975 by Murray et al.<sup>45-51</sup> Chemically modified electrodes find use in a wide range of important electrochemical studies, such as the relationship of heterogeneous electron transfer and chemical reactivity to electrode surface chemistry, electron and ionic transport in a variety of electroactive materials,<sup>52, 53</sup> or electrostatic phenomena at electrode surfaces.<sup>42</sup> Another group of studies with the application of CMEs involves design of electrochemical devices and systems for chemical sensing,<sup>54-59</sup> molecular electronics,<sup>59-61</sup> corrosion protection,<sup>62-64</sup> electro-organic syntheses, energy storage and energy conversion,<sup>65, 66</sup> or electrochromic devices.<sup>42, 67</sup>

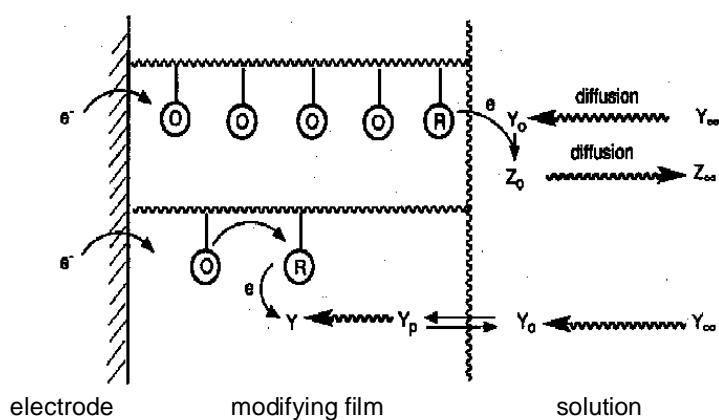


**Figure 1.17.** Polymer modified electrode. At the polymer/electrode interface, there is an electron exchange due to potential perturbation and at the film/solution interface, ion and solvent transfers occur due to electroneutrality and activity constraints. Y and Z represent electroactive species getting oxidized/reduced and the subscript “p” denotes species diffusing in the bulk of the polymer.<sup>37</sup>

Modified electrodes can be classified by the attachment method of the adlayer to the electrode substrate:

- chemisorption;<sup>68-71</sup>
- physisorption;<sup>71-73</sup>
- covalent attachment<sup>74-76</sup>

The other classification is based upon the adlayer composition. In this scheme three main categories may be recognized:<sup>77</sup>

- inorganic films as zeolites, clays or other microcrystalline materials;<sup>78-80</sup>
- self-assembled monolayers such as thiols, sulfides and disulfides;<sup>81, 82</sup>
- various types of multilayer polymer films such as polypyrrole, polyaniline or polythiophene.<sup>44</sup>

A schematic representation of a polymer modified electrode is shown in the Figure 1.17. Another interesting modification practices are application of nanoporous films, often produced through templates of spherical particles (e.g. polystyrene latex microspheres<sup>83, 84</sup>, silica particles<sup>85, 86</sup>) or incorporation of various types on (nano)particles into the polymer matrix.

### 1.5.1 Polymer Modified Electrodes

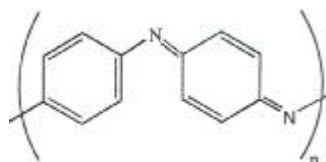
The first information about electroactive polymers (EP) was reported by Shirakawa in 1974, when he noticed that polyphenylene and polythiophene had electrical conductivity up to  $0.1 \Omega^{-1} \text{ cm}^{-1}$ .<sup>87</sup> Soon after increase of conductivity of 12 orders of magnitude by doping the polymer was reported.<sup>88-89</sup> Practical applications of these so-called synthetic metals exhibiting properties comparable to metals, and in addition mechanical and physical properties of a polymer, depend on the characteristics of the particular EP. Some of the potential applications include batteries,<sup>97-99</sup> sensors,<sup>100</sup> photovoltaic and electrochromic devices,<sup>101-103</sup> supercapacitors,<sup>104</sup> conducting textiles<sup>105</sup> and actuators.<sup>106</sup> Their limitations are at the moment relatively fast degradation of the main properties such as conductivity and electrochemical stability. For now two classes of EPs can be identified: redox polymers (RP) and conducting polymers (CP).<sup>44</sup> Example structures of commonly used CPs are presented in Figure 1.18.

Conducting polymers have important structural properties, like highly conjugated  $\pi$ -bonds, enabling movement of electrons through delocalized electronic bands (overlapping and unoccupied electronic energy states). Although there are a variety of available methods, a significant advantage of electronically conducting polymers is the facility of preparation of modified electrode by electropolymerisation.

Polyacetylene<sup>107-108</sup>



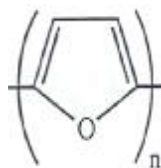
Polyaniline<sup>109-111</sup>



Polypyrrole<sup>107,109</sup>



Polythiophene<sup>107,112,113</sup>



Polyfuran<sup>107,114</sup>

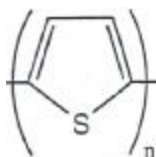


**Figure 1.18.** Examples of conducting polymer structures.

The main advantage is the fact that the reaction takes place directly on the electrode surface, which results in increased reproducibility and control over the film thickness, the possibility of use of various geometries, and the ease of the subsequent manipulation with the film (e.g. reduction and oxidation). For example, Figure 1.19 shows the cyclic voltammogram plot for electropolymerisation of 30 layers of polypyrrole in pure and nitrogen purged 1-Bu-3-Me-Imidazolium PF<sub>6</sub> (BMI PF<sub>6</sub>) ionic liquid. The growth of current magnitude in each subsequent curve is an indication of electrodeposition of the additional layers of polymer.

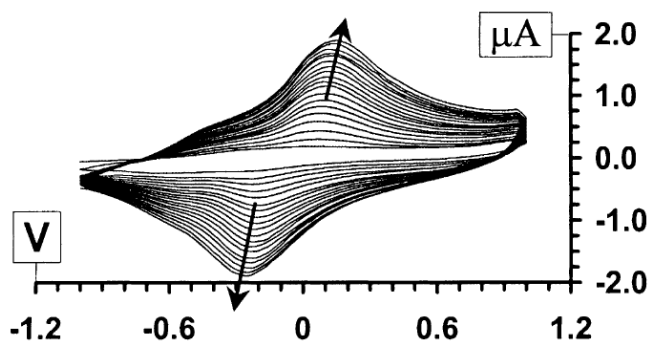


**Figure 1.19.** Cyclic voltammogram showing 30 cycles of Polypyrrole growth in pure N<sub>2</sub> purged 1-Bu-3-Me-Imidazolium PF<sub>6</sub> (BMI PF<sub>6</sub>) ionic liquid.<sup>115</sup>

The conductivity of many CPs typically is in the semiconducting range ( $10^{-14}$ – $10^2 \Omega^{-1} \text{ cm}^{-1}$ ), but doping (a term adopted from semiconductor terminology) can increase conductivity to the values characteristic for metals ( $1$ – $10^5 \Omega^{-1} \text{ cm}^{-1}$ ).<sup>116</sup> In the case of conducting polymers so-called p-doping (oxidation) is removal of electrons from the polymer backbone, producing a positive charge (hole). The opposite process, n-doping or reduction is an injection of excess electrons, which become charge carriers in this case. Incorporation and expulsion of ions from the bathing solution takes place simultaneously with doping to maintain overall electroneutrality of the film. The size and character of the dopant counter- or co- ion incorporated in the synthesis process, as well as of the one present at the potentiodynamic cycling can have a remarkable effect on the ion movement and film behaviour taking place upon redox processes. It may also influence characteristics of the polymer such as structure, conductivity, etc. Ionic liquids (IL) are an extreme example of such an influence on conducting polymer films and they are a promising novelty, among others, also in electrochemical research.

## 1.6 Ionic Liquids

Classical solutions are obtained by dissolution of salts in molecular solvents. Such solutions consist of solvated ions and solvent molecules. The other way the salt can be melted is thermally. Such systems, consisting only of ions and their combinations without any molecular solvents, are called molten salts or ionic liquids (IL). Relatively high melting points can be lowered by addition of other salts, thereby forming an

eutectic. Salts with low melting points and maintaining liquid structure at room temperature form a comparatively new class of ionic liquids and are called room temperature ionic liquids (RTIL). The physical and chemical properties of RTILs are the same as high temperature ionic liquids, but have a wide range of distinct practical applications.<sup>117</sup> The main processes that use ILs on an industrial scale are BASF's Biphasic Acid Scavenging utilizing Ionic Liquids process (BASIL), the Dimersol process<sup>118</sup> and electrodeposition/electroplating of metals. In BASIL process a 1-alkylimidazole is used to scavenge the acid from an existing reaction. This then results in the formation of an IL which can easily be removed from the reaction mixture. By using an IL it was possible to increase the space/time yield of the reaction by a factor of 80,000. The Dimersol process is a traditional way to dimerise short chain alkenes into branched alkenes of higher molecular weight. Y. Chauvin and H. Olivier-Bourbigou have developed an ionic liquid-based add-on to this process called the Difasol process. In the case of electrodeposition/electroplating because of almost zero vapour pressure ionic liquids are well suited to perform electrodeposition at a range of temperatures.

The main advantages of the use of IL in electrochemistry include:

- wide potential windows;
- high solubility of metal salts;
- low vapour pressure;
- high conductivity compared to non-aqueous solvents.<sup>118</sup>

Unfortunately, the vast majority (although not all) of the studies on CP's in IL's are performed under anaerobic conditions, because of the hygroscopic properties or sensitivity of some IL to the presence of water.<sup>119</sup> One of the exceptions includes Ethaline, which belongs to class of IL based on eutectic mixtures of choline chloride with a hydrogen bond donor species.<sup>120-122</sup>

One of the promising areas of research in ionic liquids is their utilization in the synthesis and use of conducting polymers. Although conducting polymers are widespread, one of the limitations is the relatively rapid degradation of their properties such as conductivity or electrochemical performance. This is very often an influence of electrolyte, which is a source of dopants, used for fabrication and/or further processing

of the polymer. The dopants have an impact on all the properties of the polymer, including mechanical characteristics, electrochemical efficiency, stability, morphology and structure or conductivity. Examples of polypyrrole electrodeposited from ionic liquids with different properties are shown in Figure 1.20. The stability of a CP is often limited by degradation of solvent or electrolyte at extreme potentials. Use of an ionic liquid with a wide electrochemical window of stability can be a solution to this problem.

Because a lot of the anions that are successfully used in application with conducting polymers are also commonly used in ionic liquid compounds, the appropriate ionic liquids provide an excellent source of the dopant ions. The possible advantages of the use of ILs as electrolytes in combination with conducting polymers have been widely investigated in recent years, with significant improvements in lifetimes and performances. Some of these reports include applications such as solar cells,<sup>123</sup> actuators<sup>124, 125</sup> or supercapacitors.<sup>126, 127</sup>

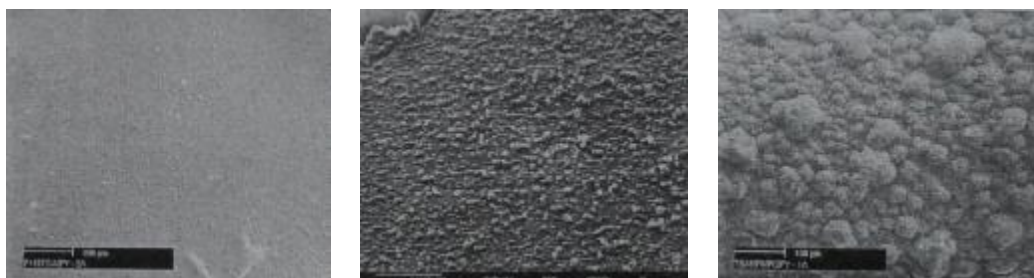


**Figure 1.20.** Examples of conducting polymer morphology electrodeposited on the Pt electrode from different room temperature ionic liquids. Polypyrrole films grown in [C<sub>4</sub>mpyr][NTf<sub>2</sub>] (left), [C<sub>2</sub>mim][NTf<sub>2</sub>] (middle) and PC/Bu<sub>4</sub>NPF<sub>6</sub> (right). Significantly smoother films were grown from the ionic liquid [C<sub>2</sub>mim][NTf<sub>2</sub>] and [C<sub>4</sub>mpyr][NTf<sub>2</sub>] compared to grown under the same experimental conditions from PC/Bu<sub>4</sub>NPF<sub>6</sub>.<sup>128</sup>

The application of ionic liquids is very often stimulated by so-called “green” safety and environmental considerations. Their negligible volatility and nonflammability makes them good potential candidates for the replacement of more toxic molecular solvents, and eliminates the problem of solvent evaporation. On the other hand issues such as ionic liquid cost, large scale availability and toxicity are also matters of concern in this rapidly developing field of electrochemistry.<sup>128</sup>

## 1.7 References

1. Briggs, D.; Seah, M. P., *Practical Surface Analysis by Auger and X-ray Photoelectron Spectroscopy*. John Wiley and Sons: New York, 1984.
2. Skoog, D. A.; Holler, F. J.; Nieman, T. A., *Principles of Instrumental Analysis*. Thomson Brooks/Cole: Belmont, CA, USA, 1998.
3. Fairley, N.; Carrick, A., *The Casa Cookbook*. Acolyte Science: Cheshire, 2005.
4. *X-ray Methods in Corrosion and Interfacial Electrochemistry (from the 180<sup>th</sup> Meeting of The Electrochemical Society, Phoenix, Oct. 13-17, 1991, ECS Proceedings, Vol. 92-1)*. Eds.: A. Davenport, J.G. Gordon, ECS: Pennington, New Jersey, 1992.
5. Foster, M. D., *Crit. Rev. Anal. Chem.* **1993**, *24*, 179.
6. Melendres, C. A.; Tadjeddine, A., *Synchrotron Techniques in Interfacial Electrochemistry*. Kulwier: London, 1992.
7. Toney, M. F.; McBreen, J., *In Situ Synchrotron X-ray Techniques for Determining Atomic Structure at Electrode/Electrolyte Interfaces*. Electrochem. Soc. Interface: 1993.
8. Newville, M., Fundamentals of XAFS. In Chicago, IL, 2004: [http://www.xafs.org/Tutorials?action=AttachFile&do=get&target=Newville\\_xas\\_fundamentals.pdf](http://www.xafs.org/Tutorials?action=AttachFile&do=get&target=Newville_xas_fundamentals.pdf), Accessed 26 Jun 2007.
9. <<http://www.chem.ucalgary.ca/research/groups/faridehj/xas.pdf>>, Accessed 15 Nov. 2009.
10. Berger, M. J.; Hubbell, J. H., *Database of Calculated Photon Cross Sections (XCOM)*, NIST: <http://physics.nist.gov/PhysRefData/Xcom/html/xcom1.html>, Accessed 14 Sep. 2009.
11. Bethe, H.; Salpeter, E., *Quantum Mechanics of One- and Two-electron Systems*. Springer: Berlin, 1959.
12. Wong, J., *Mater. Sci. Eng.* **1986**, *80*, 107.
13. Farley, N., Ph.D. Thesis, *Structural Studies of Electroactive Transition Metal Oxide Films*. University of Leicester, Leicester, 2001.
14. Fricke, H., *Phys. Rev.* **1920**, *16*, 202.
15. Hertz, G., *Phys. Z.* **1920**, *21*, 630.
16. Hertz, G., *Phys. Z.* **1920**, *3*, 19.

17. Lytle, F. W., *Physics of Non-crystalline Solids*. North-Holland Publishing Company: Amsterdam, 1965.
18. Sayers, D. E.; Lytle, F. W.; Stern, E. A., *Adv. X-ray Anal.* **1970**, *13*, 248.
19. <http://srs.dl.ac.uk/xrs/Theory/theory3.html>, Accessed 14 Sep. 2009.
20. <http://srs.dl.ac.uk/XRS/>, Accessed 14 Sep. 2009.
21. Lee, P. A.; Pendry, J. B., *Phys. Rev. B* **1975**, *11*, 2795.
22. Gurman, S. J., *J. Synchrotron Rad.* **1995**, *2*, 56-63.
23. Hasnain, S.S., *Synchrotron Radiation and Biophysics*. Ellis Horwood: Chichester, 1990.
24. Gurman, S. J.; Binsted, N.; Ross, I., *J. Phys C* **1984**, *17*, 143.
25. Charnock, J. M., *Radiat. Phys. Chem.* **1995**, *45*, (3), 385.
26. Sharpe, L. R.; Heineman, W. R.; Elder, R. C., *Chem. Rev.* **1990**, 705.
27. Toney, M. F.; McBreen, J., *Electrochem. Soc. Interface* **1993**, 22.
28. Keyes, T. E.; Forster, R. J., *Handbook of Electrochemistry*, Elsevier: Oxford 2007; pp 591.
29. Melendres, C. A.; Mansour, A. N., *Electrochim. Acta* **1998**, *43*, 631.
30. Kissinger, P. T.; Heineman, W. R., *J. Chem. Ed.* **1983**, *60*, 702.
31. Kiszka, A., *Elektrochemia II. Elektrodyka*. WNT: Warszawa, 2001.
32. Tedim, J., First year report. University of Leicester, Leicester, 2006.
33. Bard, A. J.; Faulkner, L. R., *Electrochemical Methods. Fundamentals and Applications*. John Wiley & Sons: New York, 1980; pp 109.
34. Fisher, A. C., *Electrode Dynamics*. Oxford University Press, USA, 1996.
35. Matsuda, H.; Ayabe, Y., *Z. Elektrochem.* **1955**, *59*, 494.
36. Bard, A. J.; Faulkner, L. R., *Electrochemical Methods. Fundamentals and Applications*. John Wiley & Sons: New York, 1980; pp 213.
37. Mohamoud, M. A., Ph.D. Thesis, *Gravimetric and Viscoelastic Investigations of Electroactive Films*. University of Leicester, Leicester, 2007.
38. Bandey, H. L.; Hillman, A. R.; Brown, M. J.; Martin, S. J., *Faraday Discuss.* **1997**, *107*, 105.
39. Bruckenstein, S.; Hillman, A. R., *Electrochemical Quartz Crystal Microbalance Studies of Electroactive Surface Films*. Ed.: A.T. Hubbard, CRC Press, Boca Raton, 1995.

40. Sauerbrey, G. Z., *Z. Phys.* **1959**, *155*, 206.
41. Sherman Hsu, C.-P., Chapter 15: Infrared Spectroscopy in *Handbook of Instrumental Techniques for Analytical Chemistry*. Ed.: F. Settle, Prentice-Hall, NJ, 1997.
42. Durst, R. A.; Baumner, A. J.; Murray, R. W.; Buck, R. P.; Andrieux, C. P., *Pure & Appl. Chem.* **1997**, *69*, 1317.
43. Kutner, W.; Wang, J.; L'Her, M.; Buck, R. P., *Pure & Appl. Chem.* **1998**, *70*, 1301.
44. Edwards, G. A.; Bergren, A. J.; Porter, M. D., *Chemically Modified Electrodes in Handbook of Electrochemistry*. Ed.: C.G. Zoski, Elsevier: 2007.
45. Lenhard, J. R.; Murray, R. W., *J. Electroanal. Chem.* **1977**, *78*, 195.
46. Lenhard, J. R.; Rocklin, R.; Albruna, H.; Willman, K.; Kuo, K.; Nowak, R.; Murray, W., *J. Am. Chem. Soc.* **1978**, *101*, 117.
47. Murray, R. W., *An. Rev. Mater. Sci.* **1984**, *14*, 145.
48. Murray, R. W., *Acc. Chem. Res.* **1980**, *13*, 135.
49. Faulkner, L. R., *Chem. Eng. News* **1982**, *27*, 28.
50. Albert, W. J.; Hillman, A. R., *Ann. Rev. C. R. Soc. Chem.* **1981**, 377.
51. Moses, P. R.; Wier, L. M.; Murray, R. W., *Anal. Chem.* **1975**, *78*, 1882.
52. Malkia, A.; Liljeroth, P.; Kontturi, K., *Anal. Sci.* **2001**, *17*, i345.
53. Yang, H.-H.; L., M. R., *Anal. Chem.* **1999**, *71*, 4081.
54. Flink, S.; van Veggel, F. C. J. M.; Reinhoudt, D. N., *Sensors Update* **2001**, *8*, 3.
55. Schreiber, F., *J. Phys.: Condens. Matter* **2004**, *16*, R881.
56. Adhikari, B.; Majumdar, S., *Prog. Polym. Sci.* **2004**, *29*, 699.
57. Yuqing, M.; Jianrong, C.; Xiaohua, W., *Trends Biotechnol.* **2004**, *22*, 227.
58. Ciszewski, A.; Milczarek, G., *Talanta* **2003**, *61*, 11.
59. Roberts, G. G., *Adv. Phys.* **1985**, *34*, 475.
60. Goldenberg, L. M.; Petty, M. C.; Monkman, A. P., *J. Electrochem. Soc.* **1994**, *141*, 1573.
61. Goldenberg, L. M., *J. Electroanal. Chem.* **1993**, *379*, 3.
62. Mengoli, G.; Munari, M.-T.; Folonari, C., *J. Electroanal. Chem.* **1981**, *124*, 237.
63. Mourcel, P.; Pham, M. C.; Lacaze, P. C.; Dubios, J. E., *J. Electroanal. Chem.* **1983**, *145*, 467.

64. Mengoli, G.; Bianco, R.; Daolio, S.; Munari, M.-T., *J. Electrochem. Soc.* **1981**, *128*, 2276.
65. Fauverque, J. F., *J. Chem. Phys.* **1989**, *86*, 5.
66. Sung, J.-H.; Kim, S.-J.; Lee, K.-H., *J. Power Sources* **2004**, *126*, 258.
67. Habib, M. A.; Maheswari, S. P., *J. Electrochem. Soc.* **1992**, *139*, 2155.
68. Love, J. C.; Estroff, L. A.; Kriebel, J. K.; Nuzzo, R. G.; Whitesides, G. M., *Chem. Rev.* **2005**, *105*, 1103.
69. Bain, C. D.; Biebuyck, H. A.; Whitesides, G. M., *Langmuir* **1989**, *5*, 723.
70. Laibinis, P. E.; Whitesides, G. M.; Allara, D. L.; Tao, Y.-T.; Parikh, A. N.; Nuzzo, R. G., *J. Am. Chem. Soc.* **1991**, *113*, 7152.
71. Rassaei, L.; Sillanpaa, M.; Marken, F., *Electrochim. Acta* **2008**, *53*, 5732.
72. Bradley, D. B.; Martin, H. B.; Wightman, R. M.; Anderson, M. R., *Langmuir* **2001**, *17*, 7032.
73. Endo, O.; Tsuji, K.; Ozaki, H., *J. Phys. Chem. C* **2008**, *112*, 17336.
74. Murray, R. W., *Electroanalytical Chemistry*. Marcel Dekker: New York, 1984.
75. Downard, A. J., *Electroanalysis* **2000**, *12*, 1085.
76. Barbier, B.; Pinson, J.; Desarmont, G.; Sanchez, M., *J. Electrochem. Soc.* **1990**, *137*, 1757.
77. Murray, R. W., in *Electroanalytical Chemistry*. Ed.: A.J. Bard, Marcel Dekker: New York, 1984.
78. Macha, S. M.; Fitch, A., *Microchim. Acta* **1998**, *128*, 1.
79. Ahlers, C. B.; Talbot, J. B., *Electrochim. Acta* **2000**, *45*, 3379.
80. Walcarius, A., *Electroanalysis* **1996**, *8*, 971.
81. Bubios, L. H.; Muzzo, R. G., *Anal. Rev. Phys. Chem.* **1992**, *43*, 437.
82. Walczak, M. W.; Chung, C.; Stole, S. M.; Widrig, C. A.; Porter, M. D., *J. Am. Chem. Soc.* **1991**, *113*, 2370.
83. Bartlett, M. A.; Yan, M. D., *Adv. Mat.* **2001**, *13*, 1449.
84. Bartlett, M. A.; Birkin, P. R.; Ghanem, M. A., *Chem. Comm.* **2000**, 1671.
85. Velev, O. D.; Kaler, E. W., *Langmuir* **1999**, *15*, 3693.
86. Velev, O. D.; Jede, T. A.; Lobo, R. F.; Lenhoff, A. M., *Nature* **1997**, *389*, 447.
87. Ito, T.; Shirakawa, H.; Ikeda, S., *J. Polym. Sci. Polym. Chem. Ed.* **1974**, *12*, 11.

88. MacDiarmid, A. G.; Akhtar, M.; Chiang, C. K.; Cohen, M. J.; Kleppinger, J.; Heeger, A. J.; Louis, E. J.; Milliken, E. J.; Moran, M. J.; Peebles, D. L.; Shirakawa, H., *J. Electrochem. Soc.* **1977**, *124*, C304.
89. MacDiarmid, A. G.; Heeger, A. J., *Synth. Met.* **1978**, *1*, 101.
90. Street, G. B.; Clarke, T. C., *IBM J. Res. Dev.* **1981**, *25*, 51.
91. Carlberg, C.; Chen, X.; Ingnas, O., *Solid State Ionics* **1996**, *85*, 73.
92. Greczynski, G.; Kugler, T.; Salaneck, W. R., *Thin Solid Films* **1999**, *354*, 129.
93. Vorotyntsev, M.; Casalta, M.; Pousson, E.; Roullier, R.; Boni, G.; Morse, C., *Electrochim. Acta* **2001**, *46*, 4017.
94. Gomez-Romero, P.; Chojak, M.; Kulesza, P. J.; Asensio, J. A., *Electrochem. Comm.* **2003**, *5*, 149.
95. Hillman, A. R.; Mohamoud, M. A., *Electrochim. Acta* **2006**, *51*, 6018.
96. Mohamoud, M. A.; Hillman, A. R., *J. Solid State Electrochem.* **2007**, *11*, 1043.
97. Aldissi, M., *J. Power Sources* **2001**, *94*, 219.
98. Mirmohseni, A.; Solhjo, R., *Eur. Polym. J.* **2003**, *39*, 219.
99. Nishio, K.; Fujimoto, M.; Yoshinaga, N.; Furukawa, N.; Ando, O.; Ono, H.; Suzuki, T., *J. Power Sources* **1991**, *34*, 153.
100. Chandrasekhar, P., *Conducting Polymers, Fundamentals and Applications. A Practical Approach*. Kluwer Academic Publishers: Boston, 1999; pp 101.
101. Mortimer, R. J., *Electrochim. Acta* **1999**, *44*, 2971.
102. Cutler, C. A.; Bouguettaya, M.; Kang, T. S.; Reynolds, J. R., *Macromolecules* **2005**, *38*, 3068.
103. Groenendaal, L.; Zotti, G.; Aubert, P. H.; Waybright, S. M.; Reynolds, J. R., *Adv. Mater.* **2003**, *15*, 855.
104. Hussain, A. M. P.; Kumar, A., *J. Power Sources* **2006**, *161*, 1486.
105. Wallace, G. G.; Campbell, T. E.; Innis, P. C., *Fibers and Polymers* **2007**, *8*, 135.
106. Lee, C. S.; Joo, J.; Han, S.; Koh, S. K., *Appl. Phys. Lett.* **2004**, *85*, 1841.
107. Nishio, K.; Fujimoto, M.; Yoshinaga, N.; Furukawa, N.; Ando, O.; Ono, H.; Suzuki, T., *J. Power Sources* **1991**, *34*, 153.
108. Liu, G. K.; Ren, B.; Wu, D. Y.; Lin, T. M.; Gu, R. A.; Tian, Z. Q., *J. Electroanal. Chem.* **2006**, *594*, 73.

109. Blinova, N. V.; Stejskal, J.; Trchova, M.; Prokes, J.; Omastova, M., *Eur. Polym. J.* **2007**, *43*, 2331.
110. Mohamoud, M. A.; Hillman, A. R., *J. Solid State Electr.* **2007**, *11*, 1043.
111. Hillman, A. R.; Mohamoud, M. A., *Electrochim. Acta* **2006**, *51*, 6018.
112. Ding, H.; Pan, Z.; Pigani, L.; Seeber, R.; Zanardi, C., *Electrochim. Acta* **2001**, *46*, 2721.
113. Roncali, J., *Chem. Rev.* **1992**, *92*, 711.
114. Tirkes, S.; Onal, A. M., *J. App. Polym. Sci.* **2007**, *103*, 871.
115. Mazurkiewicz, J. H.; Innis, P. C.; Wallace, G. G.; MacFarlane, D. R.; Forsyth, M., *Synth. Met.* **2003**, *135*, 31.
116. Vidal, J.-C.; Garcia-Ruiz, E.; Castillo, J. R., *Microchim. Acta* **2003**, *143*, 93.
117. Galinski, M.; Lewandowski, A.; Stepniak, I., *Electrochim. Acta* **2006**, *51*, 5567.
118. Abbott, A. P.; McKenzie, K., *Phys. Chem. Chem. Phys.* **2006**, *8*, 4265.
119. Huddleston, J. G.; Visser, A. E.; Reichert, W. M.; Willauer, H. D.; Broker, G. A.; Rogers, R. D., *Green Chem.* **2001**, *3*, 156.
120. Abbott, A. P.; Boothby, D.; Capper, G.; Davies, D. L.; Rasheed, R. K., *J. Am. Chem. Soc.* **2004**, *126*, 9142.
121. Abbott, A. P.; Capper, G.; Davies, D. L.; Rasheed, R. K.; Tambyrajah, V., *Chem. Comm.* **2003**, 70.
122. Abbott, A. P.; Nadhra, S.; Postlethwaite, S.; Smith, E. L.; Ryder, K. S., *Phys. Chem. Chem. Phys.* **2007**, *9*, 3735.
123. Yang, C.; Sun, Q.; Qiao, J.; Li, Y., *J. Phys. Chem. B* **2003**, *107*, 12981.
124. Cho, M. S.; Seo, H. J.; Nam, J. D.; Choi, H. R.; Koo, J. C.; Lee, Y., *Proc. SPIE-Int. Soc. Opt. Eng.* **2006**, *6168*, 61682E.
125. Lu, W.; Mattes, B. R., *Synth. Met.* **2005**, *152*, 53.
126. Balducci, A.; Bardi, U.; Caporali, S.; Mastragostino, M.; Soavi, F., *Electrochem. Commun.* **2004**, *6*, 566.
127. Balducci, A.; Soavi, F.; Mastragostino, M., *Appl. Phys. A* **2006**, *82*, 627.
128. Pringle, J. M.; Forsyth, M.; MacFarlane, D. R., *Electrodeposition from Ionic Liquids*. Wiley-VCH Verlag GmbH & Co. KGaA: Weinheim, 2008.

# CHAPTER II

## GENERAL EXPERIMENTAL AND DATA ANALYSIS PROCEDURES

In this chapter equipment and general procedures of sample preparation, handling and data acquisition are described. As the systems studied in this thesis are diverse, the information included here applies to all the samples, but more specific details, like electrochemical deposition of different types of films or crystal impedance analysis of polymer samples will be covered in the relevant sections of the following chapters.

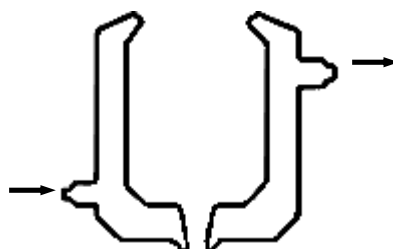
### 2.1 Experimental

#### 2.1.1 Electrochemical and EQCM Experimental Set-up

Electrochemical studies were performed using a potentiostat/galvanostat (Autolab PGSTAT 20) controlled by the computer. A standard three-electrode cell was used with a Pt disc (15mm diameter) or indium tin oxide (ITO) coated glass as the working electrode, Pt mesh as counter electrode and saturated calomel electrode (SCE) or Ag/AgCl sat'd KCl as reference electrodes. In the case of ionic liquids, a Ag wire was

used as a reference electrode. Pt working electrodes were cleaned by polishing with an aqueous 0.3 $\mu$  alumina suspension (Buehler) on polishing pad, then washed with diluted 1:1 nitric acid (70%, Fisher chemicals) and deionised water. ITO coated glass electrodes were only rinsed with electrolyte. Auxiliary electrodes were washed by elongated storage in diluted 1:1 nitric acid and rinsing with hot deionised water.

Crystal impedance spectra were recorded using a Hewlett-Packard E5061A network analyser operating in reflectance mode. The data acquisition and review software were developed using the Agilent Virtual Engineering Environment (VEE v7.52) software and the acoustic impedance spectrum was acquired approximately once every second. Analysis, modelling and fitting of the measured data was performed with Visual Basic for Applications inside Microsoft Excel (Microsoft Office Pro. 2003).<sup>1</sup>



Quartz crystal/WE electrode mounting

**Figure 2.1.** Scheme of a water jacket cell for a temperature controlled EQCM data acquisition. Quartz crystal/WE electrode mounting is at the bottom of the cell. Arrows show the direction of the water flow. Top sealing is not shown in the picture.

In EQCM experiments the quartz resonators were 10 MHz *AT*-cut unpolished crystals coated with Au or polished crystals coated with Pt (ICM, Oklahoma City, USA), with piezoelectric and electrochemically active areas 0.21 and 0.23 cm<sup>2</sup>, respectively. The quartz crystal was mounted with Dow Corning 3145 RTV silicon rubber adhesive onto a in-house built cell. The crystal was mounted in such a way that one face of it was exposed to the solution and forming working electrode. A three electrode water jacket cell was used (as shown in Figure 2.1) with an Ag wire (for experiments with use of ionic liquids) or Ag/AgCl sat'd KCl (for experiments in aqueous electrolytes) reference electrode and a Pt mesh as a counter electrode.

### 2.1.2 EXAFS Data Acquisition

XAS experiments were carried out at stations 7.1 and 16.5 of the synchrotron radiation source (SRS) at the CCLRC Daresbury Laboratory, UK, operating at electron energy of ca. 2 GeV and a synchrotron ring current of ca. 125 mA.

Station 7.1 is a medium energy XAS station using a harmonic rejecting sagittally focusing double crystal Si(111) monochromator for EXAFS measurements in the range 4 keV to 10 keV. Spectra were acquired for the Fe K-edge (7111 eV), Co K-edge (7709 eV) and Ni K-edge (8333 eV) for metal hexacyanoferrates, in fluorescence mode only, because of the low intensity of the signal. The fluorescence detector is a nine-element solid-state detector with high count rate electronics useable up to 125 kHz per channel.

Station 16.5 provides XAS measurements on ultra-dilute systems (relevant for the study presented in this thesis, as atoms under study were at low concentrations) in the energy range 7 keV to 40 keV. A pre-mirror provides collimation of the incident X-ray beam, and a double crystal monochromator with sagittal focus up to 40 keV is used at the station. The detector used was a thirty-element Ge solid-state detector with high count-rate electronics up to 200 kHz per channel.<sup>2</sup> Spectra were acquired for the Co K-edge (7709 eV) in cobalt hexacyanoferrate in fluorescence mode, Ir L<sub>III</sub>-edge (11,215 eV) in iridium oxide films and Mo K-edge (20,002 eV) in polypyrrole matrix incorporated Keggin ions in both fluorescence and transmission configurations.

For the transmission mode spectra acquisition the three ion chambers were filled with absorbing Ar or an Ar/Kr mixture of total pressure 1 bar. The partial pressures of Ar and Kr are different for different absorption edges (tabulated values), so that about 20 % of the incoming radiation is absorbed in the first ion chamber, and 70 % of the initial beam by the second chamber.

Fluorescence spectra were recorded on all electrochemical samples, using the spectroelectrochemical cell when possible. Although the thin layer cell was designed especially for this purpose, in case of metal hexacyanoferrate samples it was impossible to carry out *in situ* measurements even in fluorescence mode. This was due to the very small amount of the material incorporated onto the surface of a modified electrode, a

fact recognized in other publications. For these reasons, data for Prussian Blue analogue films were acquired *ex situ*, but in practice even this proved to be a difficult task. In other cases the data was collected *in situ* in both fluorescence and transmission mode, and the details are stated in the subsequent experimental sections. In the case of *in situ* measurements, all the electrochemical manipulations (cyclic voltammetry, reduction or oxidation) of the samples were performed without altering the setting of the optical bench or the cell position. During the recording of XAS data the potentials were held constant at selected points of interest on the cyclic voltammogram. The balance between the signal and concurrent scattering was optimised by changing the detector distance from the sample. Additional care was taken not to saturate the detector.

All experiments were carried out at room temperature. The samples were prepared in the Materials Science Laboratory at CCLRC Daresbury Laboratory (Prussian Blue, cobalt hexacyanoferrate, nickel hexacyanoferrate, iridium oxide), or directly at the station hutch (Mo Keggin ions incorporated into polymer matrices). Reference samples (standards) with well known characteristics, together with information from crystallographic databases, are necessary to make possible the analysis and interpretation of the structure and oxidation states of these initially unknown properties of studied samples. Therefore reference materials with similar constituents to the investigated materials were bought as a high purity reagent grade powders or  $\sim 10 \mu\text{m}$  metal foils. Crystalline powder standards were either dissolved in deionized water (usually 50 mM concentration) or, when insoluble in water, the powder was ground, distributed evenly onto a strip of adhesive tape, and sealed with a clean strip of tape.

### 2.1.3 Electrochemical Cells for EXAFS Spectroelectrochemistry

As mentioned before, there are a few, often conflicting criteria a spectroelectrochemical cell has to meet. The most important points that have to be taken into account when designing an *in situ* cell for EXAFS spectroelectrochemistry, apart from the fact that complete electrochemical conversion of the investigated material has to be obtained in a reasonable length of time, is that there has to be a possibility to contain enough of the material to obtain good signal-to-noise characteristics, the cell windows and other components are transparent, or not in the path of the X-ray beam. It is often a big problem that water, used so often in electrochemical systems, is a strong attenuator. A common practice to reduce to a minimum the effects of solvent absorption in both fluorescence and transmission EXAFS modes is use of thin layer cells.

The cell shown in Figure 2.2 was designed to meet all of the above requirements with minimal loss of performance, and has been successfully used for the *in situ* EXAFS data acquisition of molybdenum heteropolyanion embedded in the polymer matrix and iridium oxide electrodeposited films.

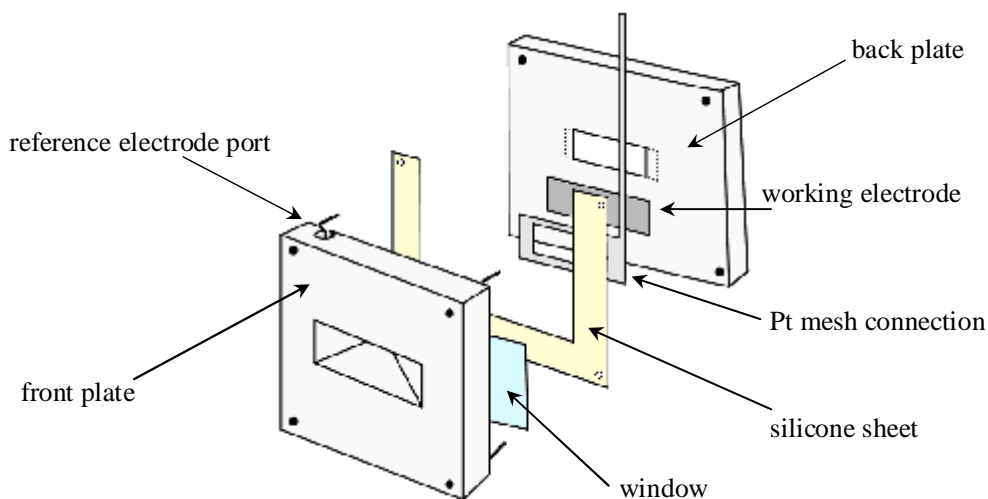


**Figure 2.2.** Exploded view of *in situ* spectroelectrochemical cell used for EXAFS data acquisition.

Thick and rigid perspex front ( $5 \times 5 \times 0.5 \text{ cm}^3$ ) and back ( $5 \times 5 \times 1 \text{ cm}^3$ ) plates of the cell in Figure 2.2 provided support for the middle flexible silicone layer. Both outer

plates had X-ray transparent windows cut with their sides at an angle of 45° to facilitate data acquisition in fluorescence and/or transmission modes. In the fluorescence mode the cell was placed at 45° with respect to the incoming X-ray beam, and fluorescent radiation was collected by a detector placed at 90° to the incoming beam, and at the same side of the front window. For the transmission mode EXAFS data acquisition, the spectroelectrochemical cell was placed perpendicular to the incoming beam. In such a configuration the X-ray beam would pass through the cell towards the transmission detector (i.e. ionisation chamber). To avoid loss of flux, the distance between both outer plates was minimised to 0.5 mm (thickness of the silicone sheet serving as separating layer and seal preventing leakage). The front and back plate were compressed with the use of stainless steel screws holding the cell together. The back plate was thicker than the front to accommodate the reference electrode port, with an opening at the top of the window, and its full length contained a slit that opened into the cell cavity. The reference electrode was Ag/AgCl/KCl(sat'd) as all the experiments were conducted in an aqueous environment. The working electrode placed at a back window was 0.75  $\mu\text{m}$  Pt foil supported by permanent polyester (Goodfellow) or 175  $\mu\text{m}$  conductive ITO coating (sheet resistance 20  $\Omega/\square$ ) on permanent polyester film (Sheldahl, MN, USA) to ensure X-ray transmittance. The front window was a piece of plain X-ray transparent nylon film. The windows were fixed to the inside surface of the plates using epoxy resin. The cell was reused after peeling away the used working electrode and attaching a new one. The Pt mesh counter electrode was placed above the working electrode in such a way as not to interfere with the incoming beam or cover the WE area. Pt mesh was attached to the working electrode with the use of self-adhesive tape in the way that the whole WE surface was surrounded by it. Strip of Pt mesh was used as connection to the potentiostat. A piece of silicone sheet was placed at a top in the gap between two plates (not shown in Figure 2.2) to stop solvent evaporation during the prolonged data acquisition times and maintain the concentration of electrolyte. The cell was mounted to the optical bench clamp with the use of a simple rectangular perspex holder, connected to two long stainless steel bottom screws.

### 2.1.4 XPS Data Acquisition

XPS measurements were done using the Scienta ESCA300 spectrometer at the National Centre for Electron Spectroscopy and Surface Analysis (NCESS) in Daresbury Laboratory. The ESCA300 photoelectron spectrometer employs a high power rotating anode and monochromatic Al K $\alpha$ /Cr K $\beta$  ( $h\nu = 1486.7/5946.7$  eV) X-ray source – for the data presented here Al K $\alpha$  was used – with selectable aluminium or chromium targets. The detection system consists of a 300 mm radius hemispherical analyser and a multi-channel detector. For sample treatment prior to measurement, argon ion bombardment (etching) and other facilities are available.<sup>3</sup> All the measurements were performed at room temperature. The following settings were used in the data acquisition (unless stated otherwise):

- Take off angle: 90°
- Slit: 0.8 mm.

The samples were always prepared (electrodeposited) prior to the experiment at University of Leicester facilities and transported to NCESS. Samples were always reduced/oxidized in solutions purged with nitrogen for at least 30 minutes, and during redox reactions a steady stream of nitrogen was blown over the solution surface. Samples were rinsed with deionised and deoxygenated water, dried with dust-off containing mix of inert gases and transferred into the chamber as fast as possible.

Fractional concentrations of a particular element A (% A) were calculated using the following equation:

$$\% A = \frac{\left(\frac{I_A}{s_A}\right)}{\sum \left(\frac{I_n}{s_n}\right)} \times 100\% \quad (2.1)$$

where  $I_n$  and  $s_n$  are the integrated peak areas and sensitivity factors (tabulated values in Analysis program designed for XPS data analysis and fitting), respectively.

## 2.2 Data Analysis

After recording the XAS data – either in fluorescence or transmittance mode – standard computational procedures are applied to obtain XANES and EXAFS spectra. From these spectra, through the comparison and using fitting procedures, the valency and structural parameters of electrochemical material are extracted. Spectra calibration, background subtraction, normalisation and evaluation of structural parameter routines are described in the following part of the chapter.

### 2.2.1 XAS Spectra Calibration, Background Subtraction and Normalisation

The Daresbury program EXCALIB<sup>4</sup> was used to calibrate all of the recorded fluorescence and transmission data. The data file of each spectrum initially consists of positions of monochromator (angles in millidegrees) and detector readings (depending on the configuration these can be  $I_0$ ,  $I_t$ ,  $I_c$ , or  $I_f$ ) as a function of time. The positions of the monochromator are converted into energy (in eV) using Bragg's equation (Equation 1.12), taking into account the type of the crystal used (e.g. Si(111), Si(220)). The XAS signal is calculated using  $I_0$  and  $I_t$  in combination with Equation 1.2 in case of transmission mode, or  $I_f$  in combination with Equation 1.13 for fluorescence mode. Subsequently, a series of aligned spectra derived in this way, typically five to ten depending on the quality of the signal (i.e. signal-to-noise ratio) is added up. The worse the quality of the signal, for example in the case of very dilute or thin samples, the more spectra have to be summed up to improve the quality of the data. The procedure described above has to be repeated for each single recorded XAS spectrum before summing them up background subtraction and normalisation are possible.

Background subtraction and normalisation procedures were carried out using yet another Daresbury program called EXBACK.<sup>4</sup> According to the definition, the EXAFS  $\chi(k)$  function in  $k$ -space is described as:

$$c(k) = \frac{m(k) - m_0(k)}{m_0(k)} \quad (2.2)$$

To extract  $\chi(k)$  from the calibrated data, the theoretical smoothly varying - without white line and EXAFS oscillations -  $\mu_0(k)$  of the isolated atom has to be simulated. It is achieved by using polynomial fits (usually polynomials of second or third order are fitted) to the pre-edge and post-edge spectra regions. Before the polynomial can be fitted, the edge energy has to be chosen and defined as 0 eV, determining the beginning of the EXAFS oscillations. Once the background is subtracted, the spectra flatten.

EXAFS spectra can now be plotted as a function of wave vector  $k$  along with a Fourier transform, and peaks corresponding to expected coordination shells can be seen. This enables the estimation of correctness of the background subtraction. At this point the data fitting procedure with use of EXCURV98 can be started.

For comparison of XAS spectra from different samples (or even the same sample but the thickness and density even in the case of the sample can vary over the extended time periods or if the position of the sample is changed) the spectra have to be normalised. It is done by dividing the spectrum by a value of a specific feature present in the whole set of spectra (e.g. in the midpoint of the first EXAFS oscillation).

## **2.2.2 Determination of Structural Parameters from EXAFS**

After the calibration of the raw XAS data in EXCALIB and background subtraction (optionally normalisation) in EXBACK, another Daresbury based program called EXCURV98<sup>4</sup> was used for fitting procedure. EXCURV98 is based on rapid curved wave theory.<sup>5</sup> EXCURV98 calculates electron scattering parameters for the atoms in the sample using the Hedin-Lundquist potential. There is also an energy offset  $E_0$  corresponding to the energy between the mean potential in the sample and the energy of the lowest unoccupied molecular orbital – it is always negative as defined in the program. The following parameters are fitted with use of EXCURV98: elemental identities of atoms, coordination numbers  $N$ , interatomic distances  $R$ , root mean square variation in interatomic distance  $2\sigma^2$  (or Debye-Waller factor – a measure of internal disorder of the sample) for the scattering atoms included in the fit. EXCURV98 also provides estimates of the uncertainty in these fitted parameters and an overall goodness of fit.

The first step – to amplify the rapidly decaying signal at high  $k$  values of spectrum – is multiplication of the  $k$ -space EXAFS spectrum by a weighting factor of  $k^n$ . Typically  $n = 3$ , and if the last part of the spectrum became too noisy after amplification, it was truncated. The following step includes defining all backscattering atoms and atomic potentials and phaseshifts are calculated by the program. Introduction of a set of approximate data (atom types and quantities, distances) is a starting point for an iterative refinement. This procedure is based on the least-squares method. The difference between the experimental data set and theoretical model is minimised with each iteration and is described as the fit factor  $R$ :

$$R = \sum_i^N \frac{1}{\sigma_i} (|k^n c_i^{\text{exp}}(k) - k^n c_i^{\text{th}}(k)|) \cdot 100\% \quad (2.3)$$

where  $N$  is the number of points in the data set and  $\sigma_i$  is the standard deviation between experimental and theoretical data points. The satisfactory value of the fit factor for the final parameters is fit index of  $\approx 20\%$ . The best results are obtained when the coordination shells are added and refined one at a time. After the first shell is acceptable, the second shell is defined and the whole fitting procedure is repeated for the newly introduced parameters, until a predicted minimum of the fit factor is obtained and iteration stopped. The whole procedure is repeated as long as the fit improves, but the distance of the furthest shell can not exceed 5 Å. At first the four main variables are refined in pairs – distances and Fermi energy  $E_f$  are refined together to adjust the phase of the fit, and the coordination number and Debye-Waller factor are refined to adjust the amplitude of the peaks) – and then the refinement is repeated for all of the parameters. The resulting final parameters for defined shell atoms include distances, coordination numbers, Debye-Waller factors and respective statistical errors of  $\pm 2\sigma$ .

There is a relationship between the bond lengths and oxidation state of the absorbing atom with the effect getting weaker with increasing distance (i.e. the first shell is the most influenced by the oxidation state change). The effect of interatomic distance changes is not as significant as absorption edge shifts or coulometric data, but is useful as the additional and guideline data. To extract information from these relationships, the graphs for reference samples or data from databases (therefore known parameters) were plotted: valency (y-axis) against the bond length (x-axis). The important issue is that all

standards should possess the same number of atoms in the first coordination shell as an investigated sample material, because the coordination number strongly affects the bond length. On this basis and knowing the distance absorber – first shell atoms, the unknown valency of analysed samples was evaluated.

In some cases (molybdenum and iridium samples) an amplitude reduction AFAC factor was used. AFAC is a k-independent correction to the EXAFS amplitude related to the proportion of electrons which perform an EXAFS type scatter on absorption. In EXCURV98 it should be normally be left at 1.0, unless one believes that spectra suffer from an amplitude damping effect. AFAC value was determined from data fitting of known (standard) samples, and then corresponding values of AFAC were used for modelling of unknown materials.

### 2.2.3 Atomic Concentrations from Transition Edge Steps

The intensity of an X-ray beam after it has travelled a distance  $x$  through a material is given by the Beer-Lambert law:

$$I = I_0 \exp\left[-x \sum m_i n_i\right] \quad (2.4)$$

where  $I_0$  is the incident intensity,  $\mu_i$  an atomic cross section ( $\text{m}^2$ ) and  $n_i$  an atomic concentration ( $\text{atoms m}^{-3}$ ). The sum is over all elements in the material. For the intensity after transmission through a sample of thickness  $t$  we replace  $x$  by  $t$  in Equation 2.4.

The experiment measures the counts in an ion chamber. This is proportional to  $I$  (or  $I_0$ ) but with an unknown, and slowly energy dependent, amplification factor. Thus the counts obey:

$$C = A(E)C_0 \exp\left[-t \sum m_i n_i\right] \quad (2.5)$$

The usual output is  $\ln\left[\frac{I_0}{I}\right]$ , described as the absorption. This is given by:

$$a = \ln\left[\frac{C_0}{C}\right] = -\ln A(E) + t \sum m_i n_i \quad (2.6)$$

At the absorption edge of a given element all the factors in Equation 2.6 are smoothly varying with energy except  $\mu$ , the absorption cross section of the given element. Thus the step in absorption at the edge,  $\Delta a$ , is given by:

$$\Delta a = t\Delta\mu m \quad (2.7)$$

which depends only on the concentration of the given element. The absorption cross-section edge step,  $\Delta\mu$ , may be obtained from tables. Hence the product  $nt$  may be found.

#### 2.2.4 Spectroelectrochemical Data Analysis

A combination of XAS and electrochemical data is a source of reciprocally supporting information. Following XAS and electrochemical information can be used for calculation of the film thickness by combining Equations 2.8 – 2.10:

$$x = \frac{\ln(I_0 / I_t)}{m} \quad (2.8)$$

from spectroelectrochemical data:

$$x = \frac{\Delta m}{\Delta sC} \quad (2.9)$$

from electrochemical data:

$$x = \frac{N}{AC} = \frac{\Gamma}{C} = \frac{Q}{nFAC} \quad (2.10)$$

where  $C$  is the concentration of the absorber,  $\Delta\mu$  is the absorption edge step, and  $\Delta\sigma$  ( $\text{cm}^2\text{mol}^{-1}$ ) is the difference in absorption cross-section between the bottom and the top of the edge.

Equation 2.9 can be used for calculating film thickness from the raw, unnormalised edge steps  $\Delta\mu$  with the use of tabulated absorption cross sections for the absorbing element at energies corresponding to the bottom and top of the absorption edge. Because unknown functions of energy are present in data collected in fluorescence mode, the above procedure could only be used for transmission mode spectra. The use

of edge steps to calculate thickness was validated by carrying out the same calculation on metal foil, where thickness and density (and therefore concentration) were known.

For the calculation of the thickness of the sample with the use of electrochemical data, the coverage of electroactive sites on the working electrode surface ( $\Gamma$ ) and their concentration ( $C$ ) in the film was evaluated coulometrically. Current-time correlations were derived from cyclic voltammograms and integrated to obtain the amount of charge ( $Q$ ) which passed during the electrochemical procedure using Equation 1.22. To make sure that obtained film thicknesses are correct, for calculated value of absorber coverage or concentration the thickness was calculated also with the use of the edge step and compared with the electrochemical calculations.

## 2.3 References

1. Abbott, A. P.; Nadhra, S.; Postlethwaite, S.; Smith, E. L.; Ryder, K. S., *Phys. Chem. Chem. Phys.* **2007**, *9*, 3735.
2. <http://www.srs.ac.uk/srs/stations.htm>
3. <http://www.dl.ac.uk/NCESS>
4. Dent, A. J.; Mosselmans, F., *An Introduction to EXAFS Data Analysis*. CLRC Daresbury Laboratory: Warrington, 1995.
5. Gurman, S. J.; Binsted, N.; Ross, I., *J. Phys. C* **1984**, *17*, 143.
6. Hillman, A. R.; Efimov, I.; Ryder, K. S., *J. Am. Chem. Soc.* **2005**, *127*, 16611.

# CHAPTER III

## METAL HEXACYANOFERRATE ELECTROACTIVE FILM MODIFIED ELECTRODES

### 3.1 Introduction

Iron(III) hexacyanoferrate(II) (Prussian Blue, PB, ferric ferrocyanide,  $\text{FeHCF}$ ) is one of the most ancient synthetic coordination materials known. The first synthesis of PB happened in Berlin, and the date is usually given as 1704.<sup>1</sup> It later became one of the most popular blue pigments, and was used to dye uniforms for the Prussian army soldiers. A colour maker Heinrich Diesbach was using cochineal, the crimson extract of the New World beetles to make a red lake. Other ingredients included also iron sulphate and potash (potassium carbonate). Diesbach got the latter component from the alchemist Johann Konrad Dippel. (Un)fortunately the potash was of a bad quality and contaminated with oil extracted from animal blood. As a result the lake made by Diesbach was very pale, and when he tried to concentrate it, it changed colour and turned blue. Although Diesbach and Dieppel had no idea what had happened, they suspected that the blood was important – potassium hexacyanoferrate, the substance formed upon the reaction of potash with the oil, is still known in German as

Blutlaugensaltz, blood-alkali salt.<sup>2</sup> The discovery was reported anonymously in 1710, and the recipe was described in 1724 by Woodward and Brown.<sup>3</sup> In 1978 there was the first report of the electrochemistry of PB films by Neff.<sup>4</sup>

### 3.2 Characterization of PB and Related Metal Hexacyanoferrates

PB and related metal hexacyanides (mHCN) are mixed-valence complexes of composition  $[A_xM_yR(CN)_6] \cdot zH_2O$ , where  $A$  is a univalent alkali metal cation ( $Li^+$ ,  $Na^+$ ,  $K^+$ ,  $Cs^+$ ) occupying interstitial sites of the mHCN network.

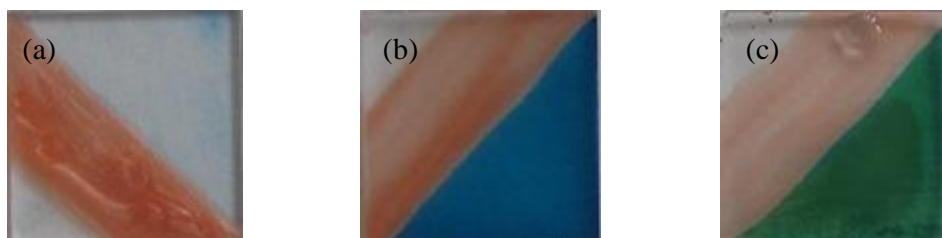
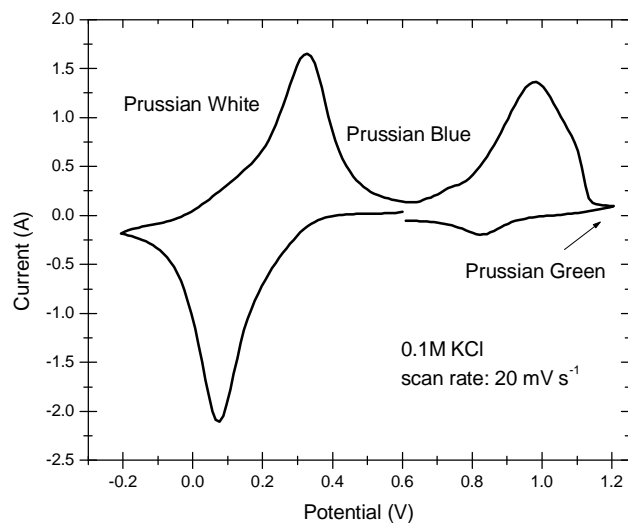


**Figure 3.1.** Cyclic voltammogram for PB film modified electrode (upper graph) and Prussian Blue films at different oxidation states on indium tin oxide coated glass slide electrodes. Prussian White or Everitt's salt:  $Fe^{II}Fe^{II}$  (a), Prussian Blue:  $Fe^{III}Fe^{II}$  (b), and Prussian Green:  $Fe^{III}Fe^{III}$  (c).

Both  $M$  and  $R$  are divalent or trivalent transition metals, with  $x$  such that it satisfies the electroneutrality condition. For the case where  $R$  is  $Fe$  the term metal hexacyanoferrates

(mHCF) will be used. The R and M sites are usually octahedral, with an almost linear network of repeating [...—N≡C—R—C≡N—M—N≡C—...] 3D units, Figure 3.2. Interstitial sites are occupied by water and counterions to compensate for the charge neutrality.<sup>5, 6</sup> The possibility to vary all three metals and the redox states of the latter two provides scope for manipulation of material properties such as electrochromism and thermochromism,<sup>6, 7</sup> ion-exchange,<sup>8-10</sup> mixed-valence electrical conductivity, charge storage capabilities,<sup>11</sup> electrocatalytic,<sup>12</sup> optical<sup>13</sup> and magnetic.<sup>13, 14</sup> Properties of metal hexacyanides can be also influenced by a range of external conditions such as temperature,<sup>13-15</sup> illumination<sup>13, 16, 17</sup> or applied potential.<sup>13, 18</sup> This makes mHCNs attractive for applications in variety of (bio)sensors,<sup>19-25</sup> batteries,<sup>26-28</sup> separations,<sup>8, 10, 29, 30</sup> optically switchable molecular compounds,<sup>13, 31</sup> high temperature molecular magnets<sup>17, 32-34</sup> and electrochromic devices.<sup>20, 35</sup> This group of materials has been studied as powders and pellets,<sup>36</sup> guests in various types of matrices<sup>6</sup> or films in modified electrodes.<sup>37</sup> Modification of an electrode surface with mHCNs can be achieved in a range of ways such as entrapment in a polymer matrix,<sup>38</sup> adsorption<sup>39</sup> or electrodeposition.<sup>40</sup>

The PB electrodeposition method proposed by Neff is based on electroreduction of solutions containing iron(III) and hexacyanoferrate(III) ions as the adduct  $\text{Fe}^{3+}[\text{Fe}^{\text{III}}(\text{CN})_6]^{3-}$ . A brown-yellow soluble one-to-one complex dominates in solutions containing ferric ( $\text{Fe}^{3+}$ ) and ferricyanide ( $[\text{Fe}^{\text{III}}(\text{CN})_6]^{3-}$ ) ions as a result of the equilibrium in Equation 3.1:<sup>41</sup>



Electrochemically deposited PB films may be partially oxidized to Prussian Green (PG). Reduction of PB yields Prussian White (PW), known also as Everitt's salt, which appears as a colourless thin film (Figure 3.1).<sup>41</sup> Since this discovery many studies on PB and numerous analogues have been reported.

There are two general electrochemical routes for preparation of cobalt hexacyanoferrate (CoHCF) and nickel hexacyanoferrate (NiHCF) modified electrodes.

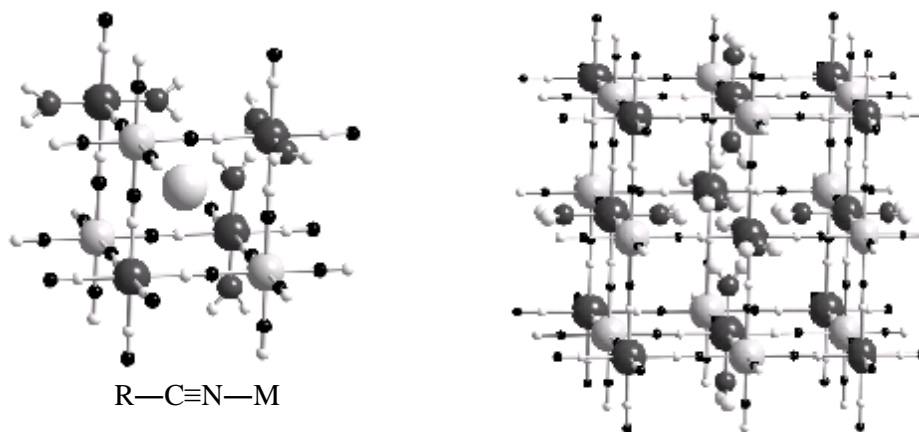


**Figure 3.2.** Schematic representation of the structure of metal hexacyanides: detail of an octahedron with an incorporated alkali countercation (left) and unit cell consisting of eight octahedra (right). Vacant sites are coordinated with  $H_2O$  molecules, M and R are divalent or trivalent transition metals.<sup>3</sup>

Potentiodynamic cycling in a solution of  $Co^{2+}$  or  $Ni^{2+}$  containing  $[Fe(CN)_6]^{3-}$  is the first preparation method. An alternative route is depositing Co or Ni and subsequent cycling in a solution of  $[Fe(CN)_6]^{3-}$  and KCl. Electro-dissolution of Co or Ni and formation of  $[Fe(CN)_6]^{4-}$  leads to the precipitation of Co/NiHCF.<sup>42</sup> Stoichiometry and structure diversity seen in mHCNs, because of their sensitivity to the procedure of preparation, is well known,<sup>43, 44</sup> therefore electrodeposited films may have different properties than chemically obtained samples. Furthermore, the use of the electrochemical potential enables one to drive charge state variations cyclically. Figure 3.3 shows electrodeposited CoHCF and NiHCF films on Pt disc and ITO electrodes.

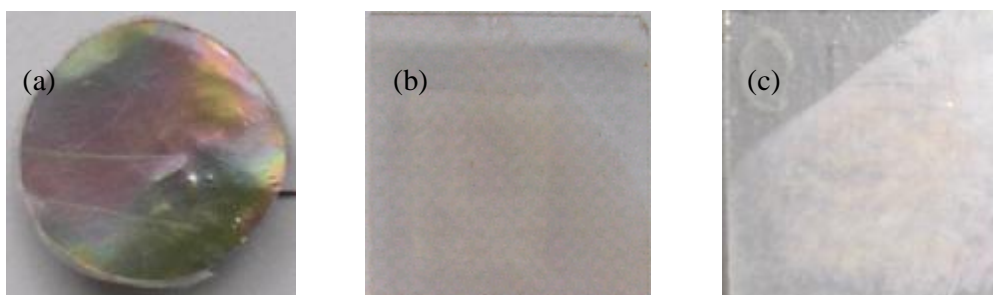


**Figure 3.3.** Cobalt hexacyanoferrate film on the Pt disc electrode (a) and ITO coated glass electrode (b); nickel hexacyanoferrate film on the ITO coated glass electrode (c).

Despite a wealth of information accumulated on mHCN systems, and more specifically on the mHCF systems over past thirty years, several ambiguities remain. EXAFS and XANES can provide valence states, coordination numbers, interatomic distances, elemental identities of neighbouring atoms, local order (expressed via the Debye-Waller factor) and oxidation state of the central atom. Both these methods have been used to explore structural features of CoHCF and NiHCF systems, but mainly for chemically prepared samples in the form of powder or pellets.<sup>7, 18, 36, 45-47</sup>

### 3.3 Iron Hexacyanoferrate Fe[Fe(CN)<sub>6</sub>]

The precise composition of any PB solid is extraordinarily preparation sensitive. Major classification of extreme cases is dependent on the counter cation and involves ‘insoluble’ PB (*i*-PB) which is  $\text{Fe}^{3+}[\text{Fe}^{3+}\{\text{Fe}^{\text{II}}(\text{CN})_6\}^{4-}]_3$  and ‘soluble’ PB (*s*-PB) which is  $\text{K}^+\text{Fe}^{3+}\{\text{Fe}^{\text{II}}(\text{CN})_6\}^{4-}$ . All forms of PB are in fact highly insoluble in water ( $K_{\text{sp}} \approx 10^{-40}$ ). The ‘solubility’ attributed to the latter form was caused by an illusion as easy dispersion of colloidal particles forms a blue sol in water that looks like a true solution.<sup>48</sup> The identity of PB as *s*-PB or *i*-PB of the initially electrodeposited PB has been discussed in the literature.<sup>48-55</sup> Generally it is agreed that *i*-PB is formed, followed by a gradual transformation and structural reorganisation to *s*-PB on subsequent potential cycling, with major conversion and introduction of  $\text{K}^+$  taking place in the first cycle. Reduction of the counter cationic  $\text{Fe}^{3+}$  to  $\text{Fe}^{2+}$  in the PB→PW transition has been suggested. If  $\text{Fe}^{2+}$  is then retained  $\text{Fe}^{2+}\text{K}^+$  becomes a ‘dispersed’ counter-cation, slowing down  $\text{K}^+$  incorporation.

Stilwell et al.<sup>56</sup> have studied in detail factors influencing the cycle stability of PB films. Films grown from chloride-containing solutions were found to be more stable compared to those grown from chloride-free solutions, although there are also some contrary conclusions.<sup>55</sup> Electrolyte pH is the main factor affecting film stability. Over 100 000 cycles were easily achieved in solutions of pH 2-3.

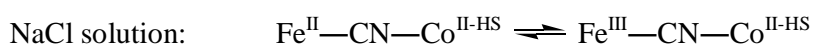
### 3.4 Complications in the Preparation of Metal Hexacyanoferrates

Despite of the apparent simplicity of the synthesis of PB and PB analogues, many complications can arise. Films may contain a variety of species in the interstitial sites. There is a tendency to fill the interstitial sites with solvent molecules or with the counterions used in the synthesis. The water content may vary from sample to sample, and is extremely sensitive to the preparation and storage conditions.<sup>57, 58</sup> Solids may contain several phases with different chemical environments around the M sites, or bridging cyanide ligands may undergo linkage isomerism. It means two possible ways that cyanide can adopt: [...R—C≡N—M...] or [...M—C≡N—R...].<sup>58, 59</sup> The extent of linkage isomerism depends strongly on the electronic structure of R and M, and does not occur at all in some PB analogues, while it is very common in others.<sup>58</sup>

### 3.5 Summary

There seem to be no doubts that Fe is the redox centre in nickel hexacyanoferrates and it was confirmed in our research. However, there are some differences in the literature whether or under which conditions it is Co or Fe that is oxidized for M = Co and N = Fe in mHCN PB analogue.<sup>6, 7, 15, 16, 18, 45</sup> Electrochemical behaviour of Co hexacyanoferrates appears to be dependant on the preparation route and on the nature of the interstitial counteraction.<sup>6, 7</sup> Some authors suggest the presence of the  $\text{Co}^{2+} \rightleftharpoons \text{Co}^{3+}$  redox process, and these exhibit performance that is opposite to other metal hexacyanoferrates with electrochemical behaviour assigned exclusively to the  $\text{Fe}^{2+} \rightleftharpoons \text{Fe}^{3+}$  redox couple.<sup>6</sup> In more recent publications by Berrottoni et al.<sup>5, 6</sup> with generation-4 poly(amidoamine) dendrimer (PAMAM) matrix entrapped CoHCF it is suggested that complex electrochemical processes involving more than one species are possible. Metal-to-metal electronic transition takes place (i.e.  $\text{Fe}^{\text{III}}\text{—CN—Co}^{\text{II}}$  to  $\text{Fe}^{\text{II}}\text{—CN—Co}^{\text{III}}$ ) and both metals can be oxidation centres. Further it is reasoned that existence of  $\text{Co}^{3+}$  is strictly associated with the presence of the “insoluble” form of hexacyanoferrates, as the lack of a  $\text{Fe}(\text{CN})_6$  unit gives more flexibility to the Co local environment, and in consequence facilitates oxidation of the cobalt redox centre. Sauter et al.<sup>18</sup> conclude that it is Co changing oxidation state in CoHCF and Fe in NiHCF, but

this group uses XPS and their electrochemical preparation method of the films is different to that used here. Photoinduced redox transformation of the form low spin (LS)  $\text{Co}^{\text{III}} \rightarrow$  high spin (HS)  $\text{Co}^{\text{II}}$  is also reported.<sup>18</sup> On the other hand Kulesza and co-workers suggest the Fe centre as the one changing oxidation state in CoHCF, but they use samples prepared by a precipitation method and in the presence of different alkali metal counteranions.<sup>7</sup> Sato et al. give a detailed description of CoHCF in the presence of  $\text{K}^+$  and  $\text{Na}^+$  cations, and with a range of methods used (Mössbauer, IR, UV-vis, EXAFS). They conclude that the behaviour of the film depends on the cation present in the electrolyte in the following way:<sup>13</sup>



Lezna et al.<sup>16</sup> describe quite complex relationships between different CoHCFs samples with use of combination of CV, IR and XPS experiments. They suggest that upon irradiation of the sample with near IR radiation it changes to a  $\text{Fe}^{\text{III}}\text{Co}^{\text{III}}$  compound. Also Fe is thought to be the active redox centre in the presence of  $\text{K}^+$  ions. Furthermore, XPS data of this group clearly displays changing Fe electron site rather than the Co one.

EXAFS research by Yokoyama et al. on the properties of chemically and electrochemically prepared Co hexacyanoferrate films as a function of temperature has been reported. In these studies change of the oxidation state in cobalt was observed from  $\text{Co}^{3+}$  at 30 K to  $\text{Co}^{2+}$  at 296 K, with significant amounts of  $\text{Co}^{3+}$  still existing at 296 K.<sup>14</sup>

### 3.6 Objectives

A significant amount of work has been done over past thirty years in characterization of electrodes modified with Prussian Blue and Prussian Blue analogues, and these materials are still of great interest. Although there is a significant amount of literature investigating electrochemistry of this group of compounds there has not been a lot of work done in the field of EXAFS on electrochemically deposited films, and the accumulated body of knowledge was insufficient for our purposes in three key respects.

First, some published EXAFS studies involve chemically prepared material,<sup>45</sup> which is not the same compositionally or structurally (i.e. the generic formula is over-simplistic) as the electrochemically prepared material. Second, signal requirements demand that we will need relatively thick films for EXAFS. Thirdly, there are additional unresolved differences in the literature, as to whether it is Co or Fe that is oxidized, and this process seems to be more complex and extremely sensitive to the external conditions.<sup>7, 45</sup>

In general, in the experiment presented in this thesis the aim was to determine the equilibrium compositions and local structures that define initial and final states of Prussian Blue type  $[A_xM_yFe(CN)_6] \cdot zH_2O$  electrodeposited materials with  $M=Fe, Co$  or  $Ni$ , and  $A=K$ . More specifically, we looked for the bond lengths, coordination numbers and Debye-Waller factors as functions of applied electrochemical potential corresponding to both complete and partial redox conversion. After determination from EXAFS perspective of signal-to-noise ratio under specified potentiostatic conditions (i.e. element, redox state, detection mode, film thickness and timescale) in order to optimise sample preparation and manipulation, a subsequent future step could possibly be potentiodynamic EXAFS experiment, and study of inter-conversion dynamics of already determined initial and final sample states.

EXAFS in combination with XPS studies on FeHCF, NiHCF and CoHCF systems allows the comparison of two sets of data. XPS yields more detailed charge state information than does the EXAFS, but only for the surface region of the films. These complementary data help to address the issue of spatial variations of the electrodeposited films. The main novelty is use of EXAFS on electrochemically prepared CoHCF and NiHCF samples to determine structure as a function of potential.

## 3.7 Experimental

### 3.7.1 X-ray Absorption Fine Structure

#### *i) Preparation of Prussian Blue Modified Electrode*

PB films were electrodeposited onto platinum disc electrodes (Goodfellow, 177 mm<sup>2</sup>) from a solution prepared as follows:

5 ml of 0.05 M HCl + 10 ml of 0.05 M K<sub>3</sub>Fe(CN)<sub>6</sub> + 10 ml of 0.05 M FeCl<sub>3</sub>

Deposition was carried out potentiostatically at +0.5 V vs. SCE. Following deposition each PB film was cycled 10 times at scan rate 0.1 V s<sup>-1</sup> in 0.1 M KCl background electrolyte. Subsequently, films were kept for 20 min. at a selected potential, removed from the background electrolyte, rinsed with de-oxygenated deionised water and transferred to the station hutch for the XAS data acquisition.

#### *ii) Preparation of CoHCF and NiHCF Modified Electrodes*

Electrochemical measurements were made in a conventional three-electrode cell, using an ECO CHEMIE  $\mu$ Autolab PGSTAT 20 potentiostat connected to a computer. CoHCF and NiHCF films for EXAFS experiments were deposited onto platinum disc electrodes by potentiodynamic cycling from 0.0 V to +0.9 V versus SCE at a scan rate of 0.1 V s<sup>-1</sup>. Films were deposited from aqueous solution prepared as follows: 25 ml of 0.5 M potassium chloride (KCl, Fisher Scientific) and 50  $\mu$ l of 0.5 M nickel(II) chloride hexahydrate (NiCl<sub>2</sub> · 6H<sub>2</sub>O, Fluka) or cobalt(II) chloride hexahydrate (CoCl<sub>2</sub> · 6H<sub>2</sub>O, Riedel-de Haën) respectively was de-oxygenated by purging by N<sub>2</sub> or Ar for 30 min. Subsequently 50  $\mu$ l of de-oxygenated 0.25 M potassium ferricyanide (K<sub>3</sub>Fe(CN)<sub>6</sub>, Sigma-Aldrich) solution was added. After each set of scans (usually 50) films were removed from the solution, rinsed with deionised H<sub>2</sub>O and the next layer was deposited in the same manner. This procedure was repeated three times for each film. During the deposition a steady stream of N<sub>2</sub> or Ar was blown across the surface of the solution. Freshly deposited films were cycled 10 times in 0.5 M KCl electrolyte at 0.1 V s<sup>-1</sup> scan rate, and afterwards kept for 20 min. at a selected potential. Prior to the XAS

experiment each film was removed from the background electrolyte, rinsed with de-oxygenated deionised water and transferred to the station hutch for the data acquisition. All experiments were carried out at room temperature.

iii) *XAS Data Collection: PB, CoHCF, NiHCF Modified Electrodes*

X-ray measurements were made at the synchrotron radiation source (SRS, Daresbury Laboratory, UK). EXAFS spectra were taken *ex situ* in fluorescence mode on beamline 16.5 (30 element solid state Ge(III) detector) or beamline 7.1 (9 element Si(III) detector). Measurements were taken at the Fe K-edge at 7125 eV, Ni K-edge at 8333 eV and Co K-edge at 7710 eV. All spectra were acquired up to the value of  $k_{max} = 14 \text{ \AA}^{-1}$ . Acquisition time of each single spectrum was about 30-40 minutes. Fluorescence spectra were summed, calibrated and background subtracted using the Daresbury programs EXCALIB<sup>60</sup> and EXBACK.<sup>60</sup> Fitting was achieved using EXCURV98,<sup>61</sup> providing interatomic distances ( $R$ ), coordination numbers ( $N$ ), root mean square deviation of bond length (i.e. r.m.s. disorder or Debye-Waller factors,  $2\sigma^2$ ) and the elemental identities of neighbouring atoms. An estimate of uncertainties in the fitted parameters is also provided by the EXCURV98 fitting program. Spectra were measured for samples and potentials summarized in Table 3.1.

method	sample	potential (V)
<b>EXAFS</b> Fe K-edge	FeHCF	-0.2, +0.2, +0.6
	CoHCF	+0.0
	NiHCF	+0.0
<b>EXAFS</b> Co K-edge	CoHCF	+0.0, +0.3, +0.9
<b>EXAFS</b> Ni K-edge	NiHCF	+0.0, +0.9
<b>XPS</b>	FeHCF	-0.2, +0.2, +0.6
	CoHCF	+0.0, +0.4, +0.6, +0.9
	NiHCF	+0.0, +0.6, +0.9
<b>IR</b>	NiHCF	+0.0, +0.9, +1.1
	CoHCF	+0.0, +0.3, +0.4, +0.5, +0.7, +0.9, +1.1

**Table 3.1.** Summary of methods and potentials at which data were collected for FeHCF, NiHCF and CoHCF modified electrodes.

### 3.7.2 X-ray Photoelectron Spectroscopy

#### *i) Preparation of Prussian Blue Modified Electrode*

Samples were prepared at the University of Leicester one day in advance. Sample preparation was identical to the EXAFS experiment, but indium tin oxide (ITO) coated glass slides were used as working electrodes. Modified electrodes were transported to the experimental site in sealed containers and handled prior to XPS data acquisition in the same way as described for EXAFS experiments.

XPS is surface sensitive method and samples may be influenced by the oxidative environment such as oxygen in the air during transport from the electrochemical cell into the XPS vacuum chamber. The most affected samples would be probably those emerged from the solution at the most reductive potentials. The attempt was made to overcome this issue by etching of the sample for extended periods of time (between 2 minutes to over 2 hours) without removing it from the vacuum chamber. As it did not result in better quality results and the structure of the sample itself was probably changed by etching process, this procedure was given up.

#### *ii) Preparation of CoHCF and NiHCF Modified Electrodes*

CoHCF and NiHCF films for XPS were deposited onto ITO glass electrodes in an identical manner to the EXAFS experiments, but with only one layer of the film, as the technique is surface sensitive. Prior to the measurements, films were cycled ten times in 0.5 M KCl, stopped at the required potential, removed from the solution, rinsed with de-oxygenated deionised H<sub>2</sub>O and dried.

#### *iii) XPS Data Collection and Spectra Processing: PB, CoHCF and NiHCF Modified Electrodes*

XPS measurements were made using monochromatic Al K $\alpha$  radiation (E=1486.7 eV) on the Scienta ESCA300 spectrometer at the National Centre for Electron Spectroscopy and Surface Analysis (NCESS) in Daresbury Laboratory. The following settings were used in the data acquisition: take off angle 90°, slit 0.8 mm, and a flood gun at 2 eV to prevent charging of samples. An insulating sample becomes charged when its electrons

are photo-ejected. In such a case, the flood gun is used to neutralize the charging effect with a beam of low energy electrons. The problem with charging may also arise for insulating electrode substrate such as ITO coated glass slides - ITO itself is a conducting material, but the supporting glass is insulating. All measurements were performed at room temperature. The spectra were fitted without taking into account shake-up satellites present at the low kinetic energy side of the peaks, as they comprise only a negligible fraction of the whole peak (within the error for our estimate). A Shirley background was used for the peak fitting. Spectra were measured at potentials summarized in Table 3.1.

### 3.7.3 Infrared Spectroscopy

IR data was recorded at the University of Leicester. CoHCF and NiHCF modified electrodes were prepared in the same manner as for XPS and EXAFS experiments. Samples were held at the selected potential for 20 minutes, rinsed with deionised water, dried and mounted in the sample holder for *ex situ* data acquisition. ITO coated glass slides were used as working electrodes, an Ag/AgCl sat'd KCl electrode was used as the reference electrode and a Pt mesh was the counter electrode. IR spectra were recorded in transmission mode. Data was acquired at samples and potentials summarized in Table 3.1.

## 3.8 Data Analysis

### 3.8.1 Prussian Blue Modified Electrode

The thickness of the films was calculated from the charge consumed during the voltammetric scans, according to Equation 3.2:<sup>62, 63</sup>

$$h = \frac{Q}{nFA} \cdot \frac{d^3 N_A}{4} \quad (3.2)$$

where:  $Q$  (C) is the charge,  $F$  (96484.56 C mol<sup>-1</sup>) is Faraday constant,  $A$  (cm<sup>2</sup>) is the electrode area,  $d$  (cm) is the length of the unit cell,  $N_A$  ( $6.022 \cdot 10^{23}$  mol<sup>-1</sup>) is the Avogadro constant,  $n$  is the number of electrons involved in the redox process (here

$n=1$ ),  $h$  (cm) is the thickness of the film. There are four effective iron atoms in the unit cell, hence the number 4 in the equation. For PB the length of the unit cell  $d=10.17 \text{ \AA}$ .<sup>62</sup>

The EXAFS signal was good enough to allow the data fitting up to the limit of  $k_{max}=10 \text{ \AA}^{-1}$ . The Fe—C and Fe—N distances are anticipated to be circa  $1.92 \text{ \AA}$  and  $2.00 \text{ \AA}$  respectively for the oxidized PB film (both Fe centres 3+ oxidation state). These distances were obtained from the crystallographic (X-ray diffraction, XRD) database<sup>64</sup> for the PB crystal. The single nearest neighbour shell was fitted and the splitting was ignored at first, as relatively small. The Fe—Fe coordination sphere at the distance of about  $5.1 \text{ \AA}$  was also included to keep the value of Fermi Energy (EF) constant, as it could drift over a wide range when short distance shells are included. Subsequently the Fe—N coordination shell was added at a distance of about  $3.1 \text{ \AA}$ . The in-line structure yields a very high Debye-Waller factor for Fe—N. To improve the fitting results the N atom was moved slightly out of line to the position at the angle of  $200^\circ$  (ANG  $200^\circ$ ). The coordination number N was kept at the fixed value 6.

Multiple scattering was not included in the data fitting as it did not give a significant improvement.

### 3.8.2 CoHCF and NiHCF Modified Electrodes

Thicknesses of CoHCF and NiHCF films were calculated using the same Equation 3.2 as in the case of PB. The only difference was the length of the unit cell  $d=10.35 \text{ \AA}$  for Co and Ni HCF samples.<sup>65</sup>

EXAFS data was also analysed in the same way as for PB, with signal-to-noise ratio allowing the data fitting up to the value of  $k_{max}=10 \text{ \AA}^{-1}$ . For the CoHCF sample for Co K-edge the first Co—N shell was fitted at first, and subsequent shells were added in the next step, always improving the fit index significantly. Although atoms [...Co—N≡C—Fe...] forming the CoHCF film lattice are almost in line including the multiple scattering did not improve the fit. In the same time the bond angles were iterating to the values where multiple scattering was very weak. Therefore multiple scattering was not included in the fits.

There was a 3 eV shift between the EXAFS data acquired at the experimental station 7.1 and 16.5 due to the monochromator calibration. For the data analysis all the results are referred to the 7.1 calibration.

## 3.9 Results

### 3.9.1 Iron Hexacyanoferrate Modified Electrode

The thickness of the PB films can be easily controlled by the time of deposition, and can be from a few nanometres to a few thousands of micrometres. In the case of this study electrodeposited PB films were of a thickness  $h$  of few dozens of micrometres, as calculated from the charge consumed during the voltammetric scans, according to the Equation 3.2.

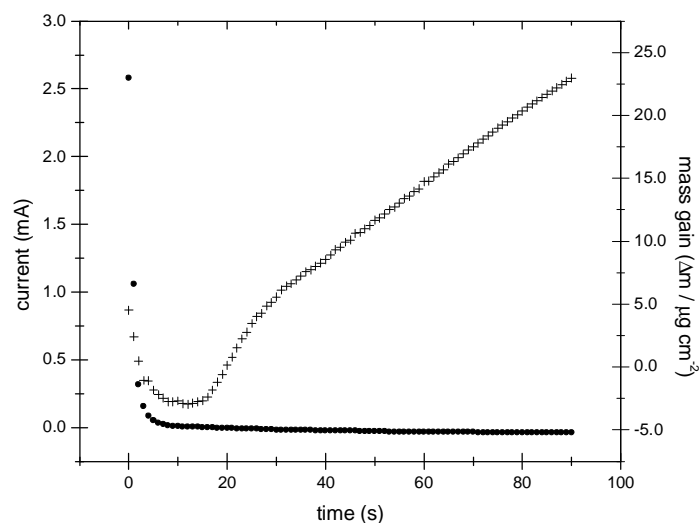


**Figure 3.4.** EQCM monitored electrodeposition of Prussian Blue film at +0.5 V vs. SCE. Deposition time: 90 s. Current (●), mass change (+).

EQCM monitored electrodeposition process of PB film is shown in the Figure 3.4 After the initial few seconds the process stabilizes, the current reaches almost constant value and the mass gain increases in a linear manner. The typical cyclic voltammogram for freshly deposited PB film in 0.5 M KCl electrolyte is shown in Figure 3.5 In this

potential range (i.e. from  $-0.2$  V to  $+0.6$  V) the film changes colour from transparent to blue at  $+0.2$  V vs. SCE. This is associated with the change of oxidation state of Fe carbon bonded redox centre from  $\text{Fe}^{2+}$  to  $\text{Fe}^{3+}$ .

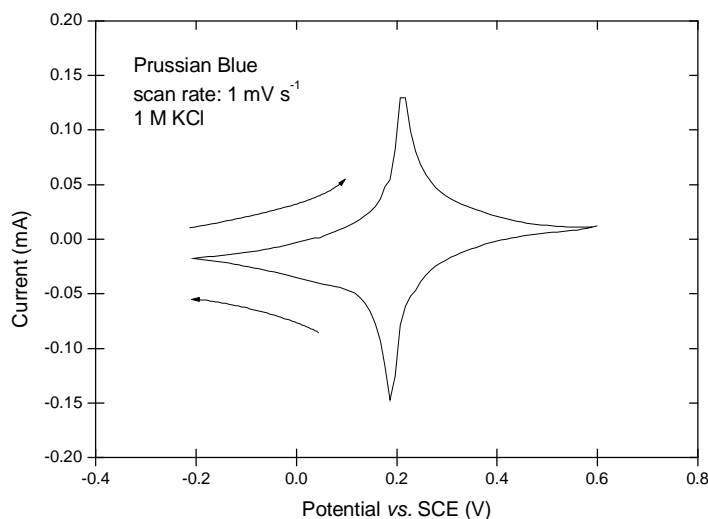


**Figure 3.5.** Cyclic voltammogram of electrodeposited PB film, electrode: ITO coated glass slide,  $1.5 \text{ cm}^2$ . Thickness of the film:  $150 \text{ }\mu\text{m}$ .

Figure 3.6 shows X-ray photoelectron spectra of Fe  $2p_{3/2}$  and Fe  $2p_{1/2}$  lines for the PB electrode emersed at three distinct potentials, i.e. fully reduced ( $-0.2$  V), fully oxidized ( $E=+0.6$  V), and partially converted ( $E=+0.2$  V). The value of potential referring to each spectrum is shown in the picture. The plotted spectra are not energy calibrated. Each of measured Fe 2p XPS spectra encompasses two lines belonging to  $\text{Fe}^{2+}$  and  $\text{Fe}^{3+}$ . Theoretically the oxidation state of carbon bonded Fe centres present in the PB electrode should be changing from the purely  $\text{Fe}^{2+}$  to the purely  $\text{Fe}^{3+}$  form. It is impossible to see this change unambiguously for two reasons. In the first place it is because of the presence of  $\text{Fe}^{3+}$  counteranions incorporated into the film structure during the electrodeposition process. Some  $\text{Fe}^{3+}$  is expelled from the film during the redox cycling, and in the case of KCl background electrolyte exchanged for  $\text{K}^+$  cations. Apart from being expelled from the film, there is a fraction of  $\text{Fe}^{3+}$  which gets reduced to  $\text{Fe}^{2+}$ , and remains in this form. The second issue is the problem of oxidative influence of the air. Contact with the air takes place during the transfer process between

electrochemical cell and XPS data acquisition vacuum chamber. Transfer was always completed in the shortest possible time, but the most prone to oxidative environment is the outermost part of the film, and XPS is sampling only up to a few microns deep into the sample. Samples emerged when in the reduced state are the most vulnerable to oxidation. Both of these factors, Fe counteraction retention in two oxidation states and influence of air, obscure the content of  $\text{Fe}^{2+}$  and  $\text{Fe}^{3+}$  redox centres in the film lattice. Probably for this reason there is no observable change in the shape or position of Fe 2p XPS electron lines shown in the Figure 3.6.

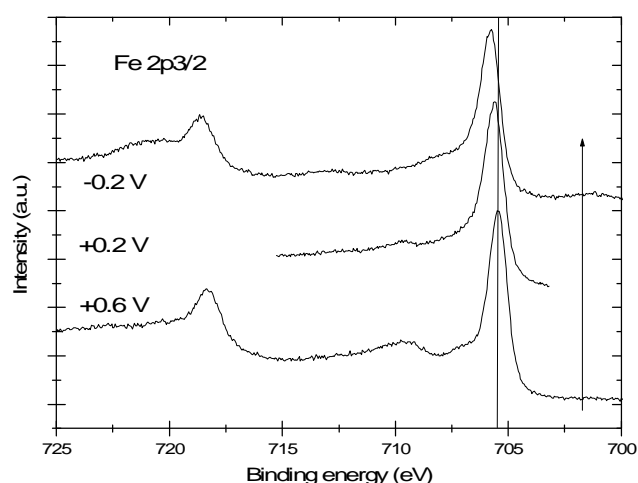


**Figure 3.6.** Fe  $2p_{3/2}$  and Fe  $2p_{1/2}$  XPS electron lines for the PB sample emerged at potentials:  $-0.2$  V,  $+0.2$  V and  $+0.6$  V vs. SCE as described in the picture. Background electrolyte:  $0.5$  M KCl. No significant change in shape or line position can be observed.

sample	binding energy (eV)					
	Fe $2p_{3/2}$	K $2p_{3/2}$	C $1s$	N $1s$	O $1s$	In $3d_{5/2}$
<b>+0.6 V</b>	705.5	290.8	281.5	394.6	527.6	441.8
<b>+0.2 V</b>	705.6	290.9	281.6	394.8	528.1	441.7
<b>-0.2 V</b>	705.7	290.9	281.8	394.9	528.2	441.7

**Table 3.2.** Binding energies (eV) of Fe  $2p_{3/2}$ , K  $2p_{3/2}$ , C  $1s$ , N  $1s$ , O  $1s$ , In  $3d_{5/2}$  obtained from XPS data for electrodeposited PB film at three different potentials:  $-0.2$  V,  $+0.2$  V and  $+0.6$  V. Energies not corrected.

Binding energies of Fe 2p<sub>3/2</sub>, K 2p<sub>3/2</sub>, C 1s, N 1s, O 1s, In 3d<sub>5/2</sub> in PB modified electrode for the different oxidation states are listed in Table 3.2.

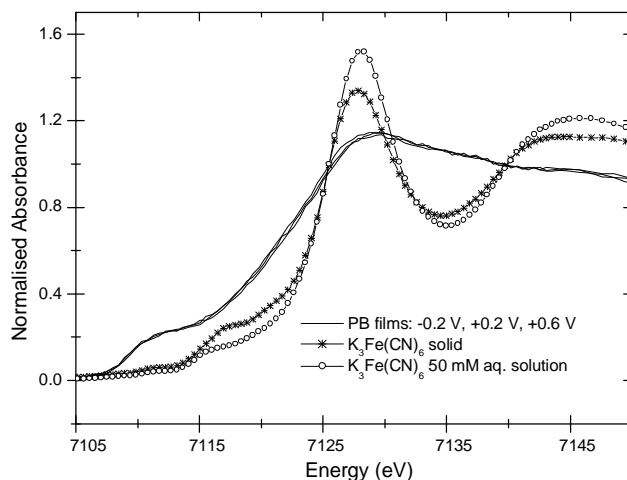


**Figure 3.7.** XANES of the Fe K-edge in PB film modified electrode at three different potentials:  $-0.2$  V,  $+0.2$  V and  $+0.6$  V (—),  $K_3Fe(CN)_6$  powder (—\*—) and  $K_3Fe(CN)_6$  50 mM aqueous solution (—○—). No visible change in XANES for three different oxidation states of PB.

Figure 3.7 presents XANES of PB films together with XANES of standards:  $K_3Fe(CN)_6$  solid powder and  $K_3Fe(CN)_6$  50 mM aqueous solution. Although it is XANES of the PB films at three different oxidation states, corresponding to applied potentials of  $-0.2$  V,  $+0.2$  V and  $+0.6$  V, there is no noticeable difference between them.

Structural parameters derived from fits to EXAFS Fe K-edge for the PB films are shown in Table 3.3. It shows data for the film emersed at three different potentials. Parameters were fitted for the first (Fe—C), second (Fe—N) and third (Fe—Fe) coordination shells. ANG values of circa  $200^\circ$  for nitrogen indicate the lack of linearity of [...Fe—C≡N—Fe...] units, with N atoms being slightly out of line. Table 3.3a with fit indexes and  $\Delta E_0$  refers to fits in Table 3.3.

Sample	element	Distance R (Å)	Coordination number N	$\sigma^2$ ( $10^{-4}$ Å)
<b>K<sub>3</sub>Fe(CN)<sub>6</sub> solid</b>	C	1.96 ± 0.01	<b>6</b>	80 ± 20
	N	3.10 ± 0.01	<b>6</b>	70 ± 10
<b>PB film</b>				
<b>-0.2 V</b>	C	1.93 ± 0.03	<b>6</b>	150 ± 50
	N	3.09 ± 0.03	<b>6</b>	60 ± 30
	Fe	5.05 ± 0.03	<b>6</b>	40 ± 30
<b>+0.2 V</b>	C	1.95 ± 0.04	<b>6</b>	150 ± 50
	N	3.11 ± 0.04	<b>6</b>	60 ± 40
	Fe	5.11 ± 0.03	<b>6</b>	5 ± 25
<b>+0.6 V</b>	C	1.94 ± 0.04	<b>6</b>	150 ± 50
	N	3.16 ± 0.04	<b>6</b>	60 ± 40
	Fe	5.14 ± 0.03	<b>6</b>	15 ± 40

**Table 3.3.** Structural parameters for the first (Fe—C), second (Fe—N) and third (Fe—Fe) coordination shells in PB film modified electrode. Data for different redox states (−0.2 V, +0.2 V and +0.6 V vs. SCE) is derived from fits to Fe K-edge EXAFS spectra. Uncertainties to coordination numbers are not shown if their values are less than 0.01. Bold coordination numbers signify the number was a fixed value (not fitted).

Sample	Fit index (%)	$\Delta E_0$ ( $\pm 5$ eV)
<b>K<sub>3</sub>Fe(CN)<sub>6</sub> solid</b>	17.0	-2.7
<b>PB film</b>		
<b>-0.2 V</b>	39.4	15.0
<b>+0.2 V</b>	37.5	8.6
<b>+0.6 V</b>	38.9	10.0

**Table 3.3a.** Fit indexes and  $\Delta E_0$  values referring to fits to EXAFS data for PB film modified electrode presented in table 3.3.

Debye-Waller factors are significantly higher for the first Fe—C coordination shell. This disorder, higher than for the further shells, is probably introduced by the very small difference between Fe—C and Fe—N distances. XRD indicates a difference of 0.08 Å. This is not resolvable over our data range, but introduces a significant amount of disorder or splitting in the nearest neighbour distances.

A significant amount of disorder is probably introduced by the interstitial  $\text{Fe}^{2+}$  and/or  $\text{Fe}^{3+}$  atoms, distributed randomly in the PB film lattice. Debye-Waller factors are relatively low for the Fe—Fe distance. It is because two (or even more if one counts interstitial Fe) iron centres introduce disorder if they are in different environments, but they yield consistent data for the coordination shell they both comprise.

### 3.9.2 Cobalt Hexacyanoferrate and Nickel Hexacyanoferrate Modified Electrodes

Figure 3.8 shows electrodeposition of a cobalt hexacyanoferrate film for the EXAFS experiment. The film was deposited by potentiodynamic cycling from  $E=0.0$  V to  $E=+0.9$  V versus SCE at a scan rate of  $0.1 \text{ V s}^{-1}$ . This is repeated three times to improve the signal-to-noise ratio in the EXAFS data.

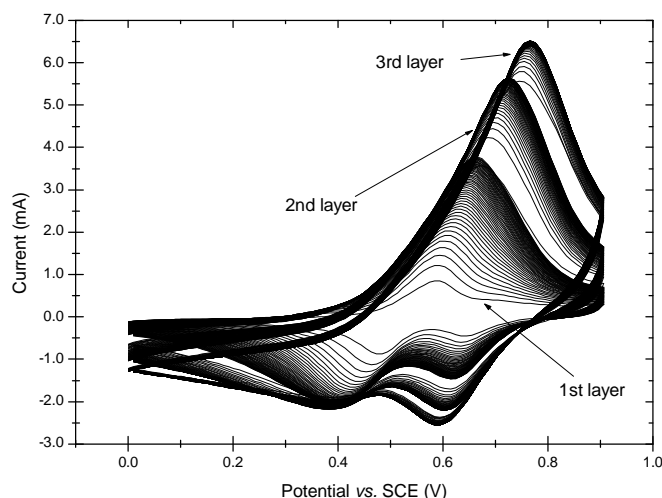


**Figure 3.8.** Potentiodynamic deposition of 3 layers of the CoHCF film onto Pt disc electrode. Scan rate  $0.1 \text{ V s}^{-1}$ .

Typical cyclic voltammograms at a range of scan rates ( $1, 2, 5$  and  $10 \text{ mV s}^{-1}$ ) for CoHCF and NiHCF electrodeposited films are shown in Figure 3.9 and Figure 3.10 respectively. Deposited films were of a thickness of  $10 \text{ nm}$  to  $70 \text{ nm}$  as calculated from the charge consumed during the voltammetric scans, according to the Equation 3.2. The size of the unit cell used for calculations was  $10.35 \text{ \AA}$ .<sup>65</sup> The recorded redox potential

for room temperature for CoHCF sample was +0.56 V and for NiHCF +0.61 V vs. SCE. It is consistent with the other results: the iron site is the electroactive centre in the NiHCF film, but its redox potential is higher than the cobalt redox potential in CoHCF, and cobalt is the active centre in the latter one.

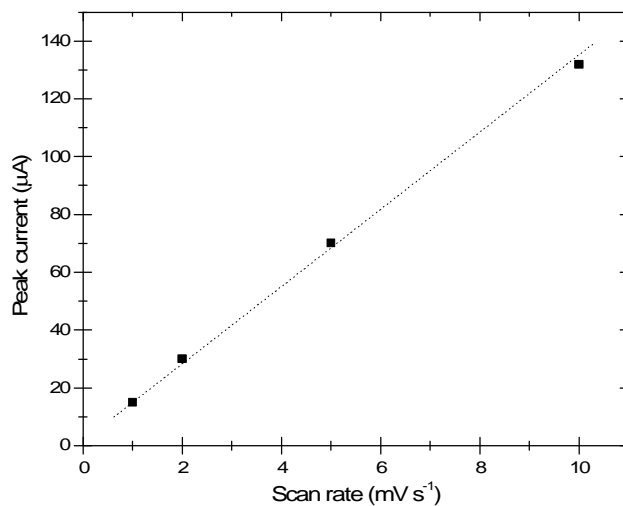
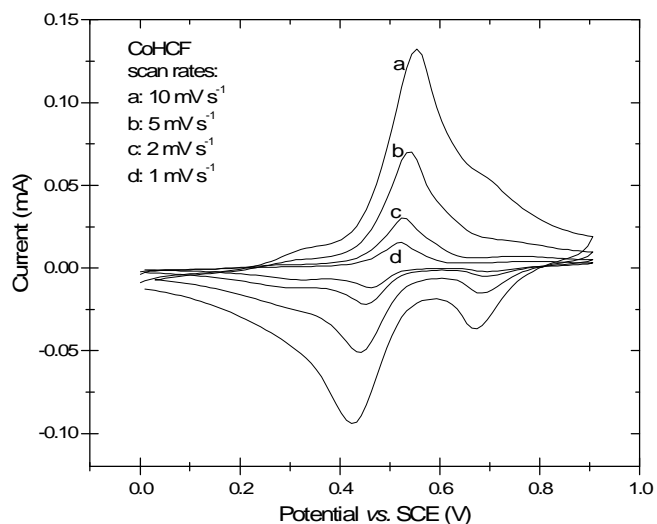


**Figure 3.9.** Typical cyclic voltammograms of cobalt hexacyanoferrate modified electrode at a range of scan rates: 1, 2, 5 and 10 mV s<sup>-1</sup>. Background electrolyte: 0.5 M KCl. Calculated coverage of the electrode:  $\Gamma = 2.7 \times 10^{-8}$  mol cm<sup>-2</sup>, yielding the thickness of the film of 45 nm. The lower graph shows the data derived from the CV plots: anodic peak current as a function of a scan rate.

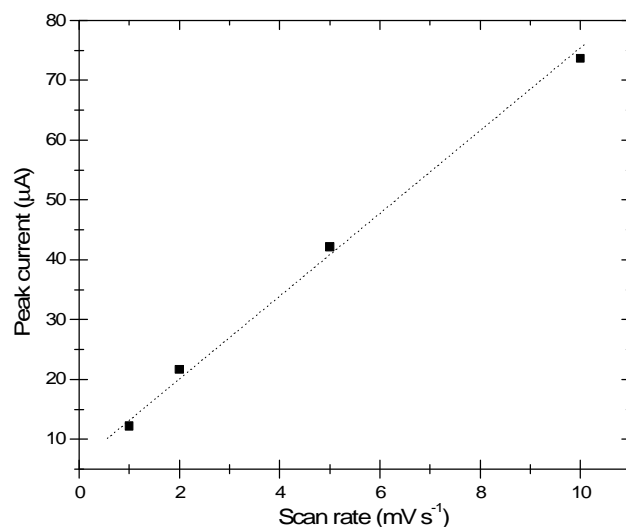
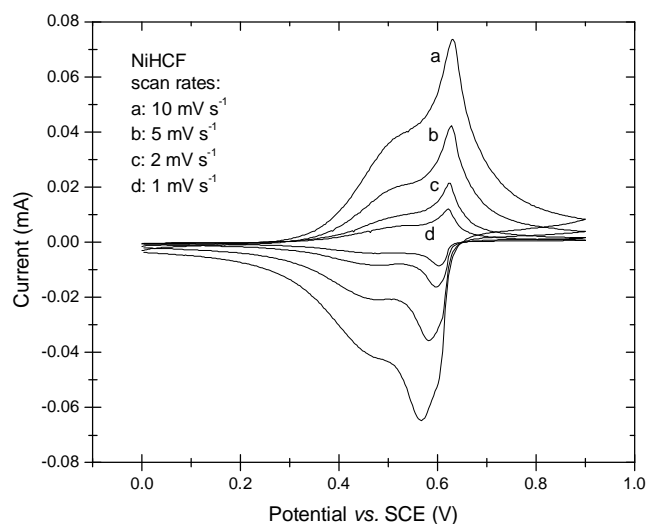


**Figure 3.10.** Typical cyclic voltammogram of nickel hexacyanoferrate modified electrode at a range of scan rates: 1, 2, 5 and 10 mV s<sup>-1</sup>. Background electrolyte 0.5 M KCl. Calculated coverage of the electrode:  $\Gamma = 6.8 \times 10^{-9}$  mol cm<sup>-2</sup>, yielding the thickness of the film of 12 nm. The lower graph shows the data derived from the CV plots: anodic peak current as a function of a scan rate.

For the both films plots of the peak currents  $i_p$  vs. scan rates  $\nu$  are shown below plots of cyclic voltammograms. As can be seen peak currents are linearly proportional to scan rate, in contrast to the  $\nu^{1/2}$  dependence observed for Nernstian waves of diffusing

species. The area under the reduction/oxidation wave, corrected for residual currents, represents the charge required for the full reduction of the layer. Hence the surface coverage can be evaluated using the relation:  $Q=nFA\Gamma$ .

*i) Extended X-ray Absorption Fine Structure*

Co K-edge  $k^3$  weighted EXAFS data with corresponding Fourier Transform (radial structure function) for CoHCF modified electrode are presented at Figure 3.11 Both spectra are fitted and these theoretical data is represented by dotted line. The signal-to-noise ratio is quite poor for the higher wave vector  $k$  values as can be seen at the EXAFS (upper) plot.

There are three distinctive peaks visible in the FT plot at distances of circa 2 Å, 3 Å and 5 Å. These peaks correspond to the distances of N, C and Fe atoms from the Co atom in the film lattice, respectively.

XANES of the Co K-edge in CoHCF film is shown at Figure 3.12. The data presented are for three different redox states of the sample acquired at the potentials:  $E=0.0$  V,  $E=+0.3$  V and  $E=+0.9$  V. There is evident change in the position and shape of the white line with the change of the redox state of the sample from reduced to oxidized. The behaviour of the white line with the broad intermediate (potential  $E=+0.3$  V) peak is characteristic for the molecular model described in the discussion part.

XANES of the Ni K-edge in NiHCF film is shown at Figure 3.13 These data are for two extreme redox states of the sample: fully reduced ( $E=0.0$  V) and fully oxidized ( $E=+0.9$  V). Alternation is noticeable neither in the white line position nor in its shape. No redox activity of Ni centre can be seen.

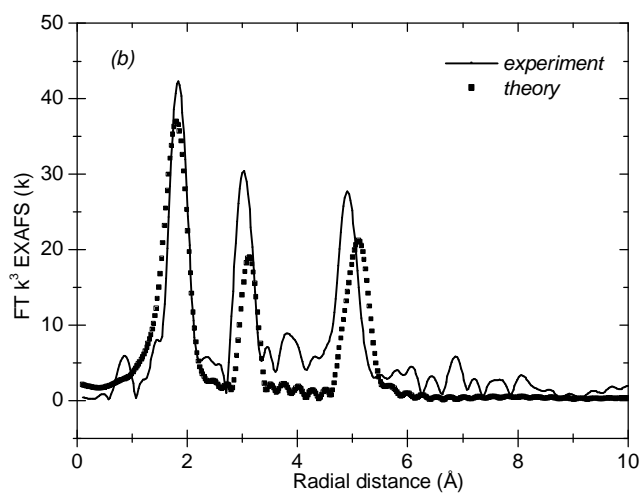
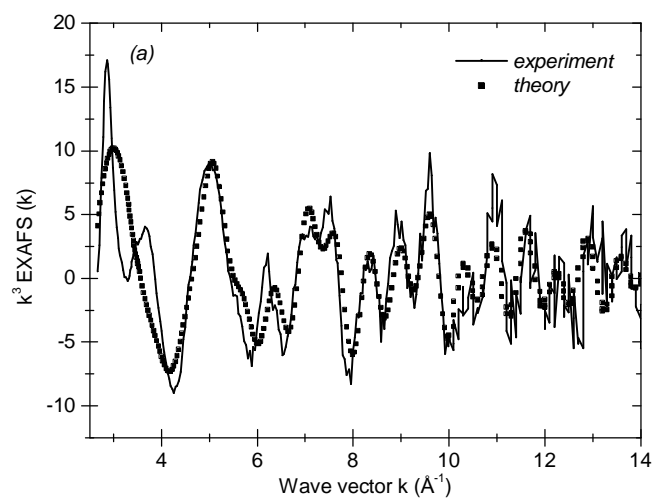


**Figure 3.11.** Co K-edge  $k^3$  weighted EXAFS spectra of cobalt hexacyanoferrate film at potential  $E=+0.9$  V (a) and corresponding Fourier Transform (b). Experimental data (—) and fitted theoretical data (■).

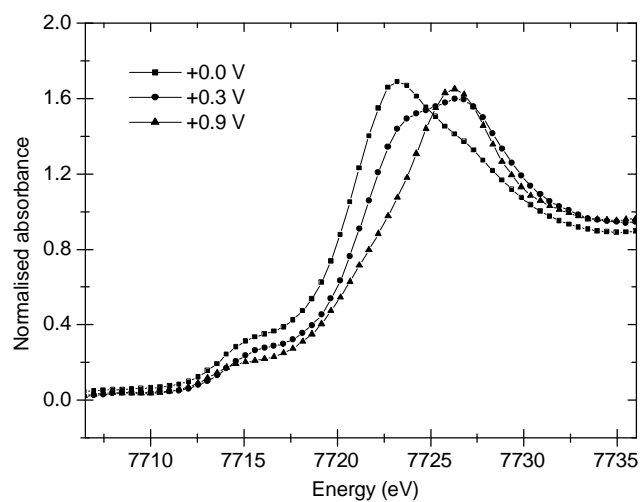


**Figure 3.12.** XANES of the Co K-edge in the cobalt hexacyanoferrate film modified electrode. The change is clear in the position and the shape of the white line with the redox process:  $\text{Co}^{2+}$  ( $E=0.0$  V,  $\blacksquare$ ) to  $\text{Co}^{3+}$  ( $E=+0.9$  V,  $\blacktriangle$ ) through the mixed intermediate form ( $E=+0.3$  V,  $\bullet$ ).

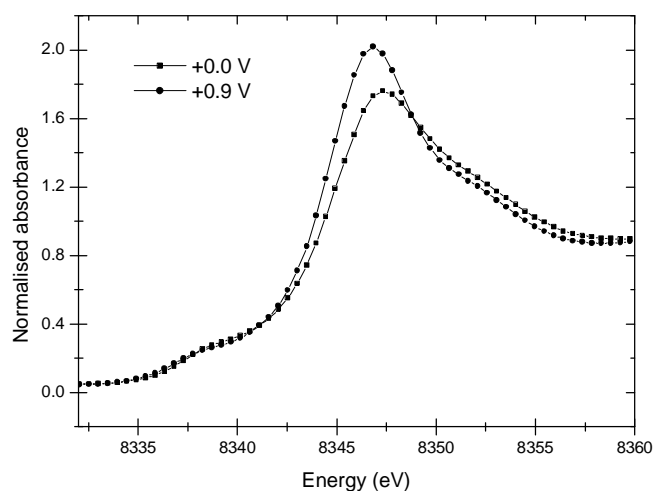


**Figure 3.13** XANES of the Ni K-edge in the nickel hexacyanoferrate film modified electrode. No significant change in the position or shape of white line is observed in XANES for two extreme oxidation states of the film:  $E=0.0$  V ( $\blacksquare$ ) and  $E=+0.9$  V ( $\bullet$ ).

EXAFS derived data for NiHCF and CoHCF sample are presented in Table 3.4 and Table 3.5 respectively, along with the parameters fitted for standards, i.e. aqueous

solutions of NiCl<sub>2</sub> and CoCl<sub>2</sub>. Data were recorded at two different stations 7.1 and 16.5 in Daresbury Laboratory, as indicated in the tables. Tables 3.4a and 3.5a correspond to Table 3.4 and 3.5 and show fit indexes and  $\Delta E_0$  for fits presented therein.

Sample	Edge	Element	Distance R (Å)	Coordination number N	$\sigma^2$ (10 <sup>-4</sup> Å)
<b>50 mM CoCl<sub>2</sub></b>	<b>Co K-edge</b>	O	2.09 ± 0.02	<b>6</b> ± 0.5	50 ± 10
<b>CoHCF film</b>	<b>Co K-edge</b>				
<b>+0.9 V</b> (station 16.5)		N	1.89 ± 0.02	<b>6</b>	130 ± 60
		C	3.15 ± 0.02	<b>6</b>	25 ± 10
		Fe	5.05 ± 0.02	<b>6</b>	50 ± 25
<b>+0.7 V</b> (station 7.1)		N	1.88 ± 0.04	<b>6</b>	130 ± 20
		C	3.18 ± 0.02	<b>6</b>	40 ± 30
		Fe	5.07 ± 0.04	<b>6</b>	40 ± 10
<b>+0.3 V</b> (station 7.1)		N	1.96 ± 0.02	<b>6</b>	270 ± 40
		C	3.27 ± 0.02	<b>6</b>	50 ± 30
		Fe	5.16 ± 0.04	<b>6</b>	120 ± 50
<b>+0.0 V</b> (station 16.5)		N	1.85 ± 0.06	—	180 ± 120
		N	2.04 ± 0.06	—	190 ± 160
		C	3.27 ± 0.02	—	50 ± 30
		Fe	5.16 ± 0.04	—	120 ± 50
		Fe	5.16 ± 0.08	<b>6</b>	140 ± 100
<b>+0.0 V</b> (station 7.1)		N	2.02 ± 0.02	<b>6</b>	220 ± 50
		C	3.33 ± 0.02	<b>6</b>	30 ± 30
		Fe	5.16 ± 0.08	<b>6</b>	140 ± 100
<b>+0.0 V</b> (station 7.1)	<b>Fe K-edge</b>	C	1.98 ± 0.02	<b>6</b>	100 ± 20
		N	3.13 ± 0.03	<b>6</b>	80 ± 50
		Co	5.21 ± 0.04	<b>6</b>	90 ± 40

**Table 3.4.** Structural parameters (elemental identities, distances, coordination numbers and Debye-Waller factors) for CoHCF film modified electrode at a range of oxidation states derived from the fits to EXAFS data truncated to  $k_{max}=10 \text{ \AA}^{-1}$ . Data for Co K-edge at potentials: +0.0 V, +0.3 V, +0.7 V and +0.9 V, and Fe K-edge at the potential +0.0 V. Coordination numbers not modelled (i.e. left at a fixed value) are bold.

Sample	Station	Edge	Fit index (%)	$\Delta E_0$ ( $\pm 5$ eV)
<b>50 mM CoCl<sub>2</sub></b>		<b>Co K-edge</b>	4.7	-7.2
<b>CoHCF film</b>		<b>Co K-edge</b>		
<b>+0.9 V</b>	16.5		34.2	-0.1
<b>+0.7 V</b>	7.1		18.1	-6.4
<b>+0.3 V</b>	7.1	single shell fit	20.5	-7.5
		split shell fit	20.4	-7.5
<b>+0.0 V</b>	16.5		42.3	-3.8
	7.1		19.1	-7.7
<b>+0.0 V</b>	7.1	<b>Fe K-edge</b>	18.1	-3.6

**Table 3.4a.** Fit indexes and  $\Delta E_0$  values referring to fits to EXAFS data for CoHCF film modified electrode presented in table 3.4.

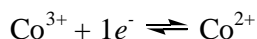
Sample	Edge	Element	Distance R ( $\text{\AA}$ )	Coordination number N	$\sigma^2$ ( $10^{-4}$ $\text{\AA}$ )
<b>50 mM NiCl<sub>2</sub></b>	<b>Ni K-edge</b>	O	$2.06 \pm 0.02$	$4.8 \pm 0.5$	$75 \pm 10$
<b>NiHCF film</b>	<b>Ni K-edge</b>				
<b>+0.9 V</b>		N	$2.04 \pm 0.02$	<b>6</b>	$70 \pm 15$
		C	$3.33 \pm 0.03$	<b>6</b>	$40 \pm 30$
		Fe	$5.24 \pm 0.02$	<b>6</b>	$60 \pm 20$
<b>+0.0 V</b>		N	$2.04 \pm 0.02$	<b>6</b>	$80 \pm 10$
		C	$3.33 \pm 0.02$	<b>6</b>	$40 \pm 20$
		Fe	$5.22 \pm 0.03$	<b>6</b>	$100 \pm 30$
<b>+0.0 V</b>	<b>Fe K-edge</b>	C	$2.01 \pm 0.01$	<b>6</b>	$40 \pm 15$
		N	$3.26 \pm 0.03$	<b>6</b>	$15 \pm 25$
		Ni	$5.17 \pm 0.04$	<b>6</b>	$80 \pm 40$

**Table 3.5.** Structural parameters (elemental identities, distances, coordination numbers and Debye-Waller factors) for NiHCF film modified electrode for different oxidation states derived from fits to EXAFS. Data for Ni K-edge at +0.0 V and +0.9 V, and Fe K-edges at +0.0 V. Data collected at experimental station 7.1. Bold coordination numbers signify values that were not modelled (i.e. kept at fixed values).

Sample	edge	Fit index (%)	$\Delta E_0$ ( $\pm 5$ eV)
50 mM NiCl <sub>2</sub>	Ni K-edge	6.2	-6.1
NiHCF film	Ni K-edge		
+0.9 V		17.6	-5.9
+0.0 V		10.4	-6.6
+0.0 V	Fe K-edge	15.6	2.2

**Table 3.5a.** Fit indexes and  $\Delta E_0$  values referring to fits to EXAFS data for NiHCF film modified electrode presented in table 3.5.

Upon the shift from the fully reduced CoHCF ( $E=0.0$  V) to the fully oxidized CoHCF ( $E=+0.9$  V) state of the sample, and hence increasing cobalt charge from 2+ to 3+, the Co—N bond distances shorten from  $2.02 \pm 0.02$  Å to  $1.82 \pm 0.02$  Å. There is also visible shortening of Co—C and Co—Fe bond lengths. In the case of the intermediate potential ( $E=+0.3$  V) there were two distances fitted (reflecting coexistence of  $\text{Co}^{2+}$  and  $\text{Co}^{3+}$  species) because the high Debye-Waller factor for one distance fitted suggests a mix of both  $\text{Co}^{2+}$  and  $\text{Co}^{3+}$  oxidation states. Even for +0.0 V and +0.9 V potentials the high Debye-Waller factors can indicate more than one Co—N distance. There are two sources of this effect. The first possible explanation is that there is a mixture of  $\text{Co}^{2+}$  and  $\text{Co}^{3+}$  even for the extreme potentials. The conversion from one form to another is never complete, which can happen for the electrochemical systems as not all the redox sites may be equally accessible, for example, due to the morphology of the film. On the other hand there may be an appreciable amount of interstitial cobalt incorporated during the process of electrodeposition. Electrodeposited films have a negative overall charge so the  $\text{K}^+$  and  $\text{Co}^{2+}$  (or  $\text{Ni}^{2+}$  in the case of NiHCF sample) counterions enter the film and occupy interstitial sites to balance the charge. The standard redox potential in aqueous solution of the process:



is +1.92 V vs. NHE,<sup>66</sup> and is much higher than redox potential of cobalt in the CoHCF network, therefore interstitial cobalt ions will not change oxidation state in the range of potentials applied. These interstitial cobalt counterions introduce additional disorder to

the data, and can not be taken into account in the fitting of EXAFS data. For the Ni and Fe K-edge, in NiHCF there is no change in XANES. Also there is no significant change in the bond lengths for NiHCF films at different oxidation states. As will be discussed for XPS, because the data was acquired *ex situ* for an extended period of time, the film could have been partially oxidized in the air.

ii) *X-ray Photoelectron Spectroscopy*

Figure 3.14 shows XPS data of Co 2 p<sub>3/2</sub> and Fe 2 p<sub>3/2</sub> photoelectron spectra for a CoHCF film and Figure 3.15 shows Ni 2 p<sub>3/2</sub> and Fe 2 p<sub>3/2</sub> photoelectron spectra for a NiHCF film. Contributions of different components to the spectral lines acquired from fitting are presented in Table 3.6 and Table 3.7. Table 3.6 presents changing fractions of Co<sup>2+</sup> and Co<sup>3+</sup> species in cobalt hexacyanoferrate sample as a function of potential prior to emersion. Potentials listed in the table relate to ones in Figure 3.14. The same dependence is presented in Table 3.7 for the Fe active redox centre (Fe<sup>2+</sup>/Fe<sup>3+</sup> couple) in a nickel hexacyanoferrate film, and potentials shown here relate to Figure 3.15.

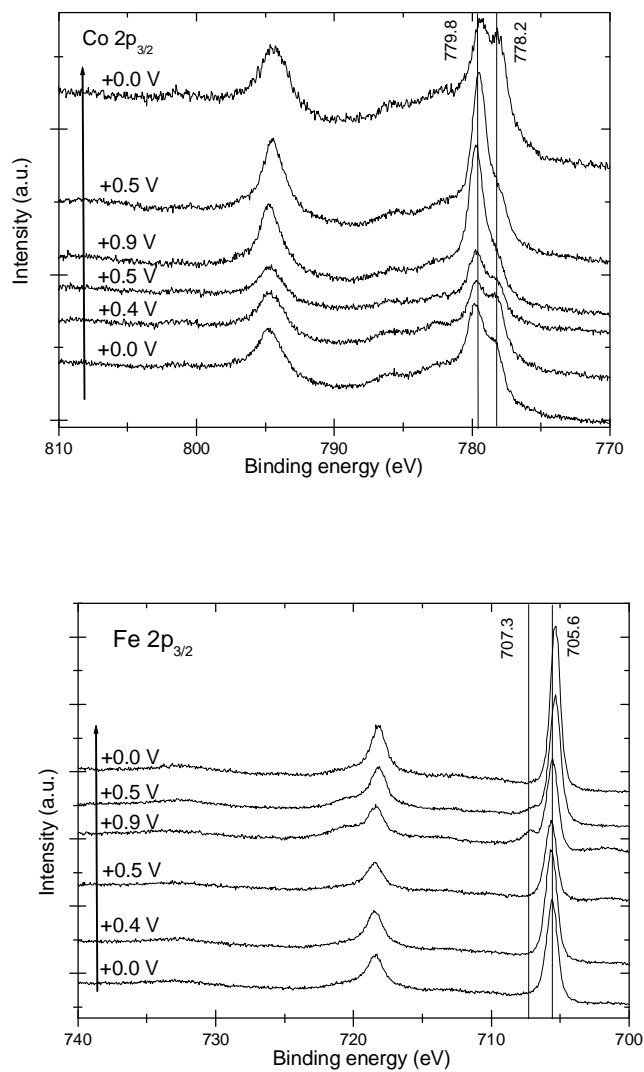


**Figure 3.14.** Co 2p<sub>3/2</sub> and Fe 2p<sub>3/2</sub> XPS data acquired for the cobalt hexacyanoferrate film modified electrode. There is a change in the shape of the cobalt line towards higher binding energies as the potential reaches the value of +0.9 V. Almost no change can be observed for Fe XPS data. Stepwise change of potentials as indicated in the picture. Arrow relates to the direction of potential cycling.

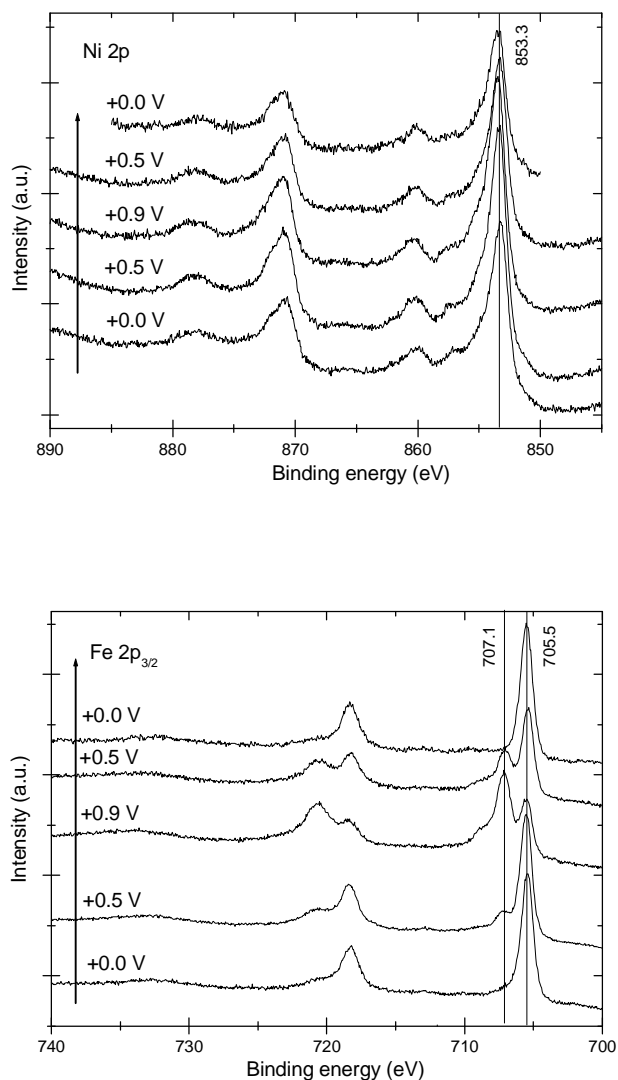


**Figure 3.15.** Ni 2p<sub>3/2</sub> and Fe 2p<sub>3/2</sub> XPS data acquired for the nickel hexacyanoferrate film modified electrode. There is a change in the shape of the iron line towards the higher binding energies as the potential reaches the value of +0.9 V. Almost no change can be observed in the Ni XPS data. Stepwise change of potentials as indicated in the picture. Arrow relates to the direction of potential cycling.

The change in the shape and position is observed in the Co XPS photoelectron line in the CoHCF sample and the Fe XPS photoelectron line in the NiHCF sample. The Ni line in NiHCF does not change. A small change can be seen in the Fe line in CoHCF film for the fully oxidative potential of E=+0.9 V. In the reduced CoHCF film both Co<sup>2+</sup> and Co<sup>3+</sup> are present in almost equal proportions. Upon oxidation the amount of Co<sup>3+</sup>

reaches only 70 % of the total cobalt present in the sample. Almost 50 % of the oxidized cobalt for the reduced sample can be explained by the oxidation of the film when transferred from the cell to the vacuum, especially as the technique is extremely surface sensitive. A very small fraction of Fe in the CoHCF film oxidizes to  $\text{Fe}^{3+}$  at the highest potential ( $E=+0.9$  V). In NiHCF it is clearly only Fe changing oxidation state, but conversion is still only 50 %.

Sample	$\text{Co}^{3+}$	$\text{Co}^{2+}$
+0.0 V	45 %	55 %
+0.4 V	51 %	49 %
+0.5 V	41 %	59 %
+0.9 V	70 %	30 %
+0.5 V	62 %	38 %
+0.0 V	37 %	63 %

**Table 3.6.** Changing fractions of  $\text{Co}^{2+}$  and  $\text{Co}^{3+}$  species in cobalt hexacyanoferrate modified electrode as a function of potential. Potentials listed in the table relate to XPS electron lines for Co in the Figure 3.14.

Sample	$\text{Fe}^{3+}$	$\text{Fe}^{2+}$
+0.0 V	0 %	100 %
+0.5 V	7 %	93 %
+0.9 V	54 %	46 %
+0.5 V	35 %	65 %
+0.0 V	0 %	100 %

**Table 3.7.** Changing fractions of  $\text{Fe}^{2+}$  and  $\text{Fe}^{3+}$  species in nickel hexacyanoferrate modified electrode as a function of potential. Potentials listed in the table relate to XPS electron lines for Fe in the Figure 3.15.

Table 3.8 summarizes atomic proportions of the elements present at the surface of NiHCF and CoHCF samples at different oxidation states. Ions from the background electrolyte move in and out of the film to compensate the charge.

sample	element	concentration (%)	
<b>NiHCF</b>	<b>+0.0 V</b>	C	50.3
		N	30.4
		K	8.7
		Ni	6.1
		Fe	4.6
	<b>+0.5 V</b>	C	50.5
		N	30.4
		K	8.6
		Ni	5.7
		Fe	4.7
	<b>+0.9 V</b>	C	48.0
		N	34.4
		K	4.6
		Ni	7.2
		Fe	5.8
<b>+0.5 V</b>	C	53.0	
	N	30.0	
	K	7.2	
	Ni	5.6	
	Fe	4.4	
<b>CoHCF</b>	<b>+0.0 V</b>	C	57.2
		N	27.5
		K	6.1
		Co	5.8
		Fe	3.4
	<b>+0.4 V</b>	C	56.3
		N	26.7
		K	8.3
		Co	5.1
		Fe	3.7
	<b>+0.5 V</b>	C	65.0
		N	22.6
		K	5.9
		Co	3.6
		Fe	2.8
<b>+0.9 V</b>	C	55.6	
	N	30.8	
	K	3.9	
	Co	6.1	
	Fe	3.7	
<b>+0.5 V</b>	C	50.3	
	N	32.4	
	K	5.9	
	Co	6.9	
	Fe	4.5	

**Table 3.8.** Atomic proportions of C, N, Co, Ni, Fe and K in the CoHCF and NiHCF electrodeposited films as a function of potential. Data acquired from the XPS data fitting.

Table 3.8 and Table 3.9 show ratios of the elements present at the surface and surface proximity (as it is XPS derived data) in NiHCF and CoHCF electrodeposited films, respectively. The content of carbon is much higher than expected: C/N is close to value of 2 for NiHCF sample and even exceeds this number in the case of CoHCF sample. Also C/Fe in both samples is very high. Carbon contamination is a common problem, especially in such a combination as surface sensitive techniques like XPS and air containing environment. This is the most probably the source of the excess C in samples discussed here. CoHCF samples seem to suffer carbon surface contamination to higher extent than NiHCF samples.

<b>NiHCF film</b>						
<b>potential</b>	<b>C/N</b>	<b>Fe/Ni</b>	<b>Fe/K</b>	<b>C/Fe</b>	<b>N/Fe</b>	<b>N/Ni</b>
+0.0 V	1.7	0.8	0.5	11	7	5
+0.5 V	1.7	0.8	0.5	11	6	5
+0.9 V	1.4	0.8	1.3	8	6	5
+0.5 V	1.8	0.8	0.6	12	7	5

**Table 3.9.** Ratios of the elements present in the nickel hexacyanoferrate electrodeposited films as a function of electrode potential. Data based on Table 3.8 summarizing XPS acquired information proportions of species present at the sample surface.

<b>CoHCF film</b>						
<b>potential</b>	<b>C/N</b>	<b>Fe/Co</b>	<b>Fe/K</b>	<b>C/Fe</b>	<b>N/Fe</b>	<b>N/Co</b>
+0.0 V	2.1	0.6	0.6	17	8	5
+0.4 V	2.1	0.7	0.5	15	7	5
+0.5 V	2.9	0.8	0.5	23	8	6
+0.9 V	1.8	0.6	1.0	15	8	5
+0.5 V	1.6	0.7	0.8	11	7	5

**Table 3.10.** Ratios of the elements present in the cobalt hexacyanoferrate electrodeposited films as a function of electrode potential. Data based on Table 3.8 summarizing XPS acquired information proportions of species present at the sample surface.

In NiHCF film content of nickel is higher than the content of iron. Theoretically Fe/Ni ration should be 1, but the presence of additional Ni can be due to retained interstitial

charge-balancing  $\text{Ni}^+$  cation, slowly exchanged in the process of redox cycling by  $\text{K}^+$ . This is consistent with N/Fe and N/Ni ratios, they are both about the expected value (there is no contamination with additional N, as in the case of C). N/Ni ratio is slightly lower, and this is supporting the view of additional charge balancing by interstitial  $\text{Ni}^+$ . The Fe/K ratio changes in the manner showing the expulsion of  $\text{K}^+$  counterions upon oxidation of the film. The fact that the amount of  $\text{K}^+$  is fluctuating over the CV scan, and  $\text{Ni}^+$  cation amount remains constant may be explained by the fact, that the majority of  $\text{Ni}^+$  is exchanged by the  $\text{K}^+$  during the first voltammetric scan in  $\text{K}^+$  containing electrolyte, and the remaining amount of  $\text{Ni}^+$  is only slowly removed from the film in the subsequent prolonged cycling. The above discussion is also valid for the CoHCF samples.

Figure 3.16 shows an example of fitted XPS data. Cobalt hexacyanoferrate sample emerged at the oxidative potential of +0.5 V was background subtracted and fitted with two Co species.  $\text{Co}^{3+}$  comprises at these potential about 62% of the total cobalt population in the film (for the sampled depth by XPS).

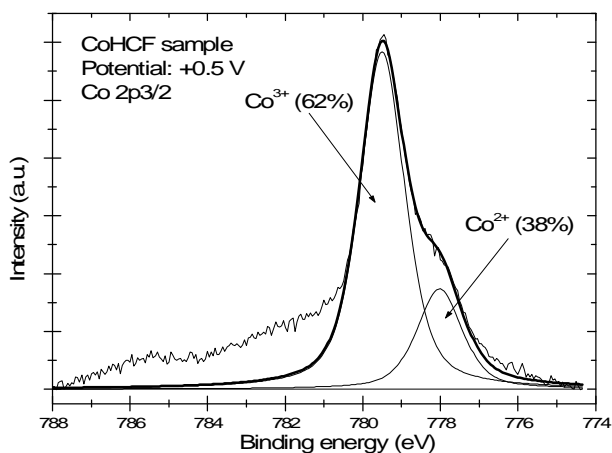


**Figure 3.16.** Example of background subtracted and fitted  $\text{Co } 2p_{3/2}$  XPS photoelectron line for the cobalt hexacyanoferrate film emerged at potential  $E=+0.5$  V. Fit includes  $\text{Co}^{2+}$  and  $\text{Co}^{3+}$  species.

iii) *Infrared Spectroscopy*

Figure 3.17 and Figure 3.18 show IR transmission spectra for the  $\nu(\text{CN})$  vibrational frequencies of CoHCF and NiHCF electrodeposited films respectively. Values of IR bands observed in our data are in agreement with IR of chemically prepared samples in other publications.<sup>67</sup> Vibrational frequencies of  $2099\text{ cm}^{-1}$ ,  $2141\text{ cm}^{-1}$  and  $2200\text{ cm}^{-1}$  in CoHCF sample can be assigned to  $\text{Fe}^{\text{II}}\text{Co}^{\text{II}}$ ,  $\text{Fe}^{\text{II}}\text{Co}^{\text{II}}\text{Co}^{\text{III}}$  and  $\text{Fe}^{\text{III}}\text{Fe}^{\text{II}}\text{Co}^{\text{III}}\text{Co}^{\text{II}}$  respectively. These signal incomplete oxidation of the film – the same effect was noticed by Sauter et al<sup>18</sup> – and bands are broad. The feature belonging to  $\text{Fe}^{3+}$  in cobalt hexacyanoferrate film is relatively small, meaning only a fraction of the iron centres are oxidized at the highest potential ( $E=+1.1\text{ V}$ ).

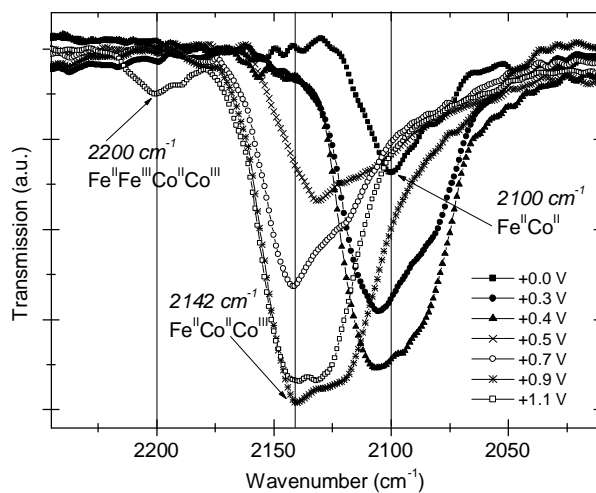


**Figure 3.17.** Cobalt hexacyanoferrate modified electrode IR transmission spectra for the  $\nu(\text{CN})$  vibrational frequency as a function of increasing potential. Vibrational frequency of  $\nu(\text{CN})$  increases from  $2099\text{ cm}^{-1}$  through  $2141\text{ cm}^{-1}$  to  $2200\text{ cm}^{-1}$ .

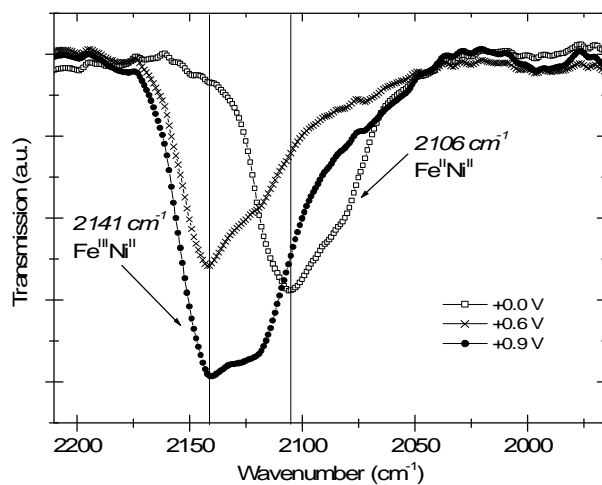


**Figure 3.18.** Nickel hexacyanoferrate modified electrode IR transmission spectra for the  $\nu(\text{CN})$  vibrational frequency at a function of increasing potential. Vibrational frequency of  $\nu(\text{CN})$  changes from  $2106\text{ cm}^{-1}$  to  $2141\text{ cm}^{-1}$ .

Vibrational frequencies of  $2106\text{ cm}^{-1}$  and  $2141\text{ cm}^{-1}$  in NiHCF sample can be assigned to  $\text{Fe}^{\text{II}}\text{Ni}^{\text{II}}$  and  $\text{Fe}^{\text{III}}\text{Ni}^{\text{III}}$  respectively.

Figure 3.19 illustrates the wavenumber vs. potential plot for the nickel hexacyanoferrate and cobalt hexacyanoferrate electrodeposited films. Data was derived from the IR transmission spectra. An abrupt jump visible at  $+0.6\text{ V}$  signifies changes occurring in the film structure at this point, i.e. oxidation/reduction of the iron and cobalt species in the nickel and cobalt hexacyanoferrate film modified electrodes, respectively.

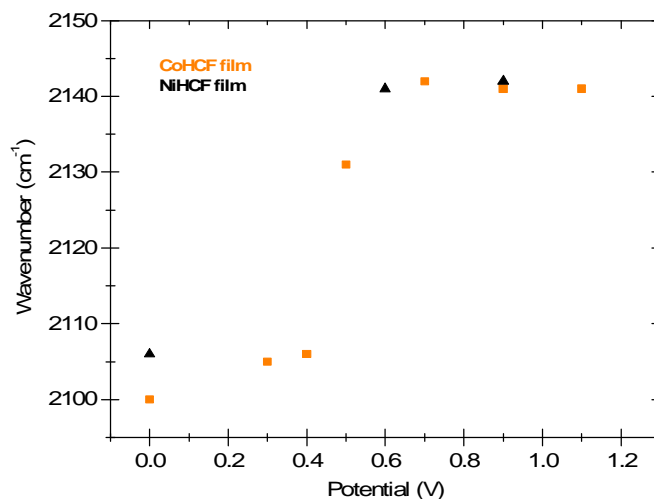


**Figure 3.19.** Wavenumber *vs.* potential plot for the nickel hexacyanoferrate and cobalt hexacyanoferrate electrodeposited films. Data derived from the IR transmission spectra. An abrupt jump visible at +0.6 V signifies changes in the film structure occurring at this point.

### 3.10 Discussion

The original project involved *in situ* electrochemical EXAFS characterization of Prussian Blue films and cobalt and nickel analogues in aqueous background electrolyte, with  $K^+$  as an exchangeable cation in a purpose-built cell. The cell had been previously used at Daresbury Laboratory on the niobium oxide electroactive films<sup>68</sup> and [Ni(salen)]-based polymer films.<sup>69, 70</sup> Experiment was designed to obtain detailed structural data on CoHCF and NiHCF systems to provide boundary conditions for dynamic studies. Understanding of the details of structural variations under stationary conditions of applied potential is a necessary step towards mapping the dynamics of redox-driven structural change. *Ex situ* XPS experiments were carried out to give complementary information to EXAFS, but due to the XPS properties only for the surface region of the films. The comparison of the two data sets is complementary as EXAFS probes the whole of the sample.

Unfortunately, the signal from the spectroelectrochemical cell proved to be too weak even to acquire strong enough fluorescence signals. Films were thin, but this did not

explain total disappearance of the signal when samples were placed in the cell – even without electrolyte. Several alterations in the cell *vs.* detector arrangements as well as in the construction of the cell have been tried. Attempts were made to minimise the electrolyte thickness by pressing the electrode with the film against the cell front window, leaving only an ultra thin layer of the solvent in the X-ray path. All these trials were to no avail and no source of the problem could be found, but it is possible that the surface of the platinum discs used were too uneven. Although the cell was successfully used for the *in situ* data acquisition for other samples described in this thesis and also in earlier experiments, there was no choice but to make measurements *ex situ* in fluorescence mode.

### **3.10.1 Prussian Blue Sample**

In the case of Prussian Blue films, the signals from the two metal sites (Fe) add, and their separation turned out not to be a solvable problem. No significant edge shifts could be observed for the three XANES spectra obtained for electrochemically deposited Prussian Blue films. All three of the white lines are identical in height and position. Also, for the modified electrode samples the white lines are much lower than the white line observed for  $\text{Fe}^{3+}$  in the solid  $\text{K}_3\text{Fe}(\text{CN})_6$  powder sample and, even more significantly, in aqueous solution. There is also a pre-edge feature which is identical in all three spectra. This structure can be seen also in the data for standards. In the powder sample it is identical to the one seen in the electrodeposited films, but it is weaker in the aqueous solution data.

### 3.10.2 Cobalt and Nickel Hexacyanoferrate Samples

In both CoHCF and NiHCF, the white line for the Fe K-edge is a little stronger than in the Prussian Blue electrodeposited sample, and about the same strength as in the aqueous solution. It is, however, at significantly higher energies than in any other spectra Fe K-edge spectra. There are no notable changes in white line position for the Ni K-edge with potential for NiHCF electrodeposited samples. Both white lines are stronger than for  $\text{Ni}^{2+}$  in aqueous solution of  $\text{NiCl}_2$ . White line for the sample at the potential  $E=+0.9$  V is higher and about the same width as white line for the sample at  $E=+0.0$  V. The pre-edge structure is very similar to that on the Fe K-edge. From the EXAFS derived data it can be seen that all three shells are significant and none of the distances change with the changing redox state of the NiHCF sample. Furthermore, there is no indication of a split first shell in either of NiHCF (in contrast to CoHCF) samples. Also no significant multiple scattering contributions can be seen. On the other hand, the low values of Debye-Waller factors ( $\sigma^2$ ) for the second and third shells suggest that there is some multiple scattering present, but it could not be fitted. The distances, combined with a Fe—C distance of about 2.0 Å from the fitting of EXAFS data for the same type of sample but for the Fe K-edge, imply a non-linear [...Ni—N≡C—Fe...] arrangement although the angles are all close to 180°.

For the Co K-edge in the CoHCF film there is a remarkable increase in white line position with the change of redox state of the electrode. For the potential  $E=+0.3$  V there is a clear doublet at energies of 7723 eV and 7726 eV. For the potential  $E=+0.0$  V the energy of the white line (at 7723 eV) is essentially the same as for  $\text{Co}^{2+}$  in aqueous solution of  $\text{CoCl}_2$ . Therefore the shift in the white line position is interpreted as a change of Co redox state from 2+ to 3+. For the potentials  $E=+0.7$  V and  $E=+0.9$  V there is a single peak at 7726 eV, signalling that conversion to  $\text{Co}^{3+}$  is essentially complete. Also in this case the pre-edge structure is very similar to that on the Fe K-edge.

The EXAFS data on the cobalt K-edge – exactly like in the case of Fe and Ni K-edges – shows three strong peaks in its Fourier Transform (Figure 3.11). These three peaks were fitted with the assumption that they belong to the [...Co—N≡C—Fe...] film lattice along the cube edge at approximate distances of 2 Å, 3 Å and 5 Å for Co—N, Co—C

and Co—Fe respectively. These values were based on the crystallographic database.<sup>64</sup> The nearest neighbour distance Co—N is well defined. At first EXAFS was fitted with the single (i.e. not split) Co—N distance. The result is presented at Figure 3.20.

A steady decrease of the bond length is visible as the redox state of the CoHCF changes with the shift of the electrode potential from +0.0 V to +0.7 V. Above a potential  $E=+0.7$  V the distance Co—N stabilizes and remains constant.

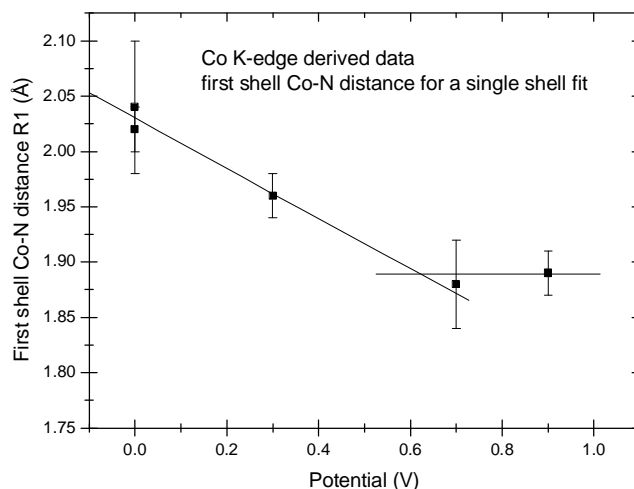


**Figure 3.20.** EXAFS derived first shell Co—N distances for a single shell fit and a linear fit of the data. EXAFS measured *ex situ* for the Co K-edge in the cobalt hexacyanoferrate modified electrode as a function of potential. The bond length decreases to the potential of circa +0.7 V and stays constant thereafter. Two values at the potential  $E=+0.0$  V refer to data acquired at two different EXAFS stations in Daresbury Laboratory: 7.1 and 16.5.

The Debye-Waller factor reaches a maximum value at about +0.3 V. From a potential  $E=+0.7$  V it remains constant and at about the value it has at potential  $E=+0.0$  V, as shown in Figure 3.21. These two facts, the previously described behaviour of the Co—N bond length and associated Debye-Waller factors, indicate the presence of two distinct Co—N distances at intermediate redox states in CoHCF electrodeposited films. The Debye-Waller factor of two unresolved contributions may be analysed in the following manner. Each bond length represents one integer oxidation state. The increase in the number of present bond lengths would also mean a change in the distribution of oxidation states. This would be reflected in the Debye-Waller factors, where  $\sigma^2$  is the

sum of thermal and static (i.e. structural) contributions to the total disorder. In the case of the experiment described here, the only variation in Debye-Waller factor has a structural origin. A plot of  $\sigma^2$  as a function of potential would follow a parabola if the mixture of different bond lengths changes with parallel movement and increase in static disorder. The existence of a single, well organized structure would result in low value of  $\sigma^2$  at the initial and final states, referring to the end-points of the parabola.

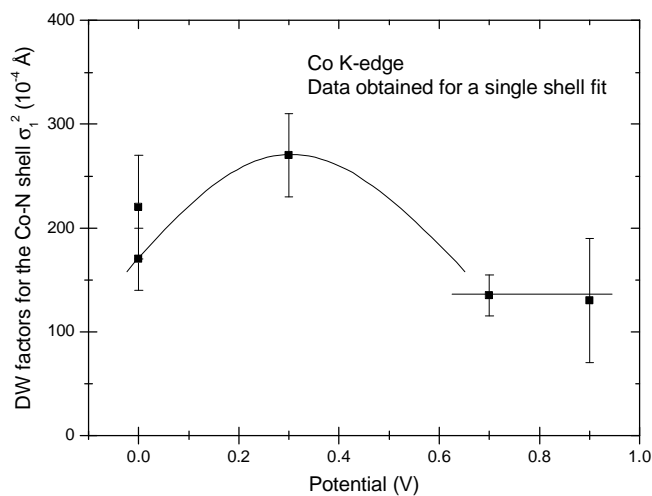


**Figure 3.21.** EXAFS derived Debye-Waller factors for the first Co—N shell in cobalt hexacyanoferrate film. The Debye-Waller factor peaks at ca. +0.3 V and is constant above +0.7 V at about the value it has at +0.0 V. EXAFS measured *ex situ* for the Co K-edge in the CoHCF modified electrode as a function of potential. Two values at the potential  $E=+0.0$  V refer to data acquired at two different EXAFS stations in Daresbury Laboratory: 7.1 and 16.5. Despite large  $2\sigma$  error bars, the data are very consistent.

Assuming that there exists a fraction  $x$  of cobalt species in one oxidation state in CoHCF at distance  $R_1$ , then the remaining  $(1-x)$  number of sites (in the model taking into account only two different redox states) will be represented by the distance  $R_2$ . The mean value – the position of unresolved peak at distance  $R$  – will be given as:

$$R = xR_1 + (1-x)R_2 \quad (3.3)$$

with an additional contribution  $S_{st}^2$  to the total Debye-Waller factor  $\sigma^2$  of:

$$S_{st}^2 = x(R_1 - R)^2 + (1-x)(R_2 - R)^2 = x(1-x)(R_1 - R_2)^2 \quad (3.4)$$

As already stated, the parabolic variation would be a clear signature of two distances. In the case of CoHCF discussed here, we find  $R_1 \cong 2.03 (\pm 0.02) \text{ \AA}$  and  $R_2 \cong 1.89 (\pm 0.02) \text{ \AA}$ , so  $(R_1 - R_2)^2 \cong 200 (\text{pm})^2$ .  $S_{st}^2$  peaks at  $x = 0.5$ , here with the value of  $50 (\text{pm})^2$ . This is in good agreement with the fitted  $S_{st}^2$  values if the vibrational contribution (represented by the single species at the end points) has the physically reasonable value of ca.  $170 (\text{pm})^2$ , and  $x=0.5$  at  $E \cong +0.3 \text{ V}$ . Furthermore, fitting EXAFS at  $E = +0.3 \text{ V}$  allowing distinct values for the first neighbour  $\text{Co}^{\text{II}}-\text{N}$  and  $\text{Co}^{\text{III}}-\text{N}$  distances generates values for these distances (in the mixed state film, where  $x \cong 0.5$ ) of  $2.04 (\pm 0.06) \text{ \AA}$  and  $1.85 (\pm 0.06) \text{ \AA}$ , respectively. These are in good agreement with the single species fits at the extremes of potential (where  $x=0$  and  $1$ ), and the associated Debye-Waller  $\sigma^2$  factor values are  $150\text{-}200 (\text{pm})^2$ . It has to be underlined that the split shell fit is not significantly better than the unresolved single shell fit, but it is preferred because of the Debye-Waller factor behaviour. The outcomes for the split first shell Co—N distances are shown in Figure 3.22.

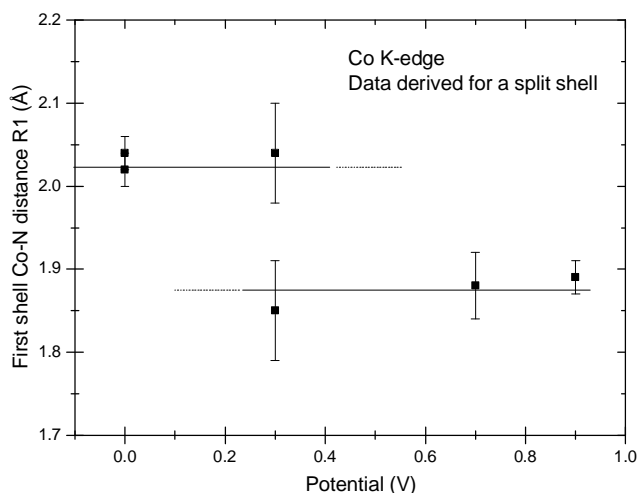


**Figure 3.22.** EXAFS derived first shell Co—N distances – split shell fit. EXAFS measured *ex situ* for the Co K-edge in the cobalt hexacyanoferrate modified electrode as a function of potential. Two values at potential  $E=0.0 \text{ V}$  refer to data acquired at two different EXAFS stations in Daresbury Laboratory (7.1 and 16.5) and show excellent reproducibility of the sample and measurement.

The presence of two distances indicates – as stated before – two distinct Co site redox states.  $\text{Co}^{2+}\text{—N}$  has a length of 2.09 Å in  $\text{Co}_3(\text{Fe}(\text{CN})_6)_2 \cdot x\text{H}_2\text{O}^{64}$  and therefore the shorter distance will correspond to the  $\text{Co}^{3+}$  redox state. The presence of two distinct distances indicates that the cobalt hexacyanoferrate sample behaves in a molecular manner (discrete  $d$  levels) rather than in a solid state manner (partially filled  $d$ -band). These two distinct models can be simplistically described as follows. Independent bonds and localised electrons for each atom would be characteristic for a molecular model. Co ions in this case would coexist as a mixture of integer oxidation states 2+ and 3+ at any time, with proportions of different species changing upon redox processes taking place during voltammetric cycling or stopping the cycle at a selected potential. In this model, electrons propagate through the material in a so-called “hopping” mechanism. This type of behaviour is generally associated with low conductivity.<sup>71</sup> The second, solid state model is described as a conducting band structure with electrons in the band not affiliated with any particular atom or bond. In this description, the valency of redox sites (here cobalt) would change in the continuous manner upon electron flow through the film/electrode interface, in contrast to the discrete integer numbers shift in the molecular model. Here the first model is evidently supported by the data. The first and most straightforward sign of it is a presence of a broad Co K-edge (Figure 3.12) enveloping both present contributing oxidation states, namely  $\text{Co}^{2+}$  and  $\text{Co}^{3+}$  signals. The width of the single broad Co K-edge white line changes along with the fraction of both redox states. The characteristics of the molecular model behaviour of the Debye-Waller  $\sigma^2$  factors have already been described.

In the second model the Co K-edge would be well defined, not distorted at any point and smoothly changing position as a function of applied potential. The Debye-Waller factor would not vary significantly at any point of the redox process, with no added any extra static disorder at any point. None of these, once more, is observed in the case of electrodeposited CoHCF, NiHCF, or FeHCF sample.

At the highest potential  $E=+0.9$  V there is indication in the fit of a weak Co—X coordination at about 2.1 Å. This is probably due to the interstitial Co or K species incorporated upon deposition and/or cycling as counterions. The second (Co—C) and third (Co—Fe) distances fall steadily with increasing oxidation state of the film as an

effect of increasingly positive potential applied to the electrode (Figure 3.22 and 3.23). The low Debye-Waller factors obtained with a use of single scattering contributions for these more distant coordination shells are an indication that there is some multiple scattering present. However, inclusion of multiple scattering effects does not improve the data fits, although it shows in a clear way that the [...Co—N≡C—Fe...] structure along the cube edge is not linear. The difference between the Co—C and Co—N distances gives a constant separation of 1.31 Å for all measured potentials. This value will be underestimated for the significantly non-linear structure. This seems to be very long for a C≡N bond in mHCNs samples – usually circa 1.15 Å – and can be an indication of other contributions to this peak.

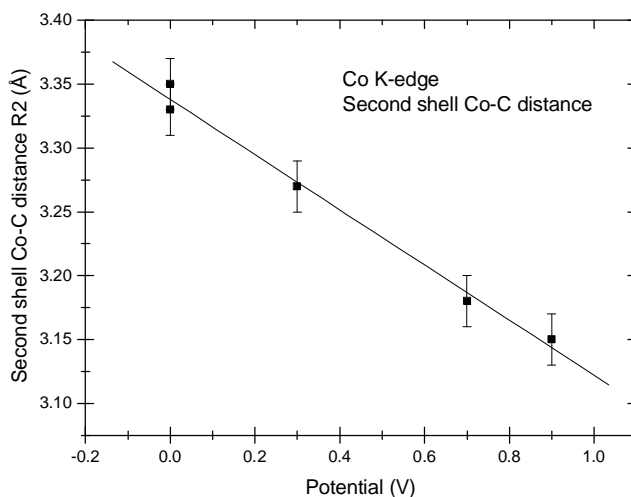


**Figure 3.23.** EXAFS derived second shell Co—C distances - single shell fit and a linear fit of the data. EXAFS measured *ex situ* for the Co K-edge in the cobalt hexacyanoferrate modified electrode as a function of potential. Two values at E=0.0 V potential refer to data acquired at two different EXAFS stations in Daresbury Laboratory: 7.1 and 16.5. They proof the excellent reproducibility of the sample and measurement.

Other EXAFS studies of this group of materials have also found quite long CN distance. The third shell distance is in a good agreement with the crystallographic data for  $\text{Co}_3(\text{Fe}(\text{CN})_6)_2 \cdot x\text{H}_2\text{O}$ . The Fe site is a strong scatterer, hence any additional/competing contributions at this distance will be comparatively weak. Once more, multiple scattering contributions are not significant for this peak.

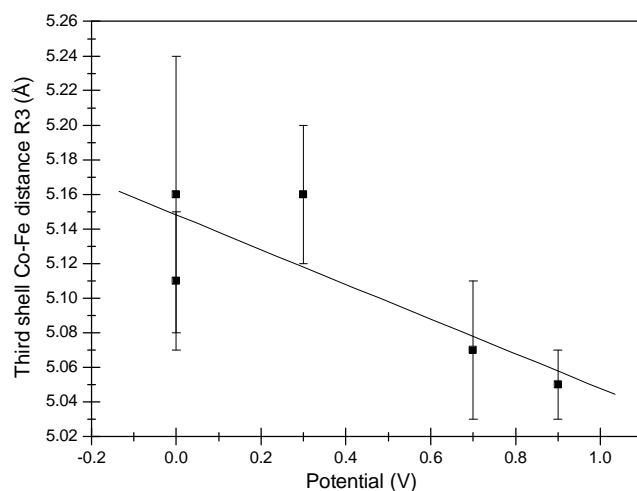


**Figure 3.24.** EXAFS derived third shell Co—Fe distances - single shell fit and a linear fit of the data. EXAFS measured *ex situ* for the Co K-edge in the cobalt hexacyanoferrate modified electrode as a function of potential. Two values at 0.0 V potential refer to data acquired at two different EXAFS stations in Daresbury Laboratory: 7.1 and 16.5.

Comparing the Co—C and Co—Fe distances yields a Fe—C separation of about 1.85 Å to 1.90 Å. This distance may be a little longer if there is a notable deviation of the bond angle from 180°. This distance is in agreement with the value found for EXAFS fitting for the Fe K-edge data for CoHCF sample.

### 3.10.3 X-ray Photoelectron Spectroscopy and Infrared Spectroscopy

It is clearly visible even from the raw XPS data that upon voltammetric cycling NiHCF and CoHCF electrodeposited films behave in a significantly different manner. In the NiHCF film Fe 2p XPS photoelectron line changes its shape and position, displaying evidently two separate peaks (different binding energies) for more oxidative potentials, namely for samples emersed at potentials  $E=+0.5$  V and  $E=+0.9$  V (Figure 3.15). At an emersion potential of  $E=+0.0$  V, when the film is supposed to be fully reduced, only one narrow line is visible in the spectra. The lower binding energy XPS line at 705.5 eV is associated with  $\text{Fe}^{2+}$  centres. As a NiHCF film is positively polarized, a second XPS line becomes clear at higher binding energy (707.1 eV). This second line corresponds to Fe redox centres changing oxidation state to  $\text{Fe}^{3+}$ . Results obtained from NiHCF film

XPS data fitting are summarized in Table 3.7. For each of the potential points for which XPS was measured, the percentage of detected  $\text{Fe}^{2+}$  and  $\text{Fe}^{3+}$  sites was estimated. Unexpectedly, the fraction of reduced  $\text{Fe}^{2+}$  site reaches 100 % of all surface (and probably also bulk) Fe sites, and does not seem to be influenced by the oxidative air environment during sample transfer to the vacuum chamber. In contrast, the fraction of oxidized  $\text{Fe}^{3+}$  sites reaches at the highest potential ( $E=+0.9$  V) only about 55 % of the entire Fe population. It is possible that more Fe sites would oxidize if the sample were kept at  $E=+0.9$  V. The same type of behaviour was noticed by Sauter et al<sup>18</sup> for Fe sites in NiHCF films. Interestingly, the same pattern is found for cobalt in CoHCF samples. Sauter's<sup>18</sup> work states that their sample contains a mixture of  $\text{Co}^{2+}$  and  $\text{Co}^{3+}$  species and it never fully oxidizes to 100 %  $\text{Co}^{3+}$ . For the NiHCF electrodeposited film, absolutely no change was observed for the Ni XPS photoelectron line. The shape and position remained constant ( $\text{Ni}^{2+}$  binding energy = 853.3 eV) throughout the whole cyclic voltammogram, as shown in Figure 3.15. The XPS data are consistent with infrared spectroscopy data acquired for NiHCF film in transmission mode. Figure 3.18 illustrates  $\nu(\text{CN})$  vibrational band region for NiHCF case. Assignment of vibrational bands at 2106 and 2141 to  $\text{Fe}^{\text{II}}\text{Ni}^{\text{II}}$  and  $\text{Fe}^{\text{III}}\text{Ni}^{\text{II}}$ , respectively, confirms the X-ray spectroscopic based deduction of no electroactive component from the Ni sites and a potential-driven shift from all  $\text{Fe}^{\text{II}}$  to dominant  $\text{Fe}^{\text{III}}$ .

In the case of CoHCF electrodeposited films it is Fe that stays at constant oxidation state and Co is redox centre. It is readily visible from the raw XPS data plotted in Figure 3.14 Co 2p XPS photoelectron line is broad and clearly comprises two overlapping spectra belonging to  $\text{Co}^{2+}$  and  $\text{Co}^{3+}$ , even for the most extreme ends ( $E=+0.0$  V and  $E=+0.9$  V) of the cyclic voltammogram. The value of 778.2 eV of the  $2p_{3/2}$  XPS line is binding energy of photoelectron in  $\text{Co}^{2+}$ . As the sample is oxidized the shape of the Co 2p XPS line changes. The binding energy of photoelectrons from  $\text{Co}^{3+}$  shifts to the higher value of 779.8 eV. Although there is a significant change in the ratio of  $\text{Co}^{2+}$  and  $\text{Co}^{3+}$  species, it only reaches 70 % conversion at the most positive potential. Varying ratios of both cobalt species obtained from fits are summarized in Table 3.6 In contrast to Fe in NiHCF, cobalt is never fully reduced and for the most reductive potential  $E=+0.0$  V,  $\text{Co}^{2+}$  comprises only about 60 %. For the most oxidative potential  $E=+0.9$  V ( $\text{Co}^{3+}$  content 70 %) a small feature appears to the higher binding energy of the Fe 2p

XPS photoelectron line and disappears again at lower potentials. This feature at 707.3 eV represents a small fraction of Fe being oxidized from  $\text{Fe}^{2+}$  to  $\text{Fe}^{3+}$ , even when not all of cobalt sites are oxidized. The same feature is seen in the IR transmission spectra of CoHCF films, where the bands are broad, as in the case of NiHCF samples. This is expected on the basis of XPS data for samples with mixed Co redox states. The vibrational frequency of the  $\nu(\text{CN})$  band changes from  $2100 \text{ cm}^{-1}$  for the CoHCF sample at  $E=+0.0 \text{ V}$  to  $2142 \text{ cm}^{-1}$  at  $E=+0.9 \text{ V}$ . A small feature appears at  $E=+1.1 \text{ V}$  potential at a wavelength of  $2200 \text{ cm}^{-1}$ . These vibrations were also observed by other groups and can be assigned to  $\text{Fe}^{\text{II}}\text{Co}^{\text{II}}$ ,  $\text{Fe}^{\text{II}}\text{Co}^{\text{II}}\text{Co}^{\text{III}}$  and  $\text{Fe}^{\text{III}}\text{Fe}^{\text{II}}\text{Co}^{\text{III}}\text{Co}^{\text{II}}$  redox states of the film respectively. In both (i.e. Ni and CoHCF) systems, the increase in  $\nu(\text{CN})$  frequency (wavenumber) upon film oxidation is a consequence of the more positively charged metal ion with drawing electron density from the  $\text{N}\equiv\text{C}$  bond. The fact that the vibrational bands undergo a blue shift indicates that the  $\text{N}\equiv\text{C}$  bond is stronger, this is consistent with removal of electron density from a  $\pi^*$  orbital.

In Prussian Blue films no changes of the oxidation state of the Fe centres for different emersion potentials could be observed. The shape of the Fe 2p XPS photoelectron lines shown in Figure 3.6 remains unchanged. There is a small shift in binding energy of circa  $-0.2 \text{ eV}$  between the most reduced ( $E=-0.2 \text{ V}$ ) and the most oxidized ( $E=+0.6 \text{ V}$ ) FeHCF samples. Because the binding energy moved only slightly and towards lower binding energy upon oxidation – i.e. in the opposite direction than expected for  $\text{Fe}^{2+}$  to  $\text{Fe}^{3+}$  change – the observed shift is probably not real but due to some charging effect (recall that these films are on ITO glass slides). It has to be taken into account that other binding energies which should remain constant (e.g.  $\text{K}^+$ , In) suffer similar small shifts – these can only be assigned to charging or statistical errors. Mixtures of  $\text{Fe}^{2+}$  and  $\text{Fe}^{3+}$  iron sites at the potential of  $E=+0.6 \text{ V}$ , with possibly not all  $\text{Fe}^{3+}$  centres becoming reduced at  $E=-0.2 \text{ V}$ , oxidative influence of air and additional interstitial Fe counteranions at both 2+ and 3+ oxidation states all limit the overall level of certainty in the data.

### 3.11 Conclusions

Detailed analysis of XAS (EXAFS and XANES), XPS and IR data were used for Prussian Blue, cobalt and nickel hexacyanoferrate electrodeposited films. In case of CoHCF films the data provides support for the molecular model behaviour with discrete  $d$  levels, rather than solid state model with partially filled  $d$ -band. Cobalt (in contrast to iron) metal atom is, with no doubt, the active redox centre. In molecular model Co ions coexist as a mixture of integer oxidation states 2+ and 3+, with proportions of both changing upon redox processes. XAS data, namely broad Co K-edge for the intermediate redox potential  $E=+0.3$  V, changing width of the white line and characteristic behaviour of Debye-Waller factor strongly support this model. The nickel hexacyanoferrate electrodeposited film performed in the way reported by other research groups, with the Fe metal centre displaying redox behaviour. The combination of techniques allowed comparison of the surface vs. bulk of the samples, and as far as it can be seen, films display exactly the same behaviour, but very detailed structural analyze could be obscured by the *ex situ* data acquisition setups.

The instrumental capability of Daresbury Laboratory SRS for carrying out XAS on Prussian Blue, cobalt and nickel hexacyanoferrate electrochemically modified electrodes has been proven to be insufficient for the *in situ* spectroelectrochemical experiment. It turned out extremely difficult to prepare films thick enough to obtain good step and therefore signal-to-noise ratio at least for the available on site beam flux. Regardless, it was possible to get structural parameters from *ex situ* XAS experiment. A more powerful synchrotron may be able to provide data of much higher quality, possibly even in the *in situ* data acquisition procedure. Especially CoHCF samples with cobalt active redox sites and clear evidence of changing bond lengths would be interesting in such an experiment. Prussian Blue films were found to be too ambiguous with two Fe redox centres and additional interstitial iron obscuring the EXAFS data, and no significant changes could be observed in XAS data for NiHCF electrodeposited films.

It has to be underlined, that the results derived from spectra recorded at different experimental stations at SRS Daresbury Laboratory (station 7.1 and 16.5), and from

different samples agree very well. Therefore they prove the excellent reproducibility of the electrodeposited samples and measurements. It is important, especially in the light of commonly reported difficulties with reproducible preparation of this type of samples. Results acquired with the use of set of diverse techniques (XAS, XPS, IR and CV) presented in this chapter were obtained from identical samples, and for the first time EXAFS at a function of potential on electrodeposited CoHCF and NiHCF were performed, providing boundary conditions for possible future *in situ* dynamic XAS experiments.

### 3.12 References

1. Diesbach, Cited in: *Handbuch der Anorganischen Chemie*. Gmelin, 1930, 59, 671.
2. Brown, D. J., *Philos. Trans.* **1724**, 17.
3. Verdaguer, M.; Girolami, G., *Magnetism: Molecules to materials V*. Eds.: M. Drillon, J. S. Miller, Wiley-VCH Verlag GmbH & Co. KGaA: Weinheim, 2004, pp 283.
4. Neff, V. D., *J. Electroanal. Chem.* **1978**, 128, 886.
5. Giorgetti, M.; Berrettoni, M.; Zamponi, S.; Kulesza, P. J.; Cox, J.A., *Electrochim. Acta* **2005**, 51, 511.
6. Zamponi, S.; Giorgetti, M.; Berrettoni, M.; Kulesza, P. J.; Cox, J. A.; Kijak, A. M., *Electrochim. Acta* **2005**, 51, 118.
7. Kulesza, P. J.; Malik, M. A.; Berrettoni, M.; Giorgetti, M.; Zamponi, S.; Schmidt, R.; Marassi, R., *J. Phys. Chem. B* **1998**, 102, 1870.
8. Mardan, A.; Ajaz, R.; Mehmood, A.; Raza, S. M.; Ghaffar, A., *Sep. Purif. Technol.* **1999**, 16, 147.
9. Hao, X.; Guo, J.; Liu, S.; Sun, Y., *Trans. Nonferrous Met. Soc. China* **2006**, 16, 556.
10. Mimura, H.; Lehto, J.; Harjula, R., *J. Nucl. Sci. Technol.* **1997**, 34, 484.
11. Kulesza, P. J.; Malik, M. A.; Schmidt, R.; Smolińska, A.; Miecznikowski, K.; Zamponi, S.; Czerwiński, A.; Berrettoni, M.; Marassi, R., *J. Electroanal. Chem.* **2000**, 487, 57.
12. Eftekhari, A., *Electroanal.* **2004**, 16, 1324.
13. Sato, O.; Hayami, S.; Einaga, Y.; Gu, Z. Z., *Bull. Chem. Soc. Jpn.* **2003**, 76, 443.
14. Yokoyama, T.; Ohta, T.; Sato, O.; Hashimoto, K., *Phys. Rev. B* **1998**, 58, 8257.
15. Sato, O.; Einaga, Y.; Iyoda, T.; Fujishima, A.; Hashimoto, K., *Phys. Chem. B* **1997**, 101, 3903.
16. Lezna, R. O.; Romagnoli, R.; Tacconi, N. R.; Rajeshwar, K., *J. Phys. Chem. B* **2002**, 106, 3612.
17. Sato, O.; Einaga, Y.; Iyoda, T.; Fujishima, A.; Hashimoto, K., *J. Electrochem. Soc.* **1997**, 144, L11.

18. Sauter, S.; Wittstock, G.; Szargan, R., *Phys. Chem. Chem. Phys.* **2001**, *3*, 562.
19. Florescu, M.; Brett, C. M. A., *Anal. Lett.* **2004**, *37*, 871.
20. de Azevedo, W. M.; de Mattos, I. L.; Navarro, M., *J. Mater. Sci: Mater. Electron.* **2006**, *17*, 367.
21. Krylov, A. V.; Lisdat, F., *Electroanal.* **2007**, *19*, 23.
22. Florescu, M.; Barsan, M.; Pauliukaite, R.; Brett, C. M. A., *Electroanal.* **2007**, *19*, 220.
23. Pauliukaite, R.; Hočevár, S. B.; Hutton, E. A.; Ogorevc, B., *Electroanal.* **2007**, *20*, 47.
24. Prabakar, S. J. R.; Narayanan, S. S., *Anal. Bioanal. Chem.* **2006**, *386*, 2107.
25. Yang, M.; Jiang, J.; Lu, Y.; He, Y.; Shen, G.; Yu, R., *Biomaterials* **2007**, *28*, 3408.
26. Tung, T. S.; Chen, L. C.; Ho, K. C., *Solid State Ionics* **2003**, *165*, 257.
27. Jayalakshmi, M.; Scholz, F., *J. Power Sources* **2000**, *91*, 217.
28. Gómez-Romero, P.; Torres-Gómez, G., *Adv. Mater.* **2000**, *12*, 1454.
29. Ambashta, R. D.; Deshingkar, D. S.; Wattal, P. K.; Bahadur, D., *J. Radioanal. Nucl. Chem.* **2006**, *270*, 585.
30. Green-Pedersen, H.; Korshin, G. V., *Environ. Sci. Technol.* **1999**, *33*, 2633.
31. Sato, O.; Einaga, Y.; Iyoda, T.; Fujishima, A.; Hashimoto, K., *J. Electrochem. Soc.* **1997**, *144*, L11.
32. Hg, C. W.; Ding, J.; Gan, L. M., *J. Solid State Chem.* **2001**, *156*, 400.
33. Martinez-Garcia, R.; Knobel, M.; Reguera, E., *J. Phys.: Condens. Matter* **2006**, *(18)*, 11243.
34. Vaucher, S.; Fielden, J.; Li, M.; Dujardin, E.; Mann, S., *Nano Lett.* **2002**, *2*, 225.
35. *U.S. Patent 7,342,708 B2* **2008**.
36. Giorgetti, M.; Berrettoni, M.; Filipponi, A.; Kulesza, P. J.; Marassi, R., *Chem. Phys. Lett.* **1997**, *275*, 108.
37. Tang, Q.; Xiong, W.; Long, L., *Anal. Lett.* **2007**, *40*, 1610.
38. Wang, P.; Yuan, Y.; Jing, X.; Zhu, G., *Talanta* **2001**, *53*, 863.
39. Bharati, S.; Nogami, M.; Ikeda, S., *Langmuir* **2001**, *17*, 7468.
40. Joseph, J.; Gomathi, H.; Prahakara, R., *J. Electroanal. Chem.* **1991**, *304*, 263.
41. Mortimer, R. J.; private materials.

42. Gao, Z.; Quang, G.; Li, P.; Zhao, Z., *Electrochim. Acta* **1991**, *36*, 147.
43. Ayralut, S.; Loos-Neskovic, C.; Fedoroff, M.; Garnier, E.; Jones, D. J., *Talanta* **1995**, *42*, 1581.
44. Loos-Neskovic, C.; Fedoroff, M.; Garnier, E.; Gravereau, P., *Talanta* **1984**, *31*, 1133.
45. Hallmeier, H. K.; Sauter, S.; Szargan, R., *Inorg. Chem. Comm.* **2001**, *4*, 153.
46. Escax, V.; Cartier dit Moulin, C.; Villain, F.; Champion, G.; Itie, J. P.; Munch, P.; Verdaguer, M.; Bleuzen, A., *C. R. Chimie* **2003**, *6*, 1165.
47. Margadonna, S.; Prassides, K.; Fitch, A. N., *J. Am. Chem. Soc.* **2004**, *126*, 15390.
48. Monk, P. M. S.; Mortimer, R. J., Rosseinsky, D. R., *Electrochromism by intervalence charge-transfer coloration: metal hexacyanometallates in Electrochromism and Electrochromic Devices*. Cambridge University Press, Cambridge 2007.
49. Beckstead, D. J.; De Smet, D. J.; Ord, J. L., *J. Electrochem. Soc.* **1989**, *136*, 1927.
50. Christensen, P. A.; Hamnett, A.; Higgins, S. J., *J. Chem. Soc., Dalton Trans.* **1990**, 2233.
51. Emrich, R. J.; Traynor, L.; Gambogi, W.; Buhks, E., *J. Vac. Sci. Technol. A* **1987**, *5*, 1307.
52. Itaya, K.; Uchida, I., *Inorg. Chem.* **1986**, *25*, 389.
53. Lundgren, C. A.; Murray, R. W., *Inorg. Chem.* **1988**, *27*, 933.
54. Feldman, B. J.; Melroy, O. R., *J. Electroanal. Chem.* **1987**, *234*, 213.
55. Rosseinsky, D. R.; Glidle, A., *J. Electrochem. Soc.* **2003**, *150*, C641.
56. Stilwell, D. E.; Park, K. W.; Miles, M. H., *J. Appl. Electrochem.* **1992**, *22*, 325.
57. Holmes, S. M.; Girolami, G. S., *J. Am. Chem. Soc.* **1999**, *121*, 5593.
58. Verdaguer, M.; Girolami, G., *Magnetic Prussian Blue Analogs in Magnetism: Molecules to materials*, Ed.: J. S. Drillon, Weinheim, 2004.
59. Gadet, V.; Mallah, T.; Castro, I., *J. Am. Chem. Soc.* **1992**, *114*, 9213.
60. Dent, A. J.; Mosselmans, J. F. W., *An Introduction to EXAFS Data Analysis. CCLRC Daresbury Laboratory, Warrington, UK*, **1995**.

61. Mosselmans, J.F.W., A Guide to EXCURV98,  
<http://srs.dl.ac.uk/XRS/Computing/Programs/excurv97/excurv98guide.htm>
62. Garcia-Jareno, J. J.; Navarro, J. J.; Roig, A. F.; Scholl, H.; Vicente, F.,  
*Electrochim. Acta* **1995**, *40*, 1113.
63. Siperko, L. M.; Kuwana, T., *J. Electrochem. Soc.* **1983**, *130*, 396.
64. <http://cds.dl.ac.uk>.
65. Kaplun, M. M.; Smirnov, Y. E.; Mikli, V.; Malev, V. V., *Russian J. Electrochem.* **2001**, *37*, 1065.
66. Bard, A. J.; Faulkner, L. R., *Electrochemical Methods. Fundamentals and Applications*. John Wiley & Sons: New Delhi, 2006.
67. Martinez-Garcia, R.; Knobel, M.; Balmaseda, J.; Yee-Madeira, H.; Reguera, E.,  
*J. Phys. Chem. Sol.* **2007**, *68*, 290.
68. Farley, N. R. J., PhD Thesis, *Structural Studies of Electroactive Transition Metal Oxide Films*. Thesis, University of Leicester, Leicester, 2001.
69. Tedim, J.; Carneiro, A.; Bessada, R.; Patricio, S.; Magalhaes, A. L.; Freire, C.; Gurman, S. J.; Hillman, A. R., *J. Electroanal. Chem.* **2007**, *610*, 46.
70. Tedim, J.; Carneiro, A.; Freire, C.; Gurman, S. J.; Hillman, A. R., *Langmuir*.
71. West, A. R., *Solid State Chemistry and its Applications*. Wiley: Chichester, 1984.

# CHAPTER IV

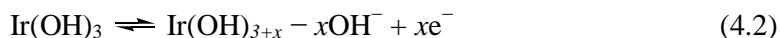
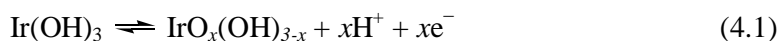
## ANODICALLY DEPOSITED IRIDIUM OXIDE ELECTROACTIVE FILMS

### 4.1 Introduction

Iridium oxide electroactive films are attractive due to their exceptional chemical stability to multiple redox switching over a wide range of pH and temperature in aqueous solution (in excess of  $8 \times 10^6$  cycles<sup>1</sup>), and facility of deposition on a wide range of different substrates. Iridium oxide films supported on electrode surfaces have found application in pH sensors (e.g. in monitoring myocardial acidosis<sup>2</sup> or in microfluidic sensor systems<sup>3</sup>), supercapacitors and electrochromic devices.<sup>4-6</sup> Attention has been brought to the possible use of this material in neural stimulation and recording electrodes.<sup>7-9</sup> It is electrochromic, with the colour change from black (oxidized) to transparent (reduced). Iridium oxide films have also attracted some attention because of their high electrocatalytic activity for chlorine and oxygen evolution.<sup>10</sup>

In the group of electrochromic metal oxides ( $\text{IrO}_2$ ,<sup>11</sup>  $\text{WO}_3$ ,<sup>12, 13</sup>  $\text{NiO}$ ,<sup>14</sup>  $\text{V}_2\text{O}_5$ <sup>15</sup>) iridium oxide shows a fast response upon cathodic bleaching and anodic colouration. Interestingly, despite this fact, iridium oxide electrochromic behaviour has not been

studied as extensively as other materials from the metal oxides family.<sup>16</sup> Three possible mechanisms of electrochromic reactions have been reported:



They include movement of proton (4.1), movement of anion (4.2) or movement of small alkali ions (4.3).<sup>16,17</sup> As can be seen, various iridium species (e.g.  $\text{IrO}_2$ ,  $\text{Ir(OH)}_3$ ) may be present in the modified electrodes discussed in this chapter, but for ease and clarity the term “iridium oxide” will be used throughout the discussion.

Diverse fabrication routes of  $\text{IrO}_2$  films are possible, and properties of the material are dependent on the fabrication conditions and preparation method. Iridium oxide films can be obtained via anodic oxidation of elemental Ir,<sup>18</sup> electrochemically induced precipitation processes,<sup>1, 19</sup> reactive sputtering,<sup>20</sup> thermal decomposition of iridium salt solution to form thermal iridium oxide films,<sup>21</sup> or thermal oxidation of pure metal.<sup>1, 22</sup> Sputtered iridium oxide films are dense ( $10 \text{ g cm}^{-3}$  to  $11.7 \text{ g cm}^{-3}$ ), and the voltammetric peaks they show in acidic solutions are broad and not very well defined.<sup>23-25</sup> In contrast, electrochemically prepared films yield well defined cyclic voltammograms, are highly porous and hydrated and of densities ca.  $2 \text{ g cm}^{-3}$ .<sup>26</sup> Moreover, it appears that all the Ir sites are electrochemically active, which makes them more suitable for quantitative analysis.<sup>1</sup>

Over the past 34 years a lot of studies have been carried out to characterize electrochemically prepared iridium oxide.<sup>27</sup> There is a general consensus that the colour change in iridium oxide is an effect of a change in iridium valency from  $\text{Ir}^{3+}$  to  $\text{Ir}^{4+}$ .<sup>28, 29</sup> In earlier, in situ iridium  $L_3$ -edge XAS studies, Scherson and co-workers studied electrochemically prepared iridium oxide electrodes.<sup>30</sup> In their study XAS was used in combination with Raman spectroscopy to study the behaviour of the films in alkaline ( $0.3 \text{ M Na}_2\text{CO}_3$ ) and acidic ( $0.5 \text{ M H}_2\text{SO}_4$ ) solutions. They assigned one broad peak in the cyclic voltammogram to the  $\text{Ir}^{3+} \rightleftharpoons \text{Ir}^{4+}$  redox process (acidic), and two well defined features to  $\text{Ir}^{3+} \rightleftharpoons \text{Ir}^{4+}$  and  $\text{Ir}^{4+} \rightleftharpoons \text{Ir}^{5+}$  (alkaline).

For sputtered iridium oxide films in 0.5 M H<sub>2</sub>SO<sub>4</sub> electrolyte Pauporte et al recognized only a one electron redox process, which they assigned to Ir<sup>3+</sup>  $\rightleftharpoons$  Ir<sup>4+</sup> change.<sup>25</sup> For the similar studies carried on by Huppaufl and Lengeler the authors concluded that the highest oxidation state of the Ir in the anodically oxidized elemental Ir foil was +4.8.<sup>18</sup>

## 4.2 Objectives

In spite of the wealth of information collected and years of research on iridium oxide electrodes – since the first report on its electrochromic properties in 1975 by Buckley and Burke<sup>27</sup> – some ambiguities still remain. These relate to the colouration – bleaching processes of this electrochromic material, valency of the iridium ions, and structural transformation taking place at different stages during electrochemical manipulation. Also the factors controlling performance of the iridium oxide electrodes are not clear. Much of the controversy is caused by the diverse ways of preparation, such as mentioned earlier sputtering, electrochemical deposition or thermal oxidation of pure metal.

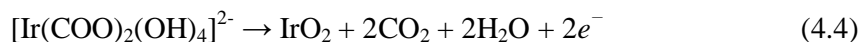
Techniques that have been used (EXAFS, XANES, CV and XPS) yield complementary information, and may be helpful when addressing a question such as relationship between the coulometrically (cyclic voltammetry) injected charge and, as a result, the oxidation state of the iridium oxide electrode, and the resulting variation in Ir local environment – these are explored in this study. The novel approach here is use of EXAFS L<sub>3</sub>-edge for determination of electrochemically deposited iridium oxide films in alkali and neutral media (*vs.* acidic and alkaline<sup>30</sup>). Moreover, in materials prepared by anodic oxidation of elemental metal<sup>18, 31</sup> and studied by Lengeler et al, grazing incidence EXAFS was used due to the X-ray opaque electrode substrate, so only the surface region of the film was sampled.<sup>18</sup> In the case of electrodeposited films, with the use of polyester supported ITO working electrode substrate (X-ray transparent) the whole film was sampled. Combination of methods exploited links electrode charge, Ir—O and Ir—Ir nearest coordination shell distance changes, coordination numbers and structural (dis)order.

### 4.3 Experimental and Sample Preparation

Iridium oxide films described in this thesis were prepared electrochemically from alkaline solutions. Iridium is a metal of the VIII group, and its oxides (hydroxides) are not soluble in alkaline solutions. Upon addition of a strong base (*e.g.* potassium hydroxide) to iridium tetrachloride aqueous solutions, insoluble iridium oxide ( $\text{IrO}_2$ ) precipitates.<sup>11</sup> Formation of an iridium complex which is stable even in alkaline solution is essential to avoid instant precipitation of iridium oxides in the deposition solution, therefore oxalic acid was used as the complex forming agent. The preparation procedure for the deposition solution was as described by Yamanaka:<sup>6, 11</sup>

- 1) 0.1125 g of iridium(IV) chloride hydrate ( $\text{IrCl}_4 \cdot \text{H}_2\text{O}$ , Aldrich) was dissolved in 75 ml of deionised  $\text{H}_2\text{O}$  by magnetic stirring for 30 minutes;
- 2) 0.75 ml of aqueous hydrogen peroxide solution (30 wt. %  $\text{H}_2\text{O}_2$ , VWR International Ltd.) was added and the resulting solution was stirred for 10 minutes;
- 3) 0.375 g of ethanedioic acid-2-water (oxalic acid,  $(\text{COOH})_2 \cdot 2\text{H}_2\text{O}$ , Scientific & Chemical Supplies Ltd.) was added and the solution was stirred for 10 minutes;
- 4) Anhydrous potassium carbonate ( $\text{K}_2\text{CO}_3$ , VWR International Ltd.) was stirred into the solution a little at a time to adjust pH of the solution to 10.5 (pH-meter 3510 Jenway).

According to Yamanaka<sup>6, 11</sup> the addition of hydrogen peroxide to the deposition solution makes it possible to deposit oxide films at lower current densities, but the mechanism of the reaction is not clear. The resulting solution was left to age for at least three days at room temperature. Later it was kept in the fridge for the maximum period of three months. Aging the deposition solutions is necessary, and no film could be deposited from freshly prepared solution. The aging process is clearly associated with hydrolysis of the  $\text{IrCl}_4$  in the basic medium. In the next step complexation of iridium by oxalate ligands takes place.<sup>1</sup> The likely reaction mechanism in which  $\text{IrO}_2$  is formed by anodic oxidation of ligands in an Ir complex compound was given by Yamanaka, where the oxalate ligand is oxidized,  $\text{CO}_2$  is formed and  $\text{IrO}_2$  deposited:<sup>11</sup>



The electrodeposition of the films was carried out at room temperature, from quiescent solution. Films were deposited at a constant current, with current densities typically 1.5 – 2.0 A m<sup>-2</sup>. The solution was purged with N<sub>2</sub> or Ar for about 30 minutes prior to the electrodeposition, and when possible (i.e. apart from the electrodeposition in the EXAFS cell) a steady stream of the inert gas was blown over the solution surface. The thickness of the film was controlled by the time of deposition. After deposition, the films (black in colour) were rinsed with deionised water and transferred into the background electrolyte for cyclic voltammetry experiments. 0.3 M sodium carbonate (Na<sub>2</sub>CO<sub>3</sub>, BDH) and 0.1 M potassium phosphate buffer solutions were used as background electrolytes, of pH 10.7 and 7.3 respectively. Ag/AgCl/saturated KCl or Hg/Hg<sub>2</sub>Cl<sub>2</sub>/saturated KCl (saturated calomel electrode, SCE) were used as a reference electrode, Pt mesh as a counter electrode, and Pt discs (Goodfellow) or ITO coated glass plates (Apex Services) as working electrodes. For EXAFS experiments 175 µm conductive ITO coating (sheet resistance 20 Ω/□) on permanent polyester film (Sheldahl, MN, USA) working electrodes were used. Use of polyester as a support for ITO coating enabled data acquisition in fluorescence and transmission modes. The fluorescence mode is more sensitive than transmission, therefore is more useful for very thin or low density/diluted samples, yielding much better signal-to-noise ratios. On the other hand transmission mode is a source of information about the absolute population of the element studied.

0.1 M potassium phosphate buffer solution was obtained by mixing 80.2 ml of 1 M dipotassium hydrogen phosphate (K<sub>2</sub>HPO<sub>4</sub>, BDH) and 19.8 ml of 1 M potassium dihydrogen orthophosphate (KH<sub>2</sub>PO<sub>4</sub>, BDH) and diluting the combined 1 M stock solutions to 1000 ml with deionised H<sub>2</sub>O. The pH value of the resulting electrolyte was measured with a pH meter.

EXAFS experiments on iridium oxide films were carried out *in situ* at station 16.5 at Daresbury Laboratory in fluorescence and transmission modes. The electrode was placed at an angle of 45° with respect to the Ge(III) detector. Spectra were measured at the Ir L<sub>3</sub>-edge (11,212 eV). The L<sub>3</sub>-edge involves a d-final state; hence it provides information on d-band occupancy. A purpose-built *in situ* spectroelectrochemical

EXAFS cell utilised in this experiment was described in Chapter II. There has to be a compromise between the demands of the electrochemical and X-ray experiments. It means that the production of a thick film is necessary to produce a sensible step and signal-to-noise ratio in the XAS experiment. Also the electrode placement might not be the most ideal, and the counter electrode could not span over the whole area of the working electrode. CVs presented in the thesis do not correspond to the films electrodeposited in the EXAFS cell, but the cell geometry had little effect on the voltammograms. EXAFS spectra were measured for iridium oxide modified electrodes and a set of reference of Ir standards: iridium(IV) chloride hydrate ( $\text{IrCl}_4 \cdot x\text{H}_2\text{O}$ , Aldrich) and iridium(III) chloride hydrate ( $\text{IrCl}_3$ , Aldrich) as 25 mM aqueous solutions and iridium(IV) oxide, 99.9 % ( $\text{IrO}_2$ , Aldrich) as a fine powder distributed evenly on self-adhesive tape.

For all XPS experiments, iridium oxide films were prepared at the University of Leicester using the procedure described in the introduction to this chapter. Samples were prepared 1-2 days in advance and transported in sealed containers to the National Centre for Electron Spectroscopy and Surface Analysis (NCESS) in Daresbury Laboratory. They were cycled in nitrogen-purged 0.3 M  $\text{Na}_2\text{CO}_3$  prior to the XPS measurement in the following sequence; each film was cycled 10 times at a scan rate of  $100 \text{ mV s}^{-1}$ . The last, 11<sup>th</sup> scan, was done at  $10 \text{ mV s}^{-1}$  scan rate and stopped at the required potential. The working modified electrode was disconnected from the circuit, removed from the background electrolyte, rinsed thoroughly with deionised (purged with  $\text{N}_2$ ) water, dried with high pressure inert gas, and placed in the vacuum chamber as fast as possible. SCE was used as a reference electrode, Pt mesh as a counter electrode, and Pt discs (Goodfellow) as working electrodes. All procedures were carried out at room temperature.

## 4.4 Data Analysis

The spectra of reference compounds and iridium oxide modified electrodes were calibrated, background subtracted, normalised and fitted using the standard procedures described in Chapter II. During data fitting, the EXAFS spectra were truncated to  $k_{max} =$

10 to remove excessive noise at high  $k$  values, and the data were fitted to the three nearest shells. All spectra were  $k^3$ -weighted and curve fitting was achieved using the EXCURV98 program.<sup>32</sup> The AFAC factor was set to a value of 0.9. This factor is related to the proportion of electrons which undergo EXAFS type scattering. In EXCURV98 it should normally be left at 1.0, unless one believes the spectrum suffers from an amplitude damping effect.<sup>33</sup> The coordination numbers for data fitting were set as integer values to obtain the best fits. The final values obtained from the data fitting were interatomic distances for the first three coordination spheres (i.e. Ir—O, Ir—Ir and Ir—Ir) and Debye-Waller factors. Edge positions and edge shifts were obtained from XANES.

The number of iridium sites in the electroactive film was calculated from the XAS data according to the procedure described in Chapter II. Electrochemical data were used for calculation of the charge inserted into the film during the anodic scan. Charge calculation was done by integration of the area under the cyclic voltammetric scan and division by the appropriate scan rate. The quotient of the XAS derived data and electrochemical data is the average number of electrons transferred per iridium atom.

The ESCA Analysis program available on site was used for XPS data analysis. Literature values of the position of XPS spectral lines were taken from the <http://srdata.nist.gov/> website database and the Handbook of X-ray Photoelectron Spectroscopy<sup>34</sup>, unless stated otherwise. These results are presented in graphs and tables, and discussed in the following section.

## 4.5 Results

A typical potential response during the deposition of an iridium oxide film is presented in Figure 4.1. After the initial 20 - 30 seconds of deposition the potential stabilizes close to +0.6 V and maintains a constant value throughout the subsequent electrodeposition time.

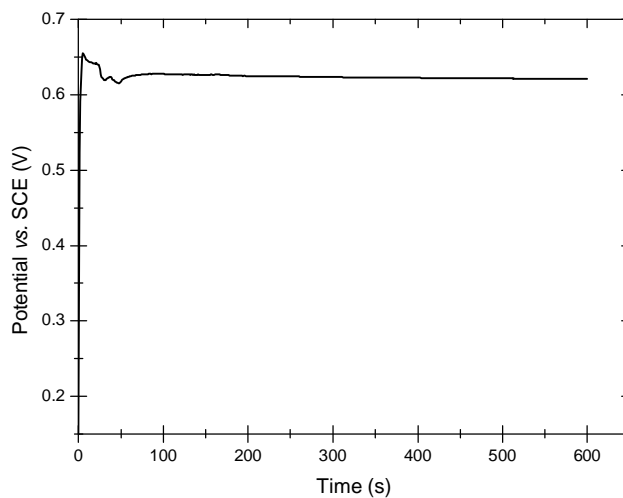


**Figure 4.1.** Electrodeposition of iridium oxide film on the Pt disc electrode. Current density:  $1.6 \text{ A m}^{-2}$ .

Cyclic voltammograms obtained from freshly deposited iridium oxide films displayed peak potentials and had a general appearance as reported by other authors.<sup>1</sup> Iridium oxide is called an oxidative coloration metal.<sup>6</sup>

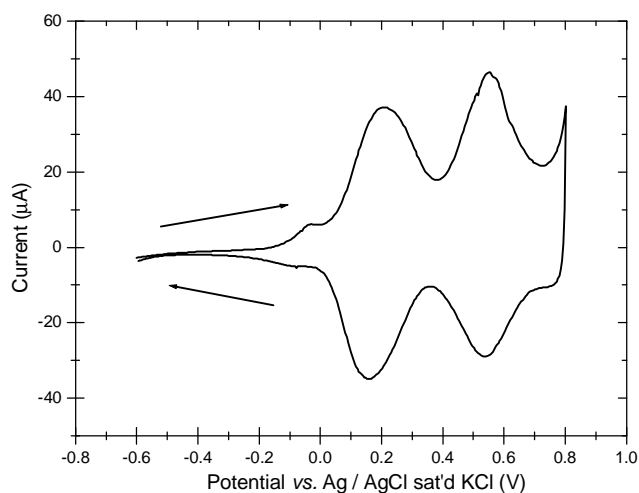


**Figure 4.2.** Cyclic voltammogram for an electrodeposited iridium oxide film (ITO coated glass plate) exposed to 0.1 M potassium phosphate buffer solution, pH 7.3. Potential scan rate:  $0.1 \text{ mV s}^{-1}$ .

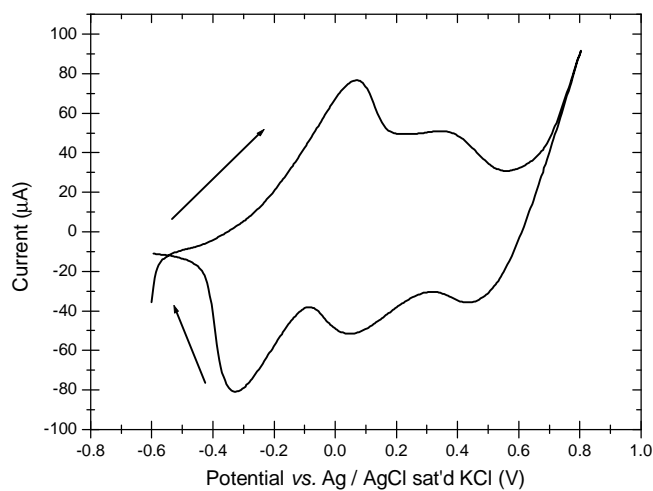


**Figure 4.3.** Cyclic voltammogram of the iridium oxide film in 0.3 M  $\text{Na}_2\text{CO}_3$  background electrolyte, pH 10.7. Potential scan rate:  $1 \text{ mV s}^{-1}$ .

It changes colour from transparent when reduced to dark blue/black upon electrolytic oxidation, and this characteristic response was also observed. Typical cyclic voltammograms are shown in Figure 4.2 for 0.1 M potassium phosphate buffer (pH 7.3) and Figure 4.3 for 0.3 M  $\text{Na}_2\text{CO}_3$  background electrolyte (pH 10.7).

### 4.5.1 X-ray Photoelectron Spectroscopy

Raw X-ray photoelectron spectra for Ir 4d<sub>5/2</sub>, C 1s, Ir 4d<sub>5/2</sub>, 4d<sub>5/2</sub> and O 1s lines of the iridium oxide modified electrode are shown in Figures 4.4 and 4.5. The electrode was removed from the background electrolyte at potentials corresponding to different oxidation states, as indicated by the value of the emersion potentials adjacent to each spectrum in Figures 4.4 and 4.5.

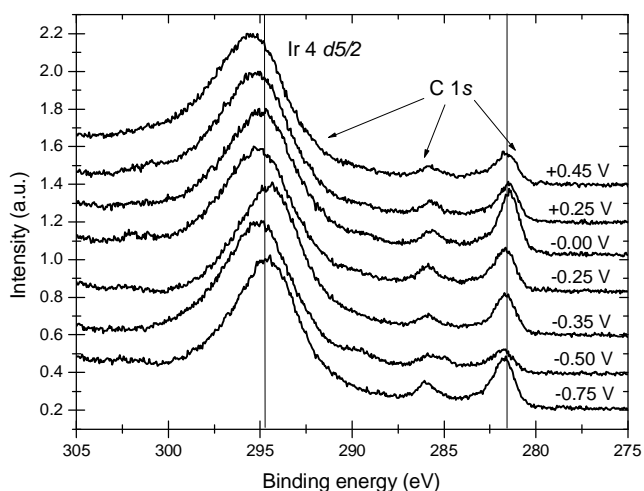


**Figure 4.4.** Ir 4d<sub>5/2</sub> and C 1s XPS electron lines as a function of emersion potential. Potentials describing each spectrum refer to the potential of the electrode at which the cyclic voltammetric scan was stopped, and sample removed from the solution. Spectra are not calibrated for energy shift, but the shift of the iridium line is evident in comparison with constant energy carbon lines. Arrows show probable contributions of different carbon types present in the sample. Background electrolyte: 0.3 M Na<sub>2</sub>CO<sub>3</sub>, reference electrode: SCE.

Plotted spectra were not energy calibrated, so the XPS lines visible on the plot can be affected by charging effect manifesting as shift in the absolute binding energy value or line shape. On the other hand relative XPS electron line distances would not be affected by this phenomenon, and allow one to recognise factual changes – in this case caused by redox processes – in the probed sample. Relative energies for the photoelectron lines for the elements present in samples discussed in this chapter are listed in Table 4.2. Distances between binding energies [O 1s—Ir 4f<sub>5/2</sub>] and [Na 1s—Ir 4f<sub>5/2</sub>] decrease as the film is oxidized. This is due to increasing binding energy of Ir 4f line. Binding

energies of the oxygen and sodium do not change, although the first one can be affected by the intake of  $\text{OH}^-$  and  $\text{CO}_3^-$  anions as the electrode is progressively oxidized. In the same table the ratio of peak areas [ $\text{Ir } 4f_{7/2} / \text{O } 1s$ ] is shown and is used to yield useful information about the structure of the film (i.e. iridium oxide vs. iridium hydroxide) and related to changes species movement. Unfortunately no potential related changes can be observed, and this may be the result of a generally oxygen rich environment and/or the surface being affected by the contact with the air.

Relative binding energy differences			
sample	O 1s—Ir 4f <sub>5/2</sub>	Na 1s—Ir 4f <sub>5/2</sub>	Ir 4f <sub>7/2</sub> / O 1s ratio
IrCl <sub>4</sub>	468.1	—	—
<b>iridium oxide film</b>			
-0.75 V	466.5	773.8	9.1
-0.50 V	466.2	773.3	10.5
-0.35 V	466.6	773.7	11.4
-0.25 V	466.2	773.1	12.2
0.00 V	466.0	773.0	10.4
+0.25 V	465.9	772.9	11.1
+0.45 V	465.8	772.7	10.5

**Table 4.2.** Relative binding energy difference between XPS lines: [O 1s—Ir 4f<sub>5/2</sub>] and [Na 1s—Ir 4f<sub>5/2</sub>] as a function of electrode potential (eV) vs. SCE. The energy difference decrease with increasing oxidation state of the film. The last column shows the ratio of Ir 4f<sub>7/2</sub> XPS peak area to O 1s XPS peak area.

Arrows in Figure 4.4 show possible contributions of several of carbon C 1s XPS lines. According to database information, binding energies for the species present in the sample discussed here may be very different from 284 eV for graphite or hydrocarbons (this value is often used for energy calibration). For example: 291.9 eV for  $\text{CO}_2$  or 289.5 eV for  $\text{Na}_2\text{CO}_3$ . The last one is very likely to have significant contribution as it is the background electrolyte solution.

The same discussion applies to the oxygen O 1s line presented in the Figure 4.5. Contributions of different ratios of oxygen species such as  $\text{H}_2\text{O}$ ,  $\text{OH}^-$ ,  $\text{Na}_2\text{CO}_3$ ,  $\text{IrO}_2$ ,  $\text{Ir}(\text{OH})_3$  influence the shape of the line. Once more this is contrasted with the behaviour

of iridium Ir 4f shown on the left side of the figure. There is a high possibility that the most reduced samples are influenced by contact with the air, despite the fact that considerable efforts were made to reduce the transfer time from electrolyte to the XPS vacuum chamber. It has to be noted that XPS is an extremely surface sensitive technique, and at the same time the outer layer is the most affected by the transfer process.

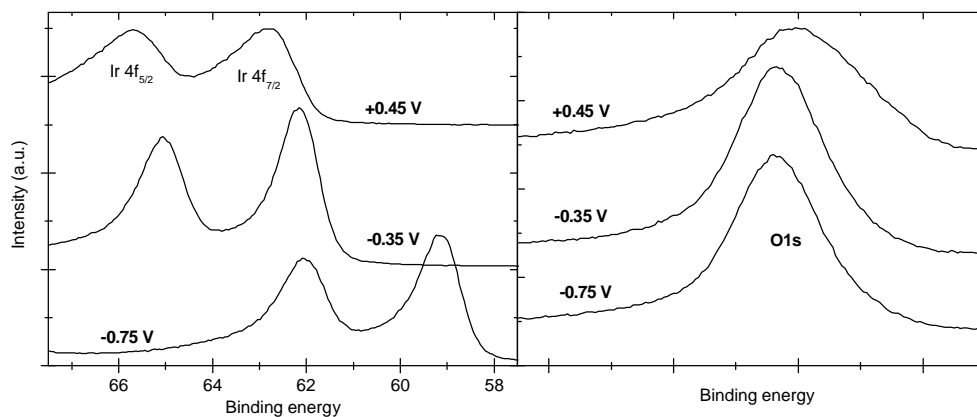


**Figure 4.5.** Ir 4f<sub>5/2</sub>, Ir 4f<sub>7/2</sub> (left) and O 1s (right) XPS lines for the sample removed at potentials: -0.75 V, -0.35 V and +0.45 V vs. SCE. Background electrolyte: 0.3 M Na<sub>2</sub>CO<sub>3</sub>. Significant change in the Ir 4f XPS electron line is shown versus relatively stable O 1s line.

Binding energies of the O 1s, Ir 4f<sub>5/2</sub>, Ir 4f<sub>7/2</sub>, C 1s and Na 1s XPS electron lines for different oxidation states of the iridium oxide film and IrCl<sub>4</sub> standard are listed in the Table 4.3. Because of the issues with carbon and oxygen lines discussed above, the Na 1s binding energy was chosen as a reference line for energy calibration.

sample	O 1s	Ir 4f <sub>5/2</sub>	Ir 4f <sub>7/2</sub>	Ir 4d <sub>5/2</sub>	C 1s	Na 1s
IrCl <sub>4</sub>	532.7	64.6	61.7	297.4	283.6	—
<b>iridium oxide film</b>						
-0.75 V (vs. SCE)	528.4	61.9	58.9	294.6	281.7	1068.4
-0.50 V	528.4	62.2	59.3	295.1	281.7	1068.4
-0.35 V	528.4	61.8	58.9	294.5	281.7	1068.2
-0.25 V	528.2	62.0	59.2	295.1	281.6	1068.2
0.00 V	528.0	62.0	59.2	295.0	281.4	1068.0
+0.25 V	528.0	62.2	59.4	295.2	281.5	1068.1
+0.45 V	528.1	62.3	59.5	295.5	281.6	1068.2

**Table 4.3.** Binding energies (eV) for: Ir 4f<sub>5/2</sub>, Ir 4f<sub>7/2</sub>, Ir 4d<sub>5/2</sub>, O 1s, C 1s and Na 1s XPS electron lines for electrodeposited iridium oxide films.

sample	O 1s	Ir 4f <sub>5/2</sub>	Ir 4f <sub>7/2</sub>	Ir 4d <sub>5/2</sub>	C 1s	Na 1s
IrCl <sub>4</sub>	532.7	64.6	61.7	297.4	283.6	—
<b>iridium oxide film</b>						
-0.75 V (vs. SCE)	531.5	65.0	62.0	297.7	284.8	1071.5
-0.50 V	531.5	65.3	62.4	298.2	284.8	1071.5
-0.35 V	531.7	65.1	62.2	297.8	285.0	1071.5
-0.25 V	531.5	65.3	62.5	298.4	284.9	1071.5
0.00 V	531.5	65.5	62.7	298.5	284.9	1071.5
+0.25 V	531.4	65.6	62.8	298.6	284.9	1071.5
+0.45 V	531.4	65.6	62.8	298.8	284.9	1071.5

**Table 4.4.** Binding energies (eV) for: Ir 4f<sub>5/2</sub>, Ir 4f<sub>7/2</sub>, Ir 4d<sub>5/2</sub>, O 1s, C 1s and Na 1s XPS electron lines for electrodeposited iridium oxide films. Energy corrected data with reference to Na 1s electron line in Na<sub>2</sub>CO<sub>3</sub> at binding energy 1071.5 eV.

The fact that Na 1s is so remote from the energies for the rest of the elements may be a disadvantage. In favour of the choice of this line are the facts, that the electrolyte could be the only source of Na in the film and the line has a very stable position and appearance for the whole data set. The value of 1071.50 eV for Na 1s in Na<sub>2</sub>CO<sub>3</sub><sup>34</sup> was chosen as a reference point, and energy corrected data are shown in Table 4.4.

#### 4.5.2 Extended X-ray Absorption Fine Structure

Edge steps of the modified electrode recorded in transmission mode were  $\Delta a = \ln(I_0/I_t) \approx 0.06$  and  $\Delta a \approx 0.035$  for the electrodes cycled in pH 7.3 and pH 10.7 electrodes, respectively. The concentration of the Ir sites of the films was calculated using the raw edge steps of the transmission spectrum according to the equation:

$$nt[m^{-2}] = \frac{\Delta a}{\Delta \mu[m^{-2}]}$$

Tabulated values for the difference in absorption cross-section of Ir were used, where  $\Delta \mu = 4.0 \times 10^4 \text{ barn/atom}^{-1} = 4.0 \times 10^{-24} \text{ m}^2$ .<sup>35</sup> Because samples were positioned at an angle of 45° relatively to the incoming X-ray beam, the resulting  $nt$  product was divided by the angle factor of  $\sqrt{2}$ . The number of Ir atoms per square metre calculated was then multiplied by the charge of one electron ( $1.6 \times 10^{-19} \text{ C}$ ), yielding the amount of charge per area unit. Charge inserted into the film during oxidation per area unit was also determined coulometrically, as described earlier. Results of these calculations are summarized in Table 4.1.

Sample	Edge step $\Delta a = \ln(I_0/I_t)$	$\sqrt{2} \cdot nt \text{ (Ir m}^{-2}\text{)}$	$nt \cdot (1.6 \times 10^{-19} \text{ C}) \text{ (C cm}^{-2}\text{)}$
iridium oxide, pH 7.3	$0.06 \pm 0.01$	$(1.0 \pm 0.2) \times 10^{22}$	0.16
iridium oxide, pH 10.7	$0.035 \pm 0.005$	$(0.6 \pm 0.1) \times 10^{22}$	0.06
Sample	Charge injected (C)		Charge (C cm <sup>-2</sup> )
iridium oxide, pH 7.3	$1.3 \times 10^{-1}$		0.15
iridium oxide, pH 10.7	$8 \times 10^{-2}$		0.09

**Table 4.1.** Amount of charge per unit area calculated from XAS data (upper chart). Charge inserted in the iridium oxide film for the oxidation half-scan. Calculation for samples prepared for XAS data acquisition. Area of the electrode: 0.85 cm<sup>2</sup> (lower chart).

The ratio of the XAS-derived values to coulometrical data is:  $0.16/0.15 = 1.07$  for the iridium oxide film measured in neutral (pH 7.3) electrolyte, and  $0.06/0.09 = 0.7$  for the alkalic (pH 10.7) electrolyte. This result shows that the amount of charge per iridium site is approximately 1.

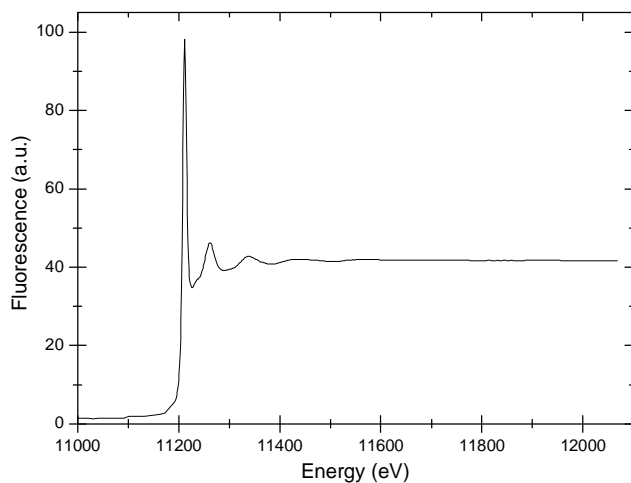


**Figure 4.6.** Raw standard fluorescence spectrum of a freshly electrodeposited iridium oxide film. Freshly electrodeposited film at potential +0.8 V vs. Ag/AgCl sat'd KCl.

Figure 4.6. is a typical raw fluorescence EXAFS spectrum of a fresh iridium oxide film. Typical fits to the EXAFS data for a iridium(IV) oxide standard and iridium oxide film modified electrode are shown together with their corresponding Fourier transforms (radial structure functions) in Figure 4.7.

Normalised Ir  $L_3$ -edge XANES of the iridium oxide films for both pH values (i.e. 7.3 and 10.7), and standards are shown in Figures 4.8, 4.9 and 4.10 correspondingly. They are shown on separate graphs for higher clarity. A change in the edge position is evident with changing oxidation state of the modified electrode. There is some broadening of the white line with increasing potential. One of several possible causes for this is the present of multiple species, which are discussed later. There is also an increase in intensity with film oxidation; since the intensity is a measure of the number of vacant d-states, this is consistent with the removal of electronic charge from the Ir sites.

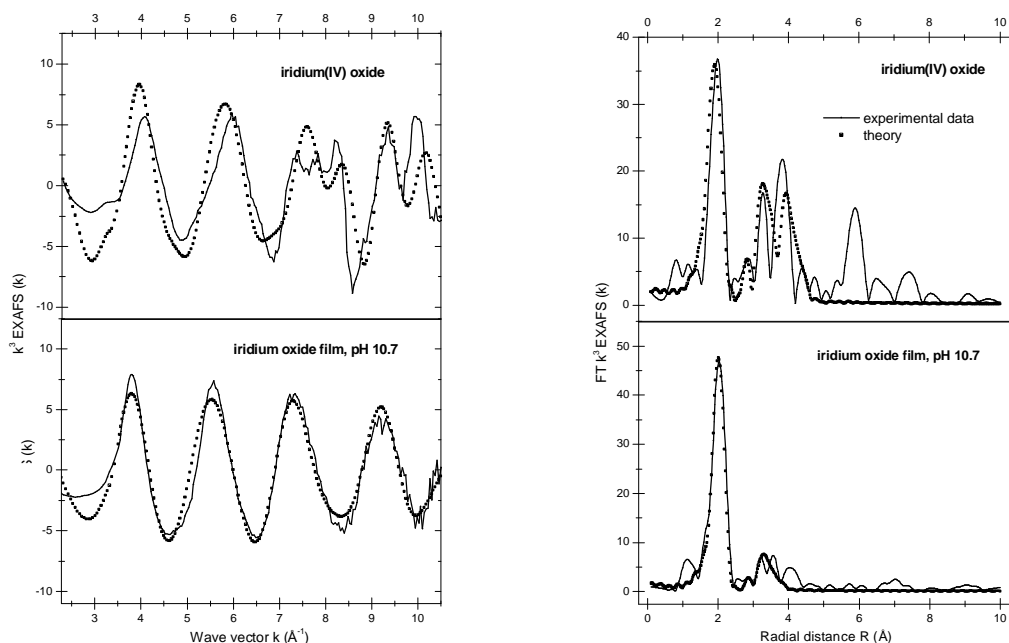


**Figure 4.7.**  $k^3$  EXAFS spectra with fits (left), and corresponding fitted Fourier transforms (right) for iridium(IV) oxide powder and electrodeposited iridium oxide film (-0.6 V, potassium phosphate buffer solution).

Progressive edge shifts taking place during the injection of the charge are listed in the Table 4.7. These data are also shown graphically in Figure 4.11 and 4.13 as a function of potential and as a function of the fraction of the charge injected into the film. The calculated amount of charge introduced in the film for each EXAFS data acquisition point (i.e. “stop” point at cyclic voltammogram) is shown in Table 4.5.

The edge shifts may be used to determine the formal charge of the iridium atom as a function of electrochemically injected charge. For platinum, the  $L_3$  edge shifts by 0.7 eV per formal charge for octahedral Pt—O bonding.<sup>36</sup> Using this as a calibration for the iridium edge shift, and noting that measured edge shifts are linear with injected charge, the data indicate a change in Ir mean formal charge from 3.3+ to 4.3+ in pH 7.3 electrolyte and from 3.6+ to 4.8+ in pH 10.7 electrolyte. The change of about one electron in each case is in good agreement with the spectroelectrochemically determined charge change per atom (ca. 0.9).

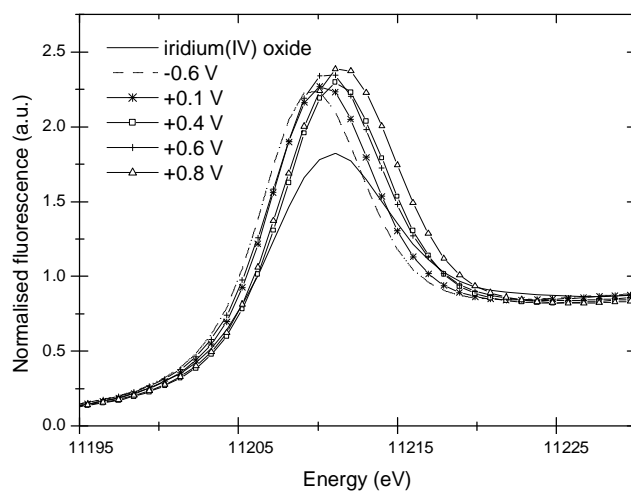


**Figure 4.8.** Normalised Ir L<sub>3</sub>-edge XANES of iridium(IV) oxide and iridium oxide film at varying charge states (0.1 M potassium phosphate buffer solution, pH 7.3).

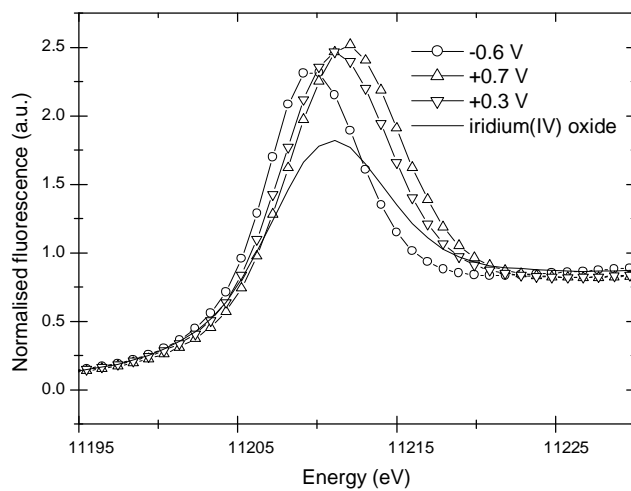


**Figure 4.9.** Normalised Ir L<sub>3</sub>-edge XANES of iridium oxide film at varying charge states (0.3 M Na<sub>2</sub>CO<sub>3</sub>, pH 10.7).

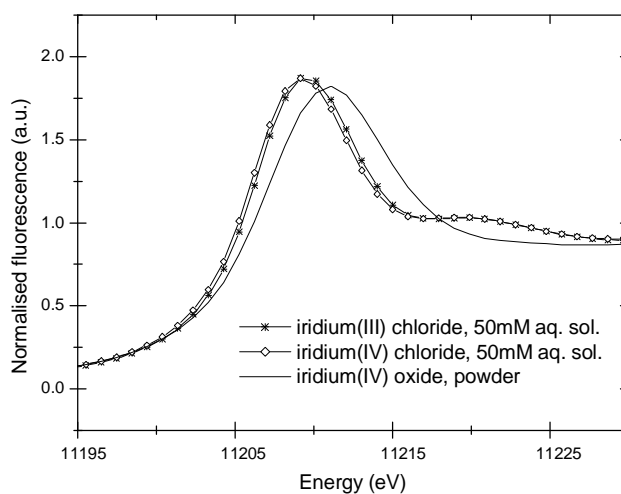


**Figure 4.10.** Normalised XANES of iridium(III) chloride and iridium(IV) chloride 50 mM aqueous solutions and iridium(IV) oxide powder.

Edge positions were measured at the maximum value of the white line, and edge shifts were calculated as the difference between sample and  $\text{IrO}_2$  standard edge positions.

In addition - apart from the white line positions - interatomic distances  $Rl$  for the first Ir—O shell around the central iridium atom, derived from the fits to EXAFS spectra, were plotted in functions of potential and of the injected charge. These display the movement of the first shell atoms as the Ir valency changes. For the most reduced film, at a potential -0.6 V, the first Ir—O shell distance is at  $2.05 \pm 0.01 \text{ \AA}$ , and it shortens to 1.95. Similar shortening of the bonds is observed for the second Ir—Ir and third Ir—Ir coordination shells. The error was only noted if it exceeded the value of  $0.01 \text{ \AA}$ , therefore for the first and second shell practically no errors are listed. Only for the furthest fitted third Ir—Ir shell do errors become significant. This effect is not unexpected, as the distance of the last fitted shell is getting close to the limit of EXAFS capability (usually regarded as ca.  $5 \text{ \AA}$  for well ordered or crystalline materials). The fact the film on the electrode is electrodeposited – and for that reason naturally has a relatively high disorder – additionally limits the effectiveness of the EXAFS fit. Debye-Waller factors were plotted only as a function of increasing electrode potential. The

results are shown in Figure 4.11 and Figure 4.13 for electrodes measured in neutral and alkali background electrolytes, respectively. Relevant data are listed in Table 4.6.

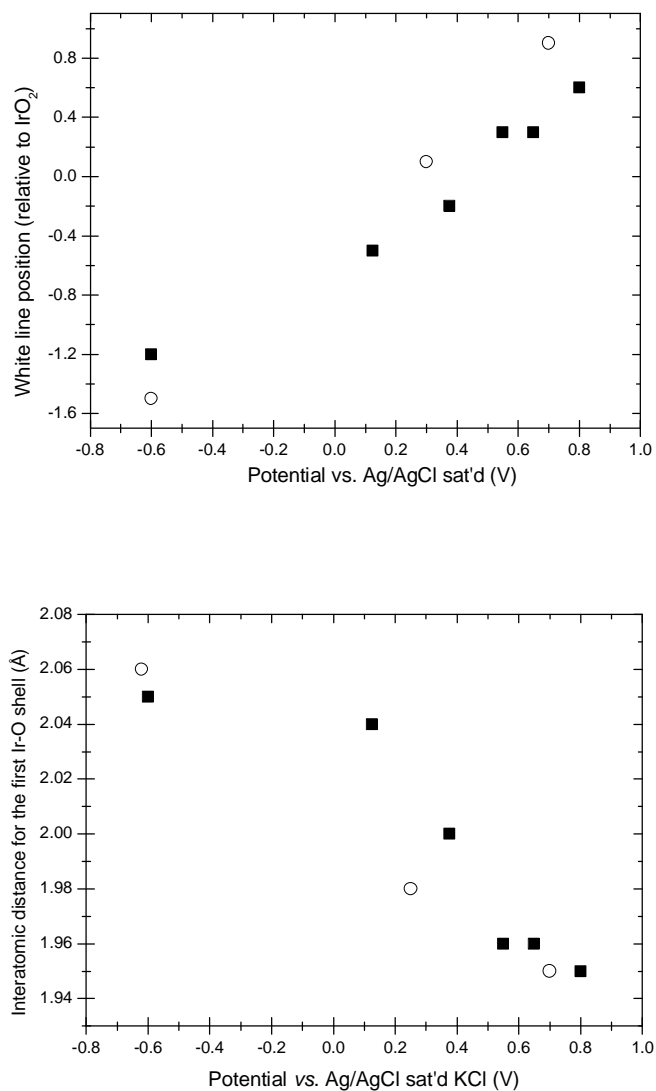


**Figure 4.11.** Interatomic distance  $R1$  and white line position for the first shell around iridium atom (Ir—O) in the electrodeposited film versus potential. Data acquired *in situ* in the spectroelectrochemical cell. (■ — 0.1 M potassium phosphate buffer solution, pH 7.3; ○ — 0.3 M Na<sub>2</sub>CO<sub>3</sub>, pH 10.7).

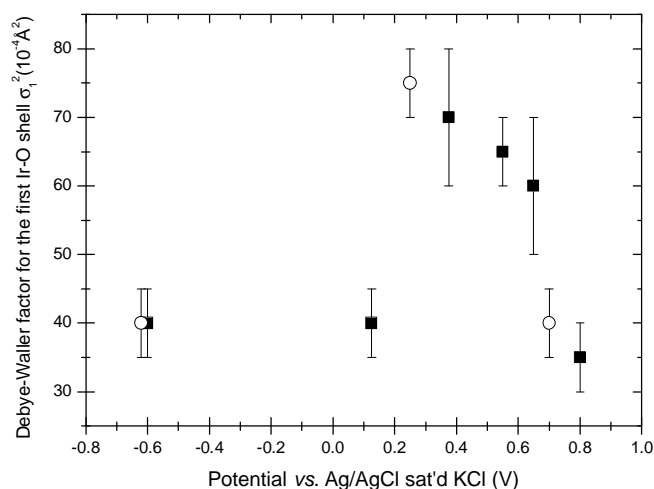


**Figure 4.12.** Debye-Waller factor  $\sigma_1^2$  for the first shell around iridium atom (Ir—O) in the electrodeposited film versus potential. Data acquired *in situ* in the spectroelectrochemical EXAFS cell. (■ — 0.1 M potassium phosphate buffer solution, pH 7.3; ○ — 0.3 M Na<sub>2</sub>CO<sub>3</sub>, pH 10.7).

---

**0.1 M potassium phosphate buffer solution (pH 7.3)**

---

potential (V)	charge (C)	charge (%)
-0.6	0	0
+0.1	$8.71 \times 10^{-3}$	7
+0.4	$5.06 \times 10^{-2}$	39
+0.6	$9.18 \times 10^{-2}$	70
+0.8	$1.3 \times 10^{-1}$	100

---

**0.3 M Na<sub>2</sub>CO<sub>3</sub> background electrolyte (pH 10.7)**

---

-0.6	0	0
+0.3	$3.68 \times 10^{-2}$	46
+0.7	$7.96 \times 10^{-2}$	100

---

**Table 4.5.** Amount of charge injected to the iridium oxide film for each EXAFS data acquisition point at cyclic voltammogram. Charge calculated from cyclic voltammograms obtained directly in the hutch. Charge calculated for the whole area of the anodic peak was defined as 100 %. Area of the electrode: 0.85 cm<sup>2</sup>.

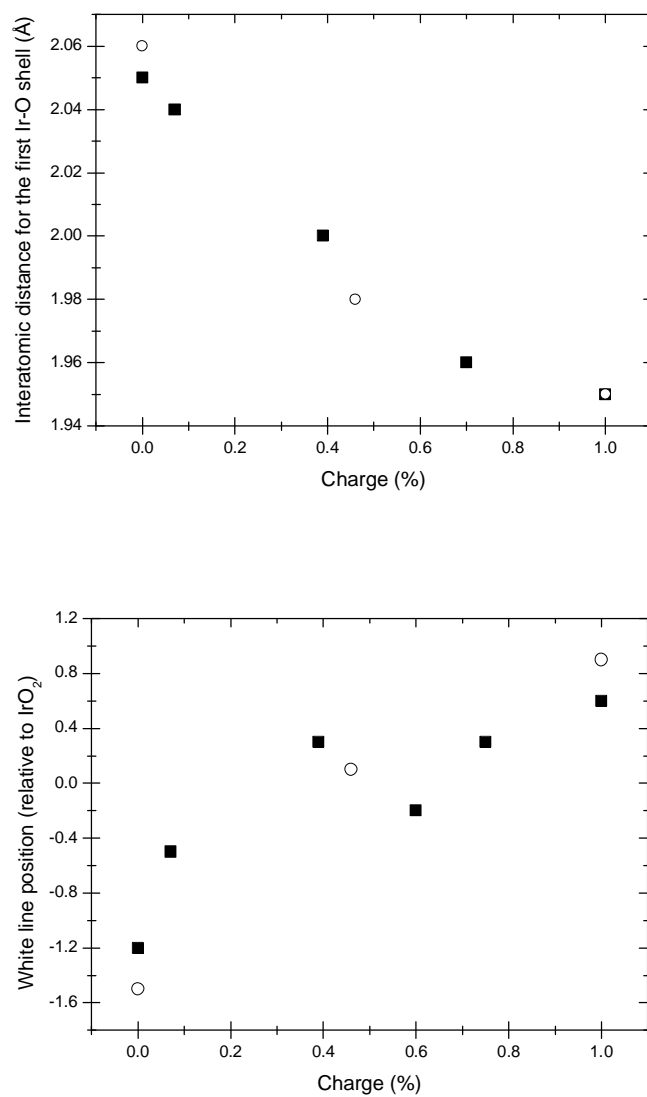


**Figure 4.13.** Interatomic distance  $Rl$  and white line position for the first Ir—O shell around Ir in an electrodeposited film versus per cent of charge injected. Data acquired *in situ* in the spectroelectrochemical cell. (■ — 0.1 M potassium phosphate buffer solution, pH 7.3; ○ — 0.3 M Na<sub>2</sub>CO<sub>3</sub>, pH 10.7)

Sample	Element	R (Å)	N	$\sigma^2$ ( $10^{-4}$ Å <sup>2</sup> )	FI	$\Delta E_0$
<b>IrO<sub>2</sub></b> (standard) $k_{\max}=15$	O	1.98 ± 0.01	<b>6</b>	30 ± 15	18.1	-1.0
	Ir	3.13	<b>2</b>	30 ± 5		
	Ir	3.81 ± 0.02	<b>8</b>	50 ± 5		
<b>iridium oxide film*</b>	O	1.97	6 ± 0.4	60 ± 10	4.9	-0.4
	Ir	3.06	<b>2</b>	70 ± 10		
	Ir	3.78	<b>8</b>	200 ± 50		
<b>electrode (pH 7.3)</b>						
-0.6 V	O	2.05	6.1 ± 0.5	40 ± 5	8.2	-2.6
	Ir	3.14	<b>2</b>	60 ± 10		
	Ir	4.55 ± 1.4	<b>8</b>	1200±5000		
+0.1 V	O	2.04	5.8 ± 0.4	40 ± 5	5.2	-2.7
	Ir	3.12	<b>2</b>	70 ± 10		
	Ir	3.90 ± 0.09	<b>8</b>	300 ± 150		
+0.4 V	O	2.00	6.4 ± 0.5	70 ± 10	6.7	-2.1
	Ir	3.11	<b>2</b>	85 ± 15		
	Ir	3.82 ± 0.05	<b>8</b>	210 ± 60		
+0.6 V	O	1.96	6.4 ± 0.5	65 ± 5	7.2	-0.2
	Ir	3.06	<b>2</b>	80 ± 10		
	Ir	3.73 ± 0.02	<b>8</b>	120 ± 30		
+0.8 V	O	1.95	5.9 ± 0.4	35 ± 5	4.5	-1.4
	Ir	3.04	<b>2</b>	40 ± 5		
	Ir	3.79 ± 0.04	<b>8</b>	200 ± 60		
<b>electrode (pH 10.7)</b>						
-0.6 V	O	2.06	5.8 ± 0.5	40 ± 5	4.3	-2.5
	Ir	3.15 ± 0.01	<b>2</b>	70 ± 10		
	Ir	3.99 ± 0.04	<b>8</b>	190 ± 60		
+0.3 V	O	1.98	5.9 ± 0.4	75 ± 5	4.8	-1.2
	Ir	3.07 ± 0.01	<b>2</b>	75 ± 10		
	Ir	3.80 ± 0.05	<b>8</b>	210 ± 65		
+0.7 V	O	1.95	6.1 ± 0.4	40 ± 5	4.2	-2.4
	Ir	3.05	<b>2</b>	60 ± 5		
	Ir	3.76 ± 0.04	<b>8</b>	165 ± 45		

**Table 4.6.** Structural parameters for first (Ir—O), second (Ir—Ir) and third (Ir—Ir) coordination shells derived from fits to L<sub>3</sub>-edge fluorescence EXAFS spectra for standards and iridium oxide modified electrode. \*Freshly electrodeposited film in the spectroelectrochemical cell. Uncertainties in distances ±0.02 Å unless otherwise stated. Bold coordination numbers signify fixed (i.e. not fitted) numbers. FI – fit index (%),  $\Delta E_0$  (± 5 eV).

Sample	White line shift (relative to IrO <sub>2</sub> standard) (eV)
<b>electrode (pH 7.3)</b>	
-0.6 V	-1.2
+0.1 V	-0.5
+0.4 V	-0.2
+0.6 V	+0.3
+0.8 V	+0.6
<b>electrode (pH 10.7)</b>	
-0.6 V	-1.5
+0.3 V	+0.1
+0.7 V	+0.9

**Table 4.7.** White line shift as a function of the sample oxidation state. Change relative to the white line of IrO<sub>2</sub> powder. Information derived from Ir L<sub>3</sub>-edge XANES Electrochemical measurements and EXAFS fluorescence fits for iridium oxide films and iridium(IV) oxide standard. Electrode: Ag/AgCl sat'd KCl.

## 4.6 Discussion

Cyclic voltammograms display two well defined peaks in the range -0.6 V to + 0.8 V vs. Ag/AgCl for iridium oxide films exposed to both alkaline and neutral background electrolytes. One hypothesis is that these could be assigned to two one-electron processes:  $\text{Ir}^{3+} \rightleftharpoons \text{Ir}^{4+}$  for the first peak, and  $\text{Ir}^{4+} \rightleftharpoons \text{Ir}^{5+}$  for the second peak of the voltammogram. Figure 4.14 shows plots of Ir 4f<sub>5/2</sub>, 4f<sub>7/2</sub> and 4d<sub>5/2</sub> XPS line binding energies as a function of charge injected into the film. It might be that the data is affected by the handling procedure - the surface of the sample can be oxidized upon contact with the air during transfer from electrochemical cell to the XPS machine vacuum chamber. The most reduced samples are the most prone to suffer from the oxidative environment. In these plots binding energies change by +0.8 (± 1) eV, +0.6 (± 1) eV and +1.1 (± 1) eV respectively, between the 0 % and 100 % charge consumption points. A similar shift in binding energy values for the Ir<sup>3+</sup> and Ir<sup>4+</sup> couple for 4f<sub>7/2</sub> XPS line is found in the database: +0.8 eV for K<sub>2</sub>IrBr<sub>6</sub> / K<sub>3</sub>IrBr<sub>6</sub> and +1.2 eV for K<sub>2</sub>IrCl<sub>6</sub> / K<sub>3</sub>IrCl<sub>6</sub>. This energy shift supports the argument for the one-electron total change in the oxidation state of iridium.

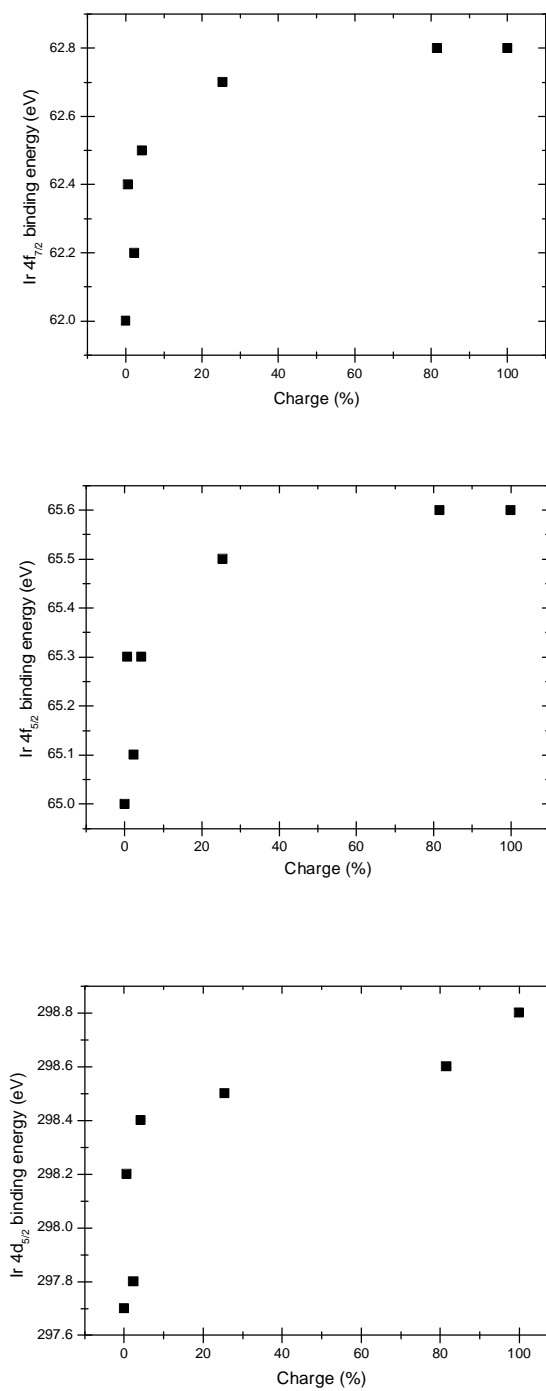


**Figure 4.14.** Ir 4f<sub>7/2</sub>, 4f<sub>5/2</sub>, 4d<sub>5/2</sub> XPS electron binding energy as a function of percent of charge injected. Value 0 % refers to the fully reduced and 100 % to the fully oxidized sample. Complete anodic peak is an equivalent to 100 % of injected charge. Binding energies change by +0.7 eV (Ir 4f<sub>7/2</sub>, 4f<sub>5/2</sub>) and +1.0 eV (4d<sub>5/2</sub>). Electrolyte: 0.3 M Na<sub>2</sub>CO<sub>3</sub>.

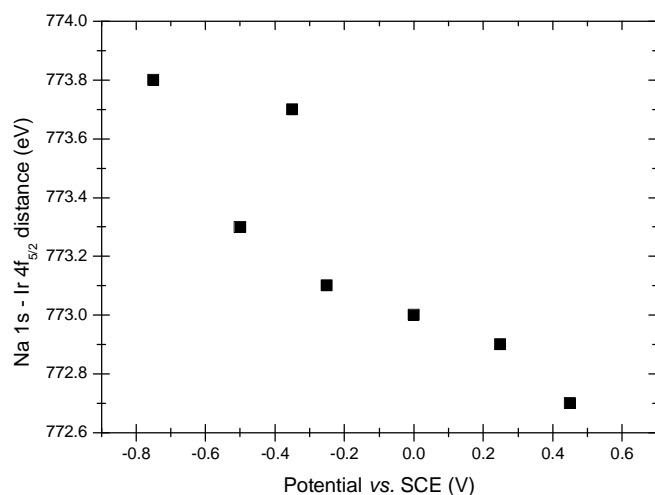


**Figure 4.15.** (Na 1s—Ir 4f<sub>5/2</sub>) XPS lines relative distances as a function of oxidation of the electrode. The distance change is -1.1 eV. Background electrolyte: 0.3 M Na<sub>2</sub>CO<sub>3</sub>.

For comparison purposes, a similar graph is plotted for the energy difference (Na 1s—Ir 4f<sub>5/2</sub>) (Figure 4.15.). This data would not be prone to the charging effect or any other externally introduced perturbation influencing the position of the XPS electron line. Again, the binding energy change observed here, (-1.1 eV) is in agreement with the absolute changes in Ir XPS electron line positions. Differences in binding energies for the Ir—Na couple shorten as the oxidation of the film increases, because Ir lines move to higher binding energies as electrons are removed, and Na 1s lines do not shift. This effect can be also observed in the data listed in Table 4.2: the Ir—O binding energy difference changes in the similar pattern to Ir—Na.

XANES show a steady shift in the position of the white line (Table 4.7) for both pH values. The position of the white line relative to iridium(IV) oxide powder and as a function of potential and consumed charge is plotted in Figure 4.11 and 4.13. Numerical values for all fitting parameters for EXAFS data of the iridium oxide film for three coordination shells are given in Table 4.6. Several conclusions can be drawn from these data. The Debye-Waller  $\sigma^2$  factors are fairly high, signalling structural disorder in electrodeposited, hydrated films. The disorder is noticeably higher for the intermediate potentials (+0.4 V and +0.6 V) in the neutral solution, and at +0.7 V in the alkaline

solution. The increase of disorder has been observed previously for electrodeposited<sup>30</sup> and anodically oxidized samples,<sup>18</sup> but not for sputtered films.<sup>25</sup> Debye-Waller factors for the third Ir—Ir shell at the distance of circa 3.8 Å are in general much higher, and no change can be observed during the redox process. It is understandable for an intrinsically not very highly ordered material – and for distances close to the limit of EXAFS capabilities – the change of oxidation state of the central iridium site will be very hard to detect in such a distant coordination shell. Regardless of this fact, shrinkage of this furthest fitted shell is observed with increasing oxidation of the film.

Films emersed at potentials between +0.4 V and +0.6 V in neutral and at +0.7 V in alkaline electrolyte yield the most similar interatomic distances to the iridium(IV) oxide powder standard and information based on X-ray diffraction obtained from the database. According to the database, the first shell Ir—O average distance is 1.98 Å. It is an average of the distorted octahedron, with four Ir—O bonds at 1.995 Å and two Ir—O bonds at 1.959 Å. It can be seen that EXAFS analysis for the powder IrO<sub>2</sub> sample gave excellent agreement with the X-ray diffraction data.

Results of spectroelectrochemical observations are shown in Table 4.1. The number of Ir sites was determined from edge steps of transmission data. The resulting values were multiplied by the charge of one electron. This is the quantity of charge that would be injected into the electroactive film if the process taking place on the electrode is a one-electron process. For the calculation of the actual amount of charge the coulometric data was used. The ratio of the XAS-obtained value to coulometrical data is:  $0.16/0.15 = 1.07$  for the iridium oxide film measured in neutral (pH 7.3) electrolyte, and  $0.06/0.09 = 0.7$  for the iridium oxide measured in alkalic (pH 10.7) electrolyte. This result shows clearly that the amount of charge per one iridium site present in the film is approximately 1 electron. XANES and XPS data show that the formal charges on the reduced and oxidized Ir sites are symmetrically placed to either side of that in bulk IrO<sub>2</sub>; since the latter contains Ir in a formal 4+ state, this indicates interchange of states with spatially averaged formal Ir charges of ca. 3.5+ and 4.5+ in the films.

## 4.7 Conclusions

The most obvious characteristic of the voltammetric responses of the iridium oxide modified electrodes is the presence of two peaks: the question then is whether this is a consequence of two sequential one-electron redox processes (for example,  $\text{Ir}^{3+} \rightarrow \text{Ir}^{4+} \rightarrow \text{Ir}^{5+}$ ) or of one-electron redox processes at two chemically distinct types of site (for example in terms of protonation and/or hydration). Careful attention to film deposition and handling ensured that this effect was not a feature of sample variation, which is a widely recognized feature of this system. The conclusion is that the two peaks visible in the cyclic voltammogram are both associated with a change of iridium oxidation state of ca. 3.5+ to 4.5+ (based – as discussed earlier - on the white line position relative to  $\text{IrO}_2$  standard), but in two different –O and –OH coordination environments. Depending on the composition (protonation) of the film, the relative magnitudes and degree of separation of the peaks can differ: in principle, one may observe the two extreme cases of a single broad peak or (as found here) two well separated peaks each representing a one-electron process.

A further argument supporting the change in the oxidation state from iridium 3.5+ to iridium 4.5+ is the characteristic behaviour of the Debye-Waller factors. In the “two-electron per iridium site” model there would be no necessary significant increase of the internal disorder, so the Debye-Waller factor would not show a maximum as the potential was varied. The increase of the value of Debye-Waller factor at intermediate potentials (a maximum was observed at ca. +0.4 V) is a signal of an increase of disorder in the structure of the electroactive film. This disorder is an effect of iridium oxidation taking place in different coordination environments (i.e. –O and –OH) with consequently different switching potentials. At the mid-potential of +0.4 V, when two Ir–O distances are present, the value of the Debye-Waller factor reaches its maximum value. These two relatively similar distances present at intermediate potentials are not resolved by fitting the EXAFS data, but their existence is clearly signaled in the behaviour of the Debye-Waller factor.

Additionally, coulometric data support the “one-electron per Ir site” model accompanied by an optical change from dark to transparent. First, the XAS intensity data allow one to assay the population of iridium atoms; this estimate is independent of the morphology, structure and density of the film. Second, the integrated voltammetric response yields the charge, which in turn (via the Faraday constant) yields the change in population of electrons in the film. The quotient of these two numbers yields a value of approximately unity for the number of electrons transferred per iridium site.

## 4.8 References

1. Petit, M. A.; Plichon, V., *J. Electroanal. Chem.* **1998**, *444*, 247.
2. Marzouk, S. A. M.; Ufer, S.; Buck, R. P.; Johnson, T. A.; Dunlap, L. A.; Cascio, W. E., *Anal. Chem.* **1998**, *70*, 5054.
3. Ges, I. A.; Ivanov, B. L.; Schaffer, D. K.; Lima, E. A.; Werdich, A. A.; Baudenbacher, F. J., *Biosens. Bioelectron.* **2005**, *21*, 248.
4. Gottesfeld, S.; McIntyre, J. D. E., *J. Electrochem. Soc.* **1979**, *126*, 742.
5. Patil, P. S.; Kavar, R. K.; Sadale, S. B., *Electrochim. Acta* **2005**, *50*, 2527.
6. Yamanaka, K., *Jpn. J. Appl. Phys.* **1991**, *30*, 1285.
7. Meyer, R. D.; Cogan, S. E.; Nguyen, T. H.; Rauh, R. D., *IEEE Trans. Neural Syst. Rehabil. Eng.* **2001**, *9*, 2.
8. Weiland, J. D.; Anderson, D. J., *IEEE Trans. Biomed. Eng.* **2000**, *47*, 911.
9. Blau, A.; Ziegler, C.; Heyer, M.; Endres, F.; Schwitzgebel, G.; Matthies, T.; Stieglitz, T.; Meyer, J. U.; Gopel, W., *Biosens. Bioelectron.* **1997**, *12*, 883.
10. Mozota, J.; Conway, B. E., *J. Electrochem. Soc.* **1981**, *128*, 2142.
11. Yamanaka, K., *Jpn. J. Appl. Phys.* **1989**, *28*, 632.
12. Wang, J.; Bell, J. M., *Sol. Energy Mater. Sol. Cells* **1996**, *43*, 377.
13. Cheng, W.; Baudrin, E.; Dunn, B.; Zink, J., *J. Mater. Chem.* **2001**, *11*, 92.
14. Velevska, J.; Ristova, M., *Sol. Energy Mater. Sol. Cells* **2002**, *73*, 131.
15. Hibino, M.; Ugaji, M.; Kishimoto, A.; Kudo, T., *Solid State Ionics* **1995**, *79*, 239.
16. Jung, Y.; Lee, J.; Tak, Y., *Electrochem. Solid St.* **2004**, *7*, H5.
17. Granqvist, C. G., *Handbook of Inorganic Electrochromic Materials*. Elsevier: Amsterdam, 1995.
18. Huppaufl, M.; Lengeler, B., *J. Electrochem. Soc.* **1993**, *140*, 598.
19. Baur, J. E.; Spaine, T. W., *J. Electroanal. Chem.* **1998**, *443*, 208.
20. Kang, K. S.; Shay, J. L., *J. Electrochem. Soc.* **1983**, *130*, 766.
21. Nishio, K.; Watanabe, Y.; Tsuchiya, T., *Thin Solid Films* **1999**, *350*, 96.
22. Bestaoui, N.; Prouzet, E., *Chem. Mater.* **1997**, *9*, 1036.
23. Pauporte, T.; Durand, R., *J. Appl. Electrochem.* **1999**, *30*, 35.
24. Hackwood, S.; Beni, G.; Gallgher, P. K., *Solid State Ionics* **1981**, *2*, 297.

25. Pauporte, T.; Aberdam, D.; Hazemann, J. L.; Faure, R.; Durand, R., *J. Electroanal. Chem.* **1999**, *465*, 88.
26. Mozota, J.; Conway, B. E., *J. Electrochem. Soc.* **1981**, *128*, 2142.
27. Kotz, E. R.; Neff, H., *Surf. Sci.* **1985**, *160*, 517.
28. McIntyre, J. D. E.; Basu, S.; Peck, W. F.; Brown, W. L.; Augustyniak, W. M., *Phys. Rev. B* **1982**, *25*, 7242.
29. Kotz, E. R.; Neff, H.; Stucki, S., *J. Electrochem. Soc.* **1984**, *131*, 72.
30. Mo, Y.; Stefan, I. C.; Cai, W.-B.; Dong, J.; Carey, P.; Scherson, D. A., *J. Phys. Chem. B* **2002**, *106*, 3681.
31. Lengeler, B.; Hippert, F., *Extended X-ray Absorption Fine Structure in Neutron and X-ray Spectroscopy*. Eds.: F. Hippert *et al*; Springer, Dordrecht: 2006; pp 131.
32. Binsted, N., EXCURV98 Manual,  
<http://www.srs.dl.ac.uk/xrs/Computing/Programs/excurv97/e61.htm>.
33. Mosselmans, J. F. W., A Guide to EXCURV98,  
<http://srs.dl.ac.uk/XRS/Computing/Programs/excurv97/excurv98guide.htm>.
34. Moulder, J. F.; Stickle, W. F.; Sobol, P. E.; Bomben, K. D., *Handbook of X-ray Photoelectron Spectroscopy*. Ed.: J. Chastain; Perkin-Elmer Corporation, Eden Prairie, MN, USA: 1992.
35. <http://physics.nist.gov/PhysRefData/XrayMassCoef/chap2.html>
36. Riley A.E., Tolbert S.H., *J. Am. Chem. Soc.*, **2003**, *125*, 4551.

# CHAPTER V

## PHOSPHOMOLYBDATE KEGGIN ANION ( $\text{PMo}_{12}\text{O}_{40}$ )<sup>3-</sup> / POLYPYRROLE HYBRID MODIFIED ELECTRODE

### 5.1 Introduction

The term polyoxometallate (POM) is applied to a very large group of typically anionic clusters composed of close packed frameworks of transition metal oxyanions, interconnected by shared oxide anions and surrounding a central atom (main group element as B, Ge, Si, P). Transition metals forming metal-oxygen frameworks are usually from group 5 and group 6 of the periodic table and in high oxidation states ( $d^0$  and  $d^1$  configurations, e.g. Mo(VI), W(VI), V(V)). The special feature of POMs is the high number of central atoms. The most frequent metal coordination is octahedral but tetrahedrons, square pyramids and pentagonal bipyramids are other common environments. The polyhedra are frequently fused, sharing vertices, edges or having common faces, and different oxide sharing arrangements can be present in the same compound.<sup>1</sup> The first account of polyoxometallates appeared in 1826.<sup>2</sup> It was a report by the Swedish chemist J. J. Berzelius, who described a yellow precipitate produced upon addition of an excess of ammonium molybdate to phosphoric acid. Today it is

known as  $(\text{NH}_4)_3[\text{PMo}_{12}\text{O}_{40}]$  with so-called 12:1 composition, but it took 38 years until the analytical composition of this class of heteropoly species was precisely determined.<sup>2</sup> It took a lot of time and study before the crystal structure of the compound was finally solved by Keggin in 1933,<sup>3</sup> and is generally known as the Keggin structure. In the period following this discovery other fundamental structures were described (e.g. Wells-Dawson or Lindqvist ion). From that time hundreds of POMs has been reported,<sup>2</sup> and the introduction of techniques such as single crystal X-ray diffraction allowed researchers to solve a vast number of structures.

POMs are a class of inorganic compounds with a wide diversity of sizes, structures and elemental compositions leading to a range of interesting properties. Therefore they find diverse applications, with many reported potential applications:<sup>4</sup> analytical chemistry,<sup>5,6</sup> catalysis,<sup>7-9</sup> biology<sup>10,11</sup> and medicine,<sup>12</sup> geochemistry,<sup>13</sup> materials science<sup>14</sup> or topology. Some POMs with transition metal atoms have unusual magnetic properties with possible application in computer nano storage devices.<sup>15,16</sup> “Green” applications have been reported as water decontamination<sup>7,17</sup> or a non-chlorine wood pulp bleaching.<sup>18</sup> Nanoporous polyoxomolybdate based capsules were reported to be introduced into the vesicles and chemistry was done inside the pores and cavities.<sup>2</sup> Examples of POMs are shown in Figure 5.2.

Sometimes a heteropolyanion (HPA) is distinguished as a category of POMs. Heteropolyanions are described as those polyanions and their derivatives made of a congregation of fused  $\text{MO}_6$  octahedra enfolding a tetrahedron containing a main group element or (less often) a transition metal.<sup>1</sup>

Heteropolyanions studied in this thesis belong to the family of Keggin anions, one of the most commonly studied classes of HPAs. Their general formula is  $[\text{XM}_{12}\text{O}_{40}]^{n-}$ , X = P, M = Mo and the value of  $n$  reflects the oxidation state of metal atoms. The schematic structure of a Keggin ion is shown in Figure 5.1.<sup>19</sup> These ions have attracted considerable interest for their (electro)catalytic properties (for example nitrite<sup>20,21</sup> or bromate<sup>22</sup> reduction, hydrogen peroxide detection,<sup>23,24</sup> and cation sensing<sup>25</sup>). The electronic and (with Fe substitution) magnetic properties of these materials have been explored theoretically.<sup>26</sup> Experimentally, the detailed structure of the polytungstate  $[\text{PW}_{12}\text{O}_{40}]^{3-}$  and analogues in which one of the tungsten atoms was removed or replaced

by iron or ruthenium has been the subject of a recent EXAFS study.<sup>27</sup> The spectroscopic data show that in some cases, although the basic Keggin anion structure is retained, the finer details of the structure respond both to metal atom substitution and to the environment in which the ion resides (e.g. solid *vs.* solution). This raises the question about the structure and behaviour of the ions when immobilised in the matrix of a polymer film, such as polypyrrole.<sup>28</sup> This kind of a gel-like environment, comprising characteristics of both a solution and a solid, is attractive for practical applications.<sup>20,21,23-25,29</sup>

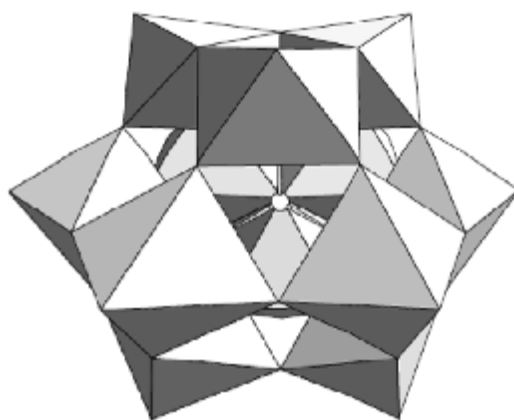


**Figure 5.1.** Structure of the Keggin heteropolyanion  $\text{PMo}_{12}\text{O}_{40}^{3-}$ . It consists of a central  $\text{PO}_4$  tetrahedron surrounded by 12  $\text{MoO}_6$  octahedra.<sup>19</sup>

There are two main methods of preparation of such composite films. The first one is based on charge-balance entrapment during the process of electrochemical deposition of the polymer. Another method is covalent attachment of desired molecules to the polymer film. The insertion of heteropolyanions significantly improves electrocatalytic<sup>30,31</sup> and catalytic<sup>32</sup> properties of the hybrid material because of chemical interaction with the host material and dispersion of anions.<sup>33</sup>

Electronically conducting polymers are extensively conjugated monomer units possessing a band-like electronic structure. These bands are formed because of splitting of molecular orbitals as in the band structure model in solid-state semiconductors. Conjugated polymers are insulators in their neutral state. The band gap is large and the number of charge carriers is small in ambient conditions. It is generally agreed that the

main factor influencing conductivity in CP is doping, and the mechanism of conductivity is based on the motion of charged defects within the conjugated framework. Upon creation of such defects (chemically or electrochemically) in the process of oxidation (p-doping) or reduction (n-doping) the increase of conductivity of CP is possible even of a few orders of magnitude.

Oxidation of the polymer chain generates a radical cation possessing both spin and charge. This defect, called a polaron, is composed of a hole and accompanying structural distortion. The cation and the radical form a bound species.

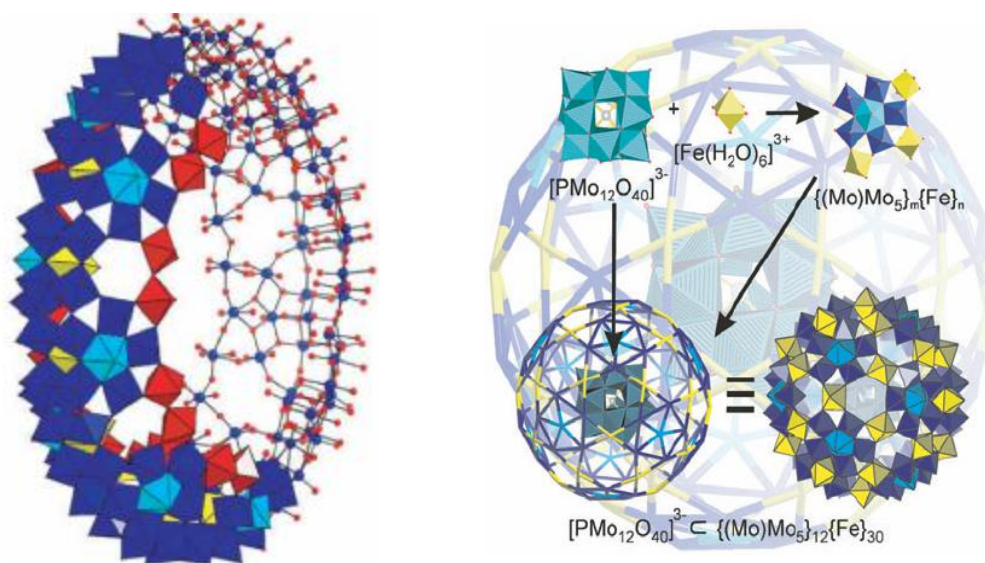


**Figure 5.2.** Example structures of polyoxometallates. Left: the Bielefeld “wheel” contains 154 Mo atoms – half with polyhedral representation with different building units ( $Mo_8$  blue,  $Mo_2$  red,  $Mo_1$  yellow), and half in ball and stick representation (Mo blue, O red).<sup>2,34</sup> Right: reaction scheme of Keggin anions with  $Fe^{III}$  ions. Fragments of the type  $\{(Mo)Mo_5\}_m\{Fe\}_n$  are generated and function as building blocks in the formation of  $\{(Mo)Mo_5\}_{12}\{Fe\}_{30}$  type cages. The remaining Keggin anions are encapsulated. The background highlights the host-guest composite obtained.<sup>2,35</sup>

A pair of two close-by polarons may combine to create a lower energy electronic structure, the more stable bipolaron. A polaron and a bipolaron in a polypyrrole (Ppy) film are shown in Figure 5.3. Migration of these is possible in either direction of the backbone of the polymer and the number and mobility of charge carriers determine the

conductivity of the CP. A typical cyclic voltammogram of such an electronically conducting polymer is a broad non-Nernstian wave.

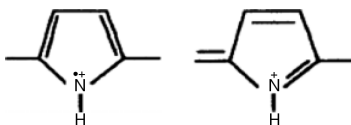


**Figure 5.3.** Polaron (left) and bipolaron (right) present in polypyrrole structure.<sup>19</sup>

Electrodes modified with electroactive conducting polymers are of great interest. In the group of conducting polymers, polypyrrole is one of the most extensively studied. It can be obtained by anodic oxidation of the monomer in the solution. Because in this manner it is formed in its oxidized state the anions are trapped into the polymer matrix, this leads to the formation of an organic-inorganic hybrid material with both components electroactive.

Upon electrochemical cycling conducting polymer electrodes such as Ppy doped with simple anions ( $\text{ClO}_4$ ,  $\text{BF}_4$ ) undergo reversible process of anion deintercalation.<sup>36</sup> In contrast to these, the behaviour of phosphomolybdate anion  $[\text{P}(\text{Mo}_3\text{O}_{10})_4]^{3-}$  is not mobile and remains an integrated part of the composite material. This retention of phosphomolybdate anions is probably due to their large size and high charge.<sup>37,38</sup> A schematic presentation of such composite polypyrrole/ $[\text{P}(\text{Mo}_3\text{O}_{10})_4]^{3-}$  film is shown in Figure 5.4.

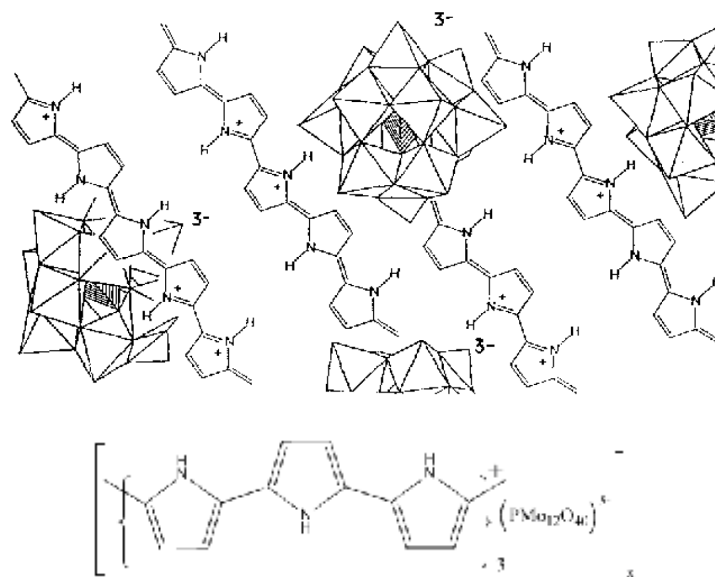


**Figure 5.4.** Schematic representation of the hybrid material composed of polypyrrole and the phosphomolybdate anion;  $[\{C_4H_5N\}_9(PMo_{12}O_{40})^{3-}]_n$ .<sup>38,39</sup>

## 5.2 Objectives

The general objective was determination of the local environments around the molybdenum atoms in the composite films, as represented by bond lengths and coordination numbers. Specific issues pursued for the polypyrrole/ $(PMo_{12}O_{40})^{3-}$  hybrid film were the variation of metal local environment (adjustment in anion structure) under systematically varied redox state conditions (i.e. film charge state) and how the charge is distributed between the metal atoms. The multi-atom nature of the Keggin ions results in a rich electrochemical response with multiple redox processes readily observable, but the distributions of electrons undefined.

The overall aim of following the dynamics of structural changes accompanying redox state changes in electroactive films can be achieved only with high quality signal-to-noise EXAFS spectra. The challenge was to have enough material exposed to the X-ray beam, but without the accompanying problems of slow charge transport across a thick – in electrochemical terms – film with slow diffusion-like charge “hopping” between redox sites. The way to do this was passing the responsibility for charge transport from the redox sites to a conducting polymer matrix. At the same time the EXAFS signal

would not be obscured as the “CHN” nature makes it relatively transparent to the X-ray beam. Hence, dispersing the redox active species in a conducting polymer allows one to prepare a film of necessary thickness to generate a satisfactory EXAFS signal and still address the sites electrochemically on a conveniently short time scale, yielding well-defined responses.

The positively charged (p-doped state) polypyrrole film irreversibly encapsulates the polyoxometallate anion to satisfy electroneutrality,<sup>23,25,28</sup> and the redox potentials are such that all the anion-related changes will take place with the polypyrrole matrix in the conducting p-doped state. There is a question about the detailed structure of the ions when immobilized within a polymer film such a polypyrrole,<sup>28</sup> Figure 5.4. Such a gel-like environment is very attractive for practical applications<sup>20,21,23-25</sup> and combines characteristics of both a solution and a solid. Earlier studies provided  $i-E$  curves, but did not provide any structural insight into the underlying molecular functionality.

## 5.3 Experimental

### 5.3.1 Experimental Measurements

The polypyrrole/phosphomolybdate anion (Ppy/[P(Mo<sub>3</sub>O<sub>10</sub>)<sub>4</sub>]<sup>3-</sup>) organic-inorganic composite films described in this thesis were prepared electrochemically from acidic solutions, as there are reports on instability and decomposition of this class of compounds at neutral and alkaline pH values.<sup>40,41</sup>

Electrochemical synthesis of the films was carried out at room temperature in quiescent solutions. Films were deposited by multiple cycling using a Pt disc as a working electrode. At first 0.091 g of phosphomolybdic acid hydrate (H<sub>3</sub>[P(Mo<sub>3</sub>O<sub>10</sub>)<sub>4</sub>] · xH<sub>2</sub>O, Riedel-de Haën) was dissolved in 5 ml of 0.5 M sulphuric acid (H<sub>2</sub>SO<sub>4</sub>, 97.5 %+, Aldrich) and mixed with a solution of 70 μl of pyrrole (C<sub>4</sub>H<sub>5</sub>N, 98 % Aldrich) in 5 ml of 0.5 M sulphuric acid. Deionised water was used to prepare solutions. The mixture turns almost instantly from yellowish to dark blue due to the partial oxidation of pyrrole by the phosphomolybdate.<sup>38</sup> The complete oxidative polymerization was carried out by repeated cyclic potential scans, typically from +0.5 V to +0.8 V at a scan rate of 2 mV s<sup>-1</sup>

<sup>1</sup>. A SCE reference electrode was used for electrochemical characterization and XPS experiments and an Ag/AgCl sat'd KCl electrode was used as reference electrode for samples for EXAFS experiments. A Pt mesh was used as a counter electrode.

The thickness of the film was controlled by the number of voltammetric scans and scan rate, and films of a thickness of a few hundreds of microns can be easily electrodeposited. After the deposition, films were rinsed with 0.5 M sulphuric acid and transferred into the 0.5 M sulphuric acid background electrolyte for the cyclic voltammetry.  $\text{H}_3[\text{P}(\text{Mo}_3\text{O}_{10})_4] \cdot x\text{H}_2\text{O}$  was diluted in order to avoid direct chemical polymerization.<sup>41</sup>

### 5.3.2 X-ray Photoelectron Spectroscopy

For all XPS experiments Ppy/[ $\text{P}(\text{Mo}_3\text{O}_{10})_4$ ]<sup>3-</sup> films were prepared at University of Leicester as described in the introduction to this chapter. Samples were prepared 1-2 days in advance and transported in sealed containers to the NCESS facility at Daresbury Laboratory. They were cycled in 0.5 M  $\text{H}_2\text{SO}_4$  background electrolyte prior to the XPS measurement in the following pattern: each film was cycled 3 times at 1  $\text{mV s}^{-1}$  scan rate. The working modified electrode was then kept at a selected potential for circa 30 minutes. In the next step the electrode was disconnected and rinsed thoroughly with deionised water and purged with  $\text{N}_2$ , dried (high pressure inert gas spray-dry) and placed in the vacuum chamber as fast as possible to minimise contact with the oxidative environment of air. SCE was used as a reference electrode, Pt mesh as a counter electrode, and Pt discs (Goodfellow) as working electrodes. The CasaXPS program available on site was used for XPS data analysis. All described procedures were carried out at room temperature.

### 5.3.3 Extended X-ray Absorption Fine Structure Measurements

EXAFS experiments on Ppy/[ $\text{P}(\text{Mo}_3\text{O}_{10})_4$ ]<sup>3-</sup> films were carried out *in situ* in fluorescence and transmission modes at station 16.5 at Daresbury Laboratory. The electrode was placed at an angle of 45° with respect to the fluorescence detector. Station 16.5 is equipped with a 30-element Ge solid-state detector with high count-rate

electronics of 200 kHz per channel, pre-mirror providing collimation and double crystal monochromator with sagittal focus up to 27 keV. Spectra were measured at the Mo K-edge at 20,000 eV. A purpose-built in situ spectroelectrochemical EXAFS cell utilised in this experiment was described in Chapter II. EXAFS spectra were measured for Keggin anion in polypyrrole matrix modified electrodes and a set of reference Mo standards: molybdenum foil, molybdenum(VI) tetrachloride oxide ( $\text{MoOCl}_4$ , Aldrich) and molybdenum(V) chloride ( $\text{MoCl}_5$ , Aldrich) as 25 mM aqueous solutions and molybdenum(IV) oxide ( $\text{MoO}_2$ , 99%, Aldrich) as a fine powder distributed evenly on self-adhesive tape. For EXAFS experiments 0.75  $\mu\text{m}$  Pt foil supported by permanent polyester (Goodfellow) working electrodes were used to enable data acquisition in fluorescence and transmission modes.

The summary of methods and potentials used is presented in Table 5.1.

Method	Potential (V)
EXAFS	Mo K-edge -0.3, +0.2, +0.3, +0.5
XPS	Mo 3d -0.2, -0.1, +0.1, +0.3, +0.5 Mo 3p

**Table 5.1.** Summary of potentials at which data were collected for EXAFS and XPS experiments for polypyrrole/phosphomolybdate anion ( $\text{Ppy}/[\text{P}(\text{Mo}_3\text{O}_{10})_4]^{3-}$ ) hybrid film modified electrode. Potential *vs.* Ag/AgCl sat'd KCl (EXAFS) and *vs.* SCE (XPS).

In order to investigate any instability of the phosphomolybdic anion in non-acidic solutions XANES of the 25 mM solutions of acid hydrate ( $\text{H}_3[\text{P}(\text{Mo}_3\text{O}_{10})_4] \cdot x\text{H}_2\text{O}$ ) in 0.3 M sodium carbonate ( $\text{Na}_2\text{CO}_3$ , BDH), deionised water and 0.5 M sulphuric acid was acquired.

## 5.4 Data Analysis

EXAFS spectra were summed, calibrated and background subtracted using the standard Daresbury programs EXCALIB and EXBACK. Resulting data were fitted using EXCURV98. All these procedures were described in previous chapters. Spectra were fitted out to an electron wave vector  $k = 12 \text{ \AA}^{-1}$ . An amplitude factor AFAC of the value

of 0.9 was used. This factor is related to the proportion of electrons which undergo EXAFS type scattering on absorption. In EXCURV98 it should normally be left at 1.0, unless one believes the spectrum suffers from an amplitude damping effect.<sup>42</sup> The coordination numbers for data fitting were set as integer values to obtain the best fits. Five shell contributions can be seen in the Fourier transforms of the data and the fit indices show that all of them are contributing to the spectra. The final values obtained from the data fitting were interatomic distances for the first five coordination spheres (i.e. first three Mo—O and two more distant Mo—Mo shells) and Debye-Waller factors. Edge positions and edge shifts were obtained from XANES data analysis. The numbers of molybdenum sites in the electroactive films and in reference solutions were calculated from the XAS data according to the procedure described in Chapter II.

Literature values of the position of spectral lines were taken from <http://srdata.nist.gov/> website database and Handbook of X-ray Photoelectron Spectroscopy<sup>43</sup> if not stated otherwise. XPS data was fitted using the program Unifit.

## 5.5 Results and Discussion

### 5.5.1 Cyclic Voltammetry

Electrodeposition of the polypyrrole/phosphomolybdate anion ( $\text{Ppy}/[\text{P}(\text{Mo}_3\text{O}_{10})_4]^{3-}$ ) hybrid film onto the polyester supported platinum electrode is shown at Figure 5.5. The film was deposited in 10 cyclic voltammetric scans at potentials in the range from +0.5 V to +0.8 V vs. Ag/AgCl (sat'd KCl) at a scan rate of  $10 \text{ mV s}^{-1}$ . Lower potentials were avoided during the deposition to retain as much phosphomolybdate as possible and avoid their expulsion from the reduced polypyrrole matrix. The current increases in a regular manner with each deposition scan, signifying accommodation of the film on the electrode surface.

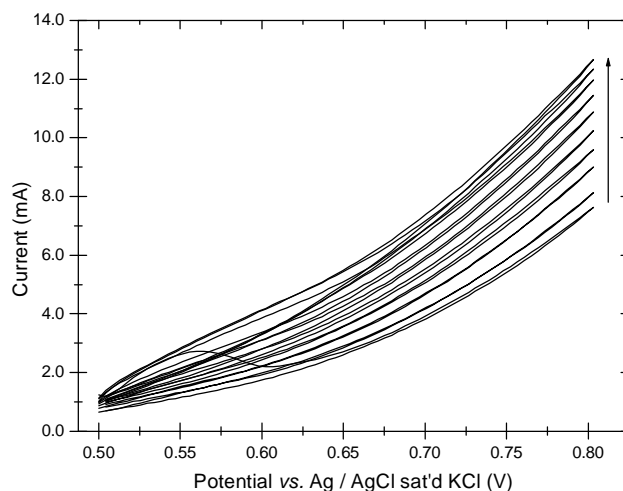


**Figure 5.5.** Electrodeposition of polypyrrole/phosphomolybdate anion ( $\text{Ppy}/[\text{P}(\text{Mo}_3\text{O}_{10})_4]^{3-}$ ) hybrid film on the Pt foil supported by permanent polyester electrode; 10 cycles were used at the potentials in the range from +0.5 V to +0.8 V vs. Ag/AgCl (sat'd KCl). Scan rate:  $10 \text{ mV s}^{-1}$ .

A typical cyclic voltammogram of the hybrid material  $\text{Ppy}/[\text{P}(\text{Mo}_3\text{O}_{10})_4]^{3-}$  modified electrode is presented in the Figure 5.6. The background electrolyte was 0.5 M  $\text{H}_2\text{SO}_4$ . There are three peaks visible in the CV, at -0.06 V, +0.19 V and +0.34 V vs. Ag/AgCl (sat'd KCl) reference electrode. These reduction and oxidation peaks correspond to redox processes in the  $\text{P}(\text{Mo}_3\text{O}_{10})_4$  anion through two-, four- and six-electron processes, respectively.<sup>24</sup> The cyclic voltammetric response of  $[\text{P}(\text{Mo}_3\text{O}_{10})_4]^{3-}$  is obscured by the broad current response of the polypyrrole matrix.

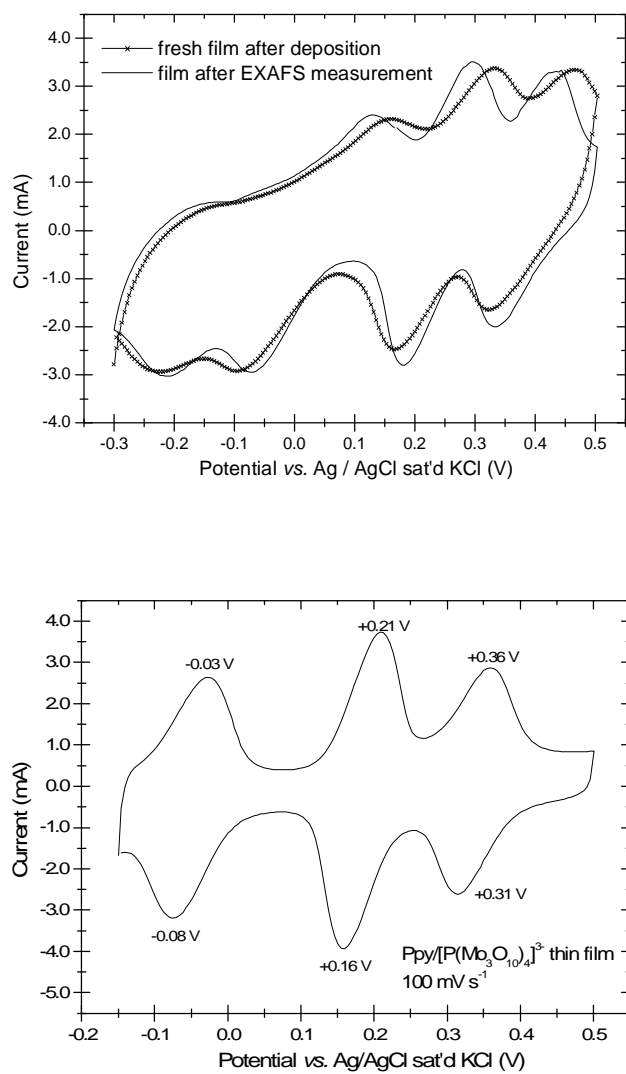


**Figure 5.6.** Top: typical cyclic voltammogram of Pt foil electrode modified with Polypyrrole/phosphomolybdate anion ( $\text{Ppy}/[\text{P}(\text{Mo}_3\text{O}_{10})_4]^{3-}$ ) hybrid film. CVs were acquired for the freshly deposited film ( $-\times-$ ) and for the film after the EXAFS experiment ( $---$ ). In this case EXAFS was measured for the film kept at +0.17 V vs. Ag/AgCl sat'd KCl electrode. EXAFS data acquisition time: circa 6 hours. Scan rate  $2 \text{ mV s}^{-1}$ . Bottom: CV of a thin hybrid film deposited on the Pt disc electrode,  $100 \text{ mV s}^{-1}$ . All CVs were measured in  $0.5 \text{ M H}_2\text{SO}_4$  background electrolyte.

The bottom CV in Figure 5.6 shows the response of a relatively thin composite film acquired in a standard electrochemical cell. The peaks are better defined than for the thick film displayed in the upper graph. For the film in the upper graph the CV was

done in the EXAFS electrochemical cell whose geometry is optimal for the EXAFS (rather than electrochemical) experiment.

There are two overlying scans shown in the top picture in Figure 5.6: CV of the freshly electrodeposited film and CV of the film after EXAFS data acquisition of about 6 hours. It is significant that there is no decay or any change in the signal which could be evidence of change of the structure or properties of the material. After an extended period of time in the background electrolyte the signal appears to be sharper and the peaks are better defined. These effects could be due to two factors. First the freshly deposited film may be thicker than the film kept for a long time in the solution and in the X-ray beam. Secondly it is possible that the polymer matrix “opens” over a time and the access to electroactive molybdenum sites is better, hence the voltammogram peaks are sharper but of the same magnitude.

### 5.5.2 X-ray Photoelectron Spectroscopy

X-ray photoelectron spectra of Ppy/[P(Mo<sub>3</sub>O<sub>10</sub>)<sub>4</sub>]<sup>3-</sup> composite modified electrodes were acquired for following elements: Mo 3d, Mo 3p, O 1s, C 1s, N 1s, P 2p, S 2p, Pt 4f. A wide-range survey scan for a composite film is shown in Figure 5.7.

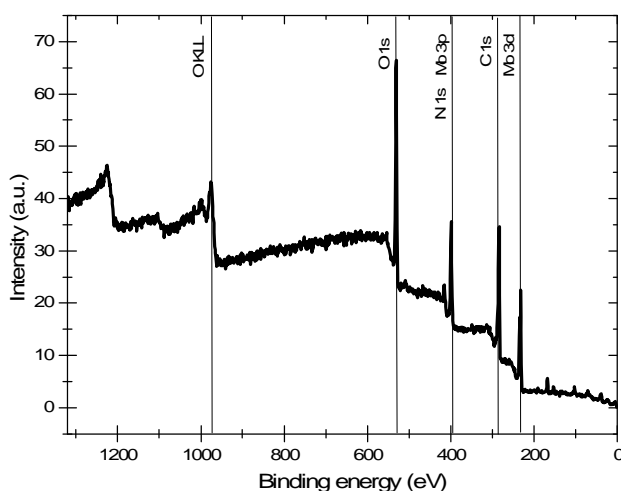


**Figure 5.7.** XPS wide-range survey scan acquired for freshly electrodeposited Ppy/[P(Mo<sub>3</sub>O<sub>10</sub>)<sub>4</sub>]<sup>3-</sup> composite film. Binding energy (eV) increases from right to left side of the graph. Positions of the XPS lines of the main elements present in the sample are shown in the graph.

As an example, for the modified composite Ppy/[P(Mo<sub>3</sub>O<sub>10</sub>)<sub>4</sub>]<sup>3-</sup> electrode emerged from the background electrolyte at a potential of -0.2 V *vs.* SCE three XPS lines are shown (Mo 3p, C 1s and O 1s) in Figures 5.8 - 5.10, and discussed below.

Two XPS lines, namely Mo 3p<sub>3/2</sub> and N 1s are merged. Therefore in the deconvoluted envelope of Figure 5.8 a several components can be identified. Apart from Mo 3p<sub>3/2</sub> contribution at 396.7 eV (Mo<sup>5+</sup>) and 398.1 eV (Mo<sup>6+</sup>) to the XPS line in the range of 390 - 400 eV, neutral N belonging to the pyrrole ring (—NH—) is visible at 400.0 eV.<sup>19,44,45</sup> Positively charged (doped) N in the form of polaron (—NH<sup>•+</sup>—) and bipolaron (=N<sup>+</sup>—) are present at 401.3 eV and 402.5 eV respectively.

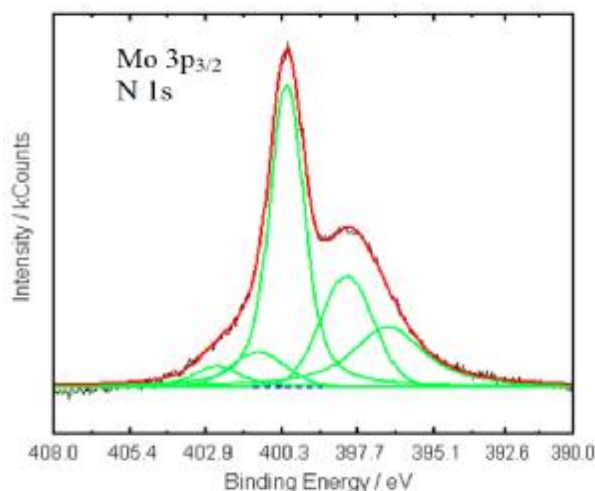


**Figure 5.8.** Mo 3p<sub>3/2</sub> and N 1s deconvoluted XPS photoelectron lines for the sample emerged at -0.2 V *vs.* SCE. Binding energies are close to each other and spectra merge. Moreover, there are multiple contributions to each line: Mo<sup>5+</sup> at 396.7 eV, Mo<sup>6+</sup> at 398.1 eV and to N 1s line at 400.1 eV (—NH— in polypyrrole ring), 401.1 eV (—NH<sup>•+</sup> in polaron) and 402.5 eV (=N<sup>+</sup> in bipolaron).

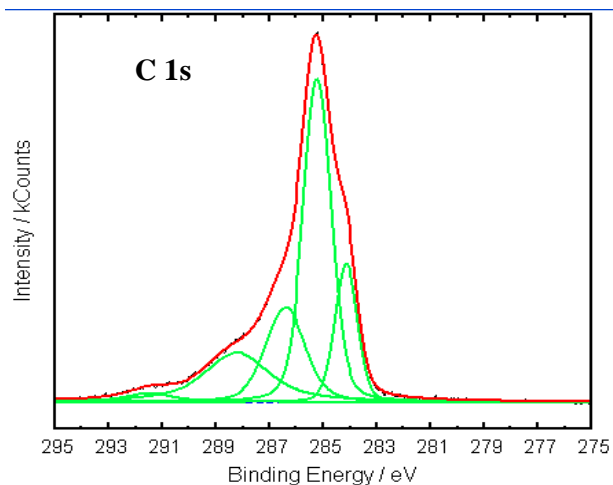


**Figure 5.9.** C 1s deconvoluted XPS photoelectron line for the sample emersed at  $-0.2$  V vs. SCE. The main contribution at BE of 285.2 eV belong to C—C and C=C in Ppy ring. Line at 286.4 eV can belong to C—OH, C=N or C—NH<sup>•+</sup> or a mix of both, 288.2 eV is due to C=O or/and —C=N<sup>+</sup> (bipolaron) and feature at 291.5 eV to  $\pi$ — $\pi$  satellite in aromatic polypyrrole. Line at BE of 284.1 eV can be Mo—C interaction but more probably it is C in Ppy matrix.

Figure 5.9 shows an example of the deconvoluted C 1s XPS photoelectron line. This line was fitted with five contributions. The main carbon contribution here at a binding energy of 285.2 eV is C—C and C=C in polypyrrole. Other possible contributions to the carbon photoelectron line are at 286.4 eV which can be attributed to C—OH, C=N or C—NH<sup>•+</sup> or a mixture of them. The peak at a binding energy of 288.2 eV is assigned to C=O or/and —C=N<sup>+</sup> and small feature at 291.5 eV to a  $\pi$ — $\pi$  satellite in aromatic polypyrrole. The XPS line at a binding energy of 284.1 eV suggests Mo—C interaction, but it could also be carbon in polypyrrole matrix.

As shown in Figure 5.10, three peaks comprise for the O 1s line. They are most probably evidence of O—Mo—O at a binding energy of 530.8 eV and of Mo—OH at a binding energy of 531.8 eV. The line at a binding energy of 533.2 eV corresponds to oxygen in the molecular water of solvation present in the film.

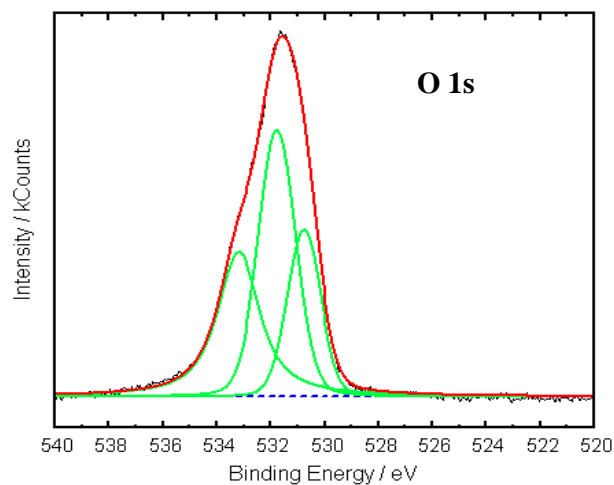


**Figure 5.10.** O 1s deconvoluted XPS photoelectron line. Electrode emersed at  $-0.2$  V vs. SCE. Peak at a BE of 530.8 eV and 531.8 eV belong to O—Mo—O and Mo—OH, respectively. The line at a BE at 533.2 eV corresponds to oxygen in H<sub>2</sub>O bound in the film.

As the electrode modified with the Ppy/[P(Mo<sub>3</sub>O<sub>10</sub>)<sub>4</sub>]<sup>3-</sup> composite is redox cycled, the site changing oxidation state is molybdenum. Figure 5.11 (a)-(e) shows Mo d<sub>3/2</sub> and Mo d<sub>5/2</sub> XPS lines at a function of potential. The distance between the two maxima for the d<sub>3/2</sub> and d<sub>5/2</sub> features is relatively small, circa 3 eV. Therefore not only Mo<sup>5+</sup> and Mo<sup>6+</sup> lines merge but also both lines belonging to the doublet. It can be seen in the plots that with the gradually increasing potential from  $-0.2$  V to  $+0.5$  V the peak belonging to Mo<sup>5+</sup> becomes less significant.

The oxidative influence of air during the transport of the sample from the electrochemical cell to the vacuum chamber should not be too significant, as the Mo HPAs are entrapped in the polymer matrix, but for some reason there is surprisingly high amount of Mo<sup>6+</sup> at the most reductive potential of  $-0.2$  V.

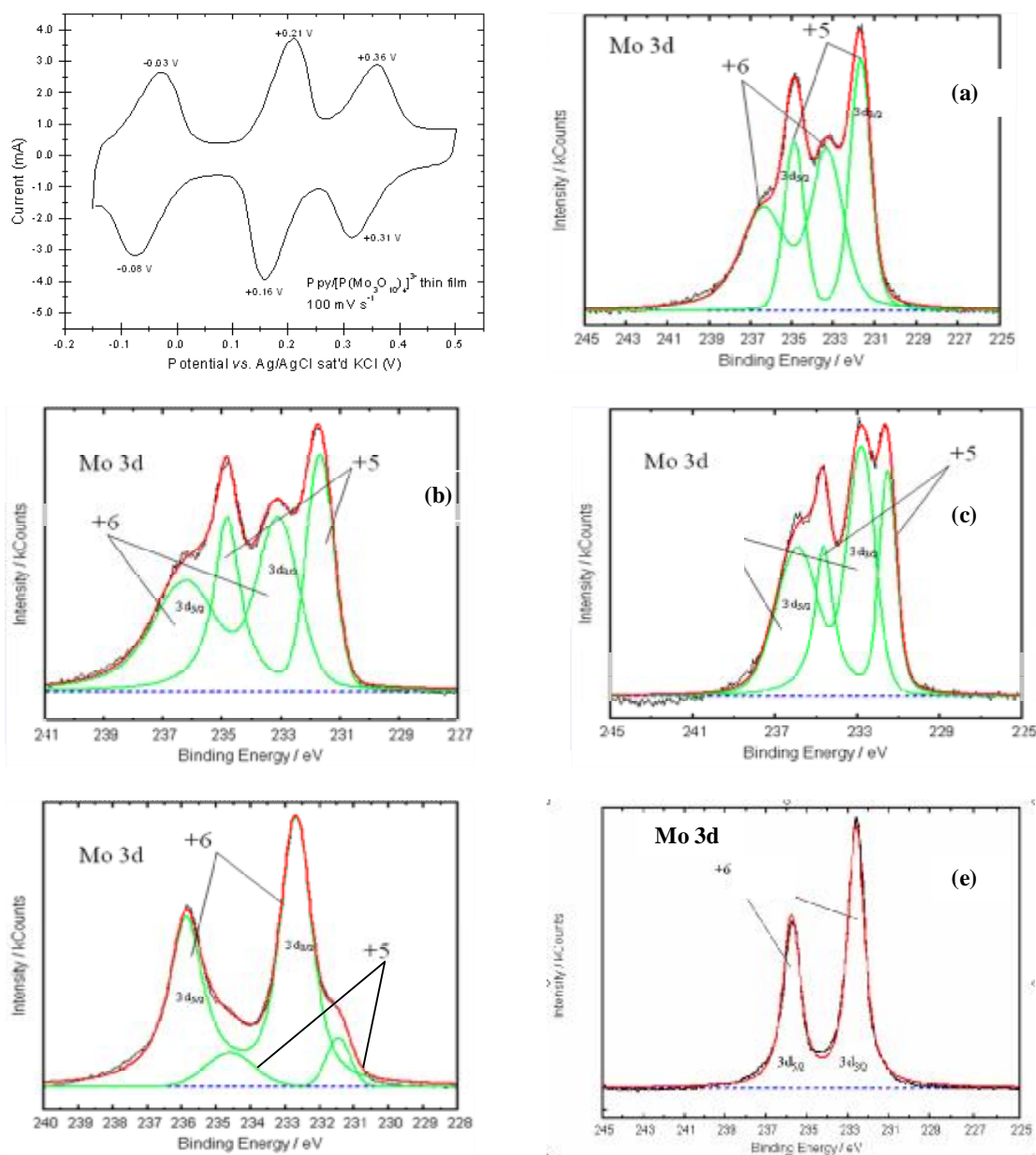


**Figure 5.11.** Mo 3d<sub>5/2</sub> and Mo 3d<sub>3/2</sub> XPS electron line in Ppy/[P(Mo<sub>3</sub>O<sub>10</sub>)<sub>4</sub>]<sup>3-</sup> composite film at different oxidation states: -0.2 V (a), -0.1 (b), +0.1 (c), +0.3 (d) and +0.5 (e) vs. SCE. The cyclic voltammogram illustrates points/potentials at which the electrode was emerged from the 0.5 M H<sub>2</sub>SO<sub>4</sub> background electrolyte.

Some groups report reduction of Mo<sup>6+</sup> to Mo<sup>5+</sup> in SiMo<sub>12</sub>O<sub>40</sub><sup>4-</sup>/polypyrrole composite under the X-ray beam.<sup>19,46</sup> Other research groups observed also that when the redox

reaction was carried out in air the reduced  $[\text{P}(\text{Mo}_3\text{O}_{10})_4]^{3-}$  anion was easily reoxidized by molecular oxygen.<sup>38,47</sup>

### 5.5.3 X-ray Absorption Fine Structure Measurements

EXAFS experiments of Ppy/ $[\text{P}(\text{Mo}_3\text{O}_{10})_4]^{3-}$  composite film modified electrodes were carried out *in situ* at station 16.5 at SRS at Daresbury Laboratory in fluorescence and transmission mode detection. Spectra were measured at the Mo K-edge at 20,000 eV.

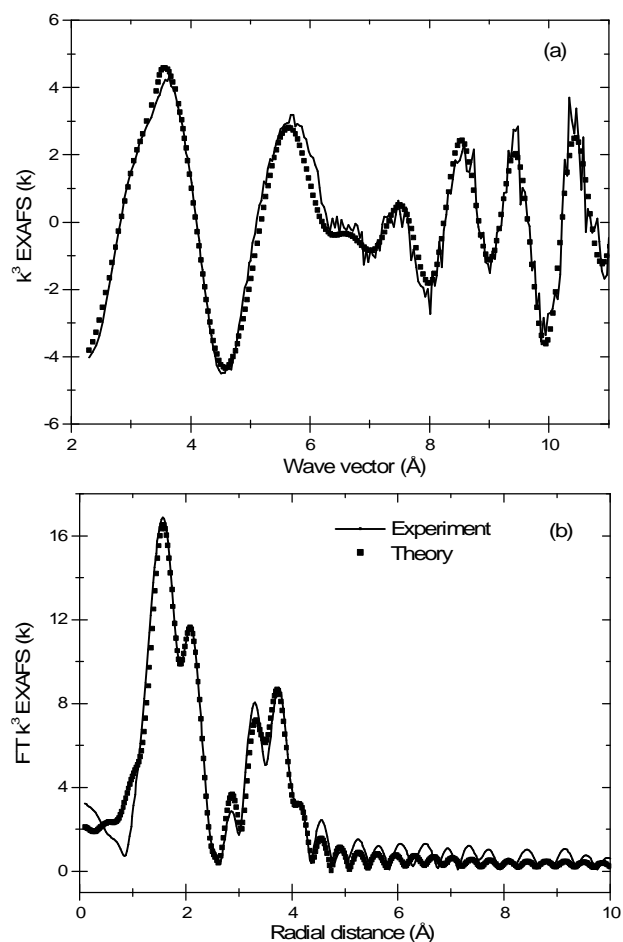


**Figure 5.12.** Measured *in situ*  $k^3$  weighted EXAFS spectrum with fit (a) and corresponding fitted Fourier transforms (b) for Ppy/ $[\text{P}(\text{Mo}_3\text{O}_{10})_4]^{3-}$  hybrid film modified electrode at the potential of -0.3 V vs. Ag/AgCl sat'd KCl. Background electrolyte: 0.5 M  $\text{H}_2\text{SO}_4$ . Experimental data (—) and theoretical EXCURV98 data fit (\*).

A purpose-built in situ spectroelectrochemical EXAFS cell utilised in this experiment was described in Chapter II. Typical  $k^3$  weighted fits to the EXAFS data for Ppy/[P(Mo<sub>3</sub>O<sub>10</sub>)<sub>4</sub>]<sup>3-</sup> hybrid film modified electrode are shown together with their corresponding Fourier transform in Figure 5.12. In the Fourier transform there are clearly visible 5 coordination shells. These was evidence and starting point for fitting Mo K-edge EXAFS data for five shells at distances of about 1.5 Å, 1.9 Å, 2.8 Å, 3.4 Å and 3.8 Å, *i.e.* at distances where peaks in FT are present.

Normalised Mo K-edge XANES of the Ppy/[P(Mo<sub>3</sub>O<sub>10</sub>)<sub>4</sub>]<sup>3-</sup> composite film modified electrode acquired *in situ* at four potentials (-0.3 V, +0.2 V, +0.3 V and +0.5 V vs. Ag/AgCl sat'd KCl) are presented in Figure 5.13 (for higher clarity no data for standards are plotted in this graph). Each of the spectra shows a broad peak (white line) but absorption edges for all samples are identical and there are no visible changes in the edge position or in the white line shapes.

In Figure 5.14 for comparison purpose XANES of Ppy/[P(Mo<sub>3</sub>O<sub>10</sub>)<sub>4</sub>]<sup>3-</sup> composite film modified electrode together with XANES of standards are shown. Standards include molybdenum at three different oxidation states: Mo<sup>5+</sup> in MoCl<sub>5</sub> and H<sub>3</sub>[P(Mo<sub>3</sub>O<sub>10</sub>)<sub>4</sub>], Mo<sup>6+</sup> in MoOCl<sub>4</sub> aqueous solutions and Mo<sup>4+</sup> in MoO<sub>2</sub> as a fine powder attached to self-adhesive tape. Very clearly white line position and shape are different for different Mo oxidation states in standard samples, but not for the ME at different potentials.

In the last graph showing XANES, Figure 5.15, there are three data sets for H<sub>3</sub>[P(Mo<sub>3</sub>O<sub>10</sub>)<sub>4</sub>] in solutions of different pH: alkaline solution (0.3 M Na<sub>2</sub>CO<sub>3</sub>, pH 10.7), acidic solution (0.5 M H<sub>2</sub>SO<sub>4</sub>) and distilled water solution (unbuffered, pH 7). These data were measured, because some authors claim that molybdenum Keggin ions are only stable in acidic environment, and undergo decomposition in alkaline or neutral pH solutions. In XANES data presented here no apparent change were observed for any of the solutions.

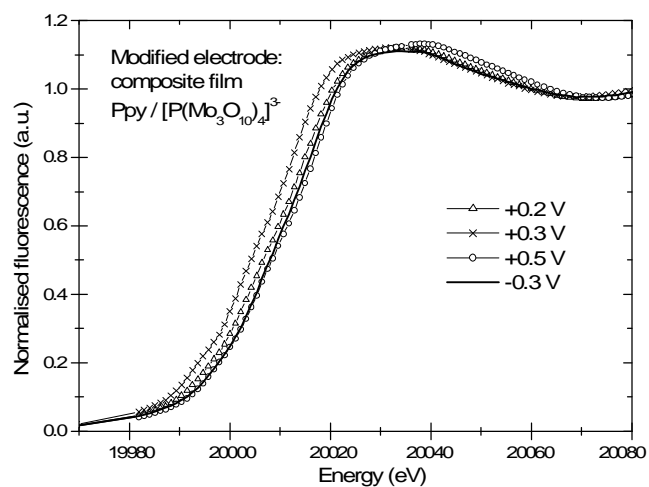


**Figure 5.13.** Normalised Mo K-edge XANES of Ppy/[P(Mo<sub>3</sub>O<sub>10</sub>)<sub>4</sub>]<sup>3-</sup> composite film modified electrode acquired in situ at -0.3 V, +0.2 V, +0.3 V and +0.5 V (vs. Ag/AgCl sat'd KCl) redox states. Background electrolyte: 0.5 M H<sub>2</sub>SO<sub>4</sub>.

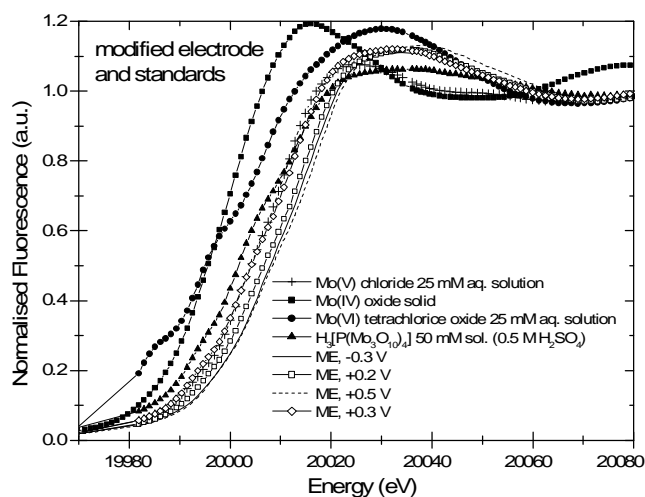


**Figure 5.14.** Normalised Mo K-edge XANES of standards (MoCl<sub>5</sub>, MoOCl<sub>4</sub> 25 mM aqueous solutions, H<sub>3</sub>[P(Mo<sub>3</sub>O<sub>10</sub>)<sub>4</sub>] 50 mM aqueous solution and MoO<sub>2</sub> fine powder on self-adhesive tape) and Ppy/[P(Mo<sub>3</sub>O<sub>10</sub>)<sub>4</sub>]<sup>3-</sup> composite film modified electrode acquired in situ at varying redox states. Background electrolyte: 0.5 M H<sub>2</sub>SO<sub>4</sub>.

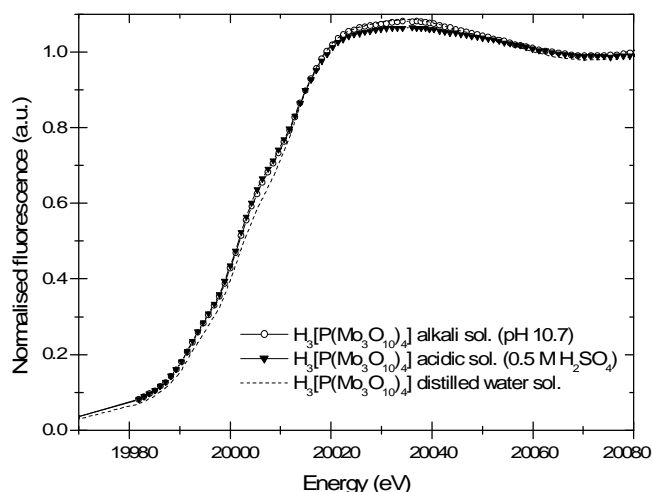


**Figure 5.15.** Normalised XANES acquired for Mo K-edge in solutions of  $\text{H}_3[\text{P}(\text{Mo}_3\text{O}_{10})_4]$  with 3 different values of pH: acidic (0.5 M  $\text{H}_2\text{SO}_4$ ), alkaline (0.3 M  $\text{Na}_2\text{CO}_3$ ) and neutral (deionised water). No change in XANES is visible for different pH of the solutions.

Sample	Element	R (Å)	N	$\sigma^2(10^{-4}\text{Å}^2)$	FI (%)	$\Delta E_0(\text{eV})$
molybdenum(IV) oxide, fine powder	O	1.73±0.03	<b>1</b>	90±40	8.3	3.8
	O	2.00±0.01	<b>5</b>	50±5		
	Mo	2.52±0.01	<b>1</b>	45±5		
	Mo	3.70	<b>6</b>	45±5		
	Mo	4.92±0.04	<b>4</b>	100±50		
molybdenum(VI) tetrachloride oxide, 25 mM aqueous solution	O	1.78	3.5±0.5	15±5	8.3	-0.7
molybdenum(V) chloride, 25 mM aqueous solution	O	1.69	2	100±20	17.8	-2.7
	O	2.01	3	140±25		
	Mo	2.54	2	80±10		
$\text{H}_3[\text{P}(\text{Mo}_3\text{O}_{10})_4]$ , 25 mM solution in 0.5 M $\text{H}_2\text{SO}_4$	O	1.70±0.01	<b>1</b>	50±10	17.2	-4.6
	O	1.94±0.02	<b>4</b>	330±45		
	O	2.32±0.04	<b>1</b>	110±50		
	Mo	3.44±0.02	<b>2</b>	90±20		
	Mo	3.70±0.02	<b>2</b>	85±20		

**Table 5.2.** Structural parameters for the nearest coordination shells derived from fits to Mo K-edge EXAFS spectra for standards:  $\text{Mo}^{4+}$  in  $\text{MoO}_2$  powder,  $\text{Mo}^{5+}$  in  $\text{MoCl}_5$  and  $\text{H}_3[\text{P}(\text{Mo}_3\text{O}_{10})_4]$  and  $\text{Mo}_{6+}$  in  $\text{MoOCl}_4$ . Data fitted up to the value of  $k_{max}=12$ . Bold coordination numbers N signify fixed values for data fitting. FI – fit index,  $\Delta E_0 \pm 5$  eV.

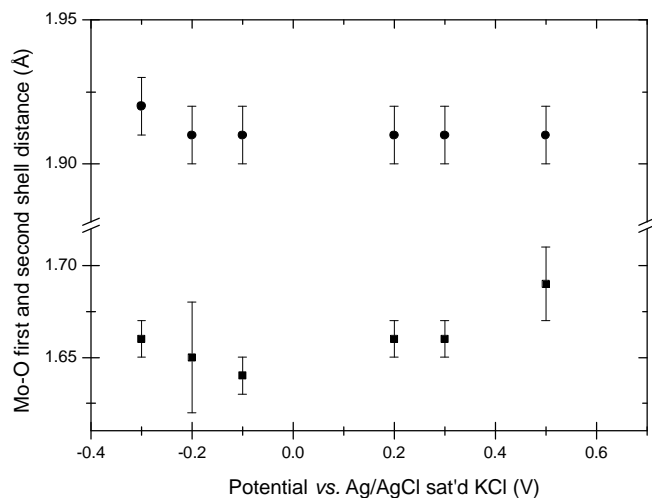
Sample	Element	R (Å)	N	$\sigma^2$ ( $10^{-4}$ Å <sup>2</sup> )	FI (%)	$\Delta E_0$ (eV)
<b>Ppy/[P(Mo<sub>3</sub>O<sub>10</sub>)<sub>4</sub>]<sup>3-</sup> modified electrode</b>						
-0.3 V	O	1.66 ± 0.01	1	40 ± 10	12.3	-7.9
	O	1.92 ± 0.01	4	140 ± 15		
	O	2.42 ± 0.12	1	40 ± 20		
	Mo	3.46 ± 0.01	2	90 ± 20		
	Mo	3.70 ± 0.02	2	60 ± 15		
-0.2 V	O	1.65 ± 0.03	1	30 ± 5	15.4	-4.8
	O	1.91 ± 0.01	4	160 ± 10		
	O	2.40 ± 0.10	1	70 ± 20		
	Mo	3.47 ± 0.01	2	60 ± 10		
	Mo	3.72 ± 0.02	2	70 ± 5		
-0.1 V	O	1.64 ± 0.01	1	20 ± 10	11.8	-4.6
	O	1.91 ± 0.01	4	150 ± 15		
	O	2.39 ± 0.10	1	30 ± 20		
	Mo	3.47 ± 0.01	2	90 ± 25		
	Mo	3.70 ± 0.01	2	55 ± 15		
+0.2 V	O	1.66 ± 0.01	1	25 ± 5	9.1	-7.0
	O	1.91 ± 0.01	4	130 ± 10		
	O	2.34 ± 0.04	1	100 ± 35		
	Mo	3.45 ± 0.01	2	80 ± 15		
	Mo	3.70 ± 0.01	2	55 ± 10		
+0.3 V	O	1.66 ± 0.01	1	25 ± 5	10.1	-4.5
	O	1.91 ± 0.01	4	130 ± 10		
	O	2.39 ± 0.01	1	30 ± 15		
	Mo	3.44 ± 0.01	2	70 ± 10		
	Mo	3.70 ± 0.02	2	90 ± 15		
+0.5 V	O	1.69 ± 0.02	1	40 ± 10	12.9	-8.3
	O	1.91 ± 0.01	4	150 ± 10		
	O	2.39 ± 0.02	1	40 ± 15		
	Mo	3.44 ± 0.01	2	60 ± 10		
	Mo	3.72 ± 0.01	2	80 ± 20		

**Table 5.3.** Structural parameters for first five coordination shells (Mo—O and Mo—Mo) derived from fits to acquired in situ Mo K-edge EXAFS spectra for Ppy/[P(Mo<sub>3</sub>O<sub>10</sub>)<sub>4</sub>]<sup>3-</sup> film modified electrode at gradually changing redox state: -0.3 V, -0.2 V, -0.1 V, +0.2 V, +0.3 V and +0.5 V vs. Ag/AgCl sat'd KCl reference electrode. Background electrolyte: 0.5 M H<sub>2</sub>SO<sub>4</sub>. Data fitted up to the value of  $k_{max}=12$ . Coordination numbers N were kept at fixed values for data fitting. FI – fit index,  $\Delta E_0 \pm 5$ eV.

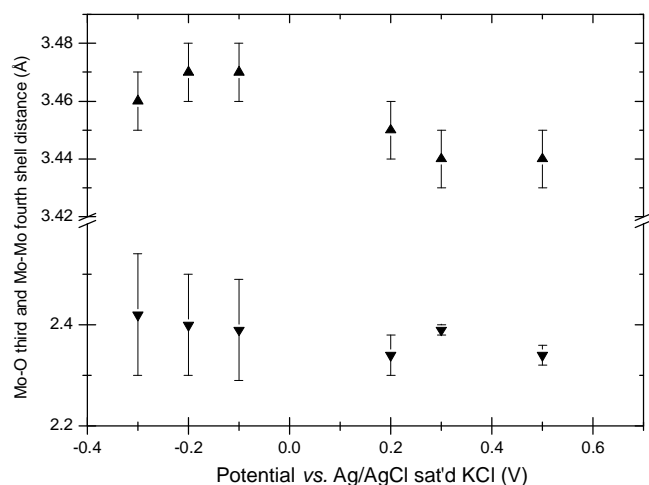
Table 5.2 shows structural parameters derived from EXAFS K-edge data for four different standards: MoO<sub>2</sub> solid powder, MoCl<sub>5</sub> and MoOCl<sub>4</sub> 25 mM aqueous solutions, and H<sub>3</sub>[P(Mo<sub>3</sub>O<sub>10</sub>)<sub>4</sub>] 25 mM solution in 0.5 M H<sub>2</sub>SO<sub>4</sub>.

Table 5.3 includes summarized structural parameters – distances, coordination numbers and Debye-Waller factors – for five coordination shells. Parameters were derived from acquired in situ EXAFS Mo K-edge data for the Ppy/P(Mo<sub>3</sub>O<sub>10</sub>)<sub>4</sub><sup>3-</sup> composite film modified electrode at five different redox states: -0.3 V, -0.2 V, -0.1 V, +0.2 V, +0.3 V and +0.5 V vs. Ag/AgCl sat'd KCl reference electrode, in 0.5 M H<sub>2</sub>SO<sub>4</sub> background electrolyte.

Plots showing bond lengths at a function of potential for the first four coordination shells around Mo atom (Mo—O and Mo—Mo) are presented in Figure 5.16. Unfortunately these do not exhibit any significant changes, not only for more distant shells, but even for the first Mo—O coordination shell at a distance of about 1.6 Å.



**Figure 5.16.** Mo—O distances for the first (—■—) and second (—●—) coordination shells as a function of redox state for the Ppy/[P(Mo<sub>3</sub>O<sub>10</sub>)<sub>4</sub>]<sup>3-</sup> composite film modified electrode. Plots based on data shown in the Table 5.3.



**Figure 5.17.** Mo—O distances for the third (—▲—) and Mo—Mo fourth (—▼—) coordination shells as a function of redox state for the Ppy/[P(Mo<sub>3</sub>O<sub>10</sub>)<sub>4</sub>]<sup>3-</sup> composite film modified electrode. Plots based on data shown in the Table 5.3.

Sample	Element	R (Å)	N	$\sigma^2(10^{-4}\text{Å}^2)$	FI (%)	$\Delta E_0(\text{eV})$
<b>Acidic solution</b> <b>0.5 M H<sub>2</sub>SO<sub>4</sub></b>	O	1.70±0.03	1	50±10	17.8	-5.6
	O	1.93±0.03	4	350±50		
	Mo	2.32±0.04	1	100±50		
	Mo	3.45±0.02	2	90±20		
	Mo	3.70±0.03	2	85±20		
<b>Neutral solution</b> <b>deionised H<sub>2</sub>O</b>	O	1.70±0.03	1	60±15	11.7	-5.5
	O	1.91±0.02	4	230±30		
	Mo	2.37±0.02	1	70±30		
	Mo	3.46±0.04	2	85±15		
	Mo	3.73±0.01	2	75±15		
<b>Alkaline solution</b> <b>0.3 M Na<sub>2</sub>CO<sub>3</sub></b>	O	1.73±0.02	1	105±25	17.2	-6.4
	O	1.94±0.02	4	340±60		
	Mo	2.38±0.03	1	90±40		
	Mo	3.46±0.01	2	90±15		
	Mo	3.72±0.04	2	90±20		

**Table 5.4.** Structural parameters derived from fits to Mo K-edge EXAFS spectra for [P(Mo<sub>3</sub>O<sub>10</sub>)<sub>4</sub>]<sup>3-</sup> anion in three different pH value solutions: acidic (0.5 M H<sub>2</sub>SO<sub>4</sub>), neutral (distilled water) and alkaline (0.3 M Na<sub>2</sub>CO<sub>3</sub>, pH 10.7). Data fitted up to the value of  $k_{max}=12$ . AFAC: 0.9. Coordination numbers N were kept at fixed values for data fitting. FI – fit index,  $\Delta E_0 \pm 5$  eV.

XANES of Ppy/[P(Mo<sub>3</sub>O<sub>10</sub>)<sub>4</sub>]<sup>3-</sup> modified electrodes at -0.3 V, +0.2 V, +0.3 V and +0.5 V along with standard samples is shown in Figure 5.14. Also in this case no significant variations in the shape or position of the spectra with changing oxidation state of Mo atoms can be seen.

Table 5.4 includes parameters derived from EXAFS fits for H<sub>3</sub>[P(Mo<sub>3</sub>O<sub>10</sub>)<sub>4</sub>] in solutions of different pH values: alkaline solution (0.3 M Na<sub>2</sub>CO<sub>3</sub>), acidic solution (0.5 M H<sub>2</sub>SO<sub>4</sub>) and neutral, distilled water solution.

## 5.6 Conclusions

Cyclic voltammograms of Ppy/[P(Mo<sub>3</sub>O<sub>10</sub>)<sub>4</sub>]<sup>3-</sup> composite film modified electrodes display well defined peaks at potentials -0.06 V, +0.19 V and +0.34 V *vs.* Ag/AgCl sat'd KCl reference electrode in the range from -0.3 V to +0.5 V in 0.5 M H<sub>2</sub>SO<sub>4</sub>. For thick hybrid films, peaks in the cyclic voltammograms become less clearly defined due to a stronger contribution from the broad polypyrrole signal. Composite films also exhibit good stability, as can be seen in voltammetric responses before and after an extended time of data acquisition during EXAFS experiments (Figure 5.6). Stability and very good heteropolyanion retention in the host matrices were also reported previously by other authors.

In X-ray photoelectron spectroscopy data, changes in the oxidation state of the molybdenum redox centre are seen very clearly in deconvoluted Mo 3d XPS photoelectron lines (Figure 5.11a–5.11e). Even for the most reduced sample (at -0.2 V *vs.* SCE) significant amounts of Mo<sup>6+</sup> are present. As was suggested in earlier chapters, it might be due to the oxidative influence of air during the transport of the sample to the XPS vacuum chamber. This effect should be diminished by the polypyrrole layer, but the surface would be the most prone to such an effect and XPS is a surface-sensitive method. Facile oxidation of polyoxometallate anions by molecular oxygen was also reported in other publications.<sup>38, 47</sup> At the most oxidative potential (+0.5 V *vs.* SCE) the majority of molybdenum atoms comprise Mo<sup>6+</sup>. It was hoped that these changes in Ppy/[P(Mo<sub>3</sub>O<sub>10</sub>)<sub>4</sub>]<sup>3-</sup> composite film modified electrode, so clearly observed in XPS data, could be studied in greater detail using the capabilities of EXAFS experiments.

Specifically, it was intended to investigate structural changes (e.g. change in the bond lengths) accompanying redox state changes and how the charge is distributed between the metal atoms. Structural parameters of the polyoxomolybdate Keggin ion derived from fits to EXAFS Mo K-edge data are summarized in Table 5.2. Unfortunately, as can be seen in the plots showing bond lengths at a function of potential for the first four coordination shells around the Mo atom (Mo—O and Mo—Mo, Figure 5.16 and 5.17, respectively) there are no significant changes, not only for more distant shells, but even for the first Mo—O coordination shell at a distance of about 1.6 Å. Also, in the case of XANES of Ppy/[P(Mo<sub>3</sub>O<sub>10</sub>)<sub>4</sub>]<sup>3-</sup> modified electrodes at -0.3 V, +0.2 V, +0.3 V and +0.5 V (Figure 5.14) no significant variations in the shape or position of the spectra with the changing oxidation state of Mo atoms can be seen. The problem with extracting information from the XANES and EXAFS data for such a complicated system as heteropolyanions may be similar to the one discussed in Chapter III – the case of multiple Fe sites in the Prussian Blue films. There are several distinct Mo sites present in the Ppy/[P(Mo<sub>3</sub>O<sub>10</sub>)<sub>4</sub>]<sup>3-</sup> composite, and the signal obtained in the XAS experiment is a sum of signals obtained from Mo atoms in different oxidation states, each with a different coordination and local environment. Therefore, although the Ppy/[P(Mo<sub>3</sub>O<sub>10</sub>)<sub>4</sub>]<sup>3-</sup> composite system was successfully electrodeposited and measured in the in situ spectroelectrochemical cell, and showed significant changes in the XPS experiment, it did not prove to be a promising material not only for dynamic EXAFS studies, but even for standard (static) EXAFS experiments.

## 5.7 References

1. Jeanin, Y. P., *Chem. Rev.* **1998**, 98, 51.
2. Gouzerh, P.; Che, M., *L'actualite chimique* **2006**, 298, 9.
3. Keggin, J. F., *Nature* **1933**, 131, 908.
4. Katsoulis, D. E., *Chem. Rev.* **1998**, 98, 359.
5. Itoh, T.; Matsubara, I.; Shin, W.; Izu, N.; Nishibori, M., *Sensors and Actuators B* **2008**, 128, 512.
6. Itoh, T.; Wang, J.; Matsubara, I.; Shin, W.; Izu, N.; Nishibori, M.; Murayama, N., *Mater. Lett.* **2008**, 62, 3021.
7. Gkika, E.; Kormali, P.; Antonaraki, S.; Dimoticali, D.; Papaconhstantinou, E.; Hiskia, A., *Int. J. Photoenergy* **2004**, 06, 227.
8. Bielanski, A.; Lubanska, A.; Micek-Ilnicka, A.; Pozniczek, J., *Coord. Chem. Rev.* **2005**, 249, 2222.
9. Malecka, A.; Pozniczek, J.; Micek-Ilnicka, A.; Bielanski, A., *J. Mol. Catal. A: Chem.* **1999**, 138, 67.
10. Li, J.; Zhai, F.; Wang, X.; Li, E.; Zhang, S.; Zhang, Q.; Du, X., *Polyhedron* **2008**, 27, 1150.
11. Li, J.; Tan, R.; Liu, R.; Wang, X.; Li, E.; Zhai, F.; Zhang, S., *Inorg. Chem. Commun.* **2007**, 10, 216.
12. Rhule, J. T.; Hill, C. L.; Judd, D. A., *Chem. Rev.* **1998**, 98, 327.
13. Spiccia, L.; Casey, W. H., *Geochim. Cosmochim. Acta* **2007**, 71, 5590.
14. Pesaresi, L.; Brown, D. R.; Lee, A. F.; Montero, J. M.; Williams, H.; Wilson, K., *Appl. Catal., A: General* **2009**, 360, 50.
15. Muller, A.; Sessoli, S.; Krickemeyer, E.; Bogge, H.; Meyer, J.; Gatteschi, D.; Pardi, L.; Westphal, J.; Hovemeier, K.; Rohlfing, R.; Doring, J.; Hellweg, F.; Beugholt, C.; Schmidtman, M., *Inorg. Chem.* **1997**, 36, 5239.
16. Lehmann, J.; Gaita-Arino, A.; Coronado, E.; Loss, D., *Nat. Nanotech.* **2007**, 2, 312.
17. Hiskia, A.; Troupis, A.; Antonaraki, S.; Gkika, E.; Kormali, P.; Papaconhstantinou, E., *Int. J. Env. Anal. Chem.* **2006**, 86, 233.

18. Gaspar, A. R.; Gamelas, J. A. F.; Evtuguin, D. V.; Neto, C. P., *Green Chem.* **2007**, *9*, 717.
19. Debiemme-Chouvy, C.; Bernard, M. C.; Cachet, H.; Deslouis, C., *Surf. Interface Anal.* **2006**, *38*, 531.
20. Fabre, B.; Bidan, G., *Electrochim. Acta* **1997**, *42*, 2587.
21. Karnicka, K.; Chojak, M.; Miecznikowski, K.; Skunik, M.; Baranowska, B.; Kolary, A.; Piranska, A.; Palys, B.; Adamczyk, L.; Kulesza, P. J., *Bioelectrochem.* **2005**, *66*, 79.
22. Balamurugan, A.; Chen, S.-M., *Electroanal.* **2007**, *19*, 1616.
23. Gaspar, S.; Muresan, L.; Patrut, A.; Popescu, I. C., *Anal. Chim. Acta* **1999**, *385*, 111.
24. Wang, X. L., *Mater. Lett.* **2004**, *58*, 1661.
25. Abrantes, L. M., *Electrochim. Acta* **2002**, *47*, 1481.
26. Maestre, J. M.; Lopez, X.; Bo, C.; Poblet, J. M.; Casan-Pastor, N., *J. Am. Chem. Soc.* **2001**, *123*, 3749.
27. Balula, M. S. S.; Santos, I. C. M.; Gamelas, J. A. F.; Cavaleiro, A. M. V.; Binsted, N.; Schlindwein, W., *Eur. J. Inorg. Chem.* **2007**, 1027.
28. Debiemme-Chouvy, C.; Cachet, H.; Deslouis, C., *Electrochim. Acta* **2006**, *51*, 3622.
29. Zhang, J., *Inorg. Chem.* **2006**, *45*, 3732.
30. Keita, B.; Nadjo, L., *J. Electroanal. Chem.* **1988**, *243*, 481.
31. Bidan, G.; Genies, E. M.; Lapkowski, M., *Chem. Commun.* **1988**, 533.
32. Pozniaczek, J.; Bielanski, A.; Kulszewicz-Bajer, I.; Zagorska, M.; Kruczala, K.; Dyrek, K.; Pron, A., *J. Mol. Catal.* **1991**, *69*, 223.
33. Wang, P.; Li, Y., *J. Electroanal. Chem.* **1996**, *408*, 77.
34. Muller, A.; Das, S. K.; Krickemeyer, E.; Kuhlmann, C., *Inorganic Synthesis*. Ed.: J. R. Shapley, Wiley & Sons, **2004**, pp 191-202.
35. Muller, A.; Das, S. K.; Bogge, H.; Schmidtman, M.; Botar, A.; Patrut, A., *Chem. Commun.* **2001**, 657.
36. Furukawa, N.; Nishio, K.; Scrosati, B., in *Applications of Electroactive Polymers*, Chapman and Hall: London, 1995, pp 150.
37. Bidan, G.; Genies, E. M.; Lapkowski, M., *J. Electroanal. Chem.* **1988**, *251*, 297.

38. Gomez-Romero, P.; Lira-Cantu, M., *Adv. Mater.* **1997**, *9*, 144.
39. Chehimi, M. M.; Abdeljalil, E., *Synth. Met.* **2004**, *145*, 15.
40. Zhu, Z.; Tain, R.; Rhodes, C., *Can. J. Chem.* **2003**, *81*, 1044.
41. Dong, S.; Jin, W., *J. Electroanal. Chem.* **1993**, *354*, 87.
42. Mosselmans, J. F. W.
43. Moulder, J. F.; Stickle, W. F.; Sobol, P. E.; Bomben, K. D., *Handbook of X-ray Photoelectron Spectroscopy*. Perkin-Elmer Corporation, Minnesota, 1992.
44. Kang, E. T.; Neoh, K. G.; Ong, Y. K.; Tan, B. T. G., *Macromolecules* **1991**, *24*, 2822.
45. Carver, J. C.; Schweitzer, G. K.; Carlson, T. A., *J. Chem. Phys.* **1972**, *57*, 973.
46. Quennoy, A.; Rothschild, A.; Gerard, I.; Etcheberry, A.; Debiemme-Chouvy, C., *J. Clust. Sci.* **2002**, *13*, 313.
47. Pope, M. T., *Heteropoly and Isopoly Oxometalates*. Springer: Berlin, 1983.

# CHAPTER VI

## NANOGRAVIMETRIC OBSERVATION OF ION EXCHANGE CHARACTERISTICS FOR POLYPYRROLE FILM p-DOPING IN THE DEEP EUTECTIC IONIC LIQUID ETHALINE

### 6.1 Introduction

Electrochemically synthesized conducting polymers (CP) are organic materials which exhibit electronic properties comparable to metals and in addition mechanical and physical properties of a polymer.<sup>1, 2</sup> Potential applications of CP include batteries/supercapacitors,<sup>3, 4</sup> (bio)chemical sensors,<sup>5-7</sup> photovoltaic<sup>8</sup> and electrochromic<sup>9</sup> devices, drug delivery,<sup>10</sup> conducting textiles,<sup>11</sup> corrosion control<sup>12</sup> and electromechanical actuators.<sup>13</sup> Their limitations are at the moment fast degradation of the main properties such as conductivity and electrochemical stability. The size and character of the dopant counterion incorporated during the synthesis, as well as of the one present during the potentiodynamic cycling can have a remarkable effect on the ion movement occurring during redox processes. It may also influence characteristics of the polymer such as structure and conductivity. Therefore ionic liquids (IL) (loosely defined as salts that are liquid below 100°C<sup>14-16</sup>) offer a combination of chemical and physical properties that make them interesting as both electrolyte and as a solvent

instead of the use of the conventional solvent/electrolyte systems, as they have very different solvation characteristics to conventional molecular solvents. Ethaline belongs to a relatively new class of IL, deep eutectic solvents, based on eutectic mixtures of choline chloride with a hydrogen bond donor species (here, ethylene glycol, EG).<sup>17-19</sup> The vast majority of reports on conducting polymers in ionic liquid media describe a need for controlled anaerobic environment conditions, due to the sensitivity of the ionic liquid to water, but Ethaline does not suffer from this problem.<sup>20</sup> Deep eutectic solvents have similar properties to ambient temperature ionic liquids but are non-reactive with water and in many cases are non-toxic and biodegradable.<sup>17</sup> One of the main advantages of the use of IL in an electrochemical context is a wide potential “window” within which to conduct electrochemical transformations (including the electrodeposition of technologically important metals<sup>16</sup>) and access to the much higher potentials previously unreachable and greater electrochemical stability.

The electrochemical quartz crystal microbalance was used to investigate redox-driven ion transfers accompanying p-doping of polypyrrole in the choline chloride-based deep eutectic ionic liquid Ethaline. Deep eutectic solvents have similar properties to ambient temperature ionic liquids but are nonreactive with water and in many cases are non-toxic and biodegradable.<sup>17</sup> Conducting polymers have been studied extensively in recent years and use of ionic liquids as electrolytes can bring potential benefits and significant improvements in lifetimes and performance of conducting polymer based devices.<sup>21</sup> The polymer chosen for this study, polypyrrole, is one of the most widely electrochemically studied conducting polymers. Since it is predominantly characterized and applied in aqueous media, where its electrochemistry is dominated by anionic dopant exchange, this provides an excellent test material delivers outcomes of wide relevance.

## 6.2 Objectives

The overwhelming majority of electrochemical studies and applications of electronically conducting polymers involve an environment dominated by a molecular fluid – water or a conventional organic solvent. The p-doping of these materials, upon which most applications rely, usually involves exchange of an anionic dopant between the polymer and electrolyte solution. Exceptions are the cases where the anion is

sufficiently large, highly charged or entangled that it is rendered immobile and only the cation can transfer (in the opposite direction). Formally, the conducting polymer/immobile anion contribution could be regarded as a cation-exchanging composite. The question addressed in this work was whether the normal pattern of behaviour is retained in the very different environment of the ionic liquid Ethaline.

Properties and possible applications of electrochemically synthesized conducting polymers invariably rely on redox-driven exchange between the polymer and its bathing fluid of charged species. These ions may play the role of dopants influencing conductivity or of charge balancing species (compensating electron population changes), analytes or reactants being pre-concentrated in the film, reagents for delivery into the ambient medium or plasticizers/stiffeners. Restriction to exchange of anions, as is commonly the case, is a major limitation on the species with which any device can interact. Additionally, both the dynamics of the system (mobile species diffusion rates and polymer viscoelasticity) and the local reaction environment are influenced by the film's solvent population. Since use of ionic liquids as novel media for a range of (electro)chemical processes is of considerable interest,<sup>14-16</sup> it was sought to explore how the above notions are changed in such an environment, where physical properties are not dominated by neutral molecules, ionic strength is extremely high and chemical interaction with the film may be dominated by either ion type.

### 6.3 Experimental

Polypyrrole (PPy) films were electrodeposited from mixture of Ethaline and deionised water (1:1 by volume) and subsequently characterized in two contrasting monomer-free electrolytes: pure ionic liquid (Ethaline) and aqueous 0.5 M KCl. Deposition was potentiodynamic in the potential range  $-0.60 < E/V$  (vs.  $\text{Ag}/\text{Ag}^+$ )  $< +0.80$  with a scan rate  $\nu = 20 \text{ mV s}^{-1}$ . The film thickness was controlled via the number of cycles. To investigate film dynamics, voltammetric characterization was performed as a function of scan rate in the range  $-0.60 < E/V < +0.50$ . Scan rates were:  $\nu = 5 \text{ mV s}^{-1}$ ,  $10 \text{ mV s}^{-1}$  and  $20 \text{ mV s}^{-1}$ . By restricting the number of deposition cycles it was possible to operate in the acoustically thin regime, in which acoustic wave resonator (QCM) frequency shifts are linearly related to film mass changes by the Sauerbrey equation.<sup>22</sup>

Choline chloride (2-hydroxyethyl-trimethylammonium chloride, ChCl) (Aldrich 99%), ethylene glycol (EG) (Aldrich 99 + %) and pyrrole (Aldrich 98%) were used as received. The eutectic solvent (Ethaline) was formed by continuous stirring and gentle heating of EG and ChCl (2:1) until a homogenous, colourless liquid was formed. Film rigidity was established via crystal impedance spectra recorded using an Agilent Technologies E5061A network analyser. The data acquisition and review software were developed using the Agilent Virtual Engineering Environment (VEE v7.52) software. Analysis, modelling and fitting of the measured data was performed with Visual Basic for Applications inside Microsoft Excel using protocols reported elsewhere.<sup>19</sup> The quartz resonators were 10 MHz AT-cut unpolished crystals coated with Au (ICM, Oklahoma City, USA), with piezoelectric and electrochemically active areas 0.21 cm<sup>2</sup> and 0.23 cm<sup>2</sup>, respectively. One face of the crystal was exposed to solution forming a working electrode in a three-electrode cell with Ag wire reference electrode (in Ethaline) and Ag/AgCl saturated KCl (in 0.5 M KCl) reference electrode and a Pt mesh as a counter electrode. All data were acquired at room temperature.

Resonator frequency changes were interpreted gravimetrically according to the Sauerbrey equation.<sup>22</sup> For the 10 MHz quartz crystal resonators used here it takes form:

$$\Delta m = -1.1 \cdot \Delta f \quad (6.1)$$

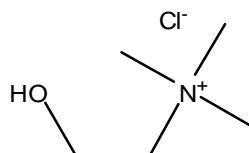
where  $\Delta m$  (ng) is mass change and  $\Delta f$  (Hz) is frequency change. Film thickness, 600 nm, was determined gravimetrically, using  $\Delta f$  for film deposition and a film density of 1 g cm<sup>-3</sup>. For Ethaline, cyclic voltammetric data were smoothed using a five point moving average.

Molar mass changes  $M$  (g mol<sup>-1</sup>) were calculated according to:

$$M = \frac{\Delta m F}{Q} \quad (6.2)$$

where  $\Delta m$  (g) is the mass change,  $F$  (C mol<sup>-1</sup>) is the Faraday constant and  $Q$  (C) is the charge passed.

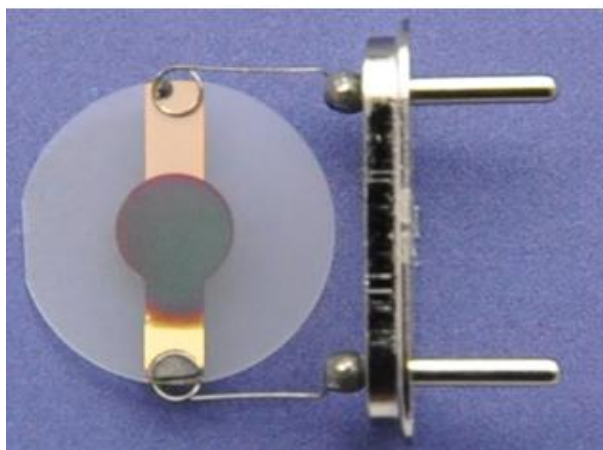
Ethaline belongs to relatively new class of ionic liquids based on eutectic mixtures of choline chloride and, here, ethylene glycol (EG) as a hydrogen bond donor. There is still a debate as to whether it is present as  $[\text{EG}\cdot\text{Cl}]^-$  or  $[(\text{EG})_2\text{Cl}]^-$ . Figure 6.1 illustrates the first possibility.



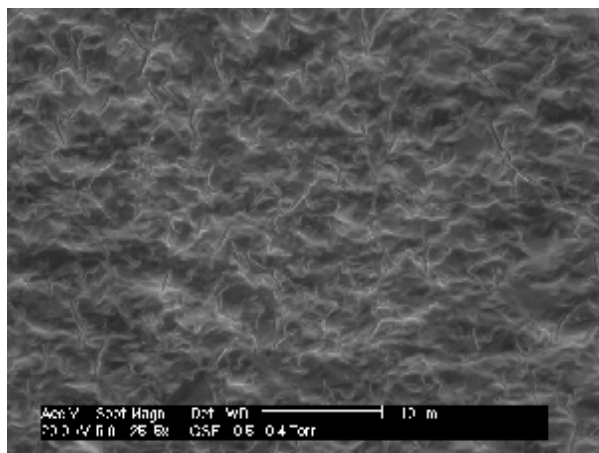
**Figure 6.1.** Ethaline: relatively new class of ionic liquids based on eutectic mixtures of choline chloride and, here, ethylene glycol (EG) as hydrogen bond donor.

## 6.4 Results

Figure 6.2 shows 10 MHz EQCM with polypyrrole film electrodeposited on the rough Au electrode ( $0.23\text{ cm}^2$  and  $0.21\text{ cm}^2$  electroactive and piezoelectric areas, respectively) from the 1:1 mixture (by volume) of deionised water and Ethaline, using the procedure described in the experimental part of this chapter.

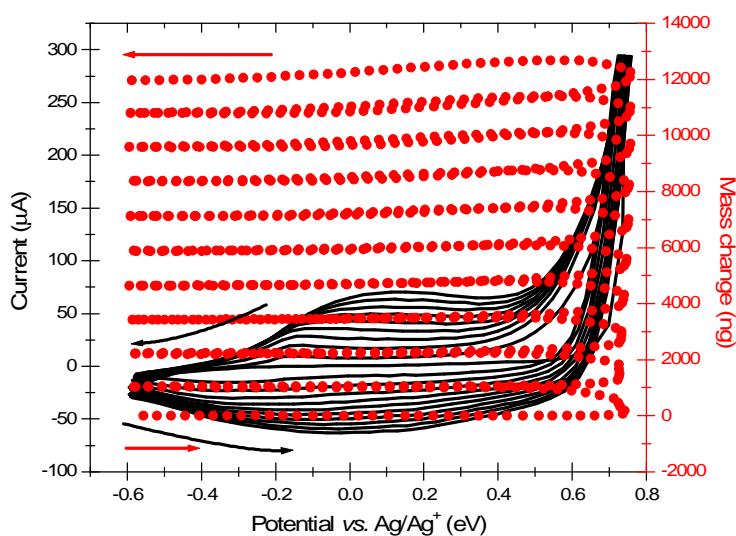


**Figure 6.2.** Polypyrrole film electrodeposited from a mixture of Ethaline and deionized water (1:1 by volume) in the range  $-0.6\text{ V} < E/\text{V vs. Ag}/\text{Ag}^+ < +0.8\text{ V}$ . Film deposited on the 10 MHz quartz resonator coated with Au electrode with piezoelectric and electrochemically active areas of  $0.1$  and  $0.23\text{ cm}^2$ , respectively.



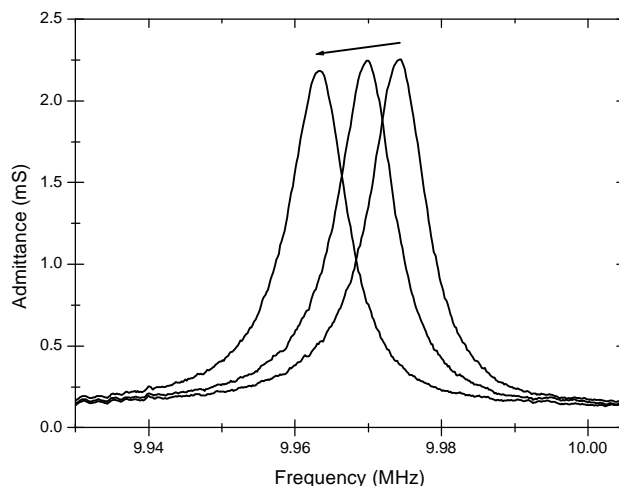
**Figure 6.3.** Scanning Electron Microscope picture of polypyrrole film electrodeposited from the deionised water-Ethaline mixture on the rough Au electrode.

Figure 6.3 shows a Scanning Electron Microscope (SEM) picture of the same Ppy film. Figure 6.4 shows potentiodynamic electrodeposition of polypyrrole film from a mixture of Ethaline and deionized water at scan rate  $20 \text{ mV s}^{-1}$  in the range  $-0.6 \text{ V} < E/\text{V vs. Ag}/\text{Ag}^+ < +0.8 \text{ V}$ . In the same graph the parallel increase of mass on the electrode with each subsequent cycle is plotted.



**Figure 6.4.** Potentiodynamic electrodeposition of polypyrrole film from a mixture of Ethaline and deionized water (1:1 by volume). Scan rate  $20 \text{ mV s}^{-1}$  in the range  $-0.6 \text{ V} < E/\text{V vs. Ag}/\text{Ag}^+ < +0.8 \text{ V}$ . Thickness controlled via the number of scans – here, 10, yielding film thickness of 600 nm. Current (—), mass (—●—).

Acoustic wave admittance spectra acquired for the deposition of Ppy film from 1:1 deionised water and Ethaline mixture are shown in Figure 6.5. Three plotted admittance spectra were measured for the beginning, midpoint and the end of deposition (from right to left). Admittance decreases only by 3% for the 600 nm film; therefore it is regarded as acoustically rigid.



**Figure 6.5.** Acoustic wave admittance spectra of electrodeposition of the PPy film from a mixture of Ethaline and deionised water (1:1 by volume). Solutions and potential control function as described in the text. Three admittance spectra shown were measured for the beginning, midpoint and the end of deposition (from right to left). Admittance decrease: 3%.

Figure 6.6 shows current and mass responses from a voltammetric experiment in which a Ppy film was redox cycled in pure ionic liquid, Ethaline. It is possible to identify three distinct regions during film oxidation: region I ( $E$  vs.  $\text{Ag}/\text{Ag}^+ < -0.1$  V) shows no mass change; region II ( $-0.1$  V  $< E$  vs.  $\text{Ag}/\text{Ag}^+ < +0.4$  V) shows an increase in current associated with a significant decrease in film mass; region III ( $E$  vs.  $\text{Ag}/\text{Ag}^+ > +0.4$  V) shows an increase in film mass (to the extent of ca. 20% of the mass loss in region II). In the reduction half cycle, these trends and changes are reversed. Without a quantitative interpretation, the simplistic overview is that electroneutrality maintenance upon Ppy film oxidation is gravimetrically dominated by cation expulsion. At a more detailed, but still qualitative level, it can be seen that hysteresis in the responses of the

region II signals kinetic effects, even on the relatively modest timescale of this experiment.

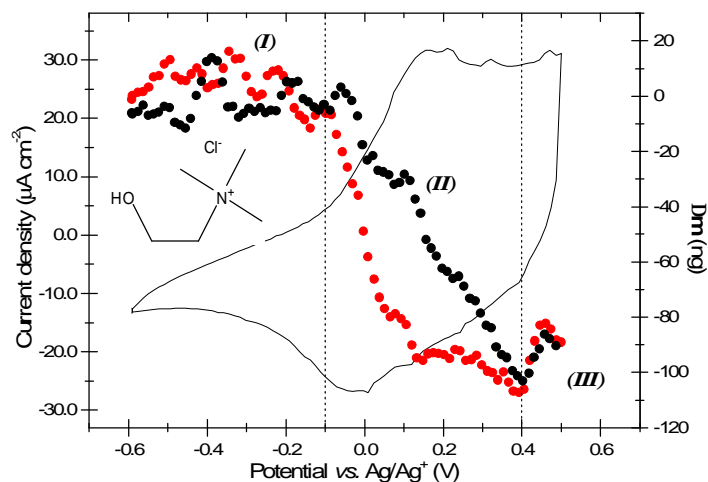


**Figure 6.6.** Current (—) and mass (••••) responses of a Ppy film during a cyclic voltammetric experiment in Ethaline background electrolyte. Scan rate  $5 \text{ mV s}^{-1}$ . Black points represent mass change ( $\Delta m$ ) during oxidation half cycle and red points represent mass change during reduction half cycle. Three distinct regions are shown: no mass change (I), decrease in film mass (II) and increase in film mass (III).

Contrasting behaviour is shown by the film in aqueous background electrolyte; Figure 6.7. Figure 6.7 shows analogous responses of the same Ppy film undergoing p-doping/undoping in KCl solution. Starting from the reduced (undoped) state there is a small film mass decrease in the beginning stages of the oxidation process. Regardless of the initial behaviour the response is dominated by a film mass increase. The possibility of this behaviour being a film “memory” of prior history (retention of mobile species) was excluded by potential cycling to exchange residual species into the effectively infinite bulk solution. This response is typical behaviour observed by a number of workers for polypyrrole redox switching in 1:1 (though not 1:2) electrolytes.<sup>23-25</sup>

Mass change vs. charge plots shown in Figure 6.8 and Figure 6.9 are derived from the data of Figure 6.5 and Figure 6.6, respectively.

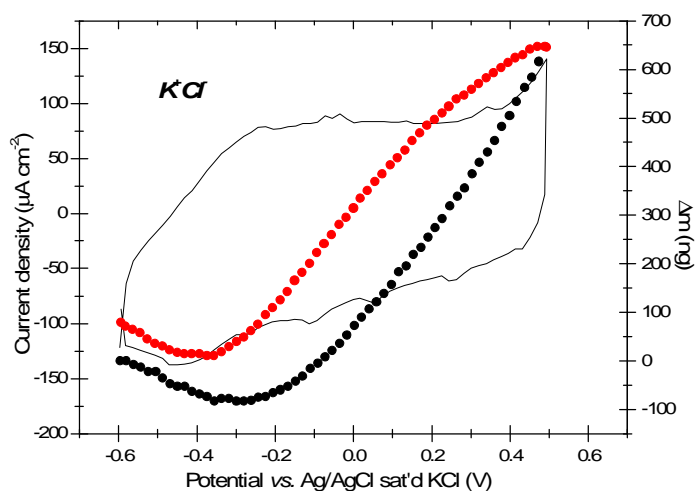


**Figure 6.7.** Current (—) and mass (•••) responses of a Ppy film (600 nm thick) during a cyclic voltammogram experiment in aqueous 0.5 M KCl background electrolyte. Scan rate  $5 \text{ mV s}^{-1}$ . Black points represent mass change ( $\Delta m$ ) during oxidation half cycle and red points represent mass change during reduction half cycle.

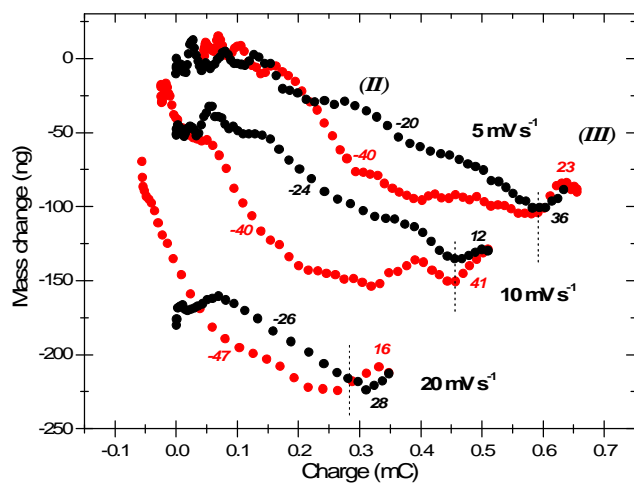


**Figure 6.8.** Mass change as a function of injected charge for a data of Figure 6.6 (scan rate  $5 \text{ mV s}^{-1}$ ) and analogues at scan rates of  $10 \text{ mV s}^{-1}$  and  $20 \text{ mV s}^{-1}$ . Black (red) points represent mass changes ( $\Delta m$ ) during oxidation (reduction) half cycles. Traces for scan rates  $10 \text{ mV s}^{-1}$  and  $20 \text{ mV s}^{-1}$  are offset vertically by  $-60 \text{ ng}$  and  $-180 \text{ ng}$ , respectively, for presentational clarity. Numbers indicate molar mass changes for indicated regions.

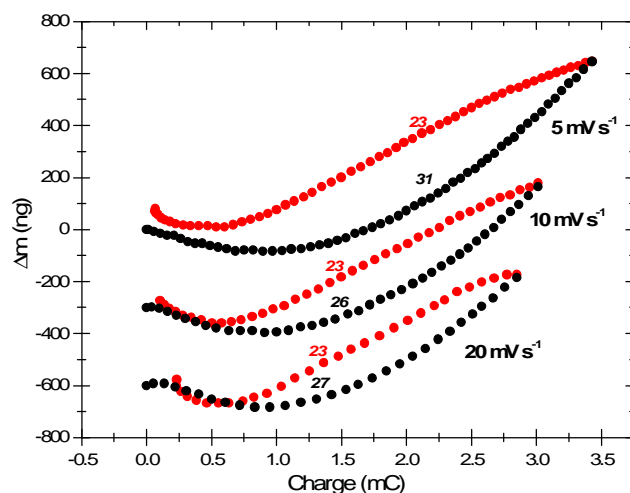


**Figure 6.9.** Mass change as a function of injected charge for (a) the data of Figure 6.7 (scan rate  $5 \text{ mV s}^{-1}$ ) and analogues at (b)  $10 \text{ mV s}^{-1}$  and (c)  $20 \text{ mV s}^{-1}$ . Black (red) points represent mass changes ( $\Delta m$ ) during oxidation (reduction) half cycles. Traces (b) and (c) are offset vertically by  $-300 \text{ ng}$  and  $-600 \text{ ng}$ , respectively. Numbers indicate molar mass changes for indicated regions.

The data is shown for two more scan rates,  $10 \text{ mV s}^{-1}$  and  $20 \text{ mV s}^{-1}$ , of the same film in ionic liquid and KCl background electrolyte. Traces are offset vertically in both figures for presentational clarity. Oxidation half cycles are represented by black points, while reduction half cycles are represented by red points. Normalized molar mass changes ( $\text{g mol}^{-1}$ ) for the oxidation and reduction half cycles for polypyrrole film cycled at  $5$ ,  $10$  and  $20 \text{ mV s}^{-1}$  in ionic liquid and aqueous solution are summarized in Table 6.1 and Table 6.2.

Ethaline				
Scan rate	Region II		Region III	
	oxidation	reduction	oxidation	reduction
<b>5 mV</b>	$-20 \pm 1$	$-40 \pm 2$	$+36 \pm 5$	$+23 \pm 5$
<b>10 mV</b>	$-24 \pm 1$	$-40 \pm 2$	$+12 \pm 2$	$+41 \pm 2$
<b>20 mV</b>	$-26 \pm 1$	$-47 \pm 2$	$+28 \pm 3$	$+16 \pm 3$

**Table 6.1.** Normalized molar mass changes ( $\text{g mol}^{-1}$ ) for the oxidation and reduction half cycles for polypyrrole film cycled at  $5$ ,  $10$  and  $20 \text{ mV s}^{-1}$  in ionic liquid (Ethaline). Data in the table refer to the plot in Figure 6.8.

0.5 M KCl		
Scan rate	oxidation	reduction
5 mV	+31 ± 2	+23 ± 1
10 mV	+26 ± 2	+23 ± 1
20 mV	+27 ± 2	+23 ± 1

**Table 6.2.** Normalized molar mass changes ( $\text{g mol}^{-1}$ ) for the oxidation and reduction half cycles for polypyrrole film cycled at 5, 10 and 20  $\text{mV s}^{-1}$  in aqueous solution of 0.5 M KCl. Data in the table refer to the plot in Figure 6.9.

These data refers to Figure 6.8 and Figure 6.9, respectively. Mass changes are not “end-to-end” values but refer to characteristic regions described in the plots.

## 6.5 Discussion and Conclusions

The behaviour of the polypyrrole film as presented in Figure 6.7 is generally attributed to predominantly anion (here chloride) exchange with the solution. This process is accompanied by some solvent transfer. Polypyrrole p-doping is clearly very different in the ionic liquid and furthermore this cannot be trivially assigned to an ion size effect. Firstly it is because it is the same anion in both cases and, secondly, the effective sizes of the cations (bearing in mind potassium ion solvation in water) are not very different.

Quantitative interpretation is facilitated by the mass change vs. charge plots shown in Figure 6.8 and Figure 6.9. In the first case of aqueous solution, the overall values of molar mass change are 18, 15 and 13 (all  $\pm 2$ )  $\text{g mol}^{-1}$  at scan rates of 5, 10 and 20  $\text{mV s}^{-1}$ , respectively. Over the most of the oxidation process, i.e. after the small initial weight loss, the corresponding values are 31, 26 and 27 (all  $\pm 2$ )  $\text{g mol}^{-1}$ . The corresponding cathodic sweep values are all  $23 \pm 1$   $\text{g mol}^{-1}$ . Polypyrrole mobile species transfers in aqueous media are a known behaviour, and broadly interpreted can be described as entry of chloride and expulsion of a small ( $< 1$   $\text{H}_2\text{O}$  per  $\text{Cl}^-$ ) amount of solvent.

In the case of the Ppy/Ethaline data presented in Figure 6.8 if the end-to-end molar mass change is calculated it yields the value of  $-17 \pm 1$   $\text{g mol}^{-1}$  if averaged over the anodic half cycles at the three scan rates, but it clearly conceals the underlying chemistry. The

three regimes of Figure 6.6 are reflected in the data of Figure 6.8 by distinct slopes, suggesting different (electro)chemical mechanisms. In the dominant region II, the normalized molar mass changes during the oxidation half cycle are -20, -24 and -26 (all  $\pm 1$ )  $\text{g mol}^{-1}$  at scan rates of 5, 10 and 20  $\text{mV s}^{-1}$ , respectively. In the reduction half cycle, the analogous values are -40, -40 and -47 ( $\pm 2$ )  $\text{g mol}^{-1}$ . In the smaller region III, the anodic half cycle values are +36, +12 and +28  $\text{g mol}^{-1}$ , and the cathodic half cycle values are +23, +41 and +16  $\text{g mol}^{-1}$  (with larger scatter due to the necessarily small number of points in this minority regime). Clearly, none of the dominant region II values coincides with the value anticipated for transfer of either ion present, namely +35.5  $\text{g mol}^{-1}$  for chloride entry and -104  $\text{g mol}^{-1}$  for choline exit.

These data signal mixed ion transfer, a feature supported by the presence of hysteresis in the  $\Delta m$ -Q plots since (irrespective of kinetics issues and the shapes of  $i$ -E and  $\Delta m$ -E plots) a  $\Delta m$ -Q plot for transfer of a single ion cannot (on grounds of electroneutrality) show hysteresis. Since the transport numbers for the anion and cation must add up to unity it is possible to calculate the fractional contributions of choline and chloride. If the transferred anion is a bare  $\text{Cl}^-$  ion, the gradient of region II suggests that charge compensation in this region is due 40% to choline exit and 60% to chloride entry. However, there is a debate as to whether the anion species is in fact  $[\text{EG}.\text{Cl}]^-$  or  $[(\text{EG})_2\text{Cl}]^-$ . In these cases choline transfer would contribute 58% and 68% (in molar terms), respectively. The explanation of the switch to region III (in the following paragraph) suggests that this involves only the anionic species, and the data are only consistent with this being transfer of  $\text{Cl}^-$ . In the same time it does not preclude the static presence of glycol/chloride aggregates, with dynamic hopping of chloride.

As the scan rate is increased, the hysteresis in the  $\Delta m$ -Q plots in regions II and III increases. At low scan rates, the mass and charge responses achieve the same values at the extrema of the scan, but at higher scan rates, the mass and charge responses at the end of a complete redox cycle fail to return to their initial values. These kinetic effects relate to the relative transfer rates of choline and chloride ions. In the light of this progressive effect, it can be speculated why there is such a sharp shift with potential from a regime gravimetrically dominated by choline expulsion (for most of the transition) to one dominated by chloride entry (for the final stages). A simple answer is

that choline expulsion is the thermodynamically favoured process, so this process operates as long as choline is available. However, there will be only a finite reservoir of choline (present as ionic liquid, analogous to “salt” in a conventional solvent medium<sup>26</sup>) in the undoped film and when this is exhausted chloride entry takes over, as the only process with available reagent – an effectively infinite reservoir in the bulk ionic liquid. Molecular explanations consistent with this might simply be that there is no room for the fully reduced film to accommodate chloride and/or that the energy of expansion to facilitate this is large. The latter is consistent with the observation from acoustic wave admittance spectra (Figure 6.5) that the film is relatively rigid. When the film is largely oxidized (region III), the free volume generated by choline expulsion allows chloride entry without the need to expand the film.

In conclusion, polypyrrole film redox switching in deep eutectic ionic liquid (Ethaline) involves very different pattern of ion transfers to aqueous media. Ionic liquid in the reduced film provides a reservoir of choline cations whose transfer (in the opposite direction to anion doping) partly satisfies electroneutrality. Quantitative nanogravimetric determination of these transfers supports and extends the only available information in this field – qualitative observation (with the use of *in situ* ECSEM) of film shrinkage upon oxidation in a 1-butyl-3-methylimidazolium bis(trifluoromethanesulfonyl)imide (BMI-TFSI) ionic liquid.<sup>27</sup>

## 6.6 References

1. Chandrasekhar, P., *Conducting Polymers, Fundamentals and Applications. A Practical Approach*. Kluwer Academic Publishers: Boston, 1999; pp 101.
2. Skotheim, T. A., *Handbook of Conducting Polymers*. 2nd ed.; Ed.: M. Dekker, New York, 1998.
3. Mastragostino, M.; Arbizzani, C.; Soavi, F., *Sol. St. Ionics* **2002**, *148*, 493.
4. Song, H. K.; Palmore, G. T. R., *Adv. Mater.* **2006**, *18*, 1764.
5. Bartlett, P. N.; Cooper, J. M., *J. Electroanal. Chem.* **1993**, *362*, 1.
6. Bobacka, J., *Electroanal.* **2006**, *18*, 7.
7. Maksymiuk, K., *Electroanal.* **2006**, *18*, 1537.
8. Giroto, E. M.; Gazotti, W. A.; Tormena, C. F.; De Paoli, M. A., *Electrochim. Acta* **2002**, *47*, 1351.
9. Marcel, C.; Tarascon, J. M., A all-plastic  $\text{WO}_3 \times \text{H}_2\text{O}$ /polyaniline electrochromic device. *Sol. St. Ionics* **2001**, *143*, 89.
10. Pernaut, J. M.; Reynolds, J. R., *J. Phys. Chem. B* **2000**, *104*, 4080.
11. Micusik, M.; Nedelcev, T.; Omastova, M.; Krupa, I.; Olejnikova, K.; Federko, P.; Chehimi, M. M., *Synth. Met.* **2007**, *157*, 914.
12. Spinks, G. M.; Dominis, A. J.; Wallace, G. G.; Tallman, D. E., *J. Sol. St. Electrochem.* **2002**, *6*, 85.
13. Smela, E., *Adv. Mater.* **2003**, *15*, 481.
14. Buzzeo, M. C.; Evans, R. G.; Compton, R. G., *Chem. Phys. Chem.* **2004**, *5*, 1106.
15. Welton, T., *Coord. Chem. Rev.* **2004**, *248*, 2459.
16. Endres, F.; Abbott, A. P.; MacFarlane, D. R., *Electrodeposition from Ionic Liquids*. Wiley-WCH: Weinheim, 2008.
17. Abbott, A. P.; Boothby, D.; Capper, G.; Davies, D. L.; Rasheed, R. K., *J. Am. Chem. Soc.* **2004**, *126*, 9142.
18. Abbott, A. P.; Capper, G.; Davies, D. L.; Rasheed, R. K.; Tambyrajah, V., *Chem. Comm.* **2003**, 70.
19. Abbott, A. P.; Nadhra, S.; Postlethwaite, S.; Smith, E. L.; Ryder, K. S., *Phys. Chem. Chem. Phys.* **2007**, *9*, 3735.

20. Huddleston, J. G.; Visser, A. E.; Reichert, W. M.; Willauer, H. D.; Broker, G. A.; Rogers, R. D., *Green Chem.* **2001**, *3*, 156.
21. Pringle, M. P.; Forsyth, M.; MacFarlane, D. R., *Conducting Polymers in Electrodeposition from Ionic Liquids*. Eds.: D. R. MacFarlane; A. P. Abbott, WILEY-VCH: Weinheim, 2008; pp 167.
22. Sauerbrey, G. Z., *Z. Phys.* **1959**, *155*, 202.
23. Bose, C. S. C.; Basak, S.; Rajeshwar, K., *J. Phys. Chem.* **1992**, *96*, 9899.
24. Maia, G.; Torresi, R. M.; Ticianelli, E. A.; Nart, F. C., *J. Phys. Chem.* **1996**, *100*, 15910.
25. Yang, H.; Kwak, J., *J. Phys. Chem. B* **1997**, *101*, 4656.
26. Bruckenstein, S.; Hillman, A. R., *J. Phys. Chem.* **1991**, *95*, 10748.
27. Arimoto, S.; Oyamatsu, D.; Torimoto, T.; Kuwabata, S., *Chem. Phys. Chem.* **2008**, *9*, 763.

## CONCLUSIONS

The specific conclusions are given at the end of each of the chapters of this thesis. The purpose of this chapter is to draw together these conclusions with the aims of identifying generic outcomes and opportunities of future research. The main achievements of the work described in the thesis are the detailed analysis of electroactive film modified electrode structures and composition by X-ray methods. EXAFS, a technique that is sensitive to atomic structure up to 5 Å, providing interatomic distances, the number and identity of neighbouring atoms, allowing study of structure and structural changes in the electroactive films. Changes were introduced and controlled via the application of different potentials to the electrode with the surface immobilized material of interest. X-ray absorption spectroscopy (EXAFS and XANES), X-ray photoelectron spectroscopy, infrared spectroscopy and electrochemical techniques were employed to study five systems: Prussian Blue and its cobalt and nickel derivatives, iridium oxide and polypyrrole/[P(Mo<sub>3</sub>O<sub>10</sub>)<sub>4</sub>]<sup>3-</sup> composite films. A key attribute of the approach adopted here is that measurements using different techniques (e.g. electrochemical, EXAFS, XPS) are made on the same sample. This removes ambiguities associated with the more common practice of making measurements on different samples, whose composition, structure and properties – though similar – may not be identical. The combination of techniques allowed also comparison of the surface (XPS) vs. bulk (EXAFS, XANES and IR) of the samples.

For Prussian Blue, cobalt and nickel hexacyanoferrates structural parameters were derived from *ex situ* XAS experiments. For cobalt hexacyanoferrate films, cobalt was identified as the active redox site, based on clear evidence of changing bond lengths with potential. This suggests it will be an interesting candidate for future dynamic EXAFS study. The behaviour of Prussian Blue films was found to be complicated to interpret. It is because of the coexistence of two Fe-based redox sites, and additional interstitial iron species. In contrast to cobalt hexacyanoferrate, no significant changes were observed in the Ni XAS data for the nickel derivative with Fe active redox sites. It

turned out to be very difficult to prepare cobalt and nickel hexacyanoferrate films thick enough to obtain a good edge step and therefore good signal-to-noise ratio for the available on site beam flux. A more powerful synchrotron may be able to provide data of much higher quality, possibly in the *in situ* data acquisition procedure.

Polypyrrole/[P(Mo<sub>3</sub>O<sub>10</sub>)<sub>4</sub>]<sup>3-</sup> composite films showed changes in oxidation state of multiple Mo sites in XPS experiment. In the case of Ppy/[P(Mo<sub>3</sub>O<sub>10</sub>)<sub>4</sub>]<sup>3-</sup> films, XAS was measured in the *in situ* spectroelectrochemical cell. Nevertheless, this is not a promising material for a dynamic EXAFS study because of the interpretational problems – the signal obtained in the XAS experiment is a sum of signals obtained from different Mo sites.

Iridium oxide films are another promising candidate for the dynamic *in situ* EXAFS experiment. Spectra were measured at the Ir L<sub>3</sub>-edge. Iridium films were successfully characterized in the *in situ* EXAFS configuration, and changing bond lengths were observed as the potential (and thus Ir oxidation state) was changed. Based on the combination of coulometric and XAS data it was concluded, that there is approximately one electron injected/ejected per iridium site: Ir<sup>3+</sup> ⇌ Ir<sup>4+</sup>.

In addition the thesis includes nanogravimetric observation of ion exchange characteristic for polypyrrole film p-doping in the ionic liquid. This is not directly related to the XAS research presented in the other chapters, but is an outcome of preparation trials to optimise samples for EXAFS experiments. It is shown that polypyrrole film redox switching in the deep eutectic ionic liquid Ethaline involves a very different pattern of ion transfers to aqueous media. Ionic liquid in the reduced film provides a reservoir of choline cations whose transfer (in the opposite direction to anion doping) partly satisfies electroneutrality.

To summarize, the work presented in this thesis provides the foundations for the studies in the area of the *potentiodynamic* EXAFS experiments. With supporting electrochemical, QCM and XPS data the sites of redox activity were identified in a range of multi-site redox systems. Structural parameters (bond lengths, coordination numbers and Debye-Waller factors) were determined as a function of potentiostatically controlled metal charge states, for both fully and partially redox converted films. From a

technique perspective, the basis for optimising sample preparation and manipulation for potentiodynamic EXAFS measurements designed to explore structural dynamics was provided. Cobalt hexacyanoferrate and iridium oxide films were identified as the most suitable for the future X-ray synchrotron-based research, in which the aim will be to monitor the structural changes of films at the solid/liquid interface in response to an external – in this case electrochemical – stimulus under dynamic conditions.

## PUBLICATIONS

Magdalena A. Skopek, Mohamoud A. Mohamoud, Karl S. Ryder and A. Robert Hillman, *Nanogravimetric observation of unexpected ion exchange characteristics for polypyrrole film p-doping in a deep eutectic ionic liquid*, Chem. Commun., 2009, 935 – 937

A. Robert Hillman, Magdalena A. Skopek, Stephen J. Gurman, *EXAFS structural studies of electrodeposited Co and Ni hexacyanoferrate films*, accepted for publication in J. Sol. St. Electrochem.

A. Robert Hillman, Magdalena A. Skopek, Stephen J. Gurman, *X-ray spectroscopy of electrochemically deposited iridium oxide films*, submitted to Phys. Chem. Chem. Phys.

Magdalena A. Skopek, Igor Efimov and A. Robert Hillman, *Determination of intrinsic polymer dynamics from the mechanical behaviour of solvated electroactive polymer films*, manuscript in preparation